UvA-DARE (Digital Academic Repository)

Making the invisible visible

Searches for invisible Higgs decays at LHC with the ATLAS detector

Sabato, G.

Link to publication

Creative Commons License (see https://creativecommons.org/use-remix/cc-licenses):
Other

Citation for published version (APA):
Sabato, G. (2019). *Making the invisible visible: Searches for invisible Higgs decays at LHC with the ATLAS detector*.

General rights
It is not permitted to download or to forward/distribute the text or part of it without the consent of the author(s) and/or copyright holder(s), other than for strictly personal, individual use, unless the work is under an open content license (like Creative Commons).

Disclaimer/Complaints regulations
If you believe that digital publication of certain material infringes any of your rights or (privacy) interests, please let the Library know, stating your reasons. In case of a legitimate complaint, the Library will make the material inaccessible and/or remove it from the website. Please Ask the Library: https://uba.uva.nl/en/contact, or a letter to: Library of the University of Amsterdam, Secretariat, Singel 425, 1012 WP Amsterdam, The Netherlands. You will be contacted as soon as possible.

UvA-DARE is a service provided by the library of the University of Amsterdam (http://dare.uva.nl)

Download date: 03 Nov 2020

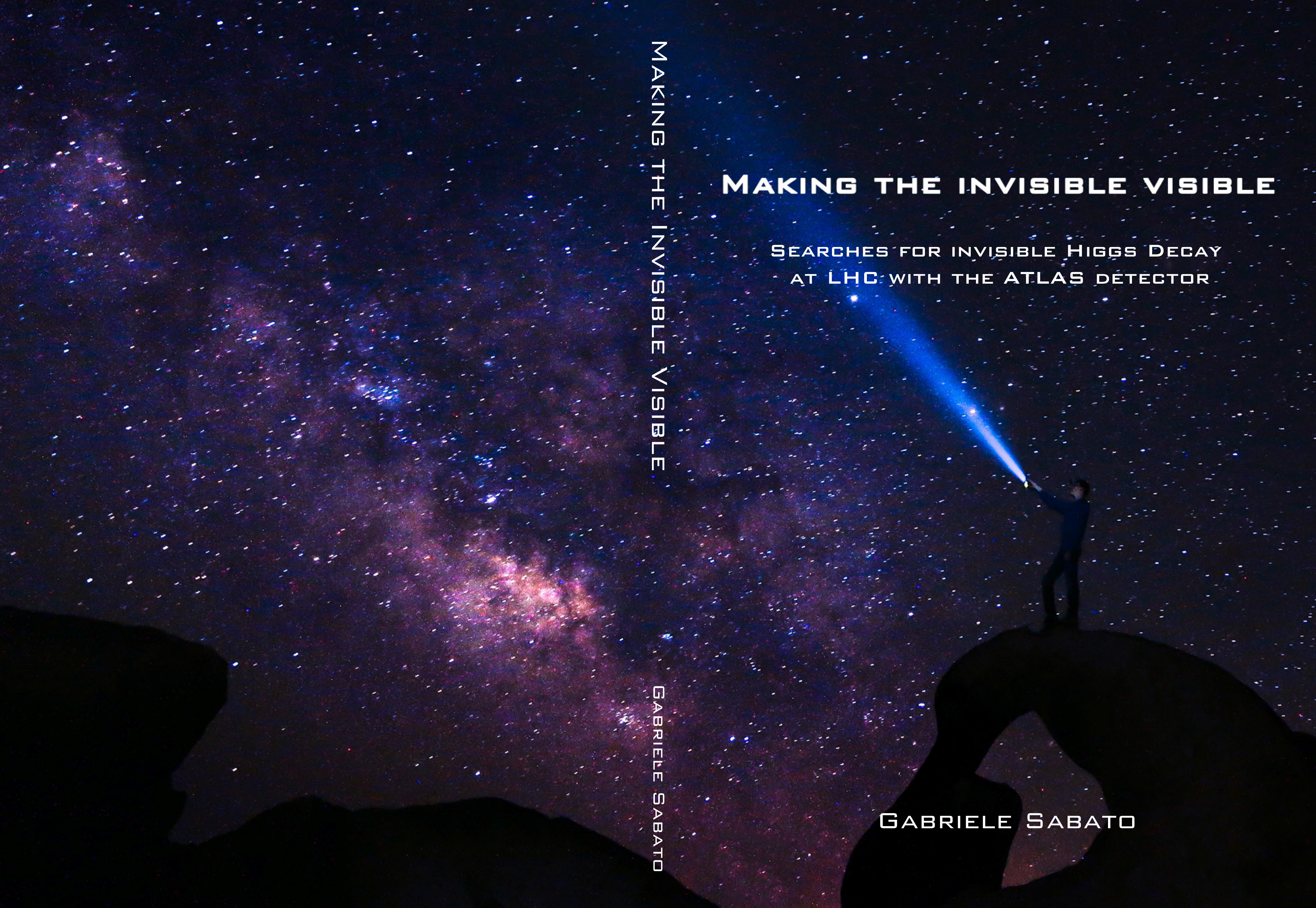

MAKING THE INVISIBLE VISIBLE

SEARCHES FOR INVISIBLE HIGGS DECAY
AT LHC WITH THE ATLAS DETECTOR

GABRIELE SABATO

MAKING THE INVISIBLE VISIBLE
GABRIELE SABATO

Making the invisible visible

Searches for invisible Higgs decays at LHC with the ATLAS detector

Gabriele Sabato

Making the invisible visible

Searches for invisible Higgs decays at LHC with the ATLAS detector

ACADEMISCH PROEFSCHRIFT

ter verkrijging van de graad van doctor aan de Universiteit van Amsterdam
op gezag van de Rector Magnificus prof. dr. ir. K.I.J. Maex
ten overstaan van een door het College voor Promoties ingestelde commissie,
in het openbaar te verdedigen in de Agnietenkapel
op dinsdag 2 Juli 2019, te 10 uur

door

GABRIELE SABATO

geboren te Belvedere Marittimo

PROMOTOR:	Prof. Dr. ir. P.J. de Jong	Universiteit van Amsterdam
COPROMOTOR:	Dr. D. Berge	Humboldt Universitat zu Berlin
OVERIGE LEDEN:	Prof. Dr. F.L. Linde	Universiteit van Amsterdam
	Prof. Dr. M.P. Decowski	Universiteit van Amsterdam
	Dr. G. Bertone	Universiteit van Amsterdam
	Prof. Dr. W. Verkerke	Universiteit van Amsterdam
	Prof. Dr. M.H.M. Merk	Vrije Universiteit Amsterdam
	Dr. J. Rojo	Vrije Universiteit Amsterdam
	Dr. S. Caron	Radboud Universiteit Nijmegen

Faculteit der Natuurwetenschappen, Wiskunde en Informatica

This work is part of the research programme of the *Stichting voor Fundamenteel Onderzoek der Materie* (FOM), which is financially supported by the *Nederlandse Organisatie voor Wetenschappelijk Onderzoek* (NWO). It was carried out at the *Nationaal Instituut voor Subatomaire Fysica (Nikhef)* in Amsterdam, the Netherlands. The author was financially supported by NWO.

Non l’avrei giammai creduto; ma farò quel che potrò

— L. Da Ponte, *Don Giovanni*

Contents

Introduction

The Standard Model (SM) of particle physics is a theoretical model which describes matter and its interaction with the three fundamental forces of nature: electromagnetic, nuclear strong and weak. This model has been proven to be extremely precise and predictive and it was completed by the discovery of the Higgs boson in 2012. Despite its extreme precision the SM has several shortcomings such as the absence of a formulation of how matter interacts with gravity or the absence of any description of the pieces of evidence from observational astrophysics that indicate the existence of Dark Matter.

The exact composition of matter in the universe is yet unknown. The most successful model, the Standard Cosmological Model, describes an universe with accelerated expansion with the majority of its composition due to Dark Energy (74%) and Dark Matter (21%), with only a fraction due to baryonic matter (5%). Dark Matter accounts therefore for the majority of matter in the universe (around 75%) compared to baryonic matter. A plethora of cosmological evidence points to its presence in the universe such as rotation curves in galaxies, gravitational lensing and the Cosmic Microwave Background. The nature of non baryonic matter is yet unknown, evidence shows that such matter interacts with ordinary matter only via gravity without any electroweak or strong interaction. A discovery would then be a major turning point for the understanding of the universe. This is why in the last years multiple theories and experimental techniques have been developed to detect Dark Matter. Dark Matter searches can be performed in different ways: by looking at the radiation spectrum in the sky searching for Dark Matter pair annihilation or by detecting the nuclear scattering of Dark Matter with ordinary matter or by producing Dark Matter at high energy colliders. The work of this thesis will be focused on the search of Dark Matter produced in proton-proton collisions at the Large Hadron Collider (LHC).

The LHC is a two-ring superconducting proton accelerator located at CERN across the French-Swiss border, with a designed center of mass of $\sqrt{s} = 14$ TeV. “A Toroidal LHC Apparatus” (ATLAS) is one of the four detectors installed at LHC and it has been recording, during 2015 and 2016, 36.1 fb^{-1} of proton-proton interactions delivered at $\sqrt{s} = 13$ TeV. With the increasing amount of data collected by CERN new analysis techniques have been implemented in the last years. Multi-variate techniques have now become widely used in the scientific community and in many companies dealing with big data. Among those techniques one of the most simple and effective is the boosted decision tree which can provide a viable alternative to traditional methodologies.

For a multi-purpose experiment such as ATLAS there are several key aspects which are crucial to implement. The data quality monitoring is surely among those as well as the possibility of having fast results on early signs of new physics. A framework that can provide such answers would then be of capital importance.

Outline of the thesis and author's contributions

This thesis describes a search for Dark Matter via Invisible Higgs decays with the ATLAS detector at LHC. The content of this thesis is divided into 6 chapters. For each one of them a small introduction and the author contribution will be provided.

- **Chapter 1** provides a theoretical background on the arguments at study in this thesis. The chapter is divided in three parts. The first part is an overview of the Standard Model of particles with a specific focus on the Higgs mechanism. The second part describes Dark Matter: the pieces of evidence, the candidates and the different searches. The third part describes the theoretical model tested in this thesis which is the Higgs portal model.
- **Chapter 2** provides an overview of the LHC and ATLAS detector. The first part is dedicated to the technical details of the collider, while the second part describes the ATLAS experiment and its subsystems.
- **Chapter 3** describes the algorithms and methods used by the ATLAS Collaboration for the reconstruction and identification of particles in proton-proton collisions.
- **Chapter 4** describes the cut-based analysis of an invisible Higgs decay in associated production with a Z boson with a final signature of two leptons and missing transverse energy. I was part of the analysis team with a specific focus on the flavour symmetry control region of which I implemented a new evaluation technique. The analysis has been published in [1].
- **Chapter 5** describes a new approach to the cut-based analysis based on the usage of a multivariate technique, specifically a Boosted Decision Tree. Such analysis was never implemented before in ATLAS and I designed and performed every part of it.
- **Chapter 6** describes the ATLAS fast physics TAg DAta (TADA) monitoring, a system to monitor a wide spectrum of new physics channels and aspects of offline data quality and physics performance. I had a key role in this project for which I worked as code developer and I was one of the main experts. This project was a success and I presented it at CHEP2016, a Computing Conference in San Francisco. This project has been published as a conference proceeding of which I am the first author in [2].

chapter one

Theory

1.1 Introduction to the Standard Model

The Standard Model (SM) of particle physics [3–7] is a theoretical model which describes three fundamental forces of nature: the electromagnetic, nuclear strong and weak. The SM does not include a description of the gravitational force. The SM classifies all the known elementary particles and describes their interactions. This theory, developed in the second half of the 20^{th} century, has been proven capable of making extremely precise experimental predictions. The discovery of the Higgs boson, performed by ATLAS [8] and CMS [9] at the LHC in 2012, confirmed the predictive power of this theory. Nevertheless the SM has several shortcomings, among others, it does not provide any description of the several observational astrophysics pieces of evidence that point to the existence of dark matter. This chapter will briefly describe the SM, the Higgs spontaneous symmetry breaking mechanism [10] and a simplified extension of the SM to include dark matter via the so-called Higgs portal model.

1.1.1 Symmetry groups and fields of the SM

The Standard Model is a non-abelian (Yang-Mills) theory [11], describing the elementary constituents of nature in terms of two different particle fields: fermions and bosons. The elementary components of the known matter are half-integer spin particles, the *fermions*, while the carriers of the force fields are integer spin particles, the *bosons*.

Fermions are divided into three flavour families of quarks and leptons which describe the whole known matter. The bosons are the mediators of the fundamental interactions: the strong interaction, mediated by the massless gluon g, the weak interaction mediated by the massive $W^{\pm}$ and Z bosons, the electromagnetic interaction mediated by the massless photon γ.

The field dynamics is described by the Lagrangian density $\mathcal{L}(\phi, \dot{\phi})$. The Lagrangian can be written as the sum of kinematic terms, describing the free particle dynamics, and interaction terms, which are defined by symmetries of different interactions between the particles.

The symmetry gauge group on which the Standard Model is based upon is:

$$SU(3)_C \otimes SU(2)_L \otimes U(1)_Y \tag{1.1}$$

where $SU(2)_L$ represents the group of transformations under left-handed chirality L, described by the special (S) unitary (U) matrices of dimension 2. $U(1)_Y$ represents the group of transformations under the hypercharge Y, $SU(3)_C$ the group of transformations under the color charge C.

The theory describes the electromagnetic and the weak interaction, based on the gauge group $SU(2)_L \otimes U(1)_Y$, combined with the strong interactions, based on the gauge group $SU(3)_C$.

Figure 1.1 provides a scheme of the SM particles with their properties.

1.1.2 The Lagrangian of the Standard Model

The Lagrangian of the Standard Model can be factorized in several parts which describe different interactions: strong, weak, the Higgs sector and the mass terms (Yukawa).

$$\mathcal{L} = \mathcal{L}_{strong} + \mathcal{L}_{weak} + \mathcal{L}_{Higgs} + \mathcal{L}_{Yukawa} \tag{1.2}$$

In the next sections each term will be described.

Strong interactions Lagrangian terms

Quantum Chromodynamics (QCD) [13] [14] is the theory that describes the strong interaction based on the $SU(3)_C$ symmetry group. The Lagrangian density has to be invariant under the group transformation and it has to describe the dynamics of both bosons and fermions. In order to write down the Lagrangian one can start by looking at the symmetry group structure.

The SU(3) group has 8 generators T^a, proportional to the Gell-Mann matrices λ^a [15]. This leads to an octet of gluonic fields G^a, the carriers of the color charge. The tensor $G^a_{\mu\nu}$, which is the gauge field kinetic term, can be written as:

$$G^a_{\mu\nu} = \partial_\mu G^a_\nu - \partial_\nu G^a_\mu + g_s f^{abc} G^b_\mu G^c_\nu \tag{1.3}$$

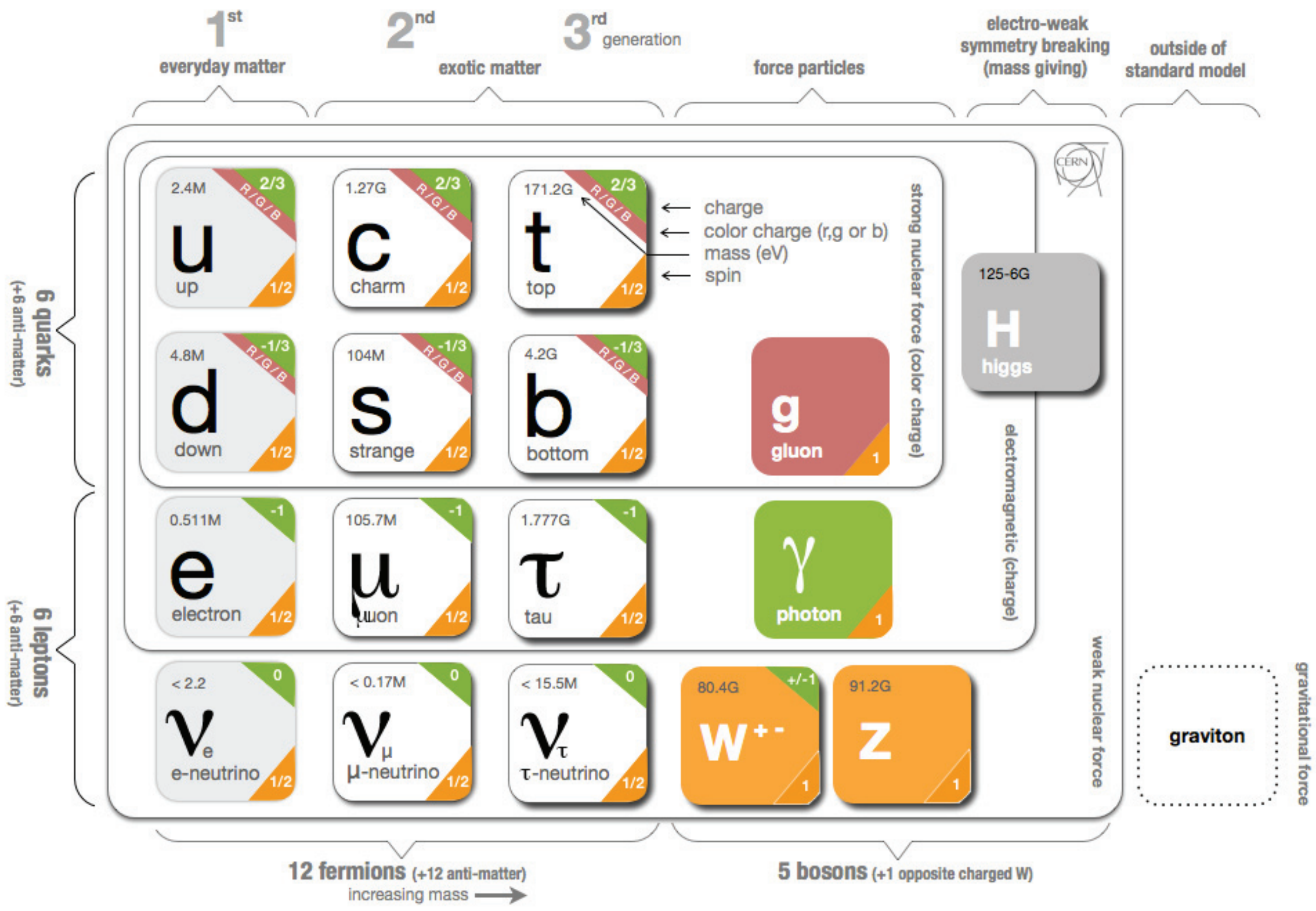

Fig. 1.1 · Standard Model particles scheme. This scheme shows the different particles of the Standard Model divided into the three fermion generations of leptons and quarks and the gauge bosons, carriers of the force. The picture shows information about the electrical charge, the color charge, the mass in eV and the spin of each particle. The picture is taken from [12]

where where f^{abc} are the structure constants of the group $SU(3)_C$ and g_s is the strong coupling constant. On the fermionic side, the quarks, having three possible color charges (red, blue and green), are arranged into $SU(3)_C$ triplets while leptons are singlets (having no color charge). Up to this moment the gauge fields and the fermions are considered massless. This is correct for the description of the gluons, while for the fermions one have to add by hand, a mass term $-m\bar{\psi}\psi$. In the case of SU(3) adding such term does not break the symmetry. One can therefore write a Lagrangian, invariant under SU(3), for a Dirac field of mass m as:

$$\mathcal{L} = \bar{\psi}(i\not{D} - m)\psi \tag{1.4}$$

where ψ is the fermionic field, $\not{D} = D_\mu\gamma^\mu$ where γ^μ are the Dirac matrices, and D_μ is the covariant derivative that can be written as:

$$D_\mu = \left(\partial_\mu - ig_s T_a G^a_\mu\right) \tag{1.5}$$

One can finally write the strong Lagrangian as the sum of the fermion component (considering all the flavors *f*) and the bosonic one as:

$$\mathcal{L}_{strong} = \sum_f \bar{\psi}_f(i\not{D} - m_f)\psi_f - \frac{1}{4}G^a_{\mu\nu}G^a_{\mu\nu} \tag{1.6}$$

Electro-weak Lagrangian terms

The Standard Model is based on the unification of the electromagnetic force [16] and the weak nuclear force by Glashow, Salam and Weinberg [4–6]. The electro-weak terms of the Lagrangian describe the interactions of leptons with the electromagnetic and nuclear weak force. As in the case of the strong interactions one can start writing down the Lagrangian analyzing the group symmetry structure.

$SU(2)_L \otimes U(1)_Y$ has 4 generators: one is the generator Y of the group $U(1)_Y$ corresponding to the gauge field B_μ and other 3 generators T^a of $SU(2)_L$, proportional to the Pauli matrices, corresponding to the gauge fields W^a_μ.

The field tensors can be written as:

$$\begin{aligned} W^a_{\mu\nu} &= \partial_\mu W^a_\nu - \partial_\nu W^a_\mu + g\,\epsilon^{abc}W^b_\mu W^c_\nu \\ B_{\mu\nu} &= \partial_\mu B_\nu - \partial_\nu B_\mu \end{aligned} \tag{1.7}$$

where *g* is the coupling constant for the weak isospin. On the fermionic side both quarks and leptons are described in terms of left-handed and right-handed chirality states ($\psi_{L,R} = \frac{1}{2}(1 \mp \gamma_5)\psi$) arranged into $SU(2)_L$ doublets or singlets:

$$\begin{aligned} L_1 &= \begin{pmatrix} \nu_e \\ e^- \end{pmatrix}_L , \; e_{R_1} = e^-_R , \; Q_1 = \begin{pmatrix} u \\ d \end{pmatrix}_L , \; u_{R_1} = u_R , \; d_{R_1} = d_R \\ L_2 &= \begin{pmatrix} \nu_\mu \\ \mu^- \end{pmatrix}_L , \; e_{R_2} = \mu^-_R , \; Q_2 = \begin{pmatrix} c \\ s \end{pmatrix}_L , \; u_{R_2} = c_R , \; d_{R_2} = s_R \\ L_3 &= \begin{pmatrix} \nu_\tau \\ \tau^- \end{pmatrix}_L , \; e_{R_3} = \tau^-_R , \; Q_3 = \begin{pmatrix} t \\ b \end{pmatrix}_L , \; u_{R_3} = t_R , \; d_{R_3} = b_R \end{aligned} \tag{1.8}$$

Neutrinos, being massless in the SM, do not have a right-handed chirality state, therefore the right-handed leptons are arranged into singlets of $SU(2)_L$.
The Lagrangian of a massless Dirac field invariant under $SU(2) \otimes U(1)$ can then be written as:

$$\mathcal{L} = \sum_f i(\bar{L} \not{D} L + \bar{e}_R \not{D} e_R + \bar{Q} \not{D} Q + \bar{u}_R \not{D} u_R + \bar{d}_R \not{D} d_R) \tag{1.9}$$

where the covariant derivative can be written as:

$$D_\mu = \left(\partial_\mu - igT_a W^a_\mu - ig_1 \frac{Y_q}{2} B_\mu \right) \psi \tag{1.10}$$

where g_1 is the coupling constant for the hypercharge Y. The hypercharge is defined by the Gell-Mann-Nishijima [17] [18] relation as $Q = I_3 + \frac{Y}{2}$ where Q is the electric charge and I_3 is the third component of the isospin. Adding the bosonic term one can write the electroweak Lagrangian as:

$$\mathcal{L}_{EW} = \sum_f i(\bar{L} \not{D} L + \bar{e}_R \not{D} e_R + \bar{Q} \not{D} Q + \bar{u}_R \not{D} u_R + \bar{d}_R \not{D} d_R) - \frac{1}{4} W^a_{\mu\nu} W^{\mu\nu}_a - \frac{1}{4} B_{\mu\nu} B^{\mu\nu} \tag{1.11}$$

It is crucial to notice that this Lagrangian does not have mass terms for neither fermions or bosons. Adding mass terms to the Lagrangian by hand such as $\frac{1}{2} M^2_V W_\mu W^\mu$ for the vector bosons, or such as $-m_f \overline{\psi}_f \psi_f$ for the fermions, would make the Lagrangian not invariant under the $SU(2)_L \otimes U(1)_Y$ symmetry, in contrast with the case of $SU(3)_C$. The absence of mass terms for the bosons goes against experimental evidence: in order to provide mass to the bosons and maintaining the Lagrangian invariant under the symmetry group a spontaneous symmetry-breaking mechanism was introduced by Higgs-Englert-Brout [10] [19].

1.1.3 Spontaneous symmetry breaking: the Goldstone theorem and the Higgs mechanism.

A simple example of spontaneous symmetry breaking in nature is the behavior of a ferromagnet. The Hamiltonian describing the spin-spin interaction is invariant under rotation, without the interaction with external fields. Nevertheless, if the temperature reaches the critical point, the ferromagnet shows a spontaneous polarization, which is not null. This makes the system not invariant under rotation anymore and the symmetry is therefore broken. A similar mechanism was introduced by Goldstone [20].

Goldstone theorem

To explain the Goldstone theorem, one can introduce the Lagrangian of a scalar field:

$$\mathcal{L} = \frac{1}{2} \partial_\mu \phi \, \partial^\mu \phi - V(\phi) \, , \; V(\phi) = \frac{1}{2} \mu^2 \phi^2 + \frac{1}{4} \lambda \phi^4 \tag{1.12}$$

The shape of the potential V depends on the sign of μ^2. For $\mu^2 > 0$ the potential has the shape of a parabola and there is a minimum for $\langle 0|\phi|0 \rangle \equiv \phi_0 = 0$. This Lagrangian describes a particle of spin 0 with mass μ. If $\mu^2 < 0$, the potential shape is different and it has a minimum for:

$$\langle 0|\phi^2|0\rangle \equiv \phi_0^2 = -\frac{\mu^2}{\lambda} \equiv \nu^2 \tag{1.13}$$

The quantity $\pm\nu \equiv \langle\, 0|\phi|0\,\rangle$ is called *vacuum expectation value* (*vev*) of the scalar field ϕ. Such a Lagrangian does not describe a particle of mass μ anymore. To interpret the theory correctly the potential has to be expanded around one of the minimum ν defining the field σ as $\phi = \nu + \sigma$. The new Lagrangian can be written as:

$$\mathcal{L} = \frac{1}{2}\partial_\mu\sigma\,\partial^\mu\sigma - (-\mu^2)\,\sigma^2 - \sqrt{-\mu^2\lambda}\,\sigma^3 - \frac{\lambda}{4}\,\sigma^4 \tag{1.14}$$

which describes a scalar field of mass $m = -2\mu^2$. The presence of cubic terms makes the Lagrangian not invariant under reflection, therefore the symmetry is broken. If one wants to generalize to a higher order, one can look at a Lagrangian of 4 scalar fields ϕ_i:

$$\mathcal{L} = \frac{1}{2}\partial_\mu\phi_i\,\partial^\mu\phi_i - \frac{1}{2}\mu^2\,(\phi_i\phi_i) - \frac{1}{4}\lambda(\phi_i\phi_i)^2 \tag{1.15}$$

Such Lagrangian is invariant under the rotation group O(4). By expanding around a minimum and interpreting the field ϕ as the pion field π, the following Lagrangian is obtained:

$$\begin{aligned}\mathcal{L} =& \frac{1}{2}\partial_\mu\sigma\,\partial^\mu\sigma - \frac{1}{2}(-2\mu^2)\sigma^2 - \lambda\nu\,\sigma^3 - \frac{\lambda}{4}\,\sigma^4 \\ &+ \frac{1}{2}\partial_\mu\pi_i\,\partial^\mu\pi_i - \frac{\lambda}{4}(\pi_i\pi_i)^2 - \lambda\nu\pi_i\pi_i\sigma - \frac{\lambda}{2}\pi_i\pi_i\sigma^2\end{aligned}$$

This Lagrangian shows the presence of a massive boson σ with $m = -2\mu^2$ but also the presence of three massless bosons. It is important to notice that while the symmetry O(4) is now broken, there is still an unbroken symmetry O(3) for the π_i fields. This lead to the enunciation of the Goldstone theorem: for every continuous symmetry spontaneously broken, the theory contains massless scalar particles called Goldstone Bosons.

The Higgs mechanism

To describe the electroweak sector, a spontaneous-symmetry breaking mechanism has to provide mass to the three bosons W^+, W^- and Z, while maintaining the photon massless. This implies that the $SU(2)_L \otimes U(1)_Y$ symmetry has to be broken but the $U(1)_Q$ has to be exact. From the Goldstone theorem one knows that once a symmetry is broken, a massless boson is formed. On the other side, there are no observed Goldstone bosons in nature. Therefore there has to be a way to break a symmetry spontaneously without producing a Goldstone boson. This is exactly what is achieved by the Higgs mechanism. A complex scalar field ϕ is introduced that can be written in terms of a $SU(2)_L$ doublet:

$$\Phi = \begin{pmatrix} \phi^+ \\ \phi^0 \end{pmatrix}, \quad Y_\phi = +1 \tag{1.16}$$

The Lagrangian of such field can be written as:

$$\mathcal{L}_{\mathrm{Higgs}} = (D^{\mu}\Phi)^{\dagger}(D_{\mu}\Phi) - \mu^2\Phi^{\dagger}\Phi - \lambda(\Phi^{\dagger}\Phi)^2 \tag{1.17}$$

For $\mu^2 < 0$ the neutral component of the doublet will have *vev* different from null, while the charged component will be null to preserve the $U(1)_Q$ symmetry:

$$\langle \Phi \rangle_0 \equiv \langle 0 | \Phi | 0 \rangle = \begin{pmatrix} 0 \\ \frac{v}{\sqrt{2}} \end{pmatrix} \quad \text{with } v = \left(-\frac{\mu^2}{\lambda}\right)^{1/2} \tag{1.18}$$

A visual representation of the Higgs potential is shown in Figure 1.2. The shape of the potential is the so-called Mexican hat. This shape leads to two interesting results: a particle that moves along the potential wall needs a quadratic energy contribution, which represents the mass of the particle. On the other side the presence of a degenerate state (*vev* not null), implies that any particle lying on the minimum potential level does not need energy to move along the circumference: this implies the presence of massless particles (Goldstone bosons). Using a similar approach to the one used to describe the π toy model one can now write the Φ field in terms of the fields $H(x)$ and $\theta_{1,2,3}(x)$ as:

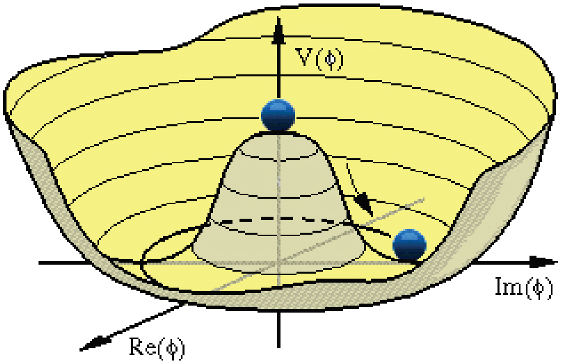

Fig. 1.2 · Higgs boson potential. This figure is a representation of the Higgs boson potential, also known as *Mexican hat* for the case $\lambda > 0, \mu^2 < 0$. In this case the fundamental state is degenerate and a particle lying on the minimum potential level does not need energy to move along the circumference (Goldstone bosons), while to move along the potential wall it needs a quadratic energy contribution, (mass of the particle). The figure is taken from [21]

$$\Phi(x) = \begin{pmatrix} \theta_2 + i\theta_1 \\ \frac{1}{\sqrt{2}}(v + H) - i\theta_3 \end{pmatrix} = e^{i\theta_a(x)\tau^a(x)/v} \begin{pmatrix} 0 \\ \frac{1}{\sqrt{2}}(v + H(x)\,) \end{pmatrix} \tag{1.19}$$

By expanding the covariant derivative, the Lagrangian presents several problems: there are terms where the vector fields are coupled with the θ fields, leading to a difficult physical interpretation. On top of that the Lagrangian after the change of variables shows an higher number of degrees of freedom. This implies the presence of non-physical fields (Goldstone bosons) which do not represent real particles and must be eliminated. To do this, one can apply to the field Φ a specific transformation:

$$\Phi(x) \to e^{-i\theta_a(x)\tau^a(x)}\,\Phi(x) = \frac{1}{\sqrt{2}}\begin{pmatrix} 0 \\ v + H(x) \end{pmatrix} \tag{1.20}$$

which is called the unitary gauge.
In this particular gauge there are no more terms in the Lagrangian which couple θ fields with the vector fields, as one can see from the covariant derivative:

$$|D_\mu\Phi)|^2 = \frac{1}{2}(\partial_\mu H)^2 + \frac{1}{8}g_2^2(v+H)^2|W^1_\mu + iW^2_\mu|^2 + \frac{1}{8}(v+H)^2|g_2W^3_\mu - g_1B_\mu|^2$$

Now by defining the vectorial fields in this way:

$$W^\pm = \frac{1}{\sqrt{2}}(W^1_\mu \mp iW^2_\mu)\ ,\ Z_\mu = \frac{g_2W^3_\mu - g_1B_\mu}{\sqrt{g_2^2+g_1^2}}\ ,\ A_\mu = \frac{g_2W^3_\mu + g_1B_\mu}{\sqrt{g_2^2+g_1^2}} \tag{1.21}$$

one can interpret the quadratic Lagrangian terms as the mass term of vector boson fields $W^\pm, Z^\mu, A^\mu$:

$$M_W^2W^+_\mu W^{-\mu} + \frac{1}{2}M_Z^2Z_\mu Z^\mu + \frac{1}{2}M_A^2A_\mu A^\mu \tag{1.22}$$

where:

$$M_W = \frac{1}{2}vg_2, M_Z = \frac{1}{2}v\sqrt{g_2^2+g_1^2}, M_A = 0 \tag{1.23}$$

To summarize, starting from a complex scalar field and massless vector fields, one ended up with a real scalar field and massive vector fields. The additional degrees of freedom, representing the nonphysical Goldstone bosons, were absorbed by the vector fields W and Z, which obtained mass in the process. At the same time the symmetry $U(1)_Q$ was unbroken and the photon did not acquire mass, as it should be. This process, where a symmetry is spontaneously broken and a massless vector field acquires mass without breaking the gauge invariance of the Lagrangian, is called Higgs mechanism and the particle associated with the field $H(x)$ is the so-called Higgs boson with mass $M_H^2 = -2\mu^2$.

Yukawa Lagrangian terms and fermion mass

While describing the Higgs mechanism, the focus was on the bosonic fields. By using the same mechanism one can show how the fermions as well can gain mass. In order to do so one can write the Yukawa Lagrangian, invariant under $SU(2)_L \otimes U(1)_Y$, for each flavour family:

$$\mathcal{L}_{Yukawa} = -\lambda_e\,\bar{L}\,\Phi\,e_R - \lambda_d\,\bar{Q}\,\Phi\,d_R - \lambda_u\,\bar{Q}\,\tilde{\Phi}\,u_R\ +\ h.c. \tag{1.24}$$

By applying the same procedure one can obtain for the electron (for example):

$$\mathcal{L}_{Yukawa} = -\frac{1}{\sqrt{2}}\lambda_e\,(\bar{v}_e, \bar{e}_L)\begin{pmatrix} 0 \\ v+H \end{pmatrix} e_R\ + \cdots = -\frac{1}{\sqrt{2}}\lambda_e\,(v+H)\,\bar{e}_Le_R\ + \cdots$$

by looking at the term $\bar{f}_L f_R$ one can define the mass of the fermions as:

$$m_e = \frac{\lambda_e v}{\sqrt{2}} \ , \ m_u = \frac{\lambda_u v}{\sqrt{2}} \ , \ m_d = \frac{\lambda_d v}{\sqrt{2}} \tag{1.25}$$

In conclusion, both fermions and bosons gain mass via the interaction with the Higgs field.

1.1.4 Standard Model shortcomings

The SM is a very successful theory tested with extremely good precision, but it has several shortcomings: the hierarchy problem [22] [23], the neutrino mass problem [24] [25] and the strong CP problem [26] [27]. More importantly for the discussion of this thesis the SM does not provide any candidate for Dark Matter (DM) in the universe, which is supported by a plethora of cosmological evidence. The next section of this chapter will be focused on DM, its astronomical evidence, candidates, and research methods.

1.2 Dark Matter

The nature of most of the matter in the universe is yet unknown. Astronomical evidence points to the presence of matter which interacts via gravitation without electroweak or strong interaction. The most successful model to describe the universe is the so-called Standard Cosmological Model or Hot Big Bang model [28, 29]. In such model the universe, formed after the Big Bang, is in expansion and it is accelerating where matter represents 26% of the total composition and Dark Energy the remaining 74%. This model also shows how the majority of matter composition, around 80%, is due to DM while the baryonic matter is only a fraction. Figure 1.3 shows the relative composition of the universe in terms of dark energy, dark matter and baryonic matter. The nature of DM is still uncertain but a plethora of cosmological evidence points at its presence in the universe.

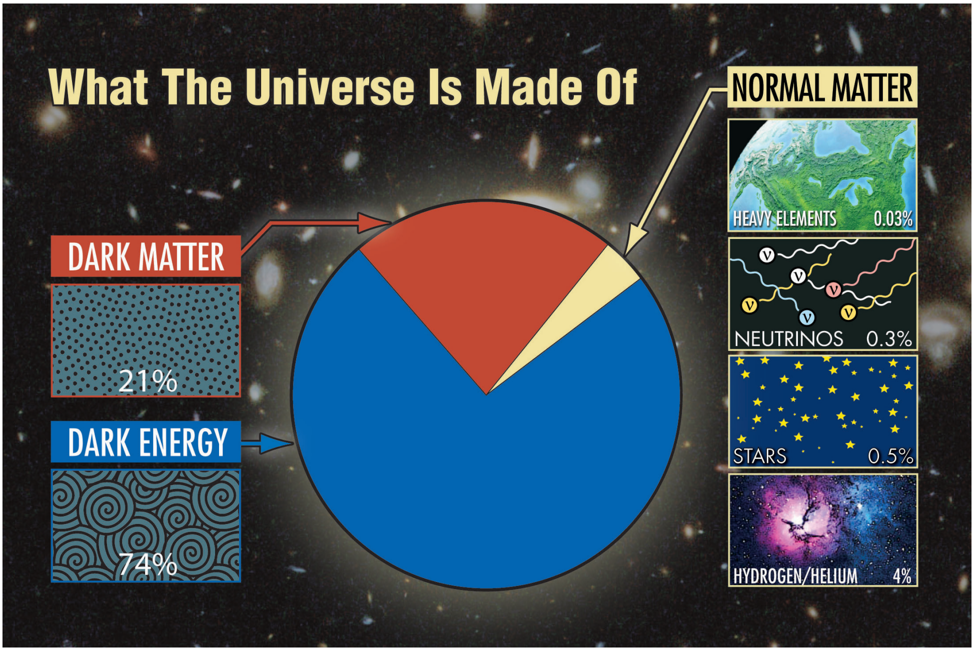

Fig. 1.3 · Universe composition chart [30]. The chart shows how Dark Energy and Dark Matter dominates the composition of the Universe, while the amount of ordinary matter is extremely low (4-5%).

1.2.1 Dark Matter evidence

The evidence for DM is numerous and comes from independent cosmological observations:

- Rotation curves in galaxies
- Galaxy clusters mass evaluation
- Gravitational lenses in galaxy clusters

- Cosmic Microwave Background (CMB)

Each evidence will be described in the following section.

Rotation curves in galaxies

A piece of evidence for DM is the measurement of spiral galaxies rotation curves. From Newton's laws one can describe the rotation velocity ν_r of a particle (or a planet) orbiting around a body of mass M as:

$$\nu_r = \sqrt{\frac{GM(r)}{r}} \tag{1.26}$$

For distances greater than the size of the body itself, the velocity drops as $r^{-1/2}$, following Kepler's law. While this stands for planets, it is not true for stars and gases orbiting in galaxies. Figure 1.4 shows the measurement of the rotation velocity of the galaxy M33. The figure shows that the velocity does not drop as it would be expected by the amount of luminous matter. The observed distribution is flat. The presence of such higher velocity points to the presence of additional not luminous matter: dark matter.

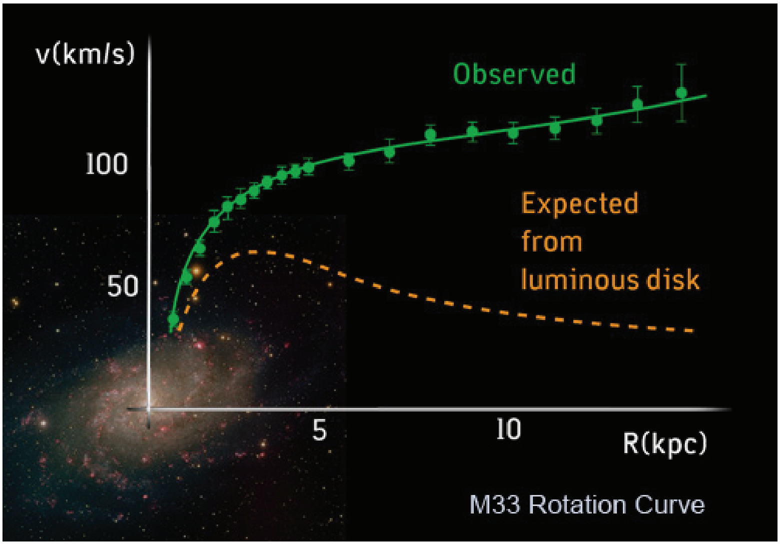

Fig. 1.4 · Galaxy velocity rotation curve. This picture shows the results on the analyzed rotation curve velocity as function of the distance from the center of the galaxy M33 . The picture shows that the expected velocity distribution from the luminous disk is not enough to described properly the observed data. The picture is taken from [31]

Galaxy clusters mass: Zwicky and the Coma galaxy cluster

The first claim on the presence of DM was made by the Swiss-American astronomer Fritz Zwicky. In 1933 [32], he found a large velocity dispersion in eight galaxies in the Coma cluster. He then measured the mass of the cluster by applying the virial theorem [1]. Using the virial theorem and knowing the velocity dispersion of the galaxies in the cluster and its size, the mass can be evaluated as:

$$M \sim \frac{2 < r >< v^2 >}{G} \tag{1.27}$$

where M is the mass, r the radius, v the velocity dispersion and G the gravitational constant. Zwicky found that the mass to light ratio was 400 times what he expected. [2] To quote Zwicky himself:

"If this would be confirmed, we would get the surprising result that dark matter is present in much greater amount than luminous matter" [33]

Figure 1.5 shows a picture of the Coma cluster.

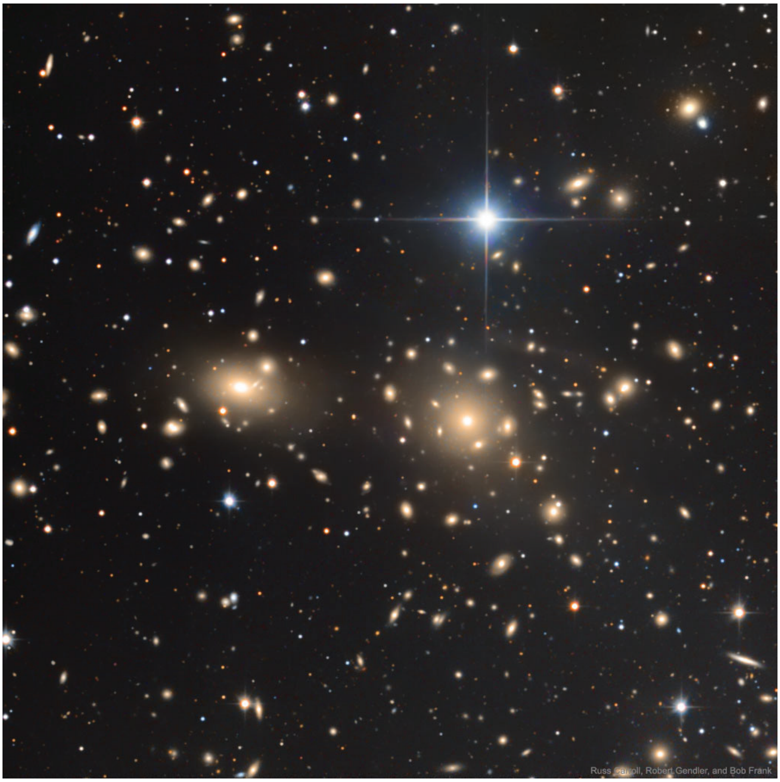

Fig. 1.5 · A picture of the Coma cluster [34].

---

[1] The virial theorem states that $< E_{pot} > +2 < E_{kin} >= 0$ where E_{pot} is the averaged potential energy of the galaxy cluster and E_{kin} is the averaged kinetic energy

[2] He actually overestimated it, recent studies show that the ratio was of the order of 50 times the expected one, not 400.

Gravitational lenses and the Bullet cluster

From general relativity one knows that gravity bends the space-time. Particles and light (photons), traveling across a massive cluster will have their trajectories bent. In case of massive bodies like galaxy clusters, the light will be bent so much as if it would go trough a lens, as shown in Figure 1.6. This effect is known as *gravitational lensing* [35]. The mass of a cluster can be determined by measuring the scale of the lensing. In a similar fashion as the Coma galaxy mass evaluation, the total mass can be compared to the luminous mass amount and the mismatch will be an estimate of DM [1]. The Bullet Cluster shown in Figure 1.7a, has been studied while undergoing a high-velocity merger. The mass profile is obtained from gravitational lensing (in blue) and the distribution of the hot gas (baryonic matter) via the detection of X-rays (in red). The peculiarity about this cluster is that most of the mass in

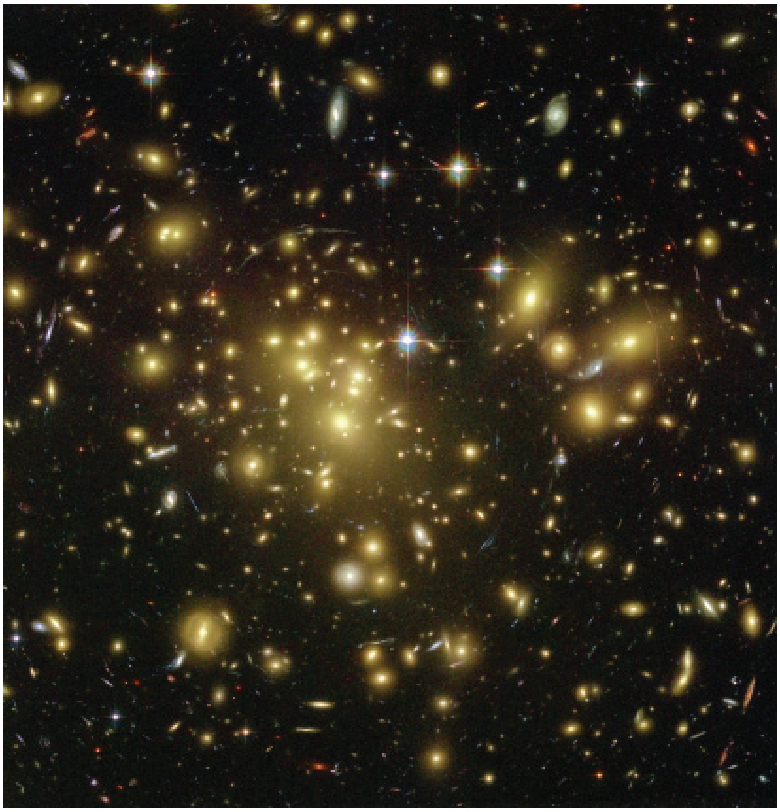

Fig. 1.6 · A picture of the Abell 1689 cluster with the Hubble space telescope combining visible and infrared data [36]. The picture provides a clear depiction of gravitational lensing as it can be seen from the electric blue streaks, circling and arcing around the cluster of galaxies in the central part of the image.

---

[1] This approach is more reliable than evaluating the mass via the virial theorem because it does not rely on dynamical assumption about the kinematic of the galaxy.

the two clusters (blue areas) is separated from the baryonic matter (red areas). The hot gas has been slowed down during the collision, while the DM (interacting only via gravity) lies ahead of it. Most of the gravitational lensing effect is therefore due to non-baryonic matter: the Bullet cluster pinpoints the presence of DM.

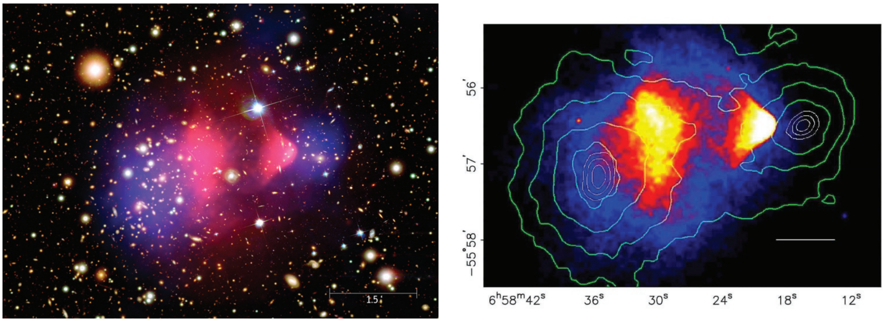

(a) **(b)**

Fig. 1.7 · Bullet cluster. On the left (a), a picture of the Bullet cluster overlaid with a visual representation of the hot gas density (red) and the gravitating mass density (blue) [37]. On the right (b) a Deep Chandra picture which shows the hot gas concentration in yellow, red and blue, while the gravitating mass distribution is showed by green contours [38]. The hot gas in each cluster was slowed down during the collision while most of the matter did not interact, if not via gravity, and just passed through. Therefore, Dark Matter moved ahead of the hot gas during the collision producing the separation showed in both figures (a) and (b).

Cosmic Microwave Background

Before the decoupling of baryons and photons the universe was an ionized opaque plasma. Once the temperature dropped below the hydrogen ionization energy, protons and electrons recombined. The recombination led to the decoupling of the photons from the baryons, in other terms the mean free path of the photons became equal to the size of the universe at that time. The photons were free to stream without scattering. The light of those primordial photons is called Cosmic Microwave Background (CMB) and it is the oldest visible light in the universe. The latest results on the CMB measurement in the whole sky map are provided by the Planck collaboration as show in Figure1.8. The sky map shows the distribution of the primordial temperature fluctuations, which are extremely small (order of $10^{-4}/10^{-5}$). The CMB is compatible with the emission of a perfect black body at a temperature of $\mathrm{T} = 2.7255 \pm 0.0006\mathrm{K}$. The study of CMB fluctuations has been crucial to better understand many cosmological features and it is a strong hint to the presence of DM. Before photons decoupling, baryons and photons formed a fluid oscillating due to the presence of a DM potential dwell. The oscillations were due to the dynamical balance of the gravity exercised on the baryons by DM potential and the pressure excited by the photons. These peaks are visible in the CMB power spectrum, shown in Figure 1.9, and they are a clear signal of the presence of DM in the universe. In other words, without the presence of DM the CMB would not have such power spectrum. The next paragraph will describe the DM most

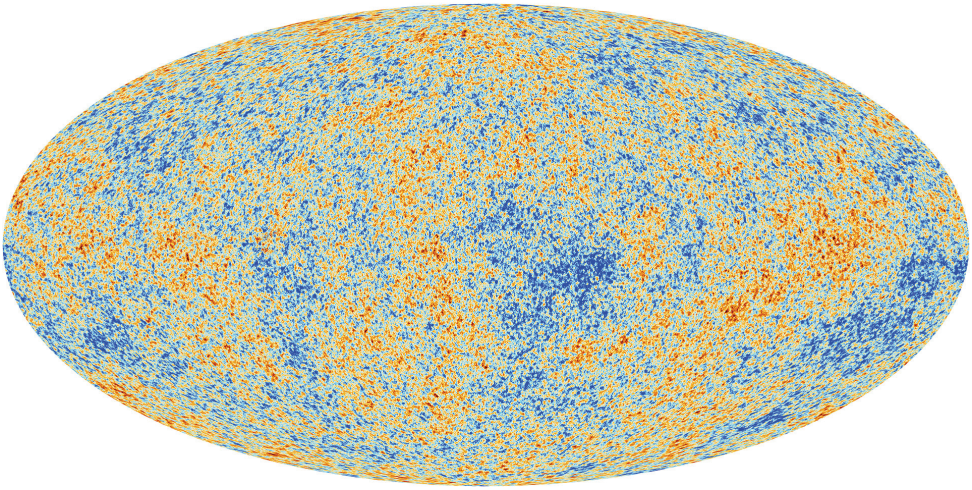

Fig. 1.8 · Cosmic microwave background. This picture represents a sky map in Galactic coordinates of the fluctuations (from red to blue) of the temperature of the universe at the time of the photon decoupling [39]. The fluctuations are very small, in the order of 10^{-5} only.

effective models and the zoology of DM candidates, focusing on the most promising one, the WIMP.

1.2.2 Dark Matter in the universe: freeze-out mechanism, DM candidates and WIMP Cold Dark Matter

From cosmological evidence, the composition of the Universe is dominated by non baryonic matter and dark energy. There are several models which try to explain DM presence in the universe and predict a plethora of DM possible candidates. DM candidates can be divided into two major groups: thermal relic and non-thermal relic[1]. When one mentions a DM WIMP thermal-relic, there are three assumptions which are made:

1. Dark matter is a particle.
2. DM interaction with the SM is weak.
3. The mass of the DM candidate is in the order of $GeV - TeV$.

The thermal relic candidates can be divided into three categories depending on their velocity at the moment of freeze-out. Relativistic DM is labeled as Hot Dark Matter (HDM), non relativistic DM is labeled as Cold Dark Matter (CDM) and almost-relativistic DM is called Warm Dark Matter (WDM). Depending on the velocity of the thermal relic there is relativistic freeze-out (neutrinos, photons, HDM) and non-relativistic freeze-out (CDM, WDM). Such process is fundamental to understand the nature of DM and it will be described in detail in the following section.

---

[1] Non-thermal relics, such as axions [42], will be described in section 1.2.2.2.

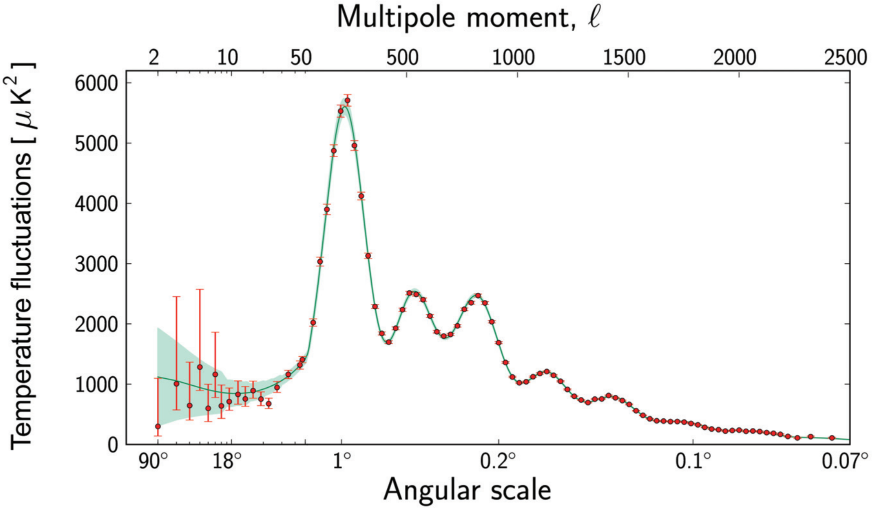

Fig. 1.9 · CMB angular power spectrum. This figure shows the temperature fluctuations of the CMB as a function of the angular scale and the multipole momentum *l*. The angular scale correspond to a specific angle opening in the sky observation. The structure of the oscillations provides information about the structure universe and its composition. Before photons decoupling, baryons and photons formed a fluid oscillating due to the presence of a DM potential dwell. The oscillations were due to the dynamical balance of the gravity exercised on the baryons by DM potential and the pressure exercised by the photons. These peaks are visible in the power spectrum and they are a clear signal of the presence of DM in the universe. Without DM the power spectrum would look completely different. The relative magnitude of the second and third peaks is also an indicator of the universe composition in terms of baryons and dark matter. More details about the acoustic signature in the CMB spectrum can be found in literature [40]. The data points correspond to the measurements from the Planck Collaboration which are in very good agreement with the Standard Cosmological Model predictions. The figure is adapted from [41].

The freeze-out mechanism and the WIMP miracle

For the majority of its expansion the universe was in thermal equilibrium. Nevertheless if the universe would have always been at thermal equilibrium the composition of it would be defined completely by the temperature at the present day. Critical events have happened when the universe went out of thermal equilibrium such as inflation, neutrino decoupling, Big Bang nucleosynthesis (BBN), DM relic formation and photon decoupling (CMB) among others [29]. In this section the formation of non-relativistic thermal relics via chemical decoupling, for a CDM candidate, will be described [1]. To describe the freeze-out mechanism let us consider a dark matter species χ, of mass m, produced in the early Universe. The evolution of the number density n is described by the Boltzmann equation:

$$\frac{dn}{dt} = -3Hn - \langle \sigma_A v \rangle (n^2 - n_{eq}^2) \tag{1.28}$$

where n_{eq} is the number density at thermal equilibrium, $\langle \sigma_A v \rangle$ is the thermally averaged annihilation cross section and H the Hubble parameter. On the right side of the equation the first term represents the effect of dilution of the species due to the expansion of the universe, the term in parentheses takes into account the balance between the annihilation and pair production process. The evolution of the number density can be divided into three different stages depending on the temperature T: $T \gg m$, $T \leqslant m$ and $T \ll m$. In the early universe for $T \gg m$, DM is ultra-relativistic and $n_{eq} \sim T^3$. In this period the pair production and the annihilation rate dominates over the expansion of the universe and a good solution of the Boltzmann equation is $n = n_{eq}$. When the universe starts to expand, the temperature drops reaching $T \leqslant m$. In this scenario, $n_{eq} \sim (m_\chi T)^{\frac{3}{2}} e^{-m_x/T}$, which means that the density is exponentially suppressed and eventually would go to zero also because the production of DM almost stops. Still, the universe is not only cooling but also expanding: due to its expansion the presence of DM dilutes, reducing the rate of the annihilation cross section until the mean interaction path becomes higher than the expansion rate of the universe H. For $T \ll m$ the freeze-out happens, producing a thermal relic. Figure 1.10 shows the evolution process just described. The y axis shows the co-moving volume number density $Y = n/s$, where s is the entropy density [2]. The x axis, $x = m/T$, is proportional to time because for increasing time the universe temperature drops, increasing the ratio x. The final value of Y is proportional to the DM relic density, $\Omega_{DM} = \rho_\chi/\rho_c$, where $\rho_\chi = m s_0 Y_0$ [3] and $\rho_c = \frac{3H^2}{8\pi G}$ is the critical density. The figure also shows that the thermally averaged annihilation cross section is inversely proportional to the relic density. This effect is simply understandable: for higher cross sections the freeze-out temperature needed will be much lower, therefore the time spent in the thermal equilibrium will be higher, therefore the density will be exponentially suppressed much longer. In formulas, by defining the freeze-

---

[1] The decoupling for neutrinos and photons, which is in a relativistic regime can be found in the literature [29]

[2] During the early Universe expansion entropy $S = s a^3$ is constant.

[3] The 0 stands for quantities evaluated at the present day

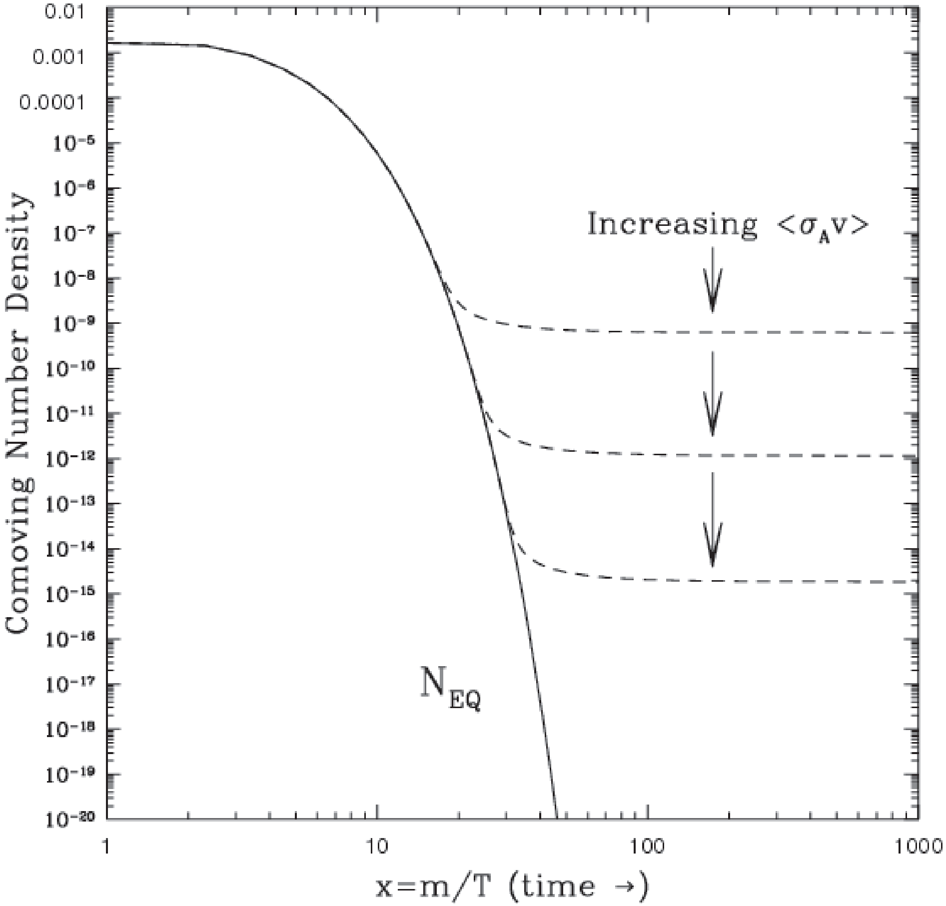

Fig. 1.10 · Freeze out mechanism. The plot shows the evolution during time (expressed as a ratio between the mass of DM m and the temperature of the universe T), of the co-moving number density Y of DM from the early universe until today [29]. The plot shows three different stages, a first one when $T \gg m$, where Y is constant, then for $T \leqslant m$, Y is exponentially suppressed and a third stage $T \ll m$ when the freeze-out takes place and the number density is fixed. The continuous line shows the exponentially suppressed evolution of the number density in thermal equilibrium n_{eq} while the dotted line represents the final density due to the freeze-out. The plot shows as well that the co-moving number density is inversely proportional to the thermally average annihilation cross section because increasing $\langle \sigma_a v \rangle$ leads to lower Y.

out time as the one when the expansion rate is equal to the average cross section times the density $n\langle\sigma_a v\rangle = H$, the thermal relic density can be written as a function of $\langle\sigma_a v\rangle$:

$$\Omega_{DM} \sim \frac{x_f T_0^3}{\rho_c}\langle\sigma_a v\rangle^{-1} \tag{1.29}$$

where the f stands for quantities measured at the freeze-out time. By an order-of-magnitude calculation one obtains $\Omega_{DM}h^2 = 3 \times \frac{10^{-27}cm^3s^{-1}}{\langle\sigma_a v\rangle}$. This is a remarkable result: by comparing the value of $\Omega_{DM}h^2$ collected by the Planck collaboration [43], $\Omega_{DM}h^2 = 0.1199 \pm 0.0027$, one obtains $\langle\sigma_a v\rangle \sim 10^{-26}cm^3s^{-1}$. The value of $\langle\sigma_a v\rangle$ which provides the correct relic abundance, coincidentally is in the order of magnitude of a weak scale interaction. To put it in other words, the best DM candidate for new physics beyond the standard model which provides the proper amount of relic density is in the range of the weak interaction which is the same one required to solve the gauge hierarchy problem [44]. This promising coincidence is often called *The WIMP miracle*. In the next section the zoology of DM candidates will be described, together with the most effective model, the WIMP.

DM candidate zoology

The candidates for DM are many and they lie in a wide mass range, from 10^{-22} eV till 10^{-8} $M_{\odot}$ [1]. The interaction strength can vary as well, from DM interacting only via gravitation to DM interacting strongly. Among the most important ones there are:

- Standard model neutrinos: Neutrinos are abundant in the universe, they are weakly interacting with standard matter therefore they look like a natural candidate for DM. However, with a limit on the mass from β-decay experiments, $m_\nu < 2.05$ eV [45], the limit on the relic abundance is $\Omega_\nu < 0.07$ which is not enough to account for the DM one. Additionally being relativistic (HDM), they would erase fluctuations necessary to structure formation. SM Neutrinos are therefore too light and too hot to be DM candidates.

- Sterile neutrinos: Sterile neutrinos [46] are hypothetical particles similar to SM neutrinos without weak interaction with the SM other than the mixing. They are heavier than SM neutrinos, from order of keV to GeV, and almost-relativistic (WDM).

- Super-symmetric candidates: Super symmetry (SUSY) [47] postulates the presence of massive super partner particles of the SM in order to resolve several theoretical problems such as naturalness and hierarchy. SUSY provides several candidates for DM, such as neutralinos, sneutrinos, gravitinos, axinos. The most studied and promising candidate is the lightest neutralino. For R-parity conserving models the lightest neutralino is stable and in a range mass compatible with a WIMP CDM candidate therefore is a good DM candidate. Several studies about neutralinos can be found in the literature [48].

- Kaluza Klein states: Extra dimension theories such as the one of Kaluza-Klein (KK), postulate the presence of an additional fifth dimension compactified and of micro-

---

[1] $M_{\odot}$ is the solar mass

scopic scale [49, 50]. Those theories are an attempt to unify gravitation and electromagnetism. Particles traveling through the fifth dimension would look very massive, because all the extra-dimensional momentum would be accounted for as mass at rest. Such excited states are called KK modes. Several extra dimension theories have been created from KK: among those the Randall-Sundrum [51] and the Universal Extra Dimension (UED) [52]. UED provides a candidate for DM, because the lightest KK particle (LKP) in this theory is stable [53]. A common example of this is the first KK excitation of the hypercharge boson $B^{(1)}$ [54].

- Axions: Axions are hypothetical particles introduced to solve the strong CP problem [42]. Axions are extremely light, with mass less than meV. If produced as a thermal relic they would not be a proper candidate, for similar reasons as the SM neutrinos. Nevertheless there are several models such as the Peccei-Quinn phase transition [55] which allows axions formation as not-thermal relic, providing a proper value for the dark matter relic density and making axions a competitive candidate for DM.
- Others: WIMPzillas [56], little Higgs model [57], self interacting DM [58], mirror particles [59], CHArged Massive Particles (CHAMPs) [60] et cetera.

This brief review shows that the most promising candidate for DM detection are CDM WIMPs. Interacting at the weak scale, WIMP are also detectable by different complementary experiments. The search for WIMP DM will be the topic of the next section.

1.2.3 WIMP Dark Matter searches: direct, indirect, production at colliders

The searches for WIMP Dark Matter can be divided into three major categories: direct, indirect, and production at colliders. Each search is linked to a specific interaction between the SM sector and the DM sector. The sketch in figure 1.11 describes them all: from right to left SM particles pair producing DM, from left to right DM annihilation into SM particles and from top to bottom DM-SM scattering. For each search the prime principles of detection, the major backgrounds and an overview of the results up to now will be provided.

Direct detection

Direct detection searches aim to detect the interaction between DM and Standard matter via nuclear recoil. Knowing the value of the DM local density, $0.3\ GeV/cm^3$ [61], one can evaluate the flux of DM onto Earth as $10^5\ cm^{-2}s^{-1}$ for a DM candidate with a mass in the range of the $GeVs$. One can then expect collisions between DM and standard matter in an Earth based detector. Knowing the velocity dispersion of DM and its escape velocity [62] [63], one can estimate that a DM particle with a mass of the order of GeV-TeV carries a momentum of tens of MeV and that the transferred energy in a nuclear recoil is below 50 keV. The number of expected interactions is of the order of 10^{-3} to 1 per kilogram of detector material per year. In order to detect such rare interactions, a detector is required to have extreme low background noise, low energy threshold and a huge amount of target mass. Depending on the way the energy emitted from the nuclear recoil is transformed, different detectors are used based on ionization, scintillation light or phonons. The most effective

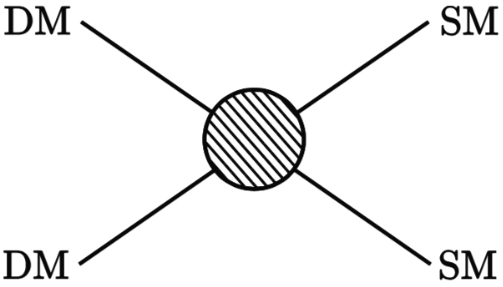

Fig. 1.11 · This sketch describes the interaction among DM and SM, mediated by a not resolved mediator, described by the blob in the center. This image is useful to describe qualitatively the possible interaction of DM with SM. From left to right it represents DM pair annihilation into SM particles, from right to left DM pair production from SM particle collisions, from top to bottom it represents DM scattering on SM particles.

experiments are based on cryogenic techniques, liquefied argon or xenon and super-heated liquid detectors [64]. The major sources of background for those experiments are radiation coming from cosmic rays, radioactive activity of the detector itself and neutrons from (α, n) reactions. While those kinds of backgrounds can be eventually bypassed with different techniques, an irreducible background is the one coming from coherent neutrino-nucleus scattering (CNNS) [65]. This kind of scattering has the same signature as WIMP-nucleon scattering, therefore it is irreducible. Neutrinos coming from the decay of boron-8 in the sun will dominate the recoil spectrum for low masses (below $10\ \mathrm{GeV}$) while atmospheric and diffuse supernova neutrinos will dominate the high mass range. Figure 1.12 shows the observed limit on the WIMP-nucleon cross section for several experiments and the projections for experiments under development. The experiment with the most stringent limit is Xenon1T, a liquid xenon based experiment [66]. Aside from the controversial results from the DAMA experiment [67] the plot shows that direct detection searches do not show any presence of WIMP DM so far.

Indirect detection

Indirect detection searches look for anomalies in the observed spectrum of particles produced by the annihilation of DM pairs in space. Areas with a high concentration of DM are of major interest, such as the Galactic Center and the Sun's core. The particles produced by a DM pair annihilation can be high energy neutrinos coming from the Sun or the Galactic Center (GC), γ-rays from GC and dwarf galaxies, e^+, $\bar{p}$, and antideuterons from the galactic halo. One of the major limitations of such searches is the understanding of the astrophysical backgrounds and the DM local density modeling. Several experiments report anomalies such as the $3.5\ \mathrm{keV}$ line of X-rays [76] from galaxy clusters and the excess of γ rays from the GC observed by the Fermi-LAT experiment [77], the positron excess observed by PAMELA [78] and AMS [79], and the excess in the anti-proton-proton ratio

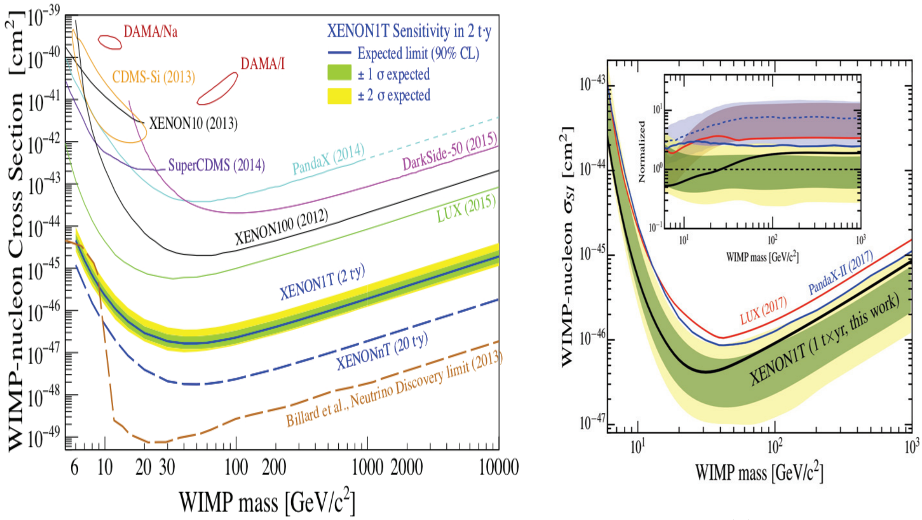

(b)

(a)

Fig. 1.12 · Direct searches: results and projections [68]. The plot (a) shows a compilation of results (claimed discovery contour and exclusion limits) from different experiments of the WIMP-nucleon cross section as a function of the WIMP mass. Aside from the controversial results from DAMA-LIBRA [67, 69] and CDMS-Si [70] all other experiments (Xenon10 [71], SuperCDMS [72], Panda [73], DarkSide-50 [74], Xenon100 [64], LUX [75]) show no presence of DM. The neutrino discovery limit due to the CNNS effect is showed as reference [65]. The most stringent limit is provided by Xenon1T [66], which is shown on the right plot (b).

in the AMS data. Those anomalies are inconsistent among each other for several reasons: the DM mass range varies from keV to TeV, the X-rays excess has not been seen by other groups, and the AMS ratio anomaly can be explained by a new modeling of the anti-proton background. Such searches are in the need of additional data in order to better understand the nature of such anomalies. Experiments as Fermi and AMS-II will keep collecting data together with a new generation of telescopes, the Cherenkov Telescope Array (CTA), which are now in development [80]. The results just illustrated show that indirect searches are still not conclusive about the presence of DM. Figure 1.13 shows the limit on the annihilation cross section as a function of the DM mass coming from $\gamma - rays$ recorded by Fermi-LAT, HESS [81] and MAGIC [82] for the $b\bar{b}$ channel (left) and the $\tau\tau$ channel (right). The DM

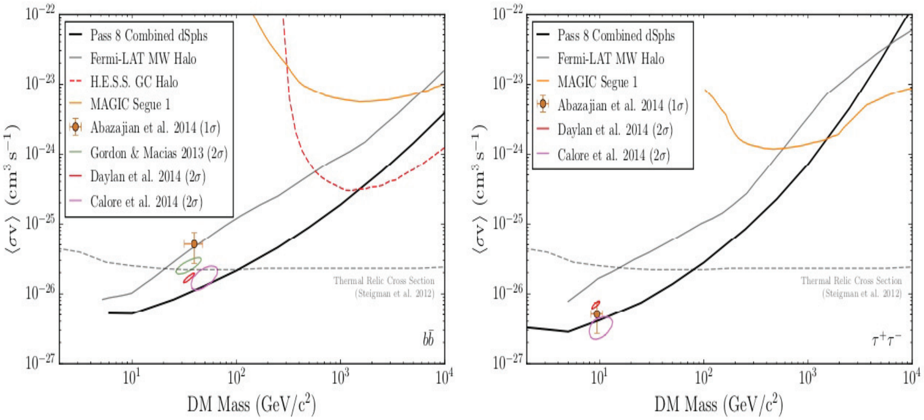

Fig. 1.13 · Indirect detection results [83]. The two plots show the limit on the thermally averaged annihilation cross section as function of the mass for several experiments: Fermi-LAT, HESS and MAGIC. The point with error bars and the closed contours show the best-fit for several interpretations of the Galactic center excess [84–87]. The plot on the left shows the $b\bar{b}$ channel while the plot on the right the $\tau\tau$ channel. The plot shows the thermal relic cross section line which provides the proper amount of DM relic density. For both plot the most stringent results come from the Fermi-LAT experiment.

thermal average annihilation cross section $< \sigma v >= 3 \times 10^{-26} cm^2 s^{-1}$, is also shown in the plot. The Fermi-LAT result is the most stringent and it probes the area up to 100 GeV. Studies on the potential performances of the CTA experiment show that it will be able to probe the area beyond 100 GeV up to the TeV scale.

Another important indirect detection search is the one linked to high energy neutrinos coming from the sun. DM traveling across the Sun can interact with the protons present in the Sun's core. If the DM velocity after the scattering is lower than the escape velocity from the Sun then DM can accumulate, increasing the DM annihilation cross section rate. The only particles which will be able to escape from the Sun as a product of the DM annihilation are high energy neutrinos detectable by experiments based on Earth such as IceCube [88], SuperKamiokande [89], Antares [90] and KM3NeT [91]. One of the advantages of studying high energy neutrinos as a product of DM annihilation is due to the low background. The neutrinos produced by baryonic interactions in the Sun are far less energetic than the neutrinos coming from DM annihilation. Given the fact that the initial process which allows the Sun to capture DM is due to the scattering among DM and protons, the study on high energy neutrinos is usually compared with direct searches results. Figure 1.14 shows the limit on the DM-proton cross section for different experiments. The most stringent limits are the ones provided by IceCube, which provides two limits for two different annihilation processes: *WW* and $b\bar{b}$. Like direct detection also indirect searches do not show any WIMP

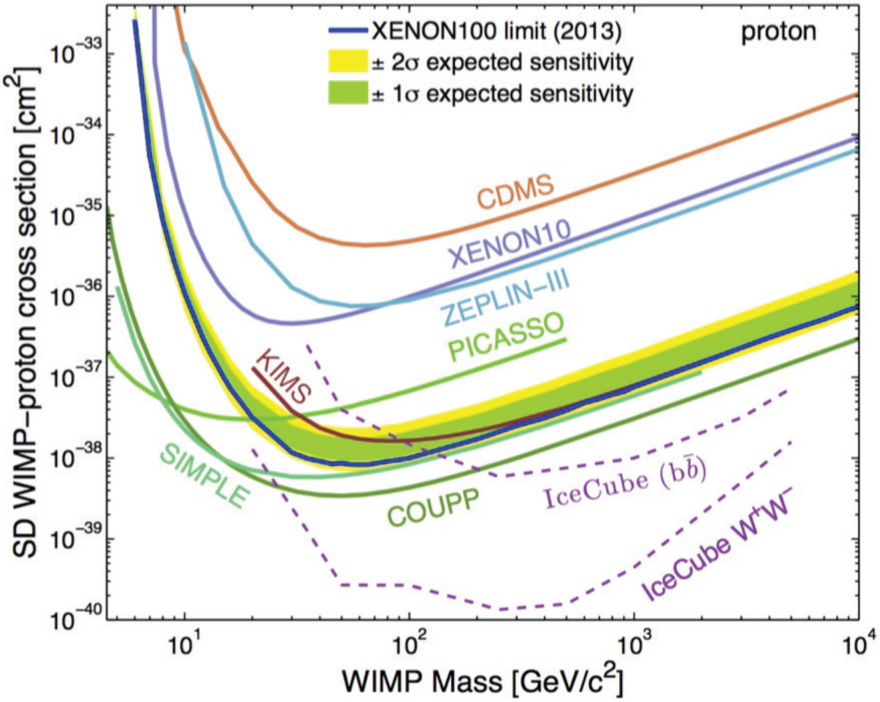

Fig. 1.14 · IceCube results. This plot shows the exclusion limit on the spin-dependent WIMP-proton cross section as function of the WIMP mass from several different experiments. The strongest exclusion limits are from IceCube for two different annihilation processes *WW* and $b\bar{b}$. The picture is taken from [92].

DM discovery so far.

Dark Matter production: collider physics

High energy colliders such as the LHC, producing particles in the mass range of GeV−TeV, can probe the mass window of WIMP DM candidates. Being weakly interacting, DM particles will escape the detector without leaving any trace. The only noticeable effect, for a proton collider, will be an imbalance in the transverse energy between the initial state, with null transverse energy, and the final state. Such imbalance in hadron colliders is called missing transverse energy E_T^{miss} and it will be described in details in the next chapter. In order to tag the DM particle, which is invisible to detection, a SM particle is needed as a probe recoiling against the DM pair. Searches which focus on SM objects recoiling against high E_T^{miss} are called mono-X searches, where X can be a photon, a jet, a top quark, the Z boson and others. The final experimental signature is therefore clear, while the interpretation of the interaction among the SM sector and the DM sector for a given signature depends on the theoretical model. DM searches at the LHC can be summarized into three different theoretical approaches: DM candidates in complete theory, effective field theory (EFT) and simplified models.

DM candidates for complete theories such as SUSY and Extra dimensions have been already described in the previous part of the chapter. Effective field theory (EFT) [93] is applied in DM searches when the energy of the interaction between DM and SM particles is much lower than the mass of the mediator. The mediator can be therefore integrated out and substituted by a set of effective operators. As an example the axial-vector operator is reported:

$$O = \frac{1}{\Lambda^2}(\bar{q}\gamma^{\mu}\gamma^{5}q)(\bar{\chi}\gamma_{\mu}\gamma^{5}\chi) \tag{1.30}$$

where χ is a fermion DM field, and Λ the effective suppression scale.[1] While EFT is always valid for direct searches, a EFT validity problem arises for collider physics. For direct detection the energy exchanged in the interaction is of the order of the keV while the mediator is much heavier (GeV). In this case the mediator can be integrated out and the scattering can be considered as a contact interaction. For collider physics the energy exchange can be of the same order as the mediator mass. In this case, the EFT approximation does not work and it can not be implemented. There are several studies on the validity of EFT and the possibility to still implement it with theoretical technique such as EFT truncation [94]. This approach, popular during Run-I at LHC, now has been substituted by a more reliable approach: simplified models [95].

For high energy exchange, like for the one reached by LHC in Run-II, the interaction once described by effective operators is within reach and therefore resolvable. The type of mediator used to resolve an effective operator depends on the exchange channel (s-channel or t-channel) and on the initial scattering particles (quark or gluons). The easiest models are the ones with quarks interacting via a scalar or a vector boson mediator via the s-channel exchange as shown in Figure 1.15a. Mediators like those can be Higgs-boson-like or a Z' [96] or a new generic mediator. For quarks interacting via the t-channel, as shown in Figure 1.15b, the mediator would be a color charged fermion, squark-like. The gluonic interaction will lead to more complex scenarios with colored scalars and fermions as shown in Figure 1.15c. Every one of these models depends on four crucial variables: the coupling constant among DM and the mediator g_χ, the coupling among the SM and the mediator g_q, the mediator mass m_{Med} and the dark matter mass m_{DM}. Each experimental result will depend on these parameters. In order to provide compatible results among different

---

[1] The suppression scale is an energy scale introduced to not let a specific interaction cross section specified by a Lagrangian term diverge for high energy breaking the unitarity.

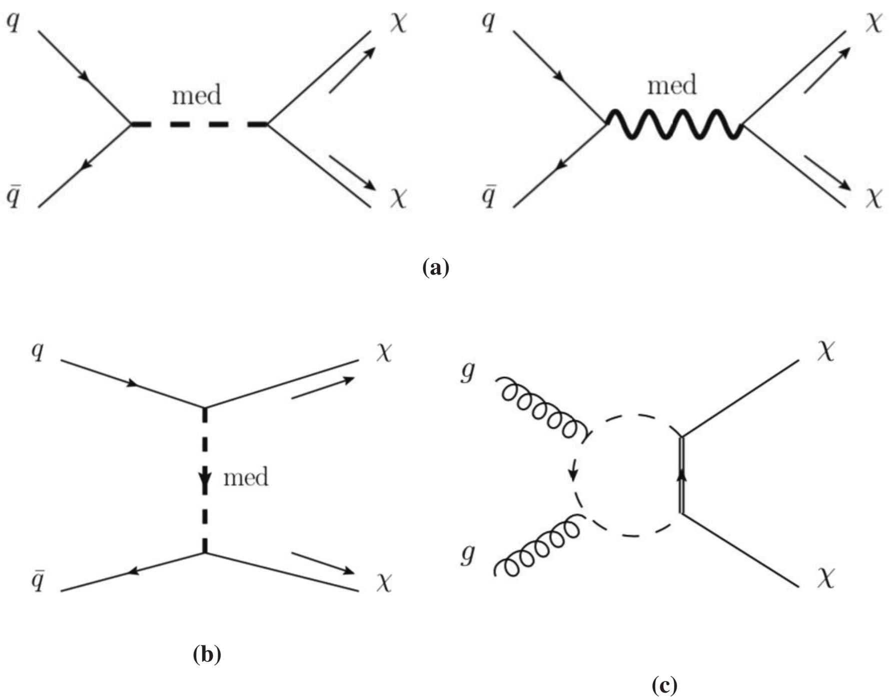

Fig. 1.15 · Feynman graph for DM production via s-channel exchange (a) of scalar and vector mediator, t-channel exchange (b) of a color charged fermion, and gluon-gluon interaction (c) mediated by colored scalars and fermions.

searches for DM for Run-II at LHC a joint task force of CMS and ATLAS Collaborations provided a guideline via the Dark Matter Forum [97]. All the results are shown in a scatter plot of DM mass versus the mediator mass for a fixed value of the two coupling constants. The results up to March 2017 for an axial-vector mediator for the mono-jet, mono-photon and dijet analyses are shown in Figure 1.16. From this plot one can see that a large part of the spectrum of available mass is ruled out, but this plot is sensitive to the coupling value chosen, here $g_q = 0.25$ and $g_{DM} = 1$. A different choice would significantly loosen the exclusion power of such limits. The work of this thesis is based on the study of a simplified model in the search of Dark Matter, the Higgs portal model.

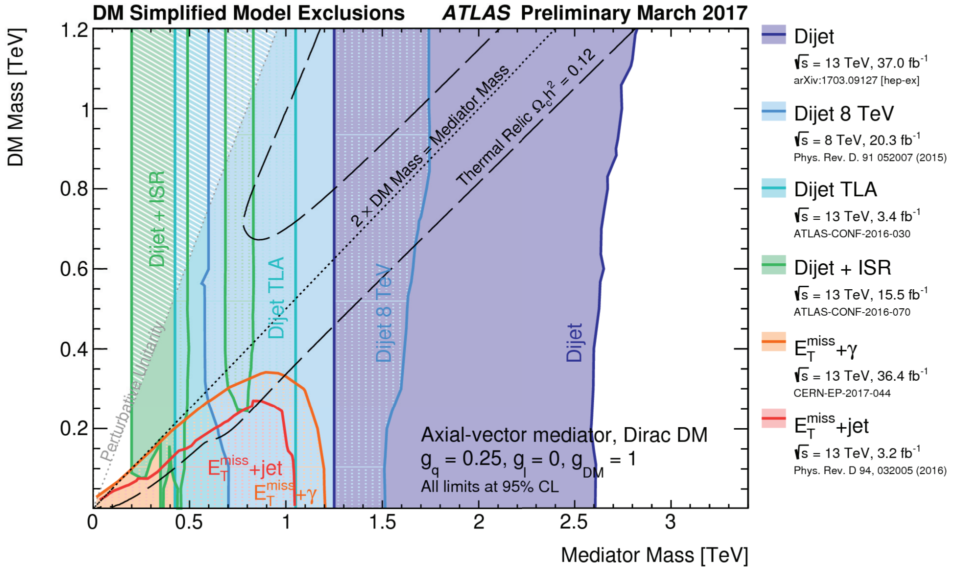

Fig. 1.16 · Results from March 2017 [98]. This plot is a summary of different searches in ATLAS for a simplified DM model with an axial-vector mediator and a fermion DM field. The plot reports observed upper limit results for the Dijet, mono-photon and mono-jet analyses as a function of the mediator mass and the DM mass. The plot show several features: the on-shell limit line 2× DM mass = Mediator Mass, a reference to the the thermal relic density, and the perturbative unitarity line, over which any results have no physical sense. The limits are extremely stringent and rule out almost all the spectrum but they heavily depend on the assumptions for the coupling constants which are: $g_q = 0.25, g_{DM} = 1$. By varying the coupling values, the same results would provide a reduced limit.

1.3 Higgs portal model

After the discovery of the Higgs boson in 2012 at the LHC, many studies were performed on its properties such as mass, spin and coupling [99]. As already discussed previously in this chapter, in the SM the mass of a particle is proportional to its coupling to the Higgs field.

The DM candidates are extremely massive and feebly interacting with the SM sector, it is therefore reasonable to think that DM can couple to the SM via the Higgs. In such a theory the DM field is gauge invariant under the SM symmetry group and the only interactions are via the Higgs field. The Higgs field would then be a portal between the SM sector and the dark sector, which is why this theory is called *Higgs portal model* (HPM) [100].
This model assumes a SM Higgs boson with a modified branching ratio (BR): this leaves room for Higgs to decay into a DM pair. The BR is the ratio between the width of a specific decay normalized to the total width of a particle. In Formulas: $\mathrm{BR}(H \rightarrow \chi\chi) = \frac{\Gamma(H\rightarrow\chi\chi)}{\Gamma_{Higgs}}$.
The total width of a particle is the defined as the width of a Breit-Wigner distribution [101] and it can be written as $\Gamma = \hbar/t$ where t is the particle lifetime. The total width is also the sum of all the partial decay widths, which are proportional to the matrix element of the specific decay following the Fermi Golden Rule. One way to put a limit on the available BR of Higgs decay to DM can be obtained via indirect measurements, by studying the coupling of the Higgs to SM particles. Another approach is via direct measurement of its decay into DM. DM is interacting weakly with ordinary matter, therefore the DM particles produced by the Higgs decay will be completely invisible for the detector: this is the reason why such studies are referred to as *Invisible Higgs* decay. The interesting aspect of this theory is that the BR of SM Higgs into neutrinos (another *invisible* particle) is negligible, therefore any proof of Invisible Higgs decay would point immediately to phenomena beyond the Standard Model.

The model

This theory is a simplified model with the exchange of a scalar boson, the Higgs boson, via the s-channel. To maintain a DM model-independent approach three possible DM fields are introduced: scalar *S*, fermion χ and vector *V*. The DM Lagrangian term will look like:

$$\begin{aligned}
\mathcal{L}_S &= -\frac{1}{2}m_S^2 S^2 - \frac{1}{4}\lambda_S S^4 - \frac{1}{4}\lambda_{HSS} H^+ H S^2 \\
\mathcal{L}_V &= -\frac{1}{2}m_V^2 (V_\mu V^\mu)^2 - \frac{1}{4}\lambda_V (V_\mu V^\mu)^2 + \frac{1}{4}\lambda_{HVV} H^+ H V_\mu V^\mu \qquad (1.31) \\
\mathcal{L}_f &= -\frac{1}{2}m_f \chi\bar{\chi} - \frac{1}{4}\frac{\lambda_{hff}}{\Lambda} H^+ H \chi\bar{\chi}
\end{aligned}$$

where $\lambda_{S,V}$ are the self-interacting coupling constants and $\lambda_{h\chi\chi}$ is the coupling constant among the Higgs and the DM field. Figure 1.17 shows the Feynman graph of the interaction among the DM and the Higgs field. The energy scale Λ is introduced to keep the interaction term of dimension 4.[1] After the spontaneous symmetry breaking, the mass of the DM

---

[1] The SM Lagrangian has dimension 4 and each term should be of dimension 4. Fermionic fields have dimension 1.5 and bosons 1. In the case of the term $H^+H\chi\bar{\chi}$, the dimension is 5 (1+1+1.5+1.5), therefore a factor $1/\Lambda^D$ with D=1 is introduced.

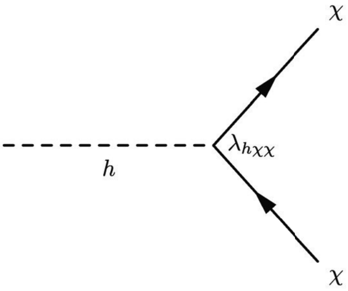

Fig. 1.17 · Feynman diagram of a decay of a Higgs into a pair of DM particles χ. $\lambda_{h\chi\chi}$ is the coupling interaction constant among the DM and the Higgs field

particles can be written as:

$$\begin{aligned} M_S^2 =& m_S^2 + \frac{1}{2}\lambda_{HSS}v^2 \\ M_V^2 =& m_V^2 + \frac{1}{2}\lambda_{HVV}v^2 \\ M_f =& m_f + \frac{1}{2}\frac{\lambda_{hff}}{\Lambda}v^2 \end{aligned} \tag{1.32}$$

where v is the vacuum expectation value of the Higgs field.
As already described previously the Feynman diagram that describes the interaction of the Higgs boson and DM can be interpreted in three different ways: annihilation of a DM pair via the exchange of the Higgs boson, Higgs produced via SM particle collisions decaying into a DM pair, and DM-nucleon scattering mediated via the Higgs boson. The coupling constant $\lambda_{h\chi\chi}$ is therefore linked to the relic density, the cross section of DM-nucleon

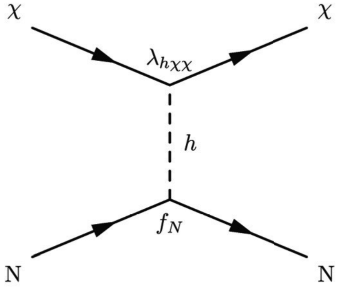

Fig. 1.18 · Feynman Diagram for interaction among DM and SM nucleon N, mediated via the Higgs boson. $\lambda_{h\chi\chi}$ is the coupling interaction constant among the DM and the Higgs field, while f_N is a parametrization factor for the coupling between the Higgs and the nucleon

scattering and the BR of invisible Higgs decay. By looking at the annihilation, the cross sections of DM can be evaluated as follows:

$$
\begin{aligned}
< \sigma^{S}_{ferm} v_r > &= \frac{\lambda^2_{hSS} m^2_{ferm}}{16\pi} \frac{1}{(4M^2_S - m^2_h)^2} \\
< \sigma^{V}_{ferm} v_r > &= \frac{\lambda^2_{hVV} m^2_{ferm}}{48\pi} \frac{1}{(4M^2_V - m^2_h)^2} \\
< \sigma^{f}_{ferm} v_r > &= \frac{\lambda^2_{hff} m^2_{ferm}}{16\pi} \frac{M^2_f}{\Lambda^2} \frac{v^2_r}{(4M^2_f - m^2_h)^2}
\end{aligned}
\tag{1.33}
$$

where v_r is the DM relative velocity.
By looking at the DM-nucleon scattering one can define the spin-independent cross section among a nucleon and DM σ^{SI}_{X-N} as:

$$
\begin{aligned}
\sigma^{SI}_{S-N} &= \frac{\lambda^2_{hSS}}{16\pi m^4_h} \frac{m^4_N f^2_N}{(M_S + m_N)^2} \\
\sigma^{SI}_{V-N} &= \frac{\lambda^2_{hVV}}{16\pi m^4_h} \frac{m^4_N f^2_N}{(M_V + m_N)^2} \\
\sigma^{SI}_{f-N} &= \frac{\lambda^2_{hff}}{4\pi \Lambda^2 m^4_h} \frac{m^4_N M^2_f f^2_N}{(M_f + m_N)^2}
\end{aligned}
\tag{1.34}
$$

where m_N is the mass of the nucleon and f_N [1] is a parametrization factor for the coupling between the Higgs and the nucleon.
Finally, in case of DM particles lighter than half the mass of the Higgs boson, the invisible Higgs BR can be written as:

$$
\begin{aligned}
\Gamma^{inv}_{h \to SS} &= \frac{\lambda^2_{hSS} v^2 \beta_S}{64\pi m_h} \\
\Gamma^{inv}_{h \to VV} &= \frac{\lambda^2_{hVV} v^2 m^3_h \beta_V}{256\pi M^4_V} \left(1 - 4\frac{M^2_V}{m^2_h} + 12\frac{M^4}{m^4_h}\right) \\
\Gamma^{inv}_{h \to XX} &= \frac{\lambda^2_{hff} v^2 m_h \beta_f}{32\pi \Lambda^2}
\end{aligned}
\tag{1.35}
$$

where $\beta_X = \sqrt{1 - 4\frac{M^2_X}{m^2_H}}$.
The equations just written show that the coupling λ_{hXX} links the three different searches for DM. Figure 1.19 shows the exclusion limit for the WIMP-nucleon cross section scanned over the mass of the DM candidate. This plot is a compilation of results from different experiments compared with the results from collider experiments in the HPM model. The BR is assumed to be lower than 22% [2] for the HPM and the confidence level (CL) of the limit is adjusted to 90% to make a fair comparison with the observed limits from experiments

---

[1] This factor is evaluated as a linear combination of two terms accounting for light quarks f_L and heavy quarks f_H. $f_N = \Sigma f_L + 3 \times \frac{2}{27} f_H$

[2] This BR limit is compatible with limits derived from the measurements of the Higgs coupling to SM particles, which restrain the invisible BR in a SM like scenario

such as Xenon100 or LUX. The plot shows that for masses higher than $m_H/2$, DM-nucleon recoiling experiments are more competitive, while for low masses results from collider experiments in the HPM model dominate. This is due to two factors. The first one is that for DM mass higher than $m_H/2$ no on-shell Higgs decay is allowed. The second one is due to the low sensitivity of experiments such as Xenon or Lux for low masses (below 30-40 GeV). This is linked to the amount of radioactive activity produced by the detector itself that reduce the sensitivity of the signal. More details can be found in literature [64]. The collider experiments using the HPM model are therefore competitive with the indirect searches and can investigate simultaneously the Higgs properties, its invisible BR, and the presence of Dark Matter. The work of this thesis will explore the invisible decay of a Higgs boson produced in associated production with a Z boson.

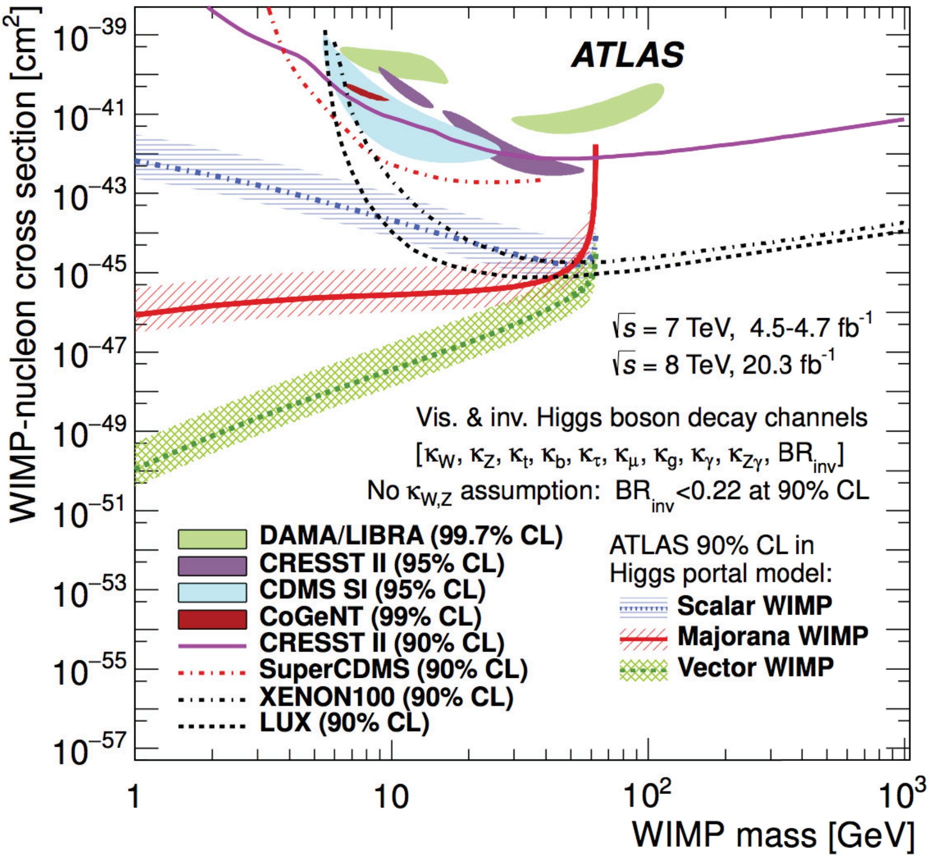

Fig. 1.19 · WIMP nucleon cross section upper limits from different searches [99]. This plot shows the upper limits of several experiments on the WIMP-nucleon cross section as a function of the WIMP mass, compared with the result for the Higgs portal model with a BR < 0.22 at 90% CL in ATLAS. Such comparison between different searches is possible in terms of $\lambda_{h\chi\chi}$. The plot shows that the HPM is extremely competitive for the low mass region with direct detection experiments such as Xenon.

chapter two

The ATLAS experiment at the Large Hadron Collider

2.1 The Large Hadron Collider

The Large Hadron Collider (LHC) [102] is a 26.7 km two-ring superconducting accelerator of protons and ions. The machine is installed inside the former LEP ring [103], which lies between 45 and 170 m under the surface in the Geneva area in Switzerland. The machine is designed to operate at a center-of-mass energy of $\sqrt{s} = 14$ TeV and uses the CERN accelerator complex as its injection system. Figure 2.1 shows the schematic of the injection procedure: ionized hydrogen atoms (protons) are accelerated up to 50 MeV in a linear accelerator (LINAC2) and they are injected in a chain of three accelerators. The Proton Synchrotron Booster (PSB) is the first ring of 157 meters and brings up the energy to 1.4 GeV, the Proton Synchrotron (PS), a ring of 628 meters, bring up the energy to 25 GeV, the Super Proton Synchrotron (SPS), a ring of 7 km, brings up the energy to 450 GeV and finally the protons are injected inside the LHC reaching the nominal center-of-mass energy. The protons are arranged in bunches of 1.15×10^{11} particles, and each bunch is separated by 25 ns from the next one. The bunches have to be accelerated, kept inside the ring, and stabilized/focused. The acceleration is performed by sixteen superconductive radio frequency cavities (RF) working at 400 MHz. The bunches are kept inside the ring thanks to 1236 superconductive dipole magnets. The beam is stabilized and focused using 392 quadrupole magnets. The two proton beams cross each other in four points around which the four major experiments are built: ATLAS [104], CMS [105], ALICE [106] and LHCb [107]. Since LHC has become operational it has worked at different center-of-mass energy: for the so called Run-I (from 2010 until 2012) LHC worked at $\sqrt{s} = 7$ TeV (2010-2011) and at $\sqrt{s} = 8$ TeV (2012). Since the starting of the Run-II (2015-2018) the machine has worked at $\sqrt{s} = 13$ TeV. This thesis will take into account the data collected in Run-II from 2015 until the summer of 2016.

2.1.1 Luminosity and pile up

The rate of events generated by collisions at the LHC is equal to $n = L\sigma$, where L is the instantaneous luminosity and σ the interaction cross section which depends on the nature of the process itself and the center-of-mass energy at which the machine is working. The

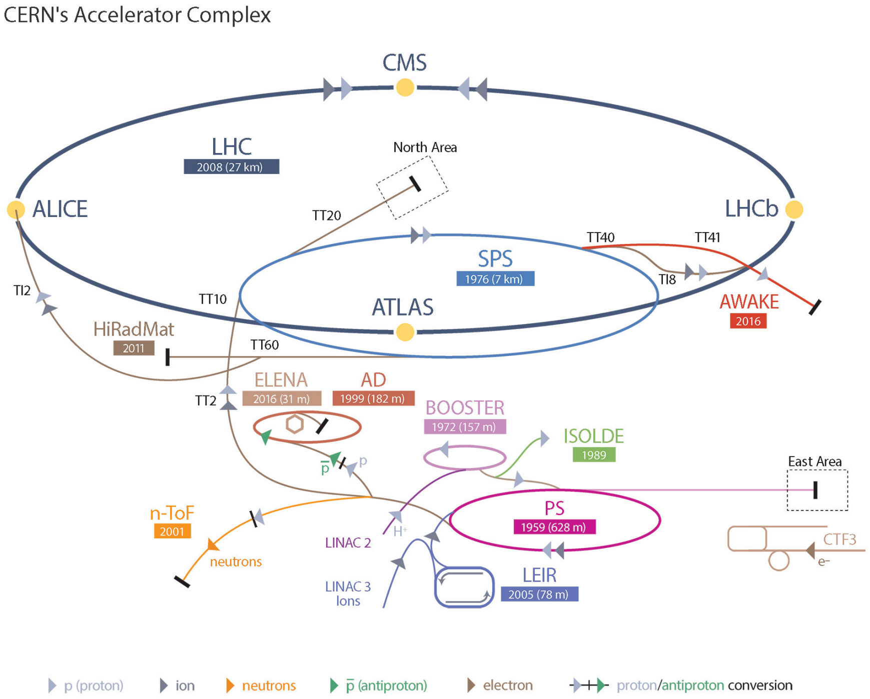

Fig. 2.1 · CERN accelerator complex and the LHC. The figure is taken from [108]

luminosity L depends only on the machine parameters which, under a Gaussian assumption, can be defined as:

$$L = \frac{N_b^2 n_b f_{rev} \gamma_r}{4\pi \epsilon_n \beta^*} F \tag{2.1}$$

where N_b is the number of particles per bunch, n_b the number of bunches per beam, f_{rev} the revolution frequency, γ_r the relativistic gamma factor, ϵ_n the normalized transverse beam emittance, β^* the beta function at the collision point, and F the geometric luminosity reduction factor due to the crossing angle θ_c at the interaction point (IP). We can define F, β^* and f_{rev} as follows:

$$\begin{aligned} F &= (1 + (\frac{\theta_c \sigma_z}{2\sigma^*})^2)^{-\frac{1}{2}}, \\ f_{rev} &= \frac{\beta c}{2\pi R}, \\ \beta^* &= \frac{\pi(\sigma^*)^2}{\epsilon_n}, \end{aligned} \tag{2.2}$$

where θ_c is the beam crossing angle at the IP, σ_z and σ^* are the longitudinal and transverse bunch length. All those equations assume round beams, $\sigma_z \ll \beta$, with identical beam parameters. The total number of events N produced at LHC can be written in terms of Integrated Luminosity $\mathcal{L} = \int L dt$ as $N = \mathcal{L}\sigma$. The Integrated Luminosity $\mathcal{L}$ is measured in inverse barn, where $1 \text{ barn} = 10^{-28}\ m^2$. Figure 2.2 shows the cumulative of the delivered (and recorded) luminosity for the year 2015 and 2016 [109] by LHC for the ATLAS detector. For a high energy hadronic collider, an interaction among two bunches can create multiple inelastic proton-proton scattering events. Such additional interactions increase the amount of occupancy of the read-out system of the detector. This effect is called pile-up. The pile-up can be of two types: in-time pile-up and out-of-time pile-up. The pile-up generated by the head-to-head collision of associated bunches is called in-time pile up, while the remainder of the pile-up signal in the electronics from interactions in previous bunch crossings is called

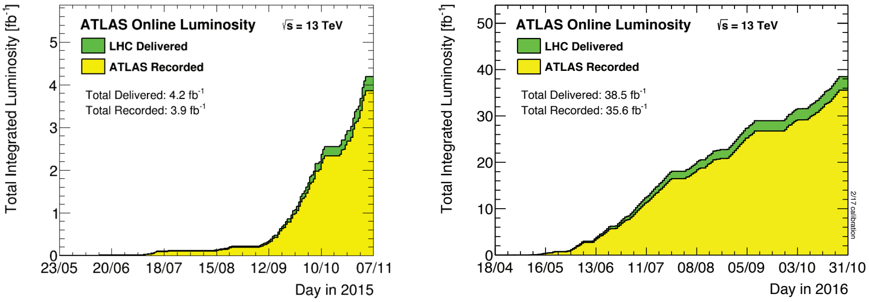

(a) **(b)**

Fig. 2.2 · Cumulative of the luminosity delivered (in green) by LHC and recorded (in yellow) by ATLAS for the year 2015 (a) and 2016 (b) [109].

out-of-time pile-up.For the in-time pile-up the mean number of interactions per crossing μ is given by the following formula:

$$\mu = \frac{L\sigma_{inel}}{n_b f_{rev}} \tag{2.3}$$

where σ_{inel} is the total inelastic cross section of proton-proton collisions[1]. From this equation we can notice that the pile up grows proportionally to the Instantaneous peak Luminosity. This means that the higher the Luminosity the higher the occupancy of the detector per crossing. This makes the pileup a challenge to face for high luminosity machine such as LHC. Figure 2.3 shows the mean number of interactions per crossing recorded by the ATLAS detector for the year 2015 and 2016 of Run-II [109]. Table 2.1 shows a summary of LHC design parameters compared to the actual ones for the Run-II.

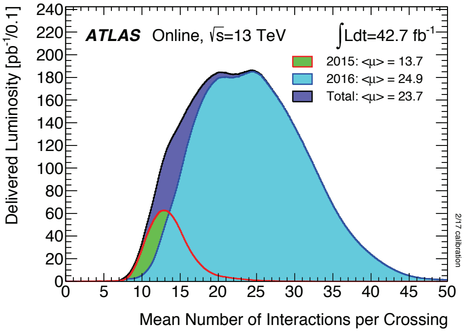

Fig. 2.3 · Mean number of interaction per crossing for the data collection 2015 and 2016 in ATLAS [109].

Parameter	2015	2016	Design
Center-of-mass energy $\sqrt{s}$	13	13	14
Peak Instantaneous Luminosity [$10^{33}cm^{-2}s^{-1}$]	5.02	13.8	10
Delivered Integrated Luminosity [fb^{-1}/year]	4.2	38.5	80-120
Recorded Integrated Luminosity by ATLAS [fb^{-1}/year]	3.9	35.6	-
Minimum bunch spacing [ns]	25	25	25
Average number of interactions $< \mu >$	13.7	24.9	19

Table 2.1 · LHC parameters for Run-II for the years 2015 and 2016 [111] compared to the design [112].

---

[1] The theoretical (experimental) inelastic cross section σ_{inel} for $\sqrt{s} = 13$ TeV has been calculated (measured) as 78.4 mb (73.1 ± 7.7 mb) [110]

2.2 The ATLAS detector

The ATLAS detector [113, 114] is a multi-purpose experiment which has been built to investigate the Standard Model phenomena with a specific focus on the search for the Higgs boson, which has been discovered in 2012, and to search for phenomena beyond the Standard Model such as SUSY, Dark Matter and many others. The ATLAS detector [115], shown in Figure 2.4, has a cylindrical shape and is 44 meters long, with a diameter of 25 meters and it weighs 7000 tons. The detector is centered on the IP and it is designed with a forward-backward symmetry. In order to collect all the possible particles produced by the proton-proton collisions the detector has a good spatial coverage thanks to a system of sub-detectors. The list of sub-detectors starting from the beam pipe are: the inner detector, the electromagnetic calorimeter, the hadronic calorimeter and the Muon Spectrometers. The ID is subjected to a solenoidal magnetic field of 2 T. The outer part of the detector is subjected to a magnetic field produced by three toroidal magnets. Each sub-detector is tailored to measure the characteristics of different particles. The ID is used to measure the position of the interaction vertex, to reconstruct the tracks of the out-coming particles. The presence of a magnetic field allows to measure the charge and the momentum of such particles. The calorimeters, positioned right around the ID, are used to evaluate the energy of an incoming particle. The outer part of the detector is used to track and reveal the presence of muons. The different parts of the detector will be described in details in the next sections.

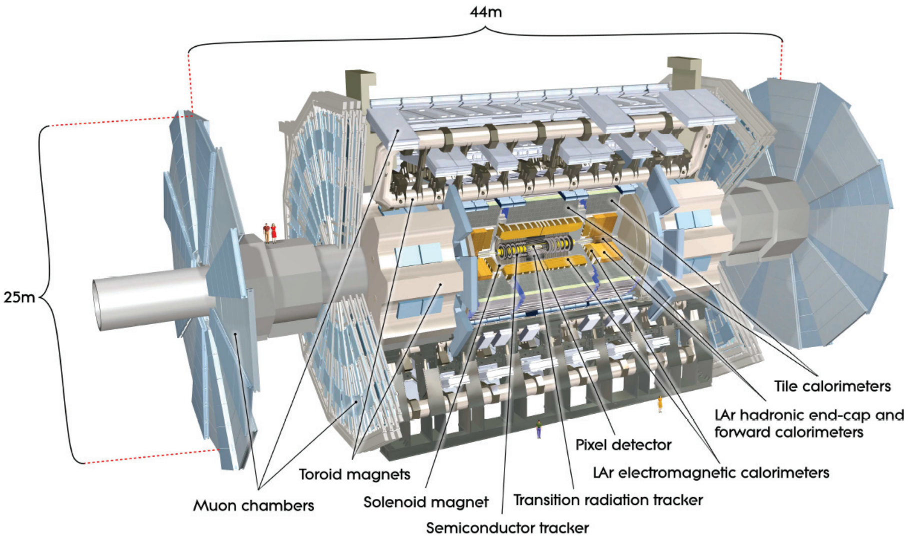

Fig. 2.4 · A cut-away of the ATLAS detector system of sub-detectors.The picture is taken from [115].

2.2.1 Coordinate system

The coordinate system for the ATLAS detector is a right-handed Cartesian one, centered in the IP. The z-axis is the one along the beam direction, with the positive direction towards the side-A of the detector. The x-y axis is the one defining the transverse plane, where the x-axis points towards the center of the LHC ring and the y-axis points upward. Two angles are defined: the polar angle $\theta \in [0, \pi]$ and the azimuthal angle $\phi \in (-\pi, \pi]$. The polar angle is defined as the angle between a vector and the beam axis while the azimuthal angle is defined as the angle around the beam axis. Given the shape of the detector, cylindrical coordinates are often use, in the form of (R,ϕ). For massless particles in hadronic colliders an angular variable is introduced called pseudo-rapidity which is defined as $\eta = -\ln\tan\frac{\theta}{2}$. This variable is introduced because it is invariant under Lorentz transformations along the z-axis. For massive objects the rapidity is used instead : $y = \frac{1}{2}\ln\frac{E+p_z}{E-p_z}$. The angular distance between two objects is expressed in terms of $\Delta R = \sqrt{\Delta\eta^2 + \Delta\phi^2}$. It is important to notice that in a hadronic collider the longitudinal momentum in the initial state is not known, therefore the variables are defined along the transverse plane x-y, where the energy has to be conserved[1]. Each variable then will have a "transverse" correspondent, such as the transverse momentum of a particle that will be defined as $p_T = p\sin\theta$ and the transverse energy as $E_T = E\sin\theta$. Another crucial variable is the missing transverse energy which is defined as:

$$E_T^{\text{miss}} = -\sum_i \vec{p}_T^{\,i}, \tag{2.4}$$

where $\vec{p}_T^{\,i}$ is the transverse momentum of each reconstructed object. The E_T^{miss} is therefore a vector in the transverse plane with same absolute values as the vectorial sum of the transverse momentum of all reconstructed objects, same direction and opposite sign. This variable is a measure of the energy imbalance in the transverse plane.

2.2.2 Inner detector

The ATLAS Inner Detector (ID) [116, 117] is designed to measure the tracks of particles, the primary and secondary interaction vertices and to measure the momentum of charged particles with extremely high resolution. The detector, embedded in a 2 T magnetic field, can measure particles with a wide range of energy and it has an angular coverage up to $|\eta| < 2.5$. The ID is composed of three different and complementary sub-detectors which fulfill different reconstruction goals. The necessity of a high resolution vertex reconstruction requires high granularity which can be provided by semiconductor detectors. Such detectors are extremely precise but also extremely costly and they introduce a significant amount of material, therefore their usage has to be limited. There are two semiconductor based detectors: the pixel detector (which includes the Insertable B-Layer (IBL) introduced in the first long shutdown (LS1) [118]) and the semiconductor Tracker (SCT). Usually a track encounters three plus one layers of pixel detector and eight layers of SCT. In order to reconstruct a track, a larger amount of tracking points is required. This is achieved by using the Transition Radiation Tracker (TRT), a straw tube tracker. The usage of such detector provides a good amount of points per track (around 36), with the advantage of being much

---

[1] The initial state energy is equal to 0 in the transverse plane.

cheaper then a semiconductor detector. Another advantage of this detector is the ability to separate electron from charged hadrons due to transition radiation photons produced in the straw tube. Figure 2.5 shows a cut-away of the ATLAS ID taken from [115].

The Pixel detector is a silicon pixel based detector composed of 1744 modules. The detector is divided into two angular areas, the barrel and the end-cap. The modules in the barrel are arranged on three concentric cylinders around the beam axis while the two end-caps are composed of three disks orthogonal to the beam axis. The modules are segmented along the (R, ϕ) plane and along z. The nominal size of the pixel module is 50×400 μm^2, the resolution is 10 μm along the transverse direction and 115 μm along the longitudinal direction.

The Insertable B-Layer is the closest detector to the beam pipe and it is part of the Pixel detector. It is a single layer of pixel detector of cylindrical shape. The nominal size of the module is 50×250 μm^2, its resolution is 8.5 μm in the transverse direction and 47 μm in the longitudinal direction.

The Semiconductor Tracker is an eight strip layer detector, composed of 4088 modules for a total of 6.3 million readout channels. The intrinsic resolution is 17 μm in the transverse direction and 580 μm in the longitudinal direction.

The Transition Radiation Tracker is a detector based on 4 mm diameter straw tubes. Each tube contains a gas mixture and an inserted 31 μm gold-plated tungsten anode wire. The resolution of the TRT is 130 μm in the transverse plane.

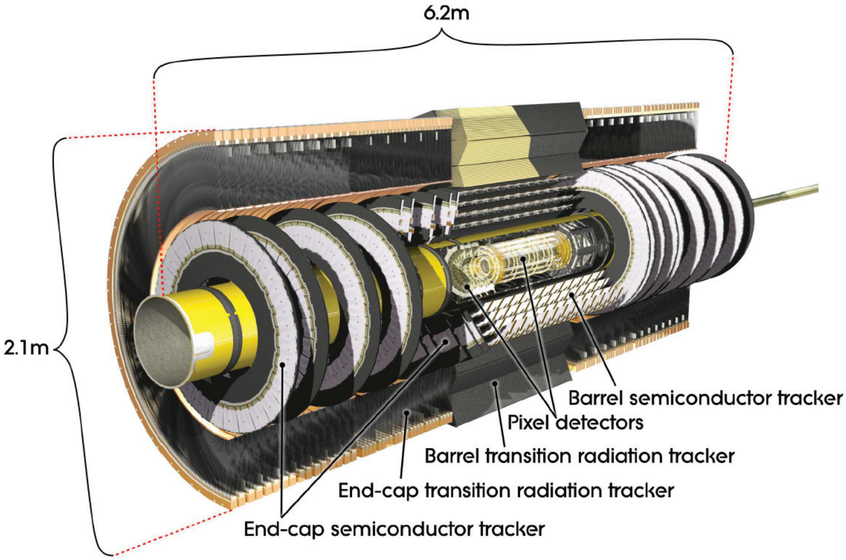

Fig. 2.5 · Cut away of the ATLAS inner detector. The picture is taken from [115]

2.2.3 Calorimeters

There are two kind of calorimeters in the ATLAS detector: electromagnetic(to measure electrons and photons) and hadronic(to measure hadrons). Each calorimeter is made of two layers, passive ones that functions as target and active ones that works as readout. It is crucial to measure the total energy deposit of the particle, therefore the particle has to be totally stopped inside of the calorimeter: therefore passive layers are used to increase the stopping power while the energy deposit is measured by the active part of the detector. Figure 2.6 shows a cut-away view of the ATLAS calorimeter system [115].

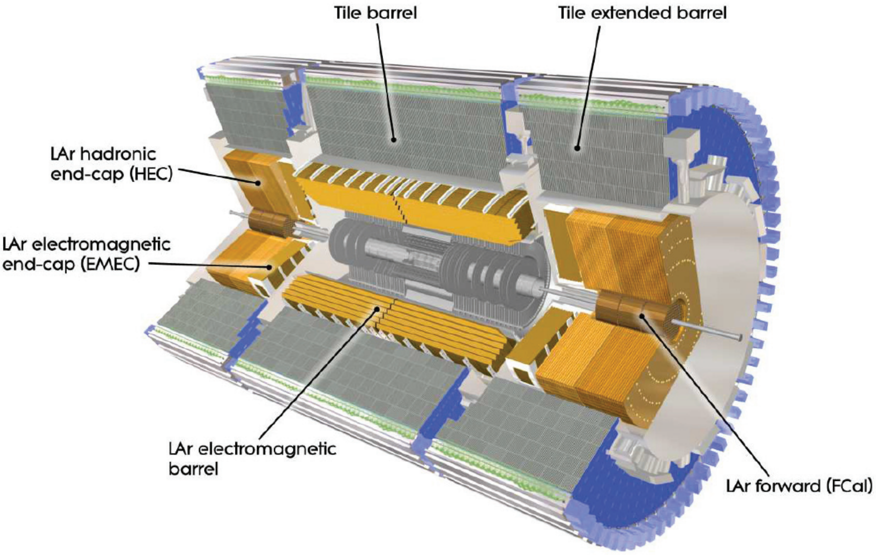

Fig. 2.6 · Cut away of the ATLAS calorimeter system. The picture is taken from [115]

The Electromagnetic calorimeter

The Electromagnetic calorimeter (ECal) [119] is built to completely stop and measure electrons and photons. In order to stop any photons and electrons the Ecal has a depth corresponding to more than 22 radiation lengths X_0. The Ecal is composed of passive layers of lead interspersed with active layers of Liquid Argon (LAr) arranged in an accordion geometry. Such choice allows the detector to be symmetric under rotation along the ϕ angle, avoiding cracks in the angular coverage. The calorimeter is divided in two regions: the barrel and the end-cap. The angular coverage of the barrel is $|\eta| < 1.475$ while the end-cap is $1.375 < |\eta| < 3.2$. To improve performances the granularity of the detector varies depending on the angle η. The energy resolution of the Ecal is $\sigma_E/E = 9\%\sqrt{E} \oplus 0.3\%$.

The Hadronic calorimeter

The Hadronic calorimeter (HCal) [120] is designed to measure and stop hadrons. The Hadronic calorimeter is composed of three different parts: the central one (barrel) is made of absorbing layers of steel interspersed with tile scintillators, the end-cap is made of layers of absorbing copper interspersed with LAr and the forward parts are made of copper and tungsten interspersed with LAr. The HCal has a depth corresponding to up to 9.7 nuclear interaction lengths λ. The angular coverage for the three parts are respectively: $|\eta| < 1.7$ (barrel) , $1.5 < |\eta| < 3.2$ (end-cap), $3.1 < |\eta| < 4.9$ (forward). The energy resolution of the HCal is $\sigma_E/E = 50\%\sqrt{E} \oplus 3\%$ for barrel and end-cap while it is $\sigma_E/E = 100\%\sqrt{E} \oplus 10\%$ for the forward calorimeter.

2.2.4 Muon spectrometer

The Muon spectrometer (MS) [121] is designed to identify and measure the particles that escape the calorimeter: the muons. The MS has an angular coverage of $|\eta| < 2.7$ and it can measure muons from a few GeV up to 3 TeV, with a resolution of $\sigma_{p_T}/p_T = 10\%$ for 1 TeV muon. The detector is built inside the toroidal magnet system and it is subjected to an azimuthal magnetic field with magnetic bending power of 1-7.5 Tm depending on the location in the detector. The MS is composed of three barrel layers and two end-cap disks with two different type of detector installed: the precision tracking chambers and the fast triggering chambers. Figure 2.7 shows the ATLAS MS detector scheme.

The Precision Tracking Chambers

The precision tracking chambers are used to measure the momentum and track of the muons and they use two different kind of sub-detectors: the Monitored Drift Tubes (MDT) and the Cathode Strip Chambers (CSC). Most of the precision tracking chambers are MDT and they provide an angular coverage of $|\eta| < 2.0$. The MDT are 30 mm aluminum tubes filled with a mixture of Argon and CO_2, with a tungsten-rhenium 60 μm anode. The MDT allow the muon to be reconstructed in 2D with a resolution of 80 μm. In the end-cap region, $2.0 < |\eta| < 2.7$, CSC are used due to their higher granularity and higher acceptance rate which makes them more adapt to the higher rate of particles passing trough. The CSC are multi-wired proportional chambers with two cathode strips perpendicular and parallel to the wire. This geometry allows the CSC to provide a 3D measure with a resolution of 60 μm on CSC plane and 5 mm along the non-bending plane.

The Fast Triggering Chambers

The fast triggering chambers are used to identify and to trigger particle as muons with a very quick response, in the order of nanoseconds. Such fast answer is required to trigger the presence of muons in the event as it is the first step in the event reconstruction in the trigger chain (more details in the next paragraph). Those chambers also provide complementary information to the measurement made by the precision tracking chambers. These chambers are of two kind: the Resistive Plate Chambers (RPC) and the Thin Gap Chambers (TGC). The area up to $|\eta| < 1.05$ contains three RPC stations while the end-cap area, $1.05 < |\eta| < 2.4$, four TGC. The RPC are made of two resistive plates separated by a chamber filled with a mixture of gas and two orthogonal strips readout. The RPC have a spatial resolution of 10 mm and a time resolution of 1.5 ns. The TGC are multi-wire proportional chambers with a resolution of 2-7 mm and a drift time measurement of 1.5 ns.

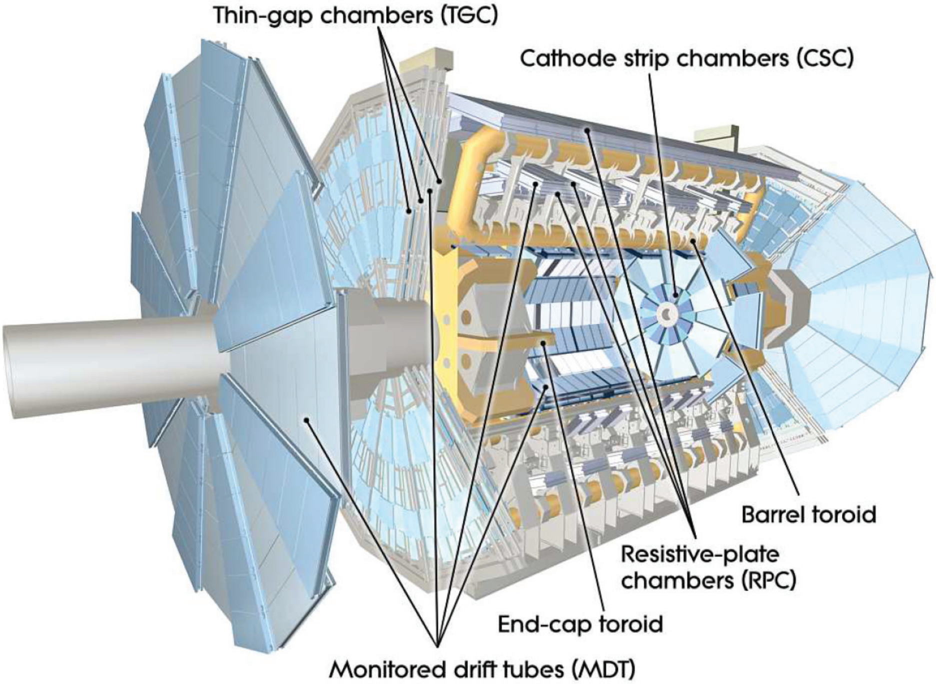

Fig. 2.7 · ATLAS Muon Spectrometer layout. The picture is taken from [115].

2.2.5 Trigger systems

At the LHC, the rate of data is extremely high, therefore a crucial part of the detector has to be dedicated to the reduction of the event rate and to its safe recording. The system that controls such operations is called Trigger and Data Acquisition (TDAQ) [122]. The event rate for the ATLAS detector is in the order of 40 MHz and taking into account all the read-out channels this sums up to a total of 1.3 MB data per event. This leads to petabytes of data to be stored per second and this is not possible given our current technology. The goal is therefore to reach a recording rate of few hundreds of Hz, which means to be able to store data in the rate of fraction of $\mathrm{Gb/s}$. This reduction is implemented in ATLAS via a two[1] level trigger system: level one (L1) and high level filter (HLF). The trigger system works in a chain, each level reduces the amount of data and increases the complexity of the selection. The high level trigger has more sophisticated selections, but at the same time higher latency time. In order to achieve proper data reduction and avoid loss of information,

---

[1] In Run-I the trigger system was based on three levels: L1, L2 and event filter. The last two trigger systems have been merged into the HLF in Run-II.

a proper balance among those two characteristics has to be found. The L1 trigger is based on a hardware system which uses the information coming from the calorimeter and the trigger muon chambers. The event rate after the L1 is reduced to $100\ \mathrm{kHz}$ and the response time is 2.5 μs. The L1 trigger creates one or more Regions of Interest (RoI's) that represents a specific area in the (η, ϕ) plane of the detector where the trigger found interesting features. The stream of selected data after the L1 trigger, together with the RoI's information, is the input for the HLF trigger. Such trigger makes its decisions based on software and it uses all the information from the detector in the RoI's. At the end of this process the HLF trigger has reduced the event rate to 1 kHz and its latency is 200 ms.

chapter three

Event reconstruction

One of the goals of a high energy physics experiment is to discover new phenomena and to analyze and measure with better precision the ones already known. In order to do so, the acquisition and processing of data are fundamental. It is then necessary to define methods and implement algorithms to reconstruct each object produced in each event in the most accurate way. In this chapter we will discuss in detail the event reconstruction starting from tracks and vertices moving to the objects used in the analysis at study in this thesis: electrons, muons, jets and missing transverse energy.

3.1 Tracks and vertices

3.1.1 Tracks

Tracks in the ATLAS detector are reconstructed using the information from the ID. Due to the presence of the magnetic field, charged particles are bent resulting in a helix trajectory. A charged particle, interacting with the ID, produces several hits in the different sub-detector modules. A track can be then reconstructed by fitting the hits. The algorithm used by ATLAS to reconstruct tracks is called NEWT [123] and it uses both local and global patter recognition algorithms. Tracks can be divided into three groups depending on their origin: primary tracks are the ones coming from the proton-proton hard scattering, secondary tracks are the ones coming from the decay of long living particles and conversion tracks are the ones originating from particles interacting with the detector material. Primary tracks are defined as the ones produced by charged particles with a lifetime greater than 3×10^{-11} s or produced by the decay product of particles with shorter lifetime. Tracks with a $p_T > 400$ MeV can be reconstructed in the angular range $|\eta| < 2.5$. For primary tracks an *inside-out* method is used. This method starts by the identification of a *seed* consisting of a triplet of hits in the pixel and SCT detector. Once the seed is defined, more hits compatible with the track trajectory are added by using a Kalman Filter [124] moving from the inner part of the detector outwards. Given the high amount of particles generated in a high energy proton-proton collision, the same set of hits can be linked to multiple tracks candidates. In order to remove this ambiguity, dedicated algorithms are used [125]. Those algorithms use track properties such as holes and shared hits. A hole is defined as a missing expected hit. Once the fit on a track is performed, the fit expects a hit in a specific area of the detector, if the hit is missing, the missing hit is labeled as a hole. Shared hits are defined as those hits which are compatible with multiple track candidates. Secondary and conversion tracks are reconstructed via an outside-in method. Such method starts by using the information from the TRT segments adding the silicon hits: such method is known as well as back-tracking. Moreover, track reconstruction can lead to *fake tracks*. Such tracks are neither primary neither secondary, they are just a random combination of hits which fits the criteria of the reconstruction algorithm without being associated with any particle or physical process. This feature is even stronger for a high pile-up environment as the one in Run-II. In order to reduce the rate of fake tracks and increase the purity of reconstructed tracks, different selections with tighter requirements are defined: Loose, Loose-Primary and Tight-Primary. The track reconstructed efficiency for the Loose and Tight selection is shown in Figure 3.1 as a function of p_T and η [126].

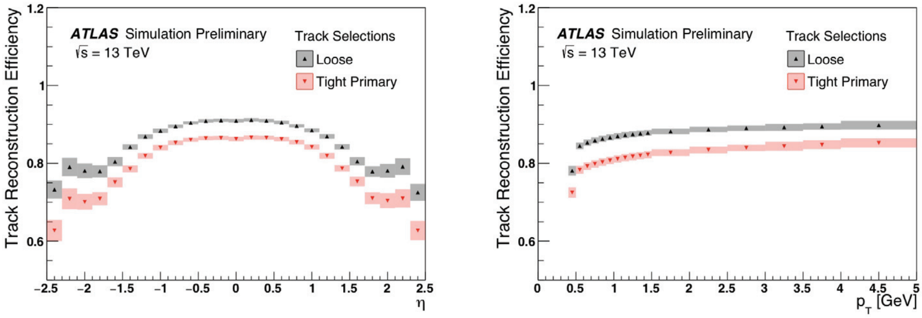

(a) (b)

Fig. 3.1 · Track reconstruction efficiency for the Loose and Tight selection as a function of η (a) and p_T (b) using a Minimum Bias [127] PYTHIA [128] simulation. The figure has been taken from [126]

3.1.2 Primary vertex reconstruction

The primary vertex is reconstructed via several algorithms using as input reconstructed primary tracks. A primary track has to fulfill the following requirements:

- $p_T > 400$ MeV and $|\eta| < 2.5$
- Number of silicon hits higher than 9 (11) for $|\eta| < 1.65$ ($|\eta| > 1.65$)
- At least one hit in the first two pixel layers
- No holes in the pixel detector
- Maximum 1 hole in the SCT

The procedure to reconstruct a primary vertex is based on two steps: vertex finding and vertex fitting [129, 130]. At first by using the information from the primary tracks, a seed for the vertex position is defined. An adaptive χ^2 fit is applied to the primary tracks associated with such vertex. All tracks are re-weighted at each fit iteration depending on their level of compatibility with the vertex. At the end of this procedure the vertex position is computed again. After the first vertex is defined, the remaining tracks are used to determine another vertex. The procedure ends when all the tracks are associated with a vertex. Each vertex has to have at least two tracks associated with, to be defined as such. The primary vertex will be the one with the highest $\sum_i^{N_{trk}} p_{T,i}^2$, where N_{trk} is the number of tracks. The other vertices will be defined as pile-up ones. The vertex reconstruction efficiency is evaluated as the ratio of the number of events with a primary vertex and the number of events with at least two primary tracks. Figure 3.2a shows the vertex efficiency for a low-μ data set as a function of the number of tracks [131]. Figure 3.2b shows the vertex reconstruction efficiency as a function of interactions per bunch crossing μ using simulated $t\bar{t}$, $Z \to \mu\mu$ and $Z \to ee$ samples [132].

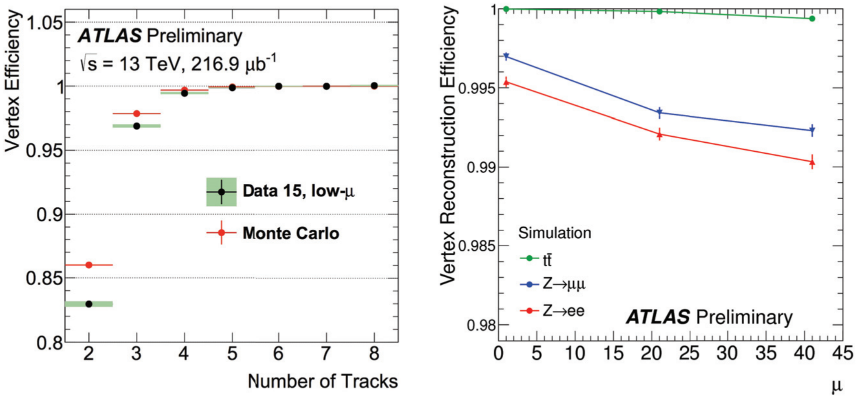

(a)

(b)

Fig. 3.2 · Vertex reconstruction efficiency for a low-μ dataset (a) as a function of the number of tracks and vertex reconstruction efficiency for simulated $t\bar{t}$, $Z \to \mu\mu$ and $Z \to ee$ samples (b) as a function of μ. Figure (a) is taken from [131] and (b) from [132]. The better performance of $t\bar{t}$ events is due to the presence of multiple tracks to fit compared to a $Z \to ll$ signature. For the $Z \to ll$ case, the muons perform better then the electrons due to the reconstruction method of the muons based on the ID information but also the muon chambers which allows better vertex reconstruction.

3.2 Objects

3.2.1 Electrons

Electrons in the ATLAS detector are reconstructed by using information from the ECal and the ID. The ECal is scoured for an energy deposit in a window of 3×5 cells of size $\Delta\eta \times \Delta\phi = 0.025 \times 0.025$, which corresponds to the granularity of the middle layer of the ECal. Once a *seed* with transverse energy higher then 2.5 GeV is found, a sliding window algorithm [133] is applied to create a cluster around it and to remove duplicates. The ID is then investigated to find a track candidate that matches the energy deposit in the ECal. The track reconstruction is done in two steps: at first the track is fitted via the ATLAS Global

χ^2 Track Fitter [134] and afterwards is re-fitted using the Gaussian Sum Filter [135], which takes into account non linear Bremsstrahlung effects. If more than one track is identified, the one that matches the energy deposit in the ECal best is chosen as the primary track and the object is identified as an electron. Many electrons that pass this procedure can be the product of semi-leptonic decays of heavy flavor hadrons or they can come from photon conversions. In order to identify an electron coming from the hard scatter interaction, stricter conditions are required. This is achieved in Run-II thanks to a multi variate technique that uses a Likelihood discriminant (LH), which has as input a combination of variables linked to the object track and energy deposit. The LH identification has three working points: *Loose, Medium, Tight*, which are in ascending order of purity and descending order of efficiency. In order to evaluate the efficiency, a *tag-and-probe* method is used on a $Z \to ee$ and $J/\psi \to ee$ sample, where the tag electron has to fulfill a tighter selection and the probe electron is used to evaluate the efficiency. This method is used for both the reconstruction and the identification efficiency and it is performed on real data and on MC simulation as well. Usually the results from data and MC differ due to an imperfect simulation of the detector response or due to an imperfect simulation of the process itself. A scale factor [1] (SF) is therefore introduced. Figure 3.3, shows the combined efficiency for both reconstruction and identification for the three different LH working points, as a function of E_T^{miss} (left) and η (right) , performed on a 3.2 fb^{-1} 2015 dataset [136].

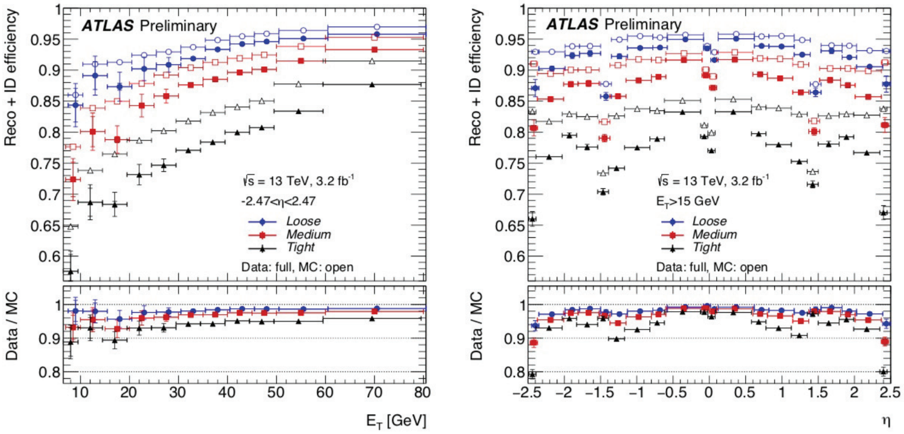

Fig. 3.3 · Electron reconstruction and identification efficiency for data and MC as a function of E_T^{miss} (left) and η (right) for the three LH working points using a $Z \to ee$ sample. The figure has been taken from [136].

Isolation

Another important part of the definition of an object is the Isolation. The Isolation is a variable that quantifies the amount of activity in the area surrounding a reconstructed object.

---

[1] A SF is the ratio of the efficiency of Data over MC as a function of E_T^{miss} and η.

It is used as a discriminant to avoid reconstructing fake leptons coming from jets, especially from semi-leptonic decays of B hadrons. The key variable that describes the level of Isolation of an object is the ΔR defined as $\Delta R = \sqrt{(\Delta\eta)^2 + (\Delta\phi)^2}$. The isolation variable is a measure for the amount of activity present around the object in a cone of radius R.

3.2.2 Muons

Muons in the ATLAS detector are reconstructed using information from three detectors: ID, MS and the ECal. Depending on the reconstruction method used, muons are divided into four categories [137]:

- **Stand Alone (SA)**: These muons are reconstructed only by using the information coming from the MS. The track parameters are extrapolated from the MS chambers towards the ID. Energy loss and multiple coulomb scattering effects are taken into account to correct the track. This reconstruction method is used to identify those muons that are outside of the ID angular coverage, $2.5 < |\eta| < 2.7$.

- **Combined (CB)**: These muons are reconstructed by using the track information in the MS, which is matched via a combined fit with the track information from the ID following an outside-in pattern recognition. These muons are the ones mostly used in physics analysis and the ones with the highest purity.

- **Segment-tagged (ST)**: These muons are reconstructed first in the ID and then they are matched with a part of a track (segment) in the MS chambers. In order to be tagged as muons, the track has to hit just one layer of the MS. This specific method is used to take into account muon with low-p_T or to tag muons that end up in area of the MS with reduced acceptance.

- **Calorimeter Tagged Muons (CaloTag)**: These muons are reconstructed first in the ID and then the track is extrapolated towards the calorimeter, looking for energy deposit compatible with a minimum ionizing particle. Such a method does not provide muons with high purity but it is useful to obtain information on the region where the MS is not instrumented ($|\eta| < 0.1$).

In Run-I the reconstruction of muons was based on two methods, called *Staco* and *Muid*. These were matching track pair candidates from the ID and the MS and performed a χ^2 test function of the track parameters and their covariance matrices [138]. The difference among the two methods lies in how they reconstruct the track parameters. The *Staco* method uses a statistical combination of ID and MS track parameters to obtain the final one, while the *Muid* method uses a global Kalman Filter fit on the tracks [124]. The two methods were then combined into a new method, *Chain 3*, which is now used in an improved version in Run-II [137]. A major improvement is the introduction of a Hough transform [139] to find the segment, the evaluation of the energy loss in the calorimeter and higher background rejection. Different definitions of Muons are then provided to fit different analysis requests: *Loose, Medium, Tight, High*-p_T. The *Medium* working point is the standard used for Run-II analyses and it is also the working point used for the analysis described in this work. The *Tight* working point is the one with the most stringent selections and provides the highest purity but with a reduced efficiency, the *High*-p_T working point is tailored to analysis that use high energetic muons with $p_T > 100$ GeV. Figure 3.4 shows the reconstruction efficiency for a muon in terms of p_T (a) and η (b) for *Loose* and *Medium* muons [137]. The reconstruction is done via the *tag-and-probe*[1] method using $Z \to \mu\mu$ and $J/\psi \to \mu\mu$ samples. The reconstruction efficiency is above 98% for muons with $|\eta| < 2.5$, and it is higher than 99% for muons with $p_T > 10$ GeV.

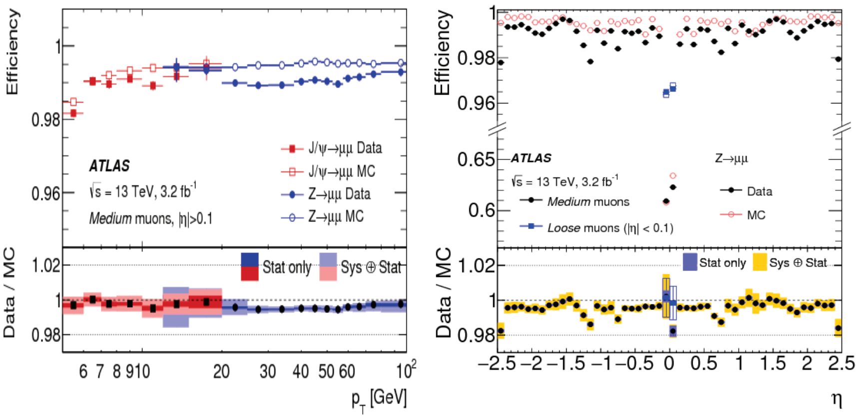

Fig. 3.4 · Muon reconstruction efficiency for data and MC as a function of p_T (a) and $|\eta|$ (b) for *Medium* and *Loose* muon selections using $Z \to \mu\mu$ and $J/\psi \to \mu\mu$ samples. The figure is taken from [137]

3.2.3 Jets

Due to QCD color confinement [140], colored particles like quarks and gluons arising from the fragmentation of the colliding proton pairs undergo a process of hadronization that leads to the formation of colorless hadrons. This process generates a spray of particles that can be grouped in a conic structure pointing to the original quark or gluon: such a structure is called a jet. Jets can be produced as well via the hadronization of initial state partons, which are not taking part into the hard scattering process: the so called underlying events. Jets can also arise from the radiative emission of gluons from quarks as initial state radiation (ISR) or final state radiation (FSR). Given the hadronic nature of the collider, jets are the most abundantly produced objects, therefore a proper reconstruction is crucial. A jet in the ATLAS detector appears as an energy deposit in both the ECal and HCal matching a spray of collimated charged particles in the ID. The method used to reconstruct jets is the so-called $\mathtt{anti}-k_T$ algorithm [141]. This algorithm, which belongs to the sequential recombination jet algorithms class, is an infrared collinear (IRC) safe and soft-resilient algorithm. Being IRC safe means that soft emissions of gluons and collinear splitting should not change the jet reconstruction outcome. Being soft-resilient means that the shape of the jet is not

---

[1] In presence of two muons produced by a resonant decay (Z or J/ψ) one has to be identified as a *Medium* muon (tag) using a reconstruction method (for example using the ID track information) and the other object (probe) has to be identified as a Muon using an independent reconstruction system (for example using the MS track information).

influenced by the presence of soft radiation in the jet proximity. The algorithm input consists of topologically connected clusters of energy in the calorimeter cells (topo-clusters) [142]. These clusters are merged together by looking at their relative distance d_{ij} and comparing it to the distance of a cluster with the beamline d_{iB}. The distances are defined as:

$$d_{ij} = min(k_{Ti}^{2p}, k_{Tj}^{2p})\frac{\Delta R_{ij}^2}{R^2}, \quad d_{iB} = k_{Ti}^{2p} \tag{3.1}$$

where R is the radius parameter, $\Delta R^2 = (y_i - y_j)^2 + (\phi_i - \phi_j)^2$, $k_{Ti,j}$, $\eta_{i,j}$ and $\phi_{i,j}$ are the transverse momentum, the rapidity and the azimuthal angle of the objects i and j. If the distance among two topo-clusters d_{ij} is lower then the distance between a topo-cluster and the beam d_{iB} ($d_{ij} < d_{iB}$) the two elements are merged and the process iterates on the next element. If $d_{ij} > d_{iB}$, then the object i is defined as a jet and it is removed from the list of objects to be reconstructed. The $anti - k_t$ algorithm has momentum power p equal to -1 and the radius parameter R [1] is chosen by the ATLAS Collaboration to be equal to 0.4. The choice of a negative power makes the algorithm soft-resilient because soft radiation energy deposits will merge first with the object coming from the hard scatter rather than merging before among themselves.

The jet energy calibration procedure is based on simulation and data driven methods. The topo-clusters are first calibrated at EM level [143]: this allows to precisely measure the energy deposits coming from electrons or photons. The next calibration is done at the hadronic energy scale: this allows to differentiate the electromagnetic topo-clusters from the hadronic ones. The jet energy scale (JES) is then applied to correct the difference between *truth* jet energy and the reconstructed one. The JES is evaluated by test beam measurements, simulation and in-situ [144] techniques like γ + jet balance (described in section 6.3.3.1) or QCD multi-jets balance. Among the many possible effects that can deteriorate the reconstruction of a jet (calorimetric noise, beam-gas interaction, cosmic rays) one of the most challenging is the pile-up effect. In order to remove jets coming from pile-up interactions a variable called jet-vertex-fraction (JVF) is introduced [145]. Such variable is defined as the fraction of transverse track-momentum associated to a jet coming from a primary vertex normalized to the whole transverse track-momentum associated with such jet. Values close to 1 suggest that the jet is more likely to come from the hard scatter process, while values close to 0 suggest the presence of a pile-up jet.

B-jet tagging

Jets originating from the hadronization of a b quark are called b-jets. To tag a b-jet, information from the ID is used that exploit the relatively long lifetime of B hadrons[2]. The algorithm used in ATLAS to discriminate a b-jet from jets produced by light quarks or from a c quark is called MV2c10 [146, 147]. This algorithm uses a multivariate approach based on a boosted decision tree. The information used as input are the jet kinematic properties, the presence of a displaced secondary vertex and its properties and the impact parameter information. The algorithm provides as output a weight that describes how likely it is for

---

[1] The radius parameter R defines the minimum distance among two separated jets and the size of the jet cone.

[2] A B hadron, having a lifetime of 1.6 ps and a mass of 5 GeV, with an energy in the order of dozens of GeV, will have a flight path of approximately 3 mm

a jet to come from a light, charm or bottom quark. By applying a cut on this weight it is possible to heavily reject jets coming from light and charm quarks. Figure 3.5a shows the light and c jets rejection as a function of the b-jet efficiency [147]. A specific background rejection is linked to a specific b-jet tagging efficiency and different working points are defined[1]. Figure 3.5b shows the b-jet tagging efficiency as a function of the jet p_T for the b-jet tagging efficiency working point $\epsilon_b = 70\%$ for both data and MC [147].

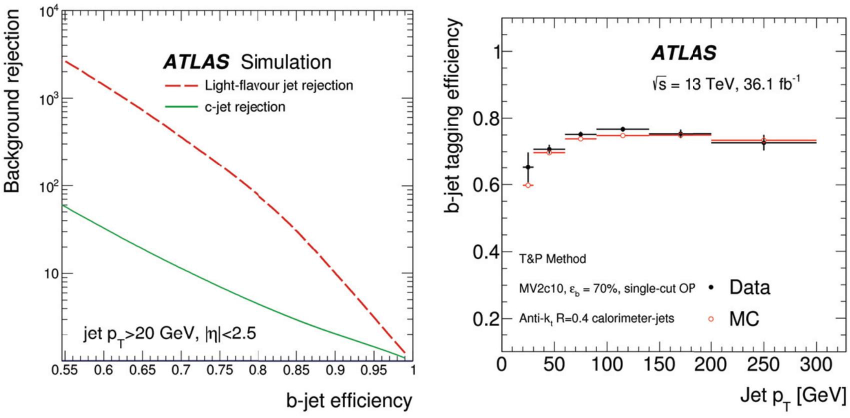

(a) (b)

Fig. 3.5 · Background rejection of light and charm jets as a function of b-jet tagging efficiency (a) and b-jet tagging efficiency as a function of jet p_T for data and MC for the working point $\epsilon_b = 70\%$ (b) . The figures are taken from [147]

3.2.4 Missing transverse energy

Neutrinos and other hypothetical particles such as Dark Matter candidates that are produced by the proton-proton collisions at the LHC do not interact with the ATLAS detector. Given that the initial transverse momentum in a proton-proton collision at LHC is equal to zero, the presence of a particle escaping the detector unobserved will produce an energy imbalance in the final state in the transverse plane. This imbalance, known as missing transverse energy $\vec{E}_T^{miss}$, is defined as the vectorial sum of the opposite of the transverse momentum of all reconstructed objects in the detector. In formulas:

$$\vec{E}_T^{miss} = \vec{E}_T^{miss,\mu} + \vec{E}_T^{miss,e} + \vec{E}_T^{miss,\gamma} + \vec{E}_T^{miss,\tau} + \vec{E}_T^{miss,jets} + \vec{E}_T^{miss,soft} \quad (3.2)$$

where $\vec{E}_T^{miss,i} = -\vec{p}_T^{\,i}$, and $soft$ stands for *soft terms* which are soft tracks and calorimeter clusters not associated with any reconstructed object. The $\vec{E}_T^{miss}$ is therefore a vector in the transverse plane x-y of magnitude:

$$E_T^{miss} = \sqrt{(E_x^{miss})^2 + (E_y^{miss})^2} \quad (3.3)$$

---

[1] As usual, higher efficiency leads to lower background rejection and vice versa

Each object used in the $\vec{E}_T^{miss}$ reconstruction has to undergo a specific selection and every contribution has to be added following a specific order to reduce double counting. In the analysis at study in this thesis the E_T^{miss} is using muons with $p_T > 10$ GeV, *medium* electrons calibrated at the EM scale with *Loose* isolation criteria with $p_T > 10$ GeV, topo-clusters jet calibrated using the EM+JES scheme [144] with $p_T > 20$ GeV. The soft term is composed of all those objects that failed the reconstruction selection of all the other objects and its main contribution is from the underlying events and pile up interactions. This is why the evaluation of the soft term is crucial in the reconstruction of the E_T^{miss} especially in an environment with high pile-up. Several techniques to reconstruct the E_T^{miss} are used taking information from the calorimeter or the ID or a combination of both [148]. The one used for the analysis in study is called track-soft term (TST). The TST E_T^{miss} uses only track information that is not associated to reconstructed hard objects. The tracks, with $p_T > 0.4$ GeV and $|\eta| < 2.5$, have to be associated with the primary vertex. The usage of such a method reduces drastically the contribution of in-time pile up for the E_T^{miss}. The TST also does not include contribution from neutral particles reconstructed from the calorimeter energy deposits. Neglecting such information reduces the out-of-time pile-up contribution of the TST E_T^{miss} compared to other methods which are affected by this problem. The resolution of a specific E_T^{miss} reconstruction method is evaluated with the root mean square (RMS) and depends on the total event activity $\sum E_T$, which is the scalar sum of the transverse energy of all reconstructed objects. The resolution is also influenced by the number of primary vertices, which is linked to the magnitude of the pile-up. Figure 3.6 shows the resolution for the TST E_T^{miss} compared with the calorimeter soft term (CST) E_T^{miss} [1] and the p_T^{miss} [2] as a function of the event activity $\sum E_T$ (a) and as a function of the number of primary vertices N_{PV} (b) for a $Z \rightarrow \mu\mu$ data sample [148]. The figure shows clearly how the TST E_T^{miss} provides better performances in high pile-up environment.

---

[1] THE CST E_T^{miss} is based on the reconstruction of the soft term by using calorimeter energy deposits.

[2] The p_T^{miss} is defined as total pile-up independent missing energy reconstruction, by ignoring all jets in its reconstruction.

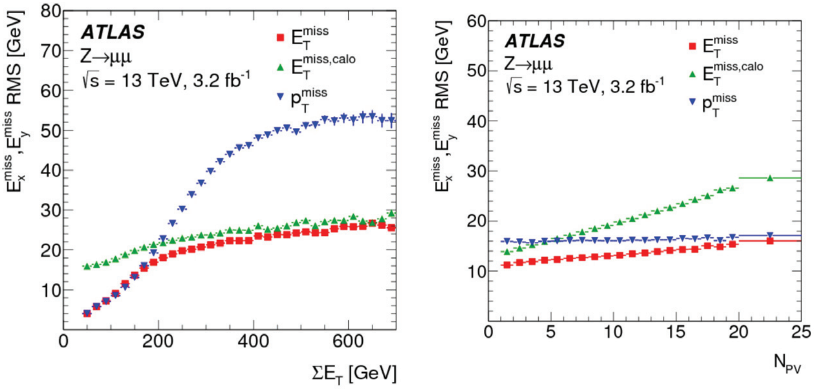

(a)

(b)

Fig. 3.6 · Resolution comparison of TST, CST and p_T^{miss} for the x and y component as a function of the event activity $\sum E_T$ (a) and as a function of the number of primary vertices N_{PV} (b) for a $Z \to \mu\mu$ data sample. The figures are taken from [148].

chapter four

ZH cut based analysis

4.1 Introduction

This chapter will illustrate the search for invisible Higgs decay in associated production with a Z boson with a final signature of two leptons and E_T^{miss}. In the SM the branching ratio (BR) of the Higgs boson to long-lived invisible particles[1] (i.e. neutrinos) is extremely small, $BR(H \to ZZ \to \nu\nu\nu\nu) \approx 0.001$. Measuring a non zero decay to invisible particles would indicate the presence of new phenomena in a BSM Higgs scenario, like the Higgs portal model described in the section 1.3. To detect *invisible particles* (characterized by E_T^{miss}) it is necessary to have a probe element: jets, leptons or photons. The work of this thesis will describe the search for invisible Higgs decays in associate production with a Z vector boson decaying to a pair of leptons (electrons or muons). Figure 4.1 shows the production of a ZH final state in an hadronic collider. The major contribution is given by quark-antiquark annihilation (86%) and from gluon-gluon fusion (14%).

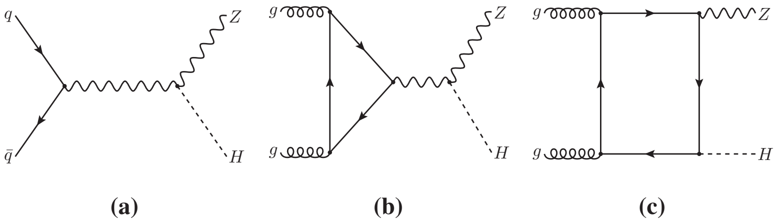

Fig. 4.1 · Feynman diagram of ZH production at LHC via quark-antiquark annihilation (a) and gluon-gluon fusion (b),(c)

4.2 Data and Monte Carlo samples

The data samples used in this analysis are recorded by the ATLAS detector during 2015 and 2016 with proton-proton collisions with 25 ns bunch spacing at $\sqrt{s} = 13$ TeV. The Monte Carlo samples are simulated using the full GEANT 4 [149] simulation of the ATLAS detector. The samples undergo a chain of reduction, until reaching an analysis-ready final

---

[1] Weakly interactive particles like neutrinos or dark matter candidates escape the ATLAS detector without any interactions being *invisible* to it.

format[1].Such format is called DxAOD (Derived xAnalysis Object Data). Each physics group has a specific subset of DxAOD with a predefined selection of physical objects. Table 4.1 shows the preselection applied to the HIGG2D1 DxAOD [150], which is the one used in this analysis [2].

Selection
Quality cut for muons
Quality cut for electrons
E_T^{miss} cut for electrons > 15 GeV for leading, > 5 GeV for sub-leading
p_T cut for muons > 15 GeV for leading, > 5 GeV for sub-leading
$N(e) + N(\mu) \geqslant 2$
$M_{ll} > 5$ GeV
L1 trigger requirement for electron or muon

Table 4.1 · Selection applied to produce the HIGG2D1 DxAOD samples. Both muons and electrons are required to pass quality cuts which are defined by requiring the muon (electron) to pass the *Loose* (*LH VeryLoose*) reconstruction criteria and other cuts that can be find in reference [150].

4.2.1 Data sample

The data used in this work are collected by the ATLAS detector in 2015 and in 2016 for a total recorded integrated luminosity of 36.1 fb^{-1}. Data samples have to satisfy certain quality requirements: the samples that fulfill such cuts are stored in the Good Run List (GRL) which contains the list of data available for analysis purposes.

4.2.2 Signal samples

The MC signal samples for the channel $ZH \to ll+$ invisible are generated by Powheg [151] and the parton showering is performed using Pythia8 [152]. Both quark-antiquark annihilation ($qq \to ZH$) and gluon-gluon fusion ($gg \to ZH$) processes are simulated. The Higgs is forced to decay into 4 neutrinos to simulate the invisible final signature: $H \to ZZ \to 4\nu$. All the results described in the thesis assume $BR(H \to inv.) = 100\%$. The parton distribution function (PDF) set used to generate the samples is CT10nlo and the AZNLO tune is used. The ZH production cross sections, obtained by the LHC XS Working Group [153], are calculated at next-to-next-to-leading order (NNLO) quantum chromodynamics (QCD) accuracy and next-to-leading order (NLO) electro weak (EW) accuracy. Table 4.2 shows the cross sections for the SM Higgs with $m_H = 125$ GeV.

---

[1] This is done to reduce the size of the samples, to introduce new variables with specific selection and to provide objects with combined performance recommendations

[2] The derivation cache used to produce the samples utilized in this analysis is the AtlasDerivation-20.7.8.2 together with the DerivationFramworkHiggs-00-44-33 for the HZZ group.

Process	σ(fb)
$qq \rightarrow ZH \rightarrow ll + inv.$	76.89
$gg \rightarrow ZH \rightarrow ll + inv.$	12.42

Table 4.2 · Cross section for $ZH \rightarrow ll+$ invisible final state with $m_H = 125$ GeV. All leptonic decays ($l = e$, μ, τ) are taken into account.

4.2.3 Background samples

Several SM processes can produce a $\ell^+\ell^-$+ E_T^{miss} experimental signature. The backgrounds that can produce such a signature can be divided into two categories: irreducible and reducible. The irreducible ones are those that have the exact same final state: 2 real leptons and real E_T^{miss} . The reducible ones mimic the signal final signature: 1 real lepton, one fake lepton plus E_T^{miss} (real or fake). The presence of reducible background is due to mis-reconstruction effects, noise in the detector, pile-up and detector limitations (resolution, mis-calibration, not complete angular coverage).

ZZ production

The main background in this analysis is irreducible and comes from pair production of Z bosons decaying in 2 neutrinos and two charged leptons: $ZZ \rightarrow \ell^+\ell^-\nu\bar{\nu}$. All ZZ final states ($ZZ \rightarrow \ell^+\ell^-\ell'^+\ell'^-$, $ZZ \rightarrow \nu\bar{\nu}\nu\bar{\nu}$ and $ZZ \rightarrow \ell^+\ell^-\nu\bar{\nu}$ where $l = e, \mu, \tau$) are simulated with the POWHEG event generator with AZNLO CTEQ6L1 tune, interfaced with Pythia8. The ZZ samples used in the analysis are shown in Table A.1 in the Appendix.

WZ and WW production

Another source of background comes from the diboson production of a pair of W's or a W with a Z. For the WW pair production, if both bosons decay leptonically with the same flavour: $WW \rightarrow \ell\nu\ell\nu$ the final state has 2 real leptons and real E_T^{miss} from the neutrinos. For the WZ case, if the W decays leptonically ($WZ \rightarrow \ell\nu\ell^+\ell^-$) but one lepton is not reconstructed (therefore accounted as E_T^{miss}) the background will look like the signal. The same holds if the Z decays in neutrinos: $WZ \rightarrow \ell\nu\nu\nu$ and one additional lepton is reconstructed by mistake from additional objects (jets for example) in the detector. The samples are simulated with POWHEG interfaced with Pythia8. The details of the samples used in the analysis are shown in Table A.2 in the Appendix.

Tri-boson production

The request of only two leptons reduces the impact of the triboson backgrounds, referred to as VVV where $V = W$, Z. The details of the samples used are shown in the Appendix in Table A.3.

Z+jets production

The background coming from a Z boson is reduced by the request of E_T^{miss} in the final state. The contribution is small but critical especially in the modeling of the E_T^{miss} because the Z+jets background is present in many control regions defined for different backgrounds.

Sherpa 2.2.1 [154] is used to simulate Z+jets processes, the samples are sliced in the variable $max(H_T(V), p_T(V))$ [1] at the parton level. The slices are also filtered to eliminate jets coming from b and c hadrons. Details of the samples used are shown in Table A.4, A.5 and A.6 in the Appendix.

W+jets production

The W+jets background, a minor background to this analysis, contributes to the final signal region if a jet is mis-identified as a lepton. The $W \rightarrow e\nu_e$, $W \rightarrow \mu\nu_\mu$ and $W \rightarrow \tau\nu_\tau$ processes have been simulated by POWHEG with AZNLO CTEQ6L1 tune, interfaced with Pythia8. The details are given in Table A.7 in the Appendix.

top pair and single top production

Top-pair production as well as single top and Wt production are an important contribution due to the presence of real leptons and real E_T^{miss}. Those background samples are simulated with POWHEG interfaced with Pythia6, with Perugia2012 tune. The $t\bar{t}$ sample is filtered requiring at least one lepton originating from a W boson with $p_T > 1$ GeV. The single top production is considered in both s and t channel. For Wt single top associated production, di-lepton filtered samples have been used. Details of the samples are shown in Table A.8 in the Appendix.

ttV and ttVV production

Top pair production associated with one or two bosons (W or Z) is not a crucial background to this analysis. The samples are simulated with MADGRAPH [155] interfaced with Pythia8. The details for those background are shown in Table A.9 in the Appendix.

4.3 Object definition

The following section will describe the definition of the objects used in the analysis.

4.3.1 Electrons

Electrons reconstruction is described in details in section 3.2.1. Electrons are identified by using the recommendations provided by the Egamma Combined Performance group (ECP) [156]. The method uses a *likelihood* criterion which takes into account different characteristics of the electron: the shower shapes, track quality and track-cluster matching. The working point selected for electrons in the analysis is the *Medium* one. The Isolation for electrons is defined by using a p_T dependent ΔR parameter. The isolation working point chosen for this analysis is the *Loose* one, which provides an isolation efficiency $\geqslant 99\%$. Calibrations and smearing corrections are applied as well [157]. Cuts on the impact parameter related to the reconstructed primary vertex are defined to reject non-prompt electrons: $|d_0/\sigma(d_0)| < 5$ and $|z_0 \cdot sin(\theta)| < 0.5$ mm. The electrons selection is summarized in Table 4.3.

---

[1] H_T is the scalar p_T sum of all jets with $p_T > 20$ GeV

Type of selection	Cut
Identification	Likelihood Medium ID
Kinematic cuts	$p_T > 20$ GeV $\lvert\eta\rvert < 2.47$
Cosmic cuts	$\lvert d_0/\sigma(d_0)\rvert < 5$ $\lvert z_0 \cdot sin(\theta)\rvert < 0.5\ mm$
Isolation	Loose

Table 4.3 · Summary of electron selection

4.3.2 Muons

Muons reconstruction is described in details in section 3.2.2. The Muons used for this analysis are the Combined Muons and the identification recommendations and selection used are the ones provided by the Muon Combined Performance Group [158] (MCP). For this analysis the *Medium* identification criteria are chosen. The isolation working point used for this analysis is the *Loose*, which corresponds to an isolation efficiency $\geqslant 99\%$ for $p_T > 20$ GeV muons. Smearing [159] is also applied to the Muons to correct for not well simulated detector resolution effects. The muons recorded by the ATLAS detector are not only coming from proton-proton collisions, also cosmic muons and non-prompt muons are recorded. To reject such muons a cut on the impact parameters is applied: $\lvert d_0/\sigma(d_0)\rvert < 3$ (d_0 significance) and $\lvert z_0 \cdot sin(\theta)\rvert < 0.5\ mm$. Table 4.4 summarizes the set of selections to tag an object as a muon.

4.3.3 Jets

Jets reconstruction is described in details in section 3.2.3. Jets are complex objects which require elaborate reconstruction algorithms, such as the anti-k_T [141] jet finder. The jets used in this analysis are reconstructed with the anti-k_T algorithm using topo-clusters information. The jets are then calibrated at the EM and hadronic scale [160]. The kinematic selection applied to the jets used in the analysis is the following: $p_T > 20$ GeV and $\lvert\eta\rvert < 4.5$. The JVF is used together with other variables to produce a multivariate discriminant, the jet-vertex-tagger (JVT) to reject pile-up jets. The cuts applied are: JVT > 0.59 for jets with $p_T < 60$ GeV, $\lvert\eta\rvert < 2.4$. This provides an efficiency of 92% and fake rate of 2%. The jets also need to pass the cleaning criteria where the *Loose* selection is the chosen one. This cut provides an efficiency above 99.5% for the selection of jets with $p_T > 20$ GeV. A veto on b-tagged jets with $p_T > 20$ GeV and $\lvert\eta\rvert < 2.5$ is applied in the analysis to

Type of selection	Cut
Identification	Combined with Medium quality
Kinematic cuts	$p_T > 20$ GeV $\lvert\eta\rvert < 2.5$
Cosmic cuts	$\lvert d_0/\sigma(d_0)\rvert < 3$ $\lvert z_0 \cdot \sin(\theta)\rvert < 0.5$ mm
Isolation	Loose

Table 4.4 · Summary of muon selection.

reject the contribution from $t\bar{t}$ events. The algorithm used for the b-tagging, the MV2c10 algorithm [161], is based on a boosted decision tree approach. The cut on the MV2c10 algorithm output is chosen to obtain approximately 85% b-tagging efficiency for b-jets in $t\bar{t}$ events. Table 4.5 summarizes the jets selection.

4.3.4 Overlap Removal

In a detector multiple objects can be reconstructed and overlap, this can be due to mis-reconstruction due to the presence of electrons and muons in the jets for example. To resolve this issue, an overlap removal (OR) is performed. Table 4.6 summarizes the order and the criteria of the OR used in the analysis.

4.3.5 Missing transverse energy

The E_T^{miss} accounts for the energy imbalance due to objects not interacting with the detector (neutrinos or particles associated with BSM scenarios[1]) or due to mis-reconstructed objects. The E_T^{miss}, described in details in section 3.2.4, is defined as:

$$E_T^{miss} = -\sum_i \vec{p}_T^{\,i} \tag{4.1}$$

Where $\vec{p}_T^{\,i}$ is the transverse momentum of each reconstructed object (electrons, muons, jets, *soft terms*[2]). Different types of E_T^{miss} are defined depending on the information used in the reconstruction algorithm.
The E_T^{miss} used in this analysis is the track-based soft term (TST E_T^{miss}) [162]. The *track-*

---

[1] Dark matter candidate, SUSY candidate, gravitons, et. cet.

[2] soft tracks and calorimeter clusters not associated with any other object

Type of selection	Cut
Identification	AntiKt4EMTopo jets
Kinematic cuts	$p_T > 20$ GeV $\|\eta\| < 4.5$
Pileup removal	JVT > 0.59 for $p_T < 60$ GeV, $\|\eta\| < 2.4$ jets
Cleaning	Loose jets accepted
b-tagging	$MV2c10 > 0.1758$ (85% efficiency)

Table 4.5 · Summary of jet selection.

	Reference objects	Criteria
Remove jets	electrons	$\Delta R_{e-jet} < 0.2$
	muons	$\Delta R_{\mu-jet} < 0.2$ if $N_{Trk}(jet) < 3$ OR ($p_T^{jet}/p_T^{\mu} < 2$ and $p_T^{\mu}/\Sigma_{TrkPt} > 0.7$)
Remove electrons	jets	$0.2 < \Delta R_{e-jet} < 0.4$ **AND** pile-up jets check
	muons	share the same ID track
remove muons	jets	$\Delta R_{\mu-jet} < 0.4$ **AND** pile-up jets check

Table 4.6 · Overlap removal criteria adopted in the analyses.
Pile-up jets check means: JVT > 0.59 if jet p_T< 60 GeV and $|\eta| < 2.4$.

based term indicates that the momentum of the soft term is computed from the tracks of charged particles associated with the primary vertex. The input for the E_T^{miss} algorithm consists of all the calibrated pre-selected objects in the event.

4.4 Event selections

This section will describe the selection applied to the event in the analysis with signature $\ell^+\ell^-$+E_T^{miss}. The selection is divided in three steps: trigger, event pre-selection (quality and cleaning cuts) and the final event selection.

4.4.1 Trigger

The trigger used for this analysis is a combination of single lepton triggers: muon or electron. The choice of a combination of single lepton triggers provides a very high efficiency $\geqslant 99\%$ as studies performed on 2015 and 2016 data as well as MC show [163]. Di-lepton trigger setups are also studied but they do not provide any improvement in the selection efficiency, therefore the simplest configuration is chosen (single lepton trigger) to reduce the systematic error. The trigger threshold is selected to be $p_T > 30$ GeV for the leading lepton and $p_T > 20$ GeV for the sub-leading lepton. The cuts are selected to provide full trigger efficiency for the offline reconstructed lepton.

4.4.2 Event pre-selection

As already mentioned in section 4.2.1, the data selected are the one in the GRL, specifically the data have to pass the “All_Good” GRL criteria. Other quality cuts, applied to avoid detector problems, are enumerated here:

- Calorimeter quality flags are required to be good
- Incomplete events are vetoed

A hard-scattering vertex with at least two associated tracks is then required, this vertex being the one with the highest sum of p_T^2. A jet cleaning cut is also applied to remove jets originating from non-collision events, cosmic-ray showers or beam related backgrounds. This cleaning cut is particularly important to limit the presence of fake E_T^{miss}.

4.4.3 Event Selection

The goal of the event selection is to maximize the background rejection and minimize the loss of signal events. The first step is the identification of the Z boson via its leptonic decay, followed by the request of E_T^{miss} coming from the Higgs invisible decay and finally more complex cuts are implemented to exploit the kinematic topology of the ZH system final signature. Additional cuts are also applied to reduce specific background contributions. In order to tag a Z boson, events are required to contain exactly two same flavour leptons (muons or electrons) with opposite charge. All leptons have to pass the object selections described in section 4.3.1 and 4.3.2. To reduce the contribution from $ZZ \rightarrow \ell^+\ell^-\ell'^+\ell'^-$ and $WZ \rightarrow \ell\nu\ell^+\ell^-$ backgrounds a third lepton veto is applied. The third lepton selection is looser, with $p_T > 7$ GeV (instead of 20 GeV) and *Loose* rather than *Medium* identification selection. Finally the invariant mass of the dilepton system is required to be in a 15

GeV window around the Z mass value: 76 GeV $\leqslant M_{\ell\ell} \leqslant$ 106 GeV. This cut reduces the presence of backgrounds with dileptonic final state as $t\bar{t}$ or $WW \to \ell\nu\ell\nu$ or $Z \to \tau\tau$.

After the reconstruction of the Z boson, the presence of an invisible Higgs decay is requested by applying a cut on the transverse missing energy ($E_T^{miss} > 90$ GeV).

Aside from the irreducible ZZ background, the major backgrounds present at this level of the analysis are two: the Z+jets and the so called flavour symmetry background composed of WW, $t\bar{t}$, $Z \to \tau\tau$. In order to reduce such backgrounds additional cuts are applied. The high p_T of the Z boson produces a pair of boosted leptons with a small angular distance, therefore a cut on the $\Delta R_{\ell\ell}$ is applied ($\Delta R_{\ell\ell} < 1.8$). The back-to-back decay of the ZH system generates a wide azimuthal angular difference among the Z and the Higgs, the $|\Delta\phi(\vec{p}_T^{\ell\ell}, \vec{E}_T^{miss})|$ is then requested to be greater then 2.7. To exploit the energy conservation in the transverse plane a cut on the so-called fractional p_T difference is applied. The fractional p_T difference is defined as the difference of the transverse momentum of the $E_T^{miss} +$ jets[1], and the Z boson p_T, divided by the Z boson p_T ($|p_T^{miss,jet} - p_T^{\ell\ell}|/p_T^{\ell\ell} < 0.2$ where $p_T^{miss,jet} = |\vec{E}_T^{miss} + \sum_{jet} \vec{p}_T^{jet}|$). In other terms the fractional p_T difference describes how far from the energy conservation the reconstructed ZH system is in units of $p_T^{\ell\ell}$. To remove events with 'fake E_T^{miss} (mostly coming from Z+jets contributions) a cut is applied on the ratio of the missing transverse energy and the scalar sum of the p_T of the leptons and jets present in the event($E_T^{miss}/H_T > 0.6$, where $H_T = \sum_{jet} p_T^{jet} + p_T^{\ell_1} + p_T^{\ell_2}$).

The final cut is a b-jet veto in order to suppress the contribution from $t\bar{t}$. The selected value for each cut is evaluated with a significance scan[2] to obtain the optimal cut value for each variable. The whole selection is summarized in Table 4.7.

4.4.4 Kinematic distributions

The distributions of E_T^{miss}, $\Delta R_{\ell\ell}$, $\Delta\phi(\vec{p}_T^{\ell\ell}, \vec{E}_T^{miss})$, fractional p_T difference, number of b-tagged jets, and E_T^{miss}/H_T in ee and $\mu\mu$ channels after the Z mass window requirement are shown in Figures 4.2 and 4.3. The data and MC agree well within uncertainty for all the distributions, apart from the number of b-tagged jets. This is due to a known issue in the MC simulation that cannot describe properly the data behavior for high jet-multiplicity. Nevertheless, the discrepancy does not affect the analysis because a veto on b-tagged jets for number of b-jet equal to 0 is applied. The MC simulation is in good agreement with the Data as it is visible in the plot (e) in Figure 4.3. Each variable used in the event selection is shown in Figure 4.4 and Figure 4.5 with all the selections applied except for the one on the variable itself, the so called *N-1 plot*. All the plots show good agreement between MC and Data.

---

[1] The jets are the soft ones present in the event

[2] A significance scan consists of varying a specific value for a cut and check how this affects the significance. The best value, which is the chosen one, is the one that maximizes the significance.

Event Pre-Selection
All_Good Good Run List events
Vertex with $\geqslant 2$ tracks with $p_T > 1$ GeV
Single lepton trigger
Event Selection
Two same flavour opposite-sign leptons (e^+e^- OR $\mu^+\mu^-$)
Veto of any additional lepton with Loose ID and $p_T > 7$ GeV
$76 < M_{\ell\ell} < 106$ GeV
$E_T^{miss} > 90$ GeV
$\Delta R_{\ell\ell} < 1.8$
$\Delta\phi(Z, E_T^{miss}) > 2.7$
Fractional p_T difference < 0.2
$E_T^{miss}/H_T > 0.6$
b-jet Veto

Table 4.7 · List of cuts applied at the event selection level for the $\ell^+\ell^-$+E_T^{miss} analysis.

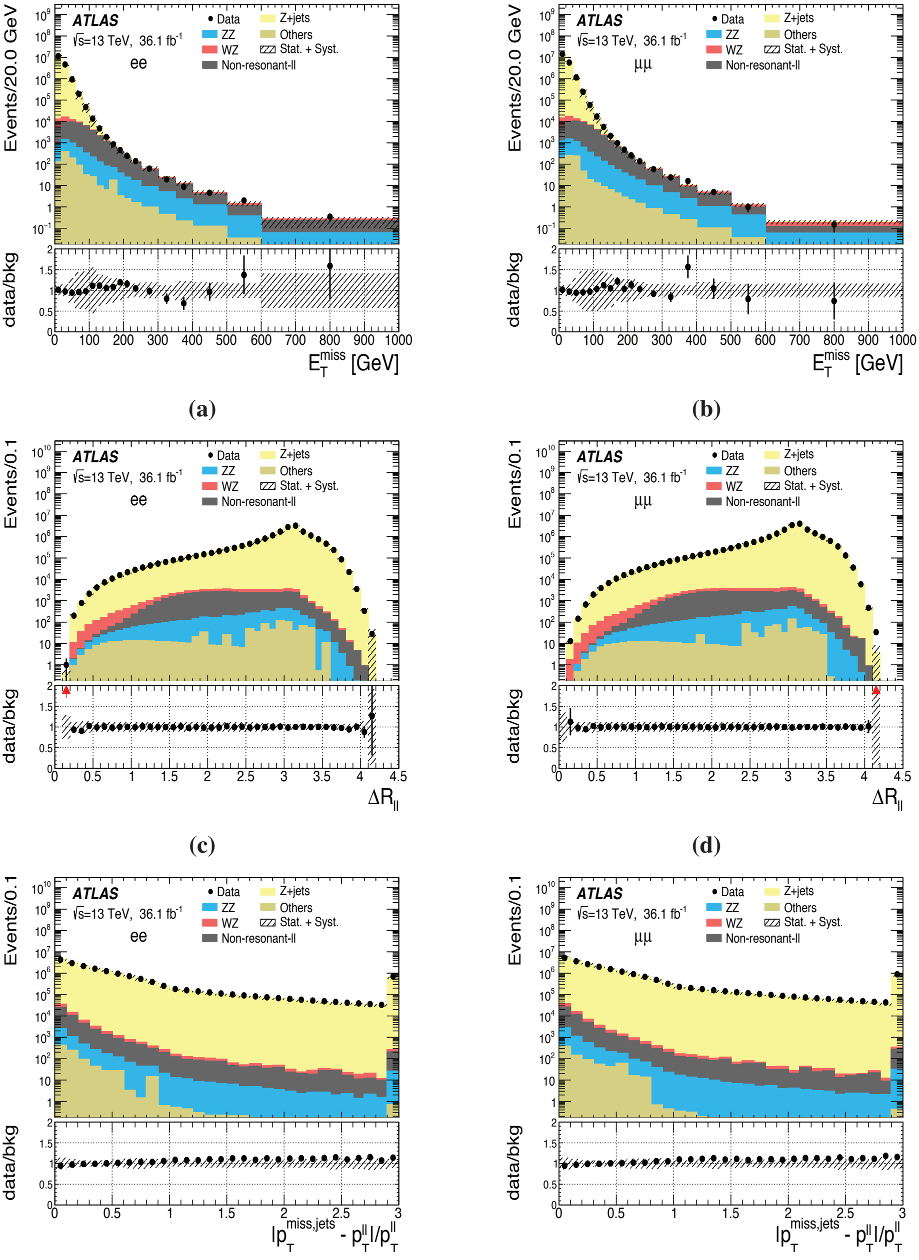

(a)

(b)

(c)

(d)

(e)

(f)

Fig. 4.2 · Kinematic distributions after the Z mass window requirement. The E_T^{miss} distribution for the (a) ee channel and (b) $\mu\mu$ channel. The $\Delta R_{\ell\ell}$ distribution for the (c) ee channel and (d) $\mu\mu$ channel. The fractional p_T difference distribution for the (e) ee channel and (f) $\mu\mu$ channel. The red arrows in the ratio plot indicate that the point is off the scale. The uncertainty band in the ratio includes systematic uncertainties, while the statistical uncertainty is propagated to the data/MC points. The non-resonant-ll background contains the background processes such as WW, $t\bar{t}$, Wt and $Z \to \tau\tau$. The minor contributions from VVV, $ttV(V)$ and W+jets are summed and labeled as "Others". The rightmost bin contains the overflow contributions. The plots have been published in the article [164].

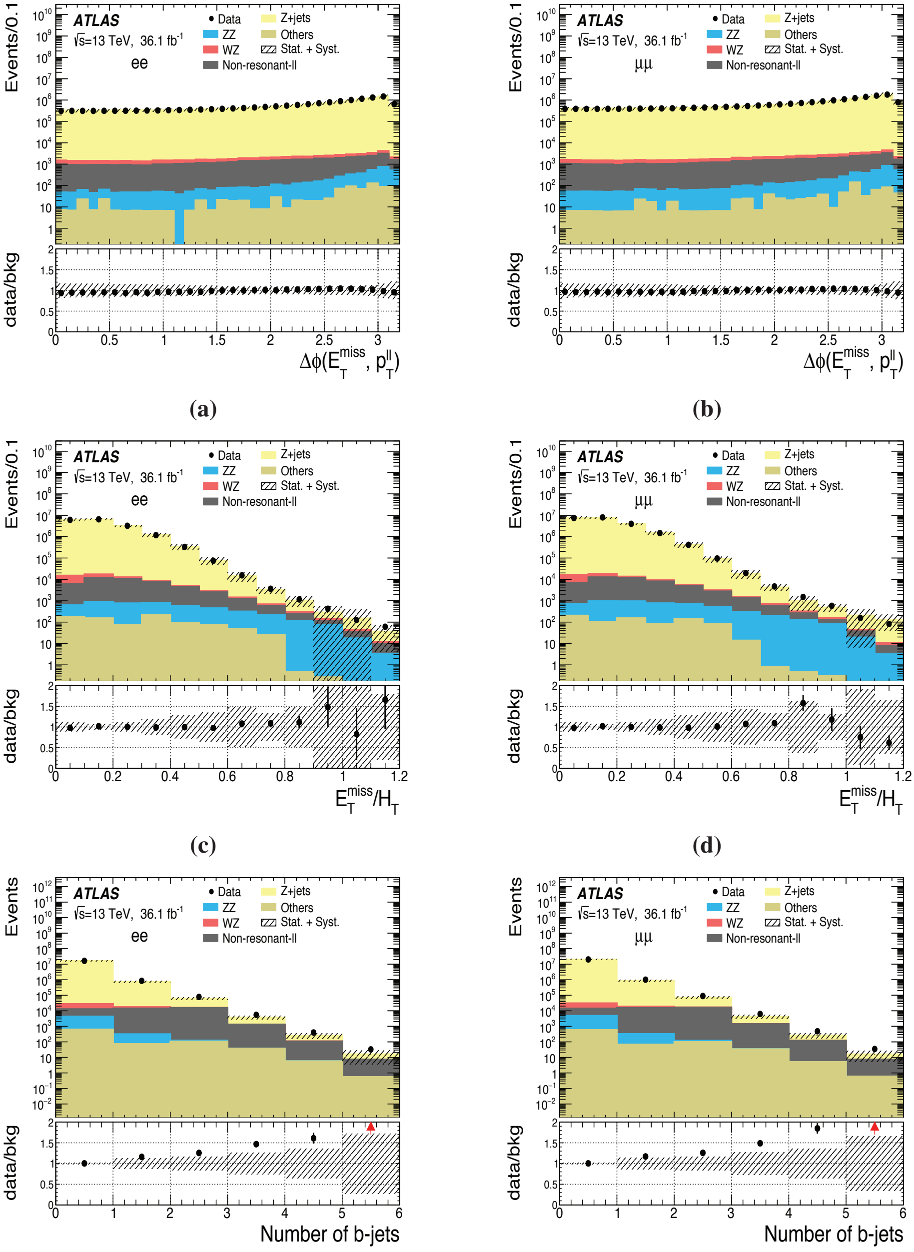

(a) (b)

(c) (d)

(e) (f)

Fig. 4.3 · Kinematic distributions after the Z mass window requirement. The $\Delta\phi(p_T^Z, E_T^{miss})$ distribution for the (a) ee channel and (b) $\mu\mu$ channel. The number of b-tagged jets distribution for the (c) ee channel and (d) $\mu\mu$ channel. The E_T^{miss}/H_T distribution for the (e) ee channel and (f) $\mu\mu$ channel. The red arrows in the ratio plot indicate that the point is off the scale. The uncertainty band in the ratio includes systematic uncertainties, while the statistical uncertainty is propagated to the data/MC points. The non-resonant-ll background contains the background processes such as WW, $t\bar{t}$, Wt and $Z \to \tau\tau$. The minor contributions from VVV, $ttV(V)$ and W+jets are summed and labeled as "Others”. The rightmost bin contains the overflow contributions. The plots have been published in the article [164].

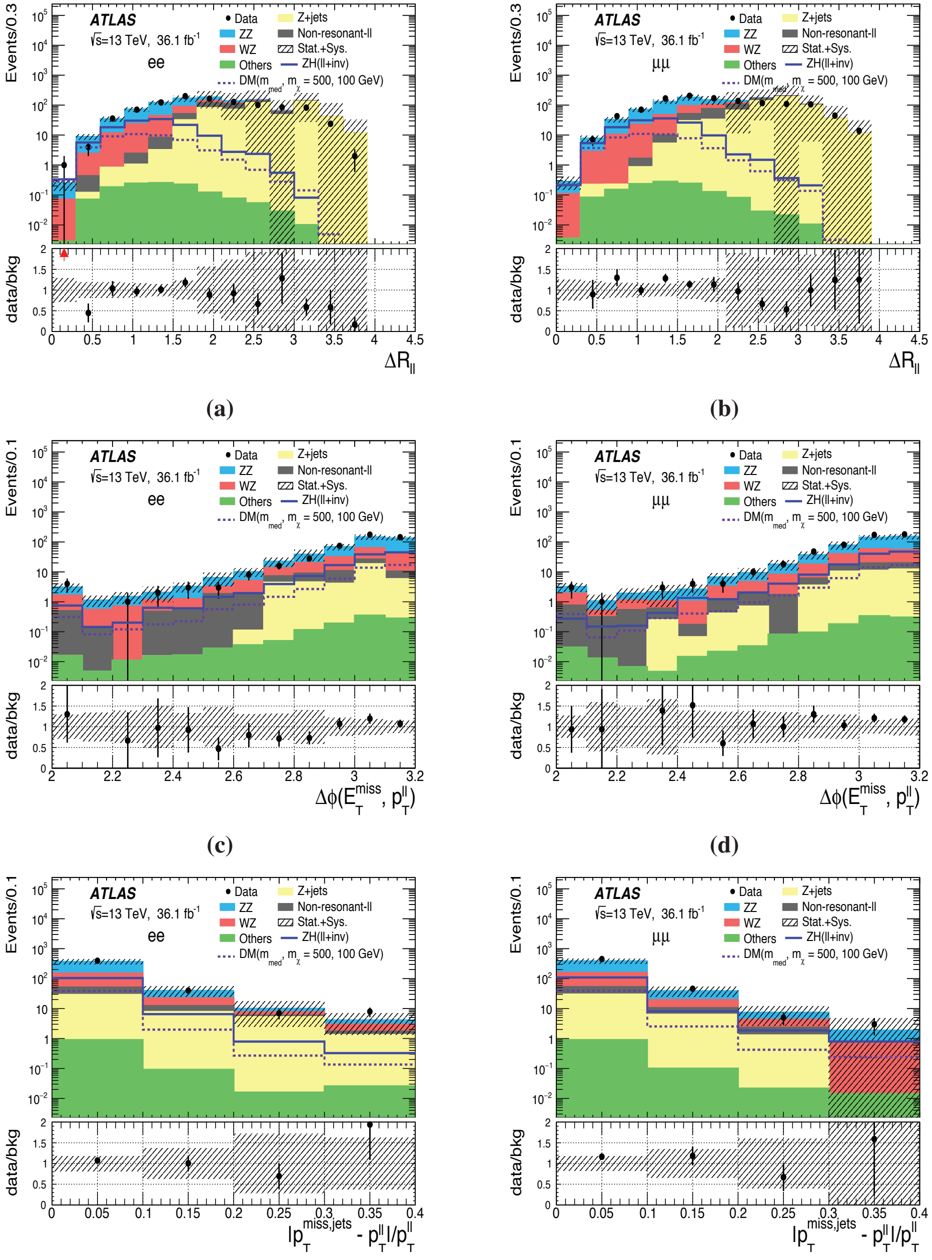

(a) (b)

(c) (d)

(e) (f)

Fig. 4.4 · *N-1* kinematic distributions. Each variable is shown with all the event selections applied except for the cut applied on the variable itself. The $\Delta R_{\ell\ell}$ distribution for the (a) ee channel and (b) $\mu\mu$ channel. The $\Delta\phi(p_T^Z, E_T^{miss})$ distribution for the (c) *ee* channel and (d) $\mu\mu$ channel. The fractional p_T difference distribution for the (e) *ee* channel and (f) $\mu\mu$ channel. The red arrows in the ratio plot indicate that the point is off the scale. The uncertainty band in the ratio includes both statistic and systematic uncertainties. The non-resonant-ll background contains the background processes such as *WW*, $t\bar{t}$, *Wt* and $Z \to \tau\tau$. The minor contributions from *VVV*, $ttV(V)$ and *W*+jets are summed and labeled as "Others". The rightmost bin contains the overflow contributions. The plots have been published in the article [164].

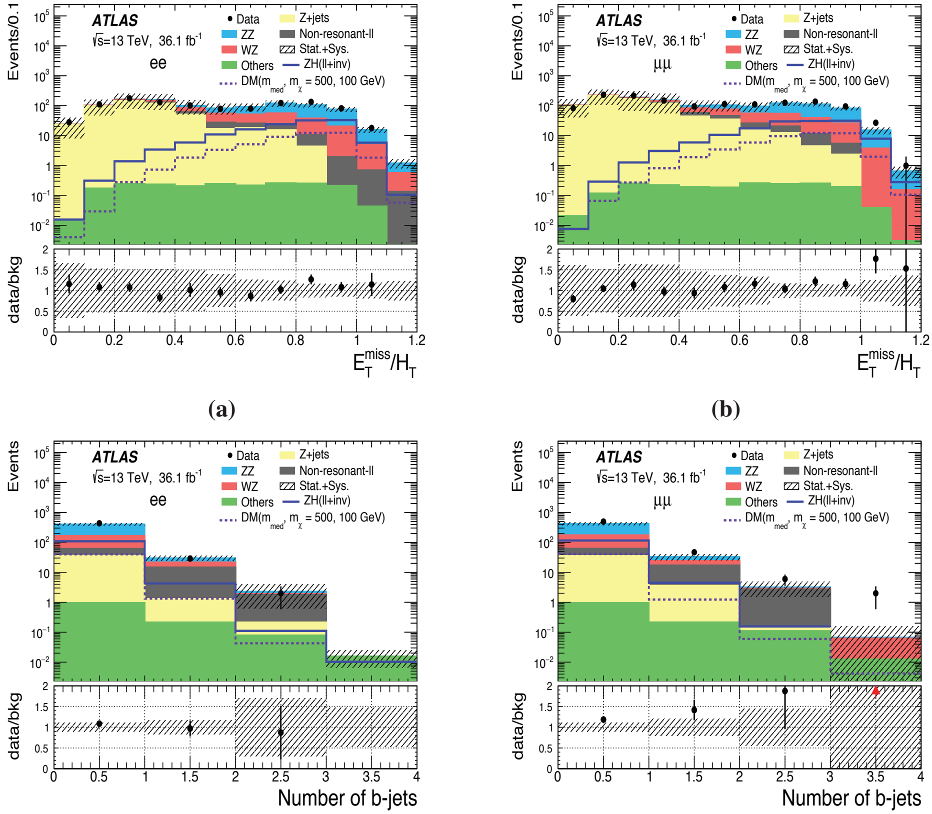

(a)

(b)

(c)

(d)

Fig. 4.5 · *N-1* kinematic distributions. Each variable is shown with all the event selections applied except for the cut applied on the variable itself. The $\mathrm{E}_{\mathrm{T}}^{\mathrm{miss}}/\mathrm{H}_{\mathrm{T}}$ distribution for the (a) ee channel and (b) $\mu\mu$ channel. The number of b-tagged jets distribution for the (c) ee channel and (d) $\mu\mu$ channel. The red arrows in the ratio plot indicate that the point is off the scale. The uncertainty band in the ratio includes both statistic and systematic uncertainties. The non-resonant-ll background contains the background processes such as WW, $\mathrm{t}\bar{\mathrm{t}}$, $W\mathrm{t}$ and $Z \rightarrow \tau\tau$. The minor contributions from VVV, $\mathrm{tt}V(V)$ and W+jets are summed and labeled as "Others”. The rightmost bin contains the overflow contributions. The plots have been published in the article [164].

4.5 Background estimations

4.5.1 Method overview

The background composition after the full event selection is shown in Table 4.8. For each background a different strategy is implemented to obtain a better estimation of the yield and the shape of the kinematic distributions. As shown in Table 4.8 the dominant background in the analysis is the ZZ, followed by the WZ, Z+jets , flavour symmetry and the relatively small contributions of W+jets and $t\bar{t}V/VVV$. The general strategy to obtain a better estimation is based on the definition of control regions (CRs). A CR is an area of the phase space where a specific background process is enriched by reversing (or introducing) a cut in the event selection. A properly defined CR should have no contamination from signal or other backgrounds events and at the same time provide a good kinematic description of the background in the SR. For each background a different CR and a different estimation method is used. An overview of the different background method estimations is briefly provided:

- ZZ background: ZZ is the dominant background (56%). The similarity among the signal kinematics and the background does not allow the definition of a control region (CR). The estimation for both yields and shape is therefore performed by using NLO QCD MC. Higher order corrections are applied from theory computations.

- WZ background: the shape is evaluated by NLO QCD MC while the normalization factor is obtained by using a 3-leptons CR (third lepton veto is removed). A scale factor is obtained for the WZ MC in the 2-leptons SR by taking the ratio of data over WZ MC in the 3-leptons CR.

- Z+jets background: the normalization is obtained by using a modified version of the ABCD method (more details in section 4.5.4.1). The shape is obtained by using MC samples.

- flavour symmetry background (WW, $t\bar{t}$, $Z \to \tau\tau$): both yield and shape is estimated from data by using the so called “flavour symmetry” method ($ee : \mu\mu : e\mu = 1 : 1 : 2$). To obtain the number of ee and $\mu\mu$ events in the SR, a CR is defined where the same flavour request is removed and the number of $e\mu$ pairs is estimated. The number of SR events is then evaluated by rescaling the $e\mu$ one with the flavour symmetry factor (0.5). Such number is then corrected by an efficiency factor related to the detector reconstruction differences between electrons and muons.

- W+jets background: both yield and shape is obtained from data by using the fake factor method. W+jets can mimic the signal signature due to the reconstruction of fake leptons coming from the jets. A CR rich in lepton-like jets is defined to evaluate the fake factor from data. Such factor is then used to estimate the events in the SR from the CR.

Background	**Estimation**	**Method**	**%**
ZZ	MC(yields+shape)	—	56%
WZ	Data (yield), MC (shape)	3 lepton CR	27%
$Z+\text{jets}$	Data (yield), MC (shape)	ABCD with booleans	8%
$WW,\ t\bar{t},\ Z\to\tau\tau$	Data (yield+shape)	$e\mu$ CR	7%
$W+\text{jets}$	Data (yield+shape)	Fake factor	< 1%
ttV/VVV	MC (yield+shape)	—	< 1%

Table 4.8 · List of backgrounds ordered by relative contribution in the SR. For each background the estimation method is shown.

4.5.2 ZZ background

The Standard Model process $ZZ \rightarrow \ell^+\ell^-\nu\bar{\nu}$ is the main background of this analysis because the final signature is the same as the signal one. The kinematic similarities do not allow the definition of a CR orthogonal to the SR: the estimation of this background is obtained from MC only. In this analysis the most advanced correction factors to both production modes, $q\bar{q} \rightarrow ZZ$ and $gg \rightarrow ZZ$, are applied. Recent theory studies [165, 166] indicate an enhancement of the inclusive cross section $pp \rightarrow ZZ$ due to NNLO QCD effects. The MC simulated events are generated only up to the NLO. To take high order effects into account a k-factor reweighting procedure is introduced. The k-factor is determined theoretically and defined as the ratio of the cross sections of a specific process evaluated at different correction orders, as shown in equation 4.2 for the $pp \rightarrow ZZ$ process.

$$k = \frac{\mathrm{NNLO}(pp \rightarrow ZZ)}{\mathrm{NLO}(pp \rightarrow ZZ)} \tag{4.2}$$

The k-factor provided by theoretical computation for the process $pp \rightarrow ZZ$ is calculated for differential cross sections binned in M_{ZZ} [167]. The evaluation is performed after the kinematic request on the leptons (p_T and η,) and the Z mass window requirement. The phase-space is more inclusive[1] compared to the final SR, this introduce acceptance uncertainties. For this reason the scale uncertainty is chosen at the NLO level (and not at the NNLO). The derived NNLO QCD k-factors binned in M_{ZZ} for the $q\bar{q} \rightarrow ZZ$ process are shown in Figure 4.6 and the E_T^{miss} distribution in the SR before and after applying the NNLO QCD k-factors is shown in Figure 4.7. The NNLO k-factor corrections provide an increment of about 10% to the $q\bar{q} \rightarrow ZZ$ yield.
A constant k-factor of 1.7 ± 1.0 is applied to correct the $gg \rightarrow ZZ$ continuum at the NLO[2] [168–172].

---

[1] The cuts applied after the Z reconstruction modify the jet-multiplicity which might introduce resummation effects which are not evaluated in the fixed order NNLO calculation.

[2] The k-factor is calculated for massless quark loops, in the heavy top approximation

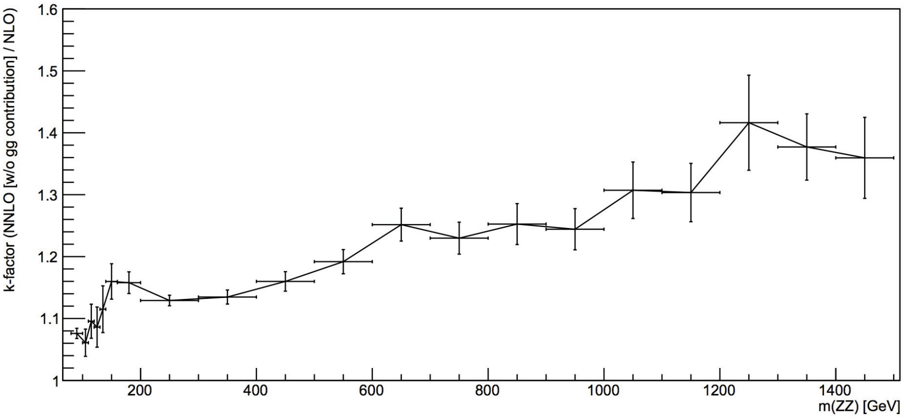

Fig. 4.6 · The derived NNLO QCD k-factors binned in M_{ZZ} for the $q\bar{q} \to ZZ$ process. The picture is taken from [173].

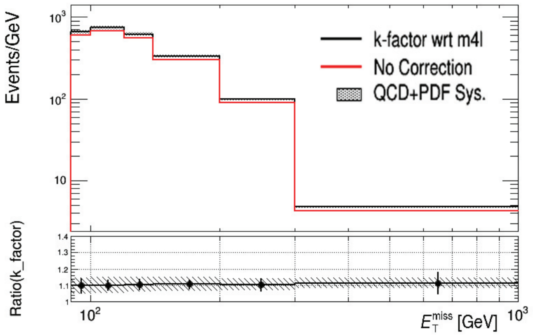

Fig. 4.7 · The detector-level E_T^{miss} distribution in the signal region after applying the NNLO QCD k-factors to the MC $q\bar{q} \to ZZ$ events; the original distribution before the correction is shown for comparison.

4.5.3 WZ background

The second largest background in this analysis comes from the WZ process. In the case of leptonic decay of both W and Z, the misreconstruction of the lepton coming from the W can reproduce the signal final signature (2 leptons from a Z decay and E_T^{miss}). The normalization for this background is obtained from data by using a three lepton control region (3lCR). Such region is defined by requiring a third lepton (the third lepton veto cut is removed) in addition to the two leptons coming from the Z boson decay. The third lepton is selected following the same criteria used for the leptons coming from the Z decay as described in Table 4.4 and Table 4.3.
In order to obtain a CR with high purity an additional cut is applied: $M_T^W > 60$ GeV[1]. The cut implies that the third lepton and the E_T^{miss} are compatible with the decay of a W boson and this removes the Z+jets contribution. As in the SR, a b-jet veto is applied to remove top related background: the purity of the region is around ~90 %. The selection applied for the 3lCR is summarized in Table 4.9.

Three Lepton CR definition
Two same flavour opposite-sign leptons (e^+e^- OR $\mu^+\mu^-$)
Require one additional lepton with $p_T > 20$ GeV
$76 < M_{\ell\ell} < 106$ GeV
$m_T(W) > 60$ GeV
b-jet Veto

Table 4.9 · Selection applied for the 3lCR.

Figure 4.8 shows the E_T^{miss} distributions after the full 3lCR selection in the four different leptonic combinations: $ee + e$, $ee + \mu$, $\mu\mu + e$, $\mu\mu + \mu$.

The 3lCR is used to obtain a scale factor (SF) among the observed (data) and expected (MC) WZ events. The final estimate is then obtained by normalizing the number of WZ expected events in the 2 leptons SR with the obtained SF as shown in equation 4.3.

$$N_{2lSR} = N_{2lSR}^{MC} \cdot \frac{N_{3lCR}^{data}}{N_{3lCR}^{MC}} \tag{4.3}$$

---

[1] The W transverse mass is defined as $m_T = \sqrt{2p_T E_T^{miss}(1 - \cos\Delta\phi)}$, where p_T is the transverse momentum of the lepton and $\Delta\phi$ is the difference between the lepton and the neutrino angle.

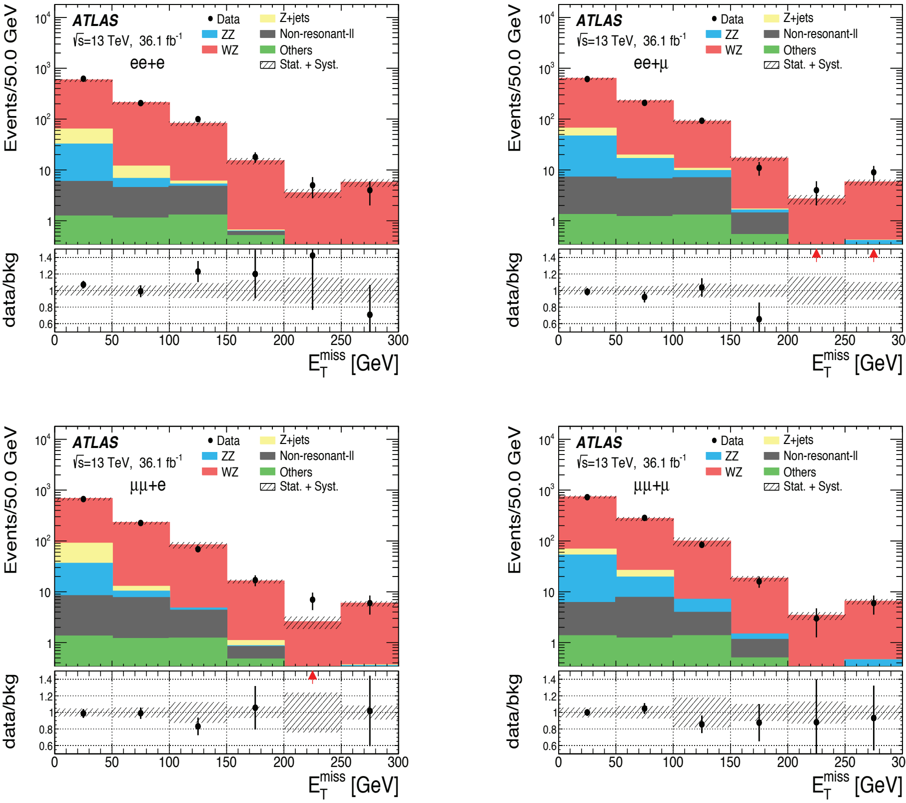

Fig. 4.8 · E_T^{miss} distributions after full 3lCR cut for data and Monte Carlo in (a) the ee + e channel, (b) ee + μ channel, (c) μμ + e channel and (d) μμ + μ channel in events with one additional electron or muon with respect to the lepton pair whose invariant mass is consistent with the Z boson mass. MC samples are normalized to their cross section values and re-scaled to the data integrated luminosity reported in the figure. For WZ background, the scale factor of $1.29 \pm 0.03 \pm 0.07$ from data-driven estimate is applied, NNLO and NLO corrections are applied for ZZ. The bottom plots show the ratio of the data and Monte Carlo. The non-resonant-ll background contains the background processes such as WW, $t\bar{t}$, Wt and $Z \rightarrow \tau\tau$. The minor contributions from VVV, $ttV(V)$ and W+jets are summed and labeled as "Others”. The rightmost bin contains the overflow contributions. The plots have been published in the article [164].

Table 4.10 shows the number of background and data events in the 3lCR for each decay mode of the WZ bosons, together with the corresponding scale factors. The final scale factor $(1.29 \pm 0.03 \pm 0.07)$ used to normalize the WZ contribution is obtained by subtracting the non-WZ backgrounds from the the data and it is evaluated by considering all the different decay modes together. The shape for the E_T^{miss} is extracted from MC, both theoretical and experimental uncertainties are taken into account.

channel	WZ	Z+jets	ZZ	non-resonant-ll	Others	Data	factor
ee + e	632.2 ± 5.0	37.58 ± 5.47	28.34 ± 0.63	11.39 ± 1.39	4.22 ± 0.10	958	1.39 ± 0.05
ee + μ	673.7 ± 5.2	23.54 ± 12.12	51.35 ± 0.85	17.30 ± 1.55	4.46 ± 0.10	941	1.25 ± 0.05
$\mu\mu$ + e	702.7 ± 5.3	55.11 ± 25.91	30.32 ± 0.68	16.62 ± 1.76	4.24 ± 0.11	993	1.26 ± 0.06
$\mu\mu$ + μ	797.6 ± 5.7	17.63 ± 8.01	60.32 ± 0.95	14.23 ± 1.38	4.50 ± 0.11	1121	1.28 ± 0.04
Total	2806 ± 11	133.85 ± 30.20	170.33 ± 1.57	59.54 ± 3.05	17.42 ± 0.21	4013	1.29 ± 0.03

Table 4.10 · The expected number of background and observed number of events in the 3lCRs in M_T^W > 60 GeV and b-jet veto region. The final column shows the scale factor for different channels, which is obtained by subtracting other backgrounds contribution from the observed yield in data, and by taking the ratio between the subtracted data and the expected number of events from the WZ MC. The number of observed events is given for an integrated luminosity of 36.1 fb^{-1}.

4.5.4 Z+jets background

The Z+jets background is due mostly to fake E_T^{miss} present in the event. It is therefore reduced mostly by the cut on the E_T^{miss} and only a small number of events get through the full event selection in the final SR. Nevertheless the systematic uncertainties introduced by the mis-modeling of E_T^{miss} in MC (detector, pile-up, jet energy scale effects), make it mandatory to use a data-driven method to evaluate such background. The strategy followed for the Z+jets background yield and E_T^{miss} shape is the following:

- Estimate the background yields in the SR by the ABCD data-driven method
- Estimate the E_T^{miss} shape from the MC

ABCD Method

The ABCD method is a data-driven technique that is used to estimate the number of background events in a defined SR (A). The method is based on the creation of 3 side band regions (B, C, D) which represent the phase-space area where the cuts on two selected variables are failing. The scheme of the ABCD method is shown in Figure 4.9.

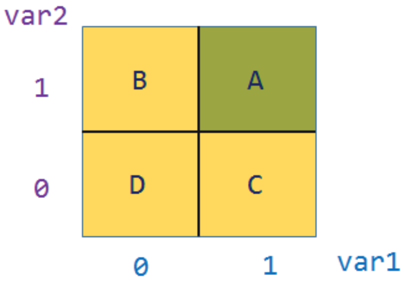

Fig. 4.9 · Scheme of the ABCD method. Signal region A is defined by the cut on both variables being true, representing all selections passed.

The pair of variables selected have to be uncorrelated and they have to be sensitive to the background: by reversing the cut on them the side band region should be enriched in background events. To increase the side-band region purity, the non-Z+jets backgrounds contribution is reduced by subtracting such backgrounds. The major advantage of this method is that, provided that the variables are uncorrelated and that the E_T^{miss} shape in region C is the same as in region A, the background yield in the SR (A) can be estimated from the side-band regions (B,C,D) using the following formula:

$$N_A^{est} = N_C^{obs,sub} \times \frac{N_B^{obs,sub}}{N_D^{obs,sub}} \tag{4.4}$$

where N_A^{est} is the number of estimated background events in SR, while $N_X^{obs,sub}$ are the numbers of observed events in side-band regions X = B-D, where the contribution of non-Z+jets background is subtracted before applying this equation. Due to tight cut against the Z+jets background such as the E_T^{miss}/H_T cut, the definition of ABCD regions by using two variables suffered from very low event counts in the side-band regions leading to poor agreement between data and MC, as well as high correlation after final cuts, resulting in non-closure.Non-closure means that the equation 4.4 no longer holds for MC, i.e. $N_C^{MC} \times \frac{N_B^{MC}}{N_D^{MC}} \neq N_A^{MC}$. To solve the issue the method was modified introducing *boolean* variables: the two selected variables are not a single cut on a single quantity but a combination of selections. A side band region is now populated if one event fails *any* of the cuts instead of just one cut as in the traditional two-variable ABCD. In order to construct combination of booleans with low correlation, cuts on highly-correlated variables were combined in one boolean variable, trying to keep low correlated variables in different booleans. The following boolean variables were chosen:

$$var1 = E_T^{miss} > 90\text{ GeV } \textbf{ AND } E_T^{miss}/H_T > 0.6 \tag{4.5}$$

$$var2 = |E_T^{miss,jets} - p_T^{\ell\ell}|/p_T^{\ell\ell} < 0.2 \textbf{ AND } \Delta\phi(Z, E_T^{miss}) > 2.7 \textbf{ AND } \Delta R_{\ell\ell} < 1.8 \textbf{ AND } N_{b-jets} = 0 \tag{4.6}$$

Two additional cuts were added to all side-band regions: $E_T^{miss} > 60$ GeV and $E_T^{miss}/H_T > 0.12$ to reduce correlation.The resulting ratios for MC, as well as for data, are shown in Tables 4.11 and the E_T^{miss} distributions for the side-band X=B,C,D for data with electron and muon channel combined are shown in Figure 4.10. Data-driven estimates are presented in Table 4.12: both statistical and systematics uncertainties are taken into account. The systematic uncertainties sources are due to the methodology used and to the subtraction of non Z+jets background samples. The methodology systematics are due to the MC non-closure (difference arising between N_A/N_C (MC) and N_B/N_D (MC)) and to the uncertainty associated with the selection of optimal additional E_T^{miss} and E_T^{miss}/H_T cuts. Table 4.13 shows the very high systematic uncertainty for both electron and muon channel due to the methodology and non-Z+jets MC samples subtraction.

	N_A/N_C [MC]	N_B/N_D [MC]	N_B/N_D [Data]	N_C [Data]
ee channel	0.017 ± 0.005	0.0137 ± 0.0004	0.0159 ± 0.0003	1915 ± 78
$\mu\mu$ channel	0.012 ± 0.003	0.0125 ± 0.0003	0.0145 ± 0.0002	2554 ± 85

Table 4.11 · Ratios N_A/N_C, N_B/N_D and N_C^{obs} for the ee and $\mu\mu$ channel. Only the statistical errors are showed. Statistical errors due to the MC subtraction are also considered for N_B/N_D (Data) and N_C [Data]. WZ background yields for subtraction from data were rescaled using a scale factor of 1.29 obtained using data-driven estimate. For ZZ background, NNLO QCD and NLO EW corrections were applied. Sherpa 2.2.1 samples are used for the Z+jets background.

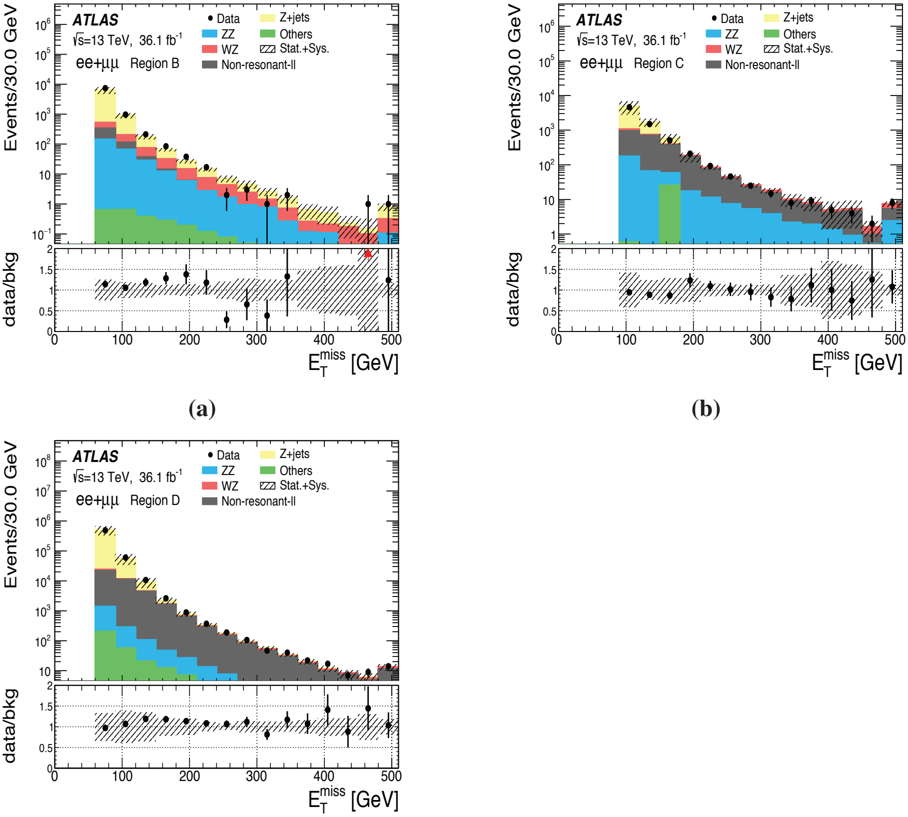

(a)

(b)

(c)

Fig. 4.10 · The E_T^{miss} distributions in the B (a), C (b) and D (c) regions for the combined ee and $\mu\mu$ channel. These regions are used in the data-driven estimation of the Z+jets background. The data are compared to the simulated backgrounds, and the error band for the total background only covers the statistical uncertainties of the simulated samples and the experimental uncertainties. The WZ background contribution is corrected by the data-driven scale factor of 1.29. The non-resonant-ll background contains the background processes such as WW, $t\bar{t}$, Wt and $Z \to \tau\tau$. The minor contributions from VVV, $ttV(V)$ and W+jets are summed and labeled as "Others”. The rightmost bin contains the overflow contributions. The plots have been published in the article [164].

	ee-channel	$\mu\mu$-channel
Z+jets	**30 ± 1** $^{+28}_{-17}$	**37 ± 1** $^{+14}_{-19}$

Table 4.12 · Summary of the Z+jets background estimation using the ABCD method with statistical and systematic uncertainties. Systematic uncertainties come from the level of correlation in MC, estimated by difference between N_A/N_C [MC] and N_B/N_D [MC], experimental uncertainties on this difference and subtraction of non-Z+jets backgrounds. The systematic uncertainty, due to the methodology and to the non-Z+jets subtraction are extremely high for this background.

	ee-channel	$\mu\mu$-channel
Methodology	$^{+90.2\%}_{-54.5\%}$	$^{+37.2\%}_{-49.4\%}$
Non-Z+jets sub.	13.6%	11.2%
Total systematic unc.	$^{+91.3\%}_{-56.2\%}$	$^{+38.8\%}_{-50.6\%}$

Table 4.13 · Systematic uncertainties from the methodology and the non-Z+jets backgrounds from MC. Methodology uncertainties consists of non closure of the method and the uncertainty associated with the selection of optimal additional E_T^{miss} and E_T^{miss}/H_T cuts. Both of these sources provide an almost equal contribution to the systematic uncertainty.

Estimation of E_T^{miss} shape

The E_T^{miss} shape of the Z+jets background is estimated through the Sherpa 2.2.1 MC simulation, and then it is scaled to the yields obtained from the ABCD method. A looser SR region[1] is used to extract the shape. The shape is not extracted from the ABCD method due to low statistics and higher contamination of the non-Z backgrounds. The experimental uncertainties and the difference with respect to the data-driven shape is used as systematics as showed in Figure 4.11.

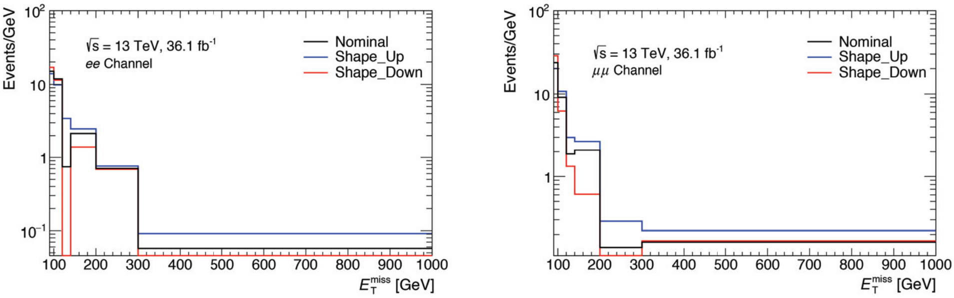

(a) **(b)**

Fig. 4.11 · Estimates of the Z+jets background shape for the E_T^{miss} in the ee (a) and $\mu\mu$ (b) channels using MC, normalized to the yields obtained in the ABCD method. A looser SR used to obtain the shape is constructed removing cuts on $\Delta\phi(Z, E_T^{miss})$, fractional p_T difference and b-jet veto. The blue and red curves correspond to up and down uncertainties obtained using difference with respect to data-driven shape and experimental uncertainties, statistical uncertainties are also taken into account.

---

[1] Cuts on $\Delta\phi(Z, E_T^{miss})$, fractional p_T difference and b-jet veto are removed.

4.5.5 flavour symmetry background

The $t\bar{t}$, WW, Wt and $Z \to \tau\tau$ backgrounds have singularly a small impact on the total background of this analysis. The b-jet veto suppresses physics processes with one or more top quarks. The WW contribution is removed by requiring first compatibility of the mass of the opposite charge di-lepton pair with the Z boson mass (the "$M_{\ell\ell}$" selection), and then by applying a high E_T^{miss} cut. The $Z \to \tau\tau$ is suppressed because the two leptons invariant mass is lower than the Z mass due to the presence of neutrinos in the tau decays which take part of the energy. Finally the Wt contribution is suppressed by the low cross section. Nevertheless those backgrounds are relevant because they have a final state with real E_T^{miss} and leptons, especially the $t\bar{t}$ process. The data-driven method chosen for such background is described in the following section.

The flavour symmetry method

The yields of $t\bar{t}$, WW, Wt and $Z \to \tau\tau$ backgrounds are estimated from data through the *flavour symmetry* method. All of those backgrounds decay in the $ee : \mu\mu : e\mu$ channel with the relative probability of 1 : 1 : 2. It is possible then to apply the same method to a merged background which is the sum of all those background, named the $e\mu$ background. The CR is built with the same selections as the SR apart from the requirement of two different flavour leptons as shown in Table 4.14. This allows the measurement of these backgrounds directly from data using the $e\mu$ final state. The contribution in the SR is then obtained by considering the difference in the electron/muon reconstruction efficiency, accounted in the so-called ϵ*-factor*, defined as:

$$\epsilon^2 = \frac{N_{ee}}{N_{\mu\mu}} \tag{4.7}$$

where N_{ee} and $N_{\mu\mu}$ are respectively the number of ee and $\mu\mu$ events with an invariant mass compatible with that of a Z for the flavour symmetry background samples ($t\bar{t}$, WW, Wt and $Z \to \tau\tau$). With this definition the number of $e\mu$ background events in the SRs is obtained as:

$$N^{e\mu}_{SRee} = \frac{1}{2} \times \epsilon \times N^{data,sub}_{e\mu} \tag{4.8}$$

$$N^{e\mu}_{SR\mu\mu} = \frac{1}{2} \times \frac{1}{\epsilon} \times N^{data,sub}_{e\mu} \tag{4.9}$$

where $N^{data,sub}_{e\mu}$ is the number of $e\mu$ data events in the CR, estimated as

$$N^{data,sub}_{e\mu} = N^{data}_{e\mu} - N^{other}_{sub} \tag{4.10}$$

N^{other}_{sub} is defined as the non-$t\bar{t}/WW/Wt/Z \to \tau\tau$ background subtracted using data-driven estimates where available, or MC simulations where no data-driven estimates are available, as in Equation 4.11.

$$N^{other}_{sub} = \sum_{i}^{non-e\mu} N_i \tag{4.11}$$

$e\mu$ **CR definition**
Two different flavour opposite sign leptons ($e^{\pm}\mu^{\mp}$)
Veto any additional lepton with Loose ID and p_T >7 GeV
$76 <$ $M_{e\mu}$ $<$ 106 GeV
E_T^{miss} $>$ 90 GeV
$\Delta R_{e\mu}$ $<$ 1.8
$\Delta\phi(Z, E_T^{miss})$ $>$ 2.7
Fractional p_T difference $<$ 0.2
E_T^{miss} $/H_T$ $>$ 0.6
b-jet Veto

Table 4.14 · Event selection applied to define the $e\mu$ Control Region. The control region reflects the SR definition apart from the different flavour requirement of the two selected leptons.

The advantage of having a CR defined with two different flavour leptons is that the purity is very high (more than 95%), since most of the contribution from processes with a Z boson is removed.

Data-driven method with efficiency factor as function of (p_T and η)

Before applying the method the modeling of the variables used to define the CR is checked with data. Figures 4.12 and 4.13 show the E_T^{miss} , p_T of the Z boson and the number of jets distributions after the Z mass window cut and the E_T^{miss} > 90 GeV cut. Data and MC show good agreement aside from the number of jets. As already discussed, the issue with the simulation of high jet-multiplicity samples is present also for the number of jets and even if there is no good agreement among data and MC, the discrepancy is covered by the systematic uncertainties. As already described the data are corrected by an efficiency factor shown in equation 4.7. In order to obtain a more precise estimation, the efficiency factor

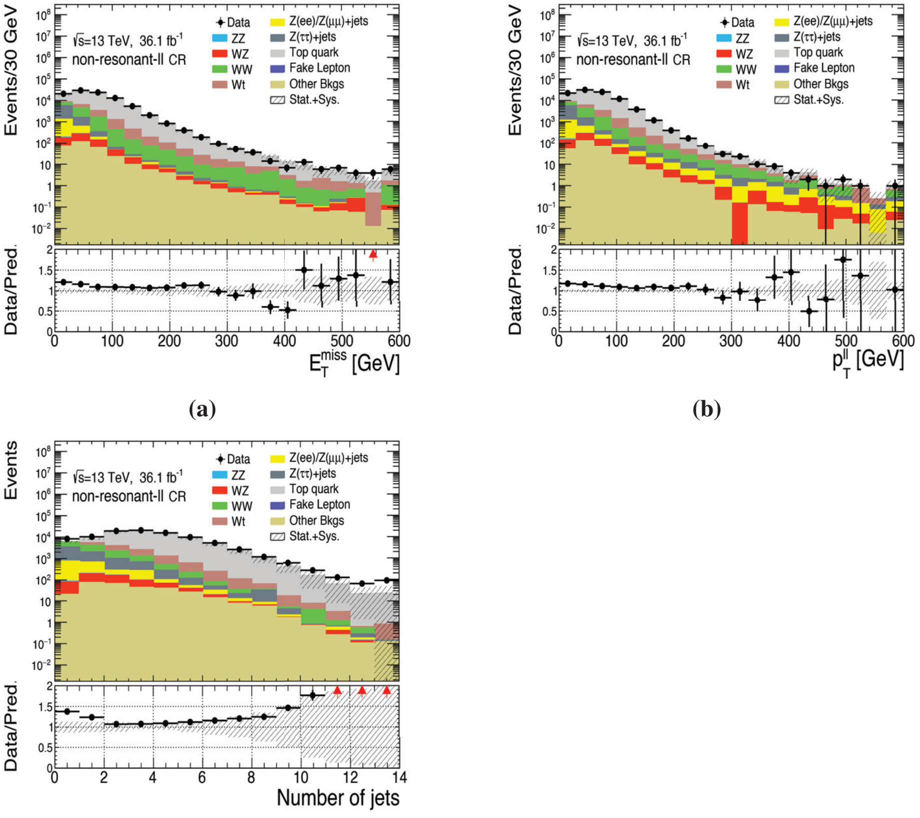

(a)

(b)

(c)

Fig. 4.12 · Data-MC comparison after the Z mass requirement in the eμ Control Region for the E_T^{miss} distribution (a) and for the Z$p_T$and number of jets distributions (b-c). Statistical and systematic errors are included in the error band of the plots.

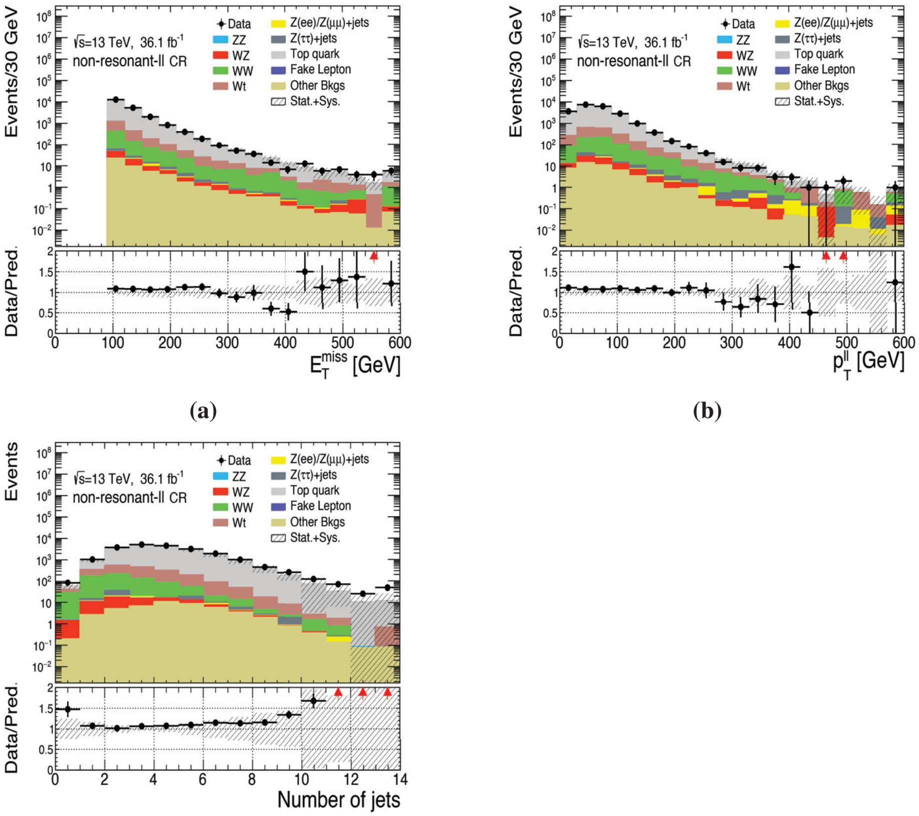

(a)

(b)

(c)

Fig. 4.13 · Data-MC comparison after the E_T^{miss} > 90 GeV requirement in the eμ CR for the E_T^{miss} (a) the Z p_T(b) and the number of jet (c) distributions. Statistical and systematic errors are included in the error band of the plots.

has been computed in bins of p_T and η for the leading and sub-leading lepton, instead of extracting one single value for the entire phase space. The latter will be referred as the "inclusive" or "unbinned" efficiency factor, and the former as "binned". For the binned efficiency factor equation 4.7 becomes:

$$\epsilon^2 = \frac{N_{e^1_{(p_T,\eta)} e^2_{(p_T,\eta)}}}{N_{\mu^1_{(p_T,\eta)} \mu^2_{(p_T,\eta)}}} \tag{4.12}$$

The binning was chosen to ensure enough statistics in each bin to obtain efficiency factors with low statistical uncertainty. The η phase space has been divided in Barrel (B) and Endcap (E), hence yielding four different bins: BB, BE, EB, EE. The order is related to the order in p_T. For example: BE stands for a leading lepton in the Barrel and subleading lepton in the Endcap. The binning in p_T has been optimized as well by requiring the same amount of events for the leading lepton in 3 p_T bins for each η region. The final choice of the 3 p_T bins is the following: $p_T < 44$ GeV, 44 GeV< $p_T < 52$ GeV, 52 GeV< $p_T < 2$ TeV. The final number of bins is then 24: 4 bins in η times 6 bins in p_T. The p_T bins are in total 9 (3x3) but 3 of them are empty due to the p_T constraint on the lepton pair (leading p_T always higher than sub-leading p_T). The efficiency factors are then evaluated in each bin using MC samples, shown in Table A.10, as well as using Data, shown in Table A.11. The results in the table show very small statistical error, less then 1% in every bin, for both MC and Data. The difference between Data and MC efficiency values has been studied as a source of systematic uncertainty.

MC closure

Before applying the method to data to extract the $e\mu$ contribution, the same steps are applied to MC $e\mu$ events and compared with the expected SR contribution from $e\mu$ processes. In this way the validity of the method, or the so-called closure was tested. To this purpose the $e\mu$ CR is defined and the amount of $e\mu$ background obtained as explained in Section 4.5.5.1. It can be observed that this CR, with the definition in Table 4.14, has a purity greater than 95%, where the only tiny contribution not coming from $e\mu$ processes is due to diboson processes. The efficiency factors extracted from the MC events with same flavour and opposite sign leptons, with $76 < M_{\ell\ell} < 106$ GeV for the so-called $e\mu$ processes ($t\bar{t}$, Wt, WW and $Z \to \tau\tau$), were already given in Table A.10. The estimation obtained through those efficiency factors is then compared with the effective number of events found in the SR for the whole $e\mu$ backgrounds. The comparison between the estimated $e\mu$ background and the MC expected yields is showed in Table 4.15. The results shows agreement within the statistical errors indicating the closure of the method. Even if the statistical error covers completely the non-closure of the method a systematic uncertainty of 5% was assigned by calculating the relative difference among the two estimations.

Data Driven estimates

The final estimates are evaluated with the binned efficiency factor. The estimates, using both MC and Data Driven method, are shown after the complete SR event selection in Table 4.16. The final estimates, performed for both inclusive and binned method, converge for the

	$Ne\mu^{est.}$	$Ne\mu^{MC}$
SR ee	24.2 ± 1.9	25.5 ± 2.6
SR $\mu\mu$	27.5 ± 2.1	26.1 ± 2.9

Table 4.15 · Closure of the $e\mu$ backgrounds estimation. $Ne\mu^{est}$ is the number of $e\mu$ events in SRs estimated through the efficiency factors in Table A.10, while $Ne\mu^{MC}$ is the expected event yields for the $e\mu$ background. Numbers are normalized to a data sample of 36.1 fb^{-1}. Errors contain statistical uncertainty only.

signal region. The final Data Driven estimates with statistics and systematics error for the SR are provided in Table 4.17.

Estimates	Inclusive	Binned (p_T,η)
N_{ee} MC	25.0 ± 2.0	24.2 ± 2.0
N_{ee} Data	28.1 ± 3.6	29.5 ± 3.8
$N_{\mu\mu}$ MC	26.9 ± 2.1	27.5 ± 2.1
$N_{\mu\mu}$ Data	34.5 ± 4.4	33.2± 4.3

Table 4.16 · Signal region final estimates results for inclusive and binned efficiency. Results obtained by MC and Data Driven methods are both shown. Errors contain statistical uncertainty only.

Extraction of the E_T^{miss} shape and systematics evaluation

The shape of the final discriminant for the $e\mu$ background in the SR is extracted from data by taking the E_T^{miss} shape in the corresponding $e\mu$ CR data events, and correcting its normalization with the binned efficiency factor reported in Table A.11. The data-driven shape in the ee and $\mu\mu$ channels for E_T^{miss} is given in Figure 4.14. The E_T^{miss} shape shows a difference between MC and Data, especially for low E_T^{miss} values. It is interesting to remark that the contribution of the MC which are not flavour-symmetric is tiny, around 3% for both signal regions (the main source being WZ, which is 2% alone). Since the E_T^{miss} tail lacks in statistics in data, unlike the MC, a conservative upper tail systematics was derived to be attached to the shape systematic on the core of the distribution. The core up/down shape systematics are derived by varying by $\pm 1\sigma$ the binned efficiency factors and extracting

Data Estimates	Binned (p_T,η)
N_{ee}	29.5 ± 3.8 ± 1.6
$N_{\mu\mu}$	33.2 ± 4.3 ± 1.6

Table 4.17 · Data Driven estimates for the signal region. Errors contain both statistical and systematic uncertainty.

again the shape. The impact on the final estimate is 1%, averaging over all the bins. To the core upper systematic, a tail is then attached, taken directly from the MC $e\mu$ events. The overall up/down systematics is then normalized to the data-driven estimate (nominal shape) in the corresponding SR. The systematic up/down and the nominal shape are shown in Figure 4.15.

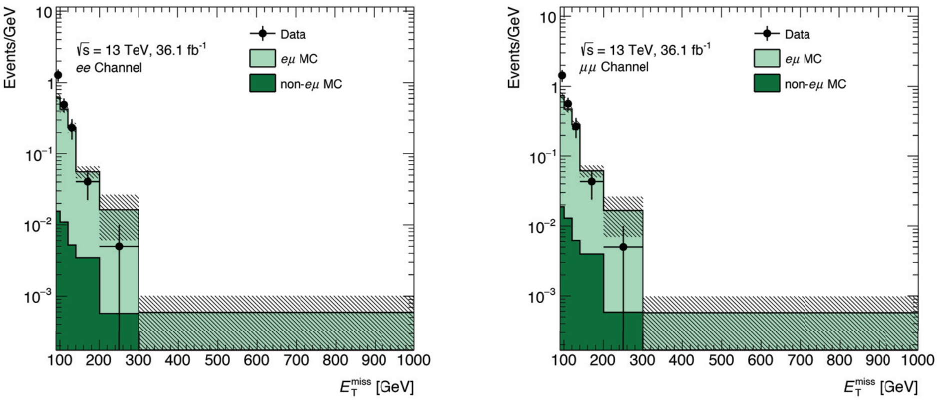

(a) **(b)**

Fig. 4.14 · E_T^{miss} shape for the $e\mu$ background in the signal region SR for electrons (a) and muons (b). The error bands include statistical uncertainty only.

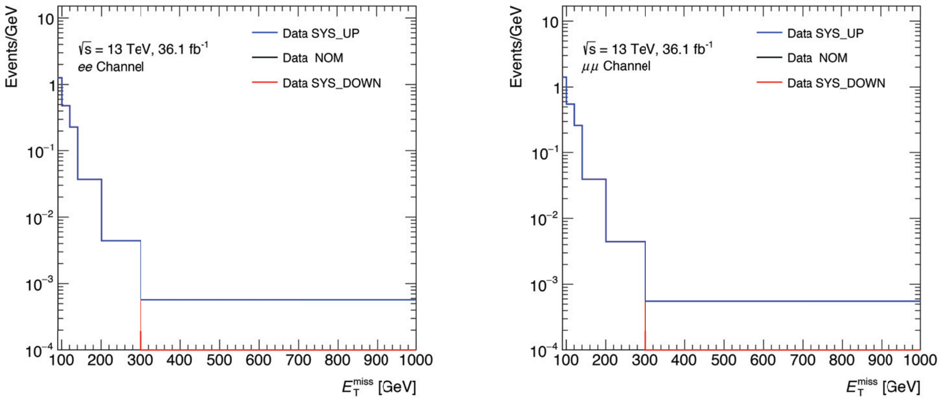

(a) (b)

Fig. 4.15 · E_T^{miss} systematic up (blue), down (red) and nominal (black) shape for the eμ background in the SR for electrons (a) and muons (b). The nominal shape is not visible in the plots because the upper systematic shape overlaps it, showing again the small impact of such systematic on the shape.

4.5.6 W+jets background

If a jet is misidentified as a lepton and it is produced in association with a leptonically decaying W boson, this signature (W+jets) can mimic a signal event. The rate at which hadronic jets are misidentified as leptons is related to rare fragmentation processes and interactions with the detector, therefore it may not be accurately described in the simulation. Even if this background is negligible, both yield and shape are determined from data with the fake-factor method.

Fake factor method

The fake-factor method consists of estimating the W+jets contribution in the SR from data, by first evaluating the probability for a jet to be mis-identified as a lepton, and then by applying this fake factor to data events in a W+jets control sample. An enriched W+jets CR is defined as the one containing a "Good" and a "Bad" lepton. A good lepton is defined as a lepton which passes all the SR event selection, while the bad lepton (a lepton-like jet) is defined by reversing one or two cuts in the selection which are linked to the track reconstruction and isolation. Table 4.18 shows the requirements for good and bad leptons. The fake-factor is defined as the ratio of the probability for a jet to satisfy the full lepton identification criteria to the probability to satisfy the lepton-like jet criteria, in other words as the ratio of good over bad leptons as shown in Equation 4.13:

	Good	Bad
Electron	Track iso: Loose, LH: Medium,	Track iso: !Loose, or LH: !Medium
Muon	Track iso: Loose,	Track iso: !Loose

Table 4.18 · Requirements for good and bad leptons

$$F_i = N^{fake}_{Good}/N^{fake}_{Bad} \tag{4.13}$$

The fake factor is then evaluated, as function of η and p_T , via a *tag-and-probe* method using the good lepton as tag and the bad lepton as probe on the W+jets CR. Table 4.19 show the W+jets CR selection requirements. The final estimates are then evaluated by applying the fake factor to the data after subtracting all the MC backgrounds which can produce the same final signature (WW, WZ, ZZ and $t\bar{t}$).The final results obtained for the W+jets yields are reported in Table 4.20, and the shape for the E_T^{miss} distribution is shown in Figure 4.16.

Criteria	Selection
Tag lepton	1 selected Muon or Electrons
Probe lepton	only one extra lepton
Trigger	Single lepton trigger
E_T^{miss}	> 20 GeV

Table 4.19 · *W*+jets control sample definition

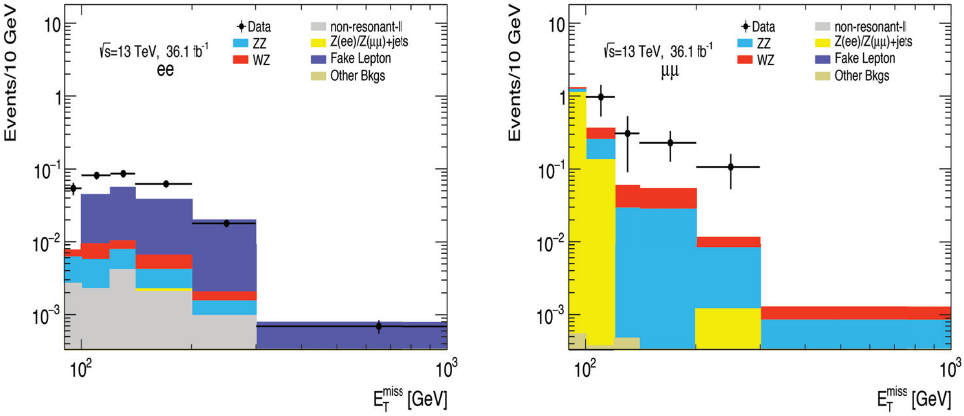

Fig. 4.16 · Data driven estimate of the *W*+jets background by the fake factor method. The E_T^{miss} distributions for *W*+jets SR for the *ee* channel (a) and μμ channel (b) are shown.

	Final estimates
ee	$0.43 \pm 0.09 \pm 0.04$
$\mu\mu$	$1.53 \pm 1.92 \pm 0.73$

Table 4.20 · W+jets data-driven estimation in the electron and muon channel as obtained from the data-driven technique.

4.6 Systematic uncertainties

The systematic uncertainties that affect an analysis arise from different sources. They affect both SRs and CRs and they are caused by the multiple procedures used to reconstruct and calibrate the various objects, the computation of the MC processes and the method utilized to evaluate the different backgrounds. All those contributions can be divided in two groups: experimental and theoretical.
In the following sections, both experimental and theoretical uncertainties will be described.

4.6.1 Experimental uncertainties

Each object in this analysis is reconstructed and calibrated following a specific procedure as described in Chapter 3. Uncertainties on these procedures as well as non-closure among MC and data are accounted as systematic uncertainties.

Luminosity uncertainty

The calculation of the luminosity is affected by several systematic sources: the beam intensities evaluation, length scale calibration procedure, imperfect beam centering. Details about the procedure can be found in reference [174]. The uncertainty on the combined 2015 and 2016 integrated luminosity is $\pm 3.2\%$, which assumes partially correlated uncertainties, and is applied to signal and the background estimated from MC predictions.

Pile-up uncertainty

The pile-up reweighting method is used to match the simulated average number (μ) of proton-proton interactions per bunch crossing to the one measured from real data. The estimation of the uncertainty on the pile-up reweighting procedure is done by varying the data μ scale value. The pileup-reweighting is performed again and the variations from the nominal result are treated as systematic uncertainties.

Electrons and Muons

The systematic uncertainties for electrons and muons come from different sources:

- Electron energy scale and resolution:
  Energy mis-calibration effects arise from different calorimeter response between simulated and real data. The calibration procedures (performed on well known processes as $Z \to ee$) are affected by systematic uncertainty. A detailed description of how the uncertainties are taken into account is described in reference [175]. A simplified uncertainty model, which combines all the uncertainties for scale and resolution in two systematic variables, is used for this analysis.

- Muon momentum calibration and smearing:
  Smearing variations for ID and MS tracks and scale variation of the muon momentum are used as systematic variation.

- Electron and muon reconstruction, identification, isolation and trigger efficiency:
  Similarly as the energy scale and resolution also the reconstruction, identification, isolation and trigger efficiencies are corrected based on the difference between MC

and Data. A scale factor to correct MC to data is obtained and the corresponding uncertainties are treated as systematic ones.

Jets

Jets are complex objects and their reconstruction and calibration are based on simulation and real data techniques leading to many systematic uncertainties. The major sources of uncertainties come from:

- Jet energy scale (JES):
  Evaluating the energy of a jet is a complex task in a hadronic particle collider experiment. Several procedures are used in order to calibrate properly the JES and several systematic uncertainties are associated with such procedures. More detail about the JES can be found in reference [160]. In this analysis a highly reduced model is used.

- Jet energy resolution (JER):
  Jets resolution are corrected due to the difference of data and MC with assigned uncertainty.

- The efficiency of JVT requirement:
  As described previously in this chapter the JVT cut is applied to remove pile-up effects. The jets reconstruction efficiency depends on the choice of this cut. Variations on the efficiency due to the modification of the cut are taken as a source of systematic.

Jet-flavour tagging

The jet-flavour tagging efficiency has been corrected comparing data and MC. This analysis only considers three systematic uncertainties corresponding to the uncertainties for the correction on the tagging efficiency of bottom, charm and light jets. Two additional systematic uncertainties are considered for the jets with $p_T > 300$ GeV. For such high-p_T jets the data-based correction cannot be performed and the uncertainties are extrapolated from simulation only. More details can be found in reference [176].

E_T^{miss}

The determination and description of the E_T^{miss} systematic uncertainty is detailed in reference [162]. In this analysis, the systematic uncertainties are estimated only on the E_T^{miss} soft term (track-based soft term or TST) for E_T^{miss} related uncertainty. The effects on E_T^{miss} from other terms will be automatically considered when varying their corresponding objects uncertainties. Three systematic uncertainties are included in this analysis: one for the TST scale and two for the resolution along the perpendicular and the parallel direction to the vector sum of hard objects p_T (p_T^{hard}).

All the experimental systematics used in the analysis are summarized in Table 4.21.

Systematic variation
Luminosity
Total integrated Luminosity
Pile up reweighting
pileup μ profile reweighting
Electrons
electron resolution smearing
electron energy calibration
electron identification efficiency
electron reconstruction efficiency
electron trigger efficiency
Muons
muon ID track smearing
muon MS track smearing
muon momentum calibration
muon reconstruction efficiency
muon reconstruction efficiency
muon trigger efficiency
muon trigger efficiency
Jets
Jet energy scale
Jet energy scale
Jet energy resolution
Flavor tagging
b-jet tagging efficiency
c-jet tagging efficiency
light-jet tagging efficiency
b-jet tagging efficiency with high pt extrapolation
c-jet tagging efficiency with high pt extrapolation
$E_{\mathrm{T}}^{\mathrm{miss}}$
$E_{\mathrm{T}}^{\mathrm{miss}}$ soft term scale
$E_{\mathrm{T}}^{\mathrm{miss}}$ soft term resolution
$E_{\mathrm{T}}^{\mathrm{miss}}$ soft term resolution

Table 4.21 · The Summary of experimental systematic uncertainties

4.6.2 Theory systematic uncertainties

Theoretical uncertainties are considered for MC-based backgrounds: the ZZ yield and E_T^{miss} shape, the shape of the WZ background and for the signal. The uncertainties for both signal and backgrounds come from different sources as the choice of the parton density function (PDF) sets and the QCD scale.

- PDF uncertainties: The estimation of systematic uncertainty on the PDF is done by varying the chosen PDF set and its parameters. Different MC weights are stored in the samples for different PDF sets. The envelope that can cover the difference among the nominal results and the ones obtained by the alternative PDF set is defined as the systematic uncertainty. The details can be found in reference [167].
- QCD scale uncertainties: The choice of the QCD renormalization (μ_R) and factorization (μ_F) scale is arbitrary. To estimate the QCD uncertainties the μ_R and μ_F scales are varied with respect to the nominal values. With a procedure similar to the PDF uncertainties evaluation, the alternative MC weights are stored in the samples and the envelope that covers the differences between the scale variations and the nominal results is taken as systematic uncertainty.

For the ZZ background additional uncertainties on the NNLO QCD correction for cross section and EW NLO correction are introduced; details can be found in reference [173].

The combination of all experimental and theoretical uncertainties will be used in the evaluation of the final results. The impact of each nuisance parameter for each channel will be shown and described in the Results section.

4.7 Statistical Analysis

Test statistics based on the likelihood ratio method are widely used in high energy physics experiments. In this analysis a background-only hypothesis test is performed to check for a potential discovery. If the test cannot reject a background-only hypothesis then an exclusion fit is performed, resulting in an upper limit on the signal strength. This section will describe briefly the likelihood function, the definition of a test statistic, the discovery and the exclusion limit procedure.

4.7.1 Likelihood, nuisance parameters and test statistic $\tilde{q}_\mu$

The statistical analysis of the data uses a binned likelihood function $\mathcal{L}$ constructed as the product of Poisson probability $\mathcal{P}$ terms,

$$\mathcal{L}(N^{obs}|\mu, s, B, \theta) = \mathcal{P}(N^{obs}|N^{exp}(\mu, s, B, \theta)) \prod_j G(\theta_j), \tag{4.14}$$

where the Poisson distribution depends on the number of observed events N^{obs} and the number of expected events N^{exp}. The N^{exp} depends on the signal strength μ, the number of signal and background events s and B, and the nuisance parameters (NPs) θ. The number of expected events is evaluated in each bin and N^{exp} can be written as:

$$N^{exp} = \sum_{b \in bins}^{n} \mu \nu_b^{sig}(\theta) + \nu_b^{bkg}(\theta) \tag{4.15}$$

where μ, the signal strength parameter, multiplies the expected signal yield ν_b^{sig} in each bin b, and ν_b^{bkg} represents the background content for each bin b. The dependence of the signal and background predictions on the systematic uncertainties is described by the set of NPs θ, which are constrained by Gaussian distributions. The systematics are allowed to vary around their nominal value and within their assigned uncertainties. The nominal fit result in terms of μ is obtained by maximizing the likelihood function with respect to all parameters. This is referred to as the maximized log-likelihood value, MLL. The test statistic $\tilde{q}_\mu$ is then constructed according to the profile likelihood:

$$\tilde{q}_\mu = \begin{cases} -2\ln \dfrac{\mathcal{L}(\mu, \hat{\hat{\theta}}(\mu))}{\mathcal{L}(0, \hat{\hat{\theta}}(0))} & \hat{\mu} < 0 \\ -2\ln \dfrac{\mathcal{L}(\mu, \hat{\hat{\theta}}(\mu))}{\mathcal{L}(\hat{\mu}, \hat{\theta})} & 0 \leqslant \hat{\mu} \leqslant \mu \\ 0 & \hat{\mu} > \mu \end{cases}, \tag{4.16}$$

where $\hat{\mu}$ and $\hat{\theta}$ are the parameters that maximize the likelihood, and $\hat{\hat{\theta}}$ are the nuisance parameter values that maximize the likelihood for a given μ.

4.7.2 Discovery test, p-value and CL_s method

Once the test statistic is defined a discovery test is firstly effectuated. The goal of this test is to check the compatibility between the observed data and the background only hypothesis. The signal strength μ is set to zero and the test is performed by evaluating the corresponding p-value defined as (for a generic μ):

$$p_\mu = \int_{\tilde{q}_{\mu,obs}}^{\infty} f(\tilde{q}_\mu|\mu) d\tilde{q}_\mu \tag{4.17}$$

Here $f(\tilde{q}_\mu|\mu)$ is the probability density function of $\tilde{q}_\mu$ assuming the μ hypothesis, and $\tilde{q}_{\mu,obs}$ is the value of $\tilde{q}_\mu$ computed for the observed data. The integral in Eq. 4.17 cannot be solved exactly. The common procedure in ATLAS is to use asymptotic formulae [177], that allow to calculate the closed form for $f(\tilde{q}_\mu|\mu)$ and evaluate p_μ If the p-value result is smaller then $2.87 \cdot 10^{-7}$, the discovery test rejects the background-only hypothesis and the presence of new phenomena can be claimed. The value of $2.87 \cdot 10^{-7}$ can be interpreted as a fluctuations of 5σ from the mean of the Gaussian.[1] In case the discovery test cannot reject

---

[1] The translation of the p-value result into significance fluctuation comes from the following formula: $Z = \Phi^{-1}(1-p)$ where Φ^{-1} is the cumulative of the Gaussian.

the background-only hypothesis an exclusion limit test is performed. This analysis uses the $\mathrm{CL_s}$ method, where the p-value, or the "$\mathrm{CL_s}$ value", is defined as:

$$\mathrm{CL_s} \equiv \frac{p_{s+b}}{1-p_b}, \tag{4.18}$$

where

$$p_b = P(\tilde{q}_\mu \leqslant \tilde{q}_{\mu,\mathrm{obs}}|b). \tag{4.19}$$

In other terms the $\mathrm{CL_s}$ estimator is defined as the ratio between the p_{s+b} (signal plus background hypothesis) and $1-p_b$ (background only hypothesis). Using the $\mathrm{CL_s}$ method, any μ values that give $\mathrm{CL_s} < 0.05$ are excluded at the 95% Confidence Level (CL). The observed limit can be compared with the expected limit derived using an Asimov dataset treated as the $E_\mathrm{T}^\mathrm{miss}$ distribution after profiling the background-only model ($\mu = 0$) to data. In this case, the $\pm 1\sigma$ and $\pm 2\sigma$ bands on the expected limits can also be reported to test the compatibility between observed and expected limits. The corresponding limits on $\sigma(ZH \to \ell\ell + inv.)$ are calculated based on the limits on μ depending on the theoretical cross section for a SM Higgs.

4.8 Results

Table 4.22 shows the observed data yields, the estimated background contributions and the expectations for the signal process after the final selection. Figure 4.17 shows the simulated and observed $E_\mathrm{T}^\mathrm{miss}$ distributions for the ee, $\mu\mu$ and combined $ee + \mu\mu$ channel. A small excess is present in the muon channel in the observed data.

4.8.1 Systematic Ranking plot

During the fit, the value and error of each nuisance parameter changes, as well as its impact on the signal strength μ. After the fit, the variation of the parameter value and error is called "pull", while the importance in term of signal strength is called "ranking". The rankings are obtained by first performing the global fit and determining the best-fit values (and the best-fit errors) for each nuisance parameter. Then, for each parameter, the fit is redone four separate times, each time with the parameter fixed to its pre-fit value $+1\sigma$, its pre-fit value -1σ, its post-fit value $+1\sigma$, and its post-fit value -1σ. During each of these fits, all other nuisance parameters are initially set to their best-fit value, and are allowed to float during the fit. After each fit, the impact on the signal strength, i.e. the change in μ, $\Delta\mu$, is calculated. After all of the fits are done for each parameter, they are ranked by which parameter had the largest $\Delta\mu$. Figures 4.18, 4.19, 4.20 show both the pull and ranking for each nuisance parameter for the ee, $\mu\mu$, and $ee + \mu\mu$ combined fit cases. The features in these plots are checked and found consistent with expectation, for example: 1) asymmetric systematic uncertainties give asymmetric impact on the signal strength; 2) major systematic sources get higher ranks; 3) nuisance parameters correlated with the signal strength get larger pulls after the fit.

Final State	ee	$\mu\mu$
Observed Data	437	497
Signal		
ZH ($BR(H \to inv.) = 30\%$)	$32 \pm 1 \pm 3$	$34 \pm 1 \pm 3$
Backgrounds		
$qq \to ZZ$	$212 \pm 3 \pm 15$	$221 \pm 3 \pm 17$
$gg \to ZZ$	$18.9 \pm 0.3 \pm 11.2$	$19.3 \pm 0.3 \pm 11.4$
WZ	$106 \pm 2 \pm 6$	$113 \pm 3 \pm 5$
Z+jets	$30 \pm 1 \pm 28$	$37 \pm 1 \pm 19$
$t\bar{t}, WW, Wt, Z \to \tau\tau$	$30 \pm 4 \pm 2$	$33 \pm 4 \pm 2$
Others	$1.4 \pm 0.1 \pm 0.2$	$2.5 \pm 2.0 \pm 0.8$
Total Background	$399 \pm 6 \pm 34$	$426 \pm 6 \pm 28$

Table 4.22 · Observed data yields and expectations for the signal and background contributions in the signal region. The first error is statistical, and the second systematic. The signal contribution is shown with $BR(H \to inv.) = 0.30$, which is the value most compatible with data, after the fit. The $e\mu$ background arises from $t\bar{t}$, Wt, WW and $Z \to \tau\tau$ production. The background contributions from the W+jets, VVV and $t\bar{t}V(V)$ processes are summed and presented with the label "Others". The uncertainty on the total background prediction is quadratically summed from those on the individual background contributions.

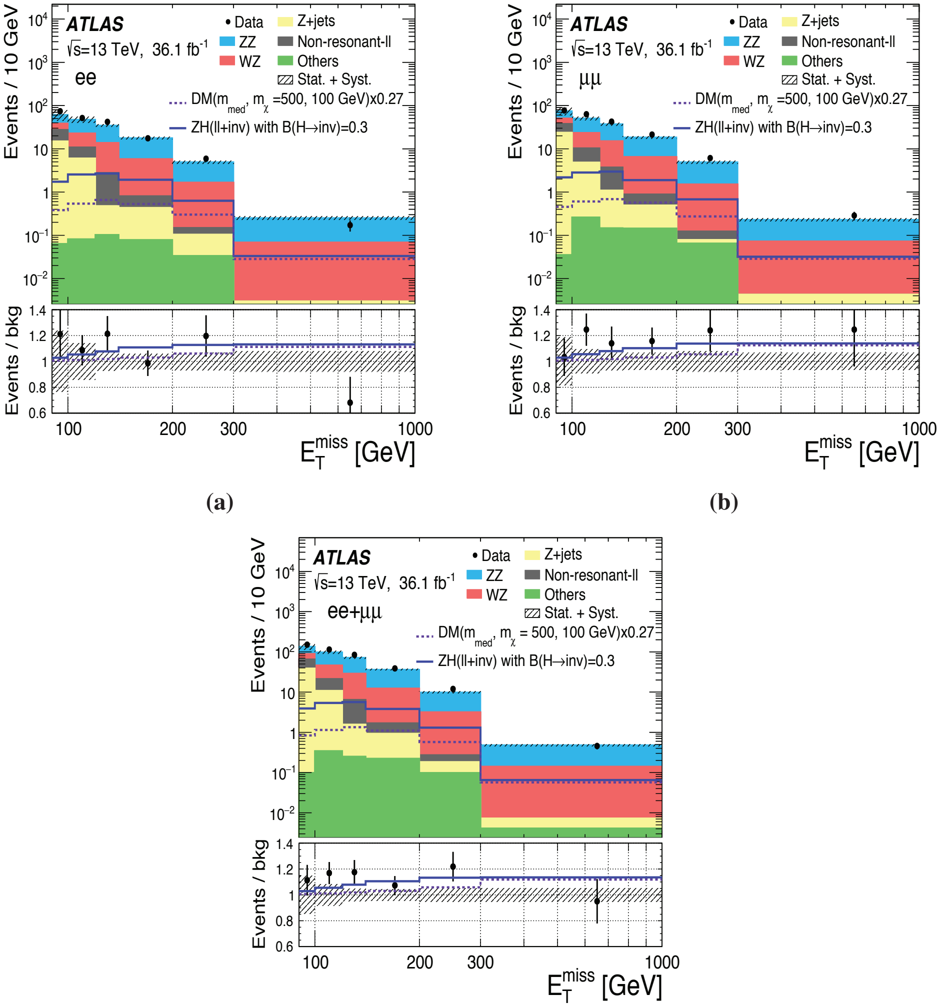

(a)

(b)

(c)

Fig. 4.17 · Observed E_T^{miss} distribution in the ee (a), $\mu\mu$ (b) and combined $ee + \mu\mu$ (c) channel compared to the signal and background predictions. The error band shows the total statistical and systematic uncertainty on the background prediction. The ratio plot gives the observed data yield over the background prediction (black points) as well as the signal-plus-background contribution divided by the background prediction (blue line) in each E_T^{miss} bin. The rightmost bin contains the overflow contributions. The ZH signal distribution is shown with $\mathrm{BR}(H \to inv.) = 0.3$, which is the value most compatible with data. The plots have been published in the articles [1, 164].

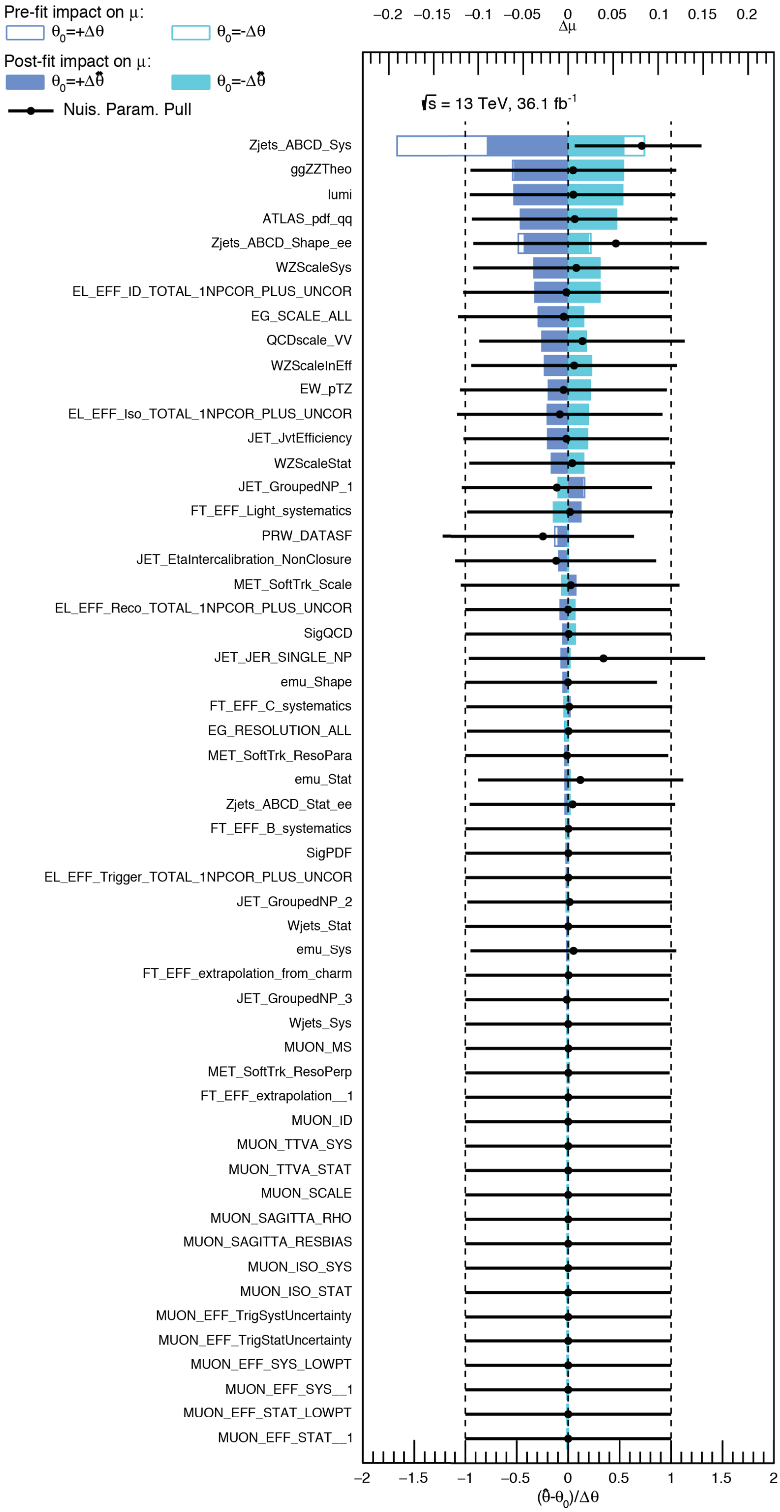

Fig. 4.18 · The nuisance parameter pulls and ranking when fitting signal+background model to data for the ee channel. Here, μ corresponds to the parameter of interest, $\mathrm{BR}(H \to inv.)$.

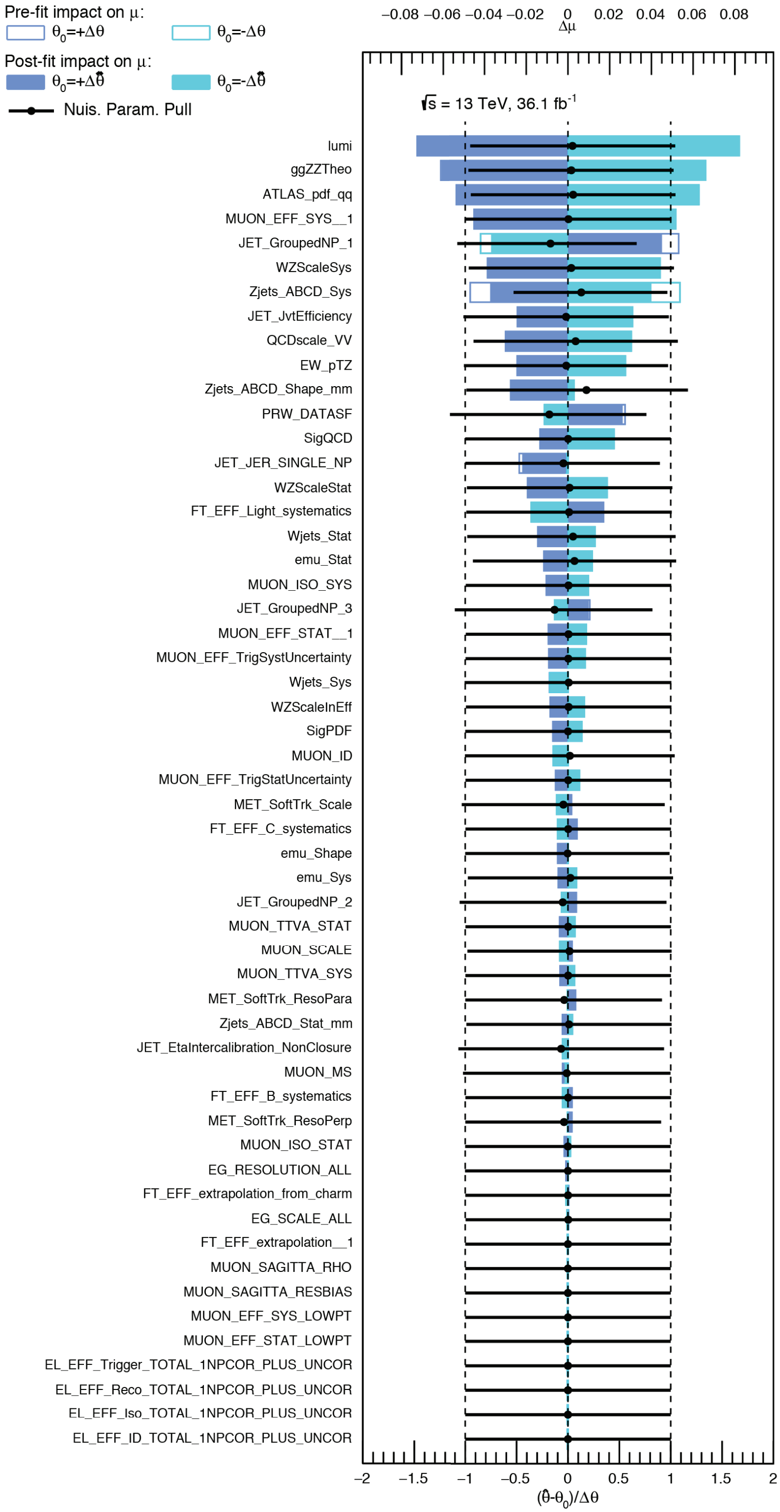

Fig. 4.19 · The nuisance parameter pulls and ranking when fitting signal+background model to data for the μμ channel. Here, μ corresponds to the parameter of interest, $\mathrm{BR}(H \rightarrow \mathrm{inv}.)$.

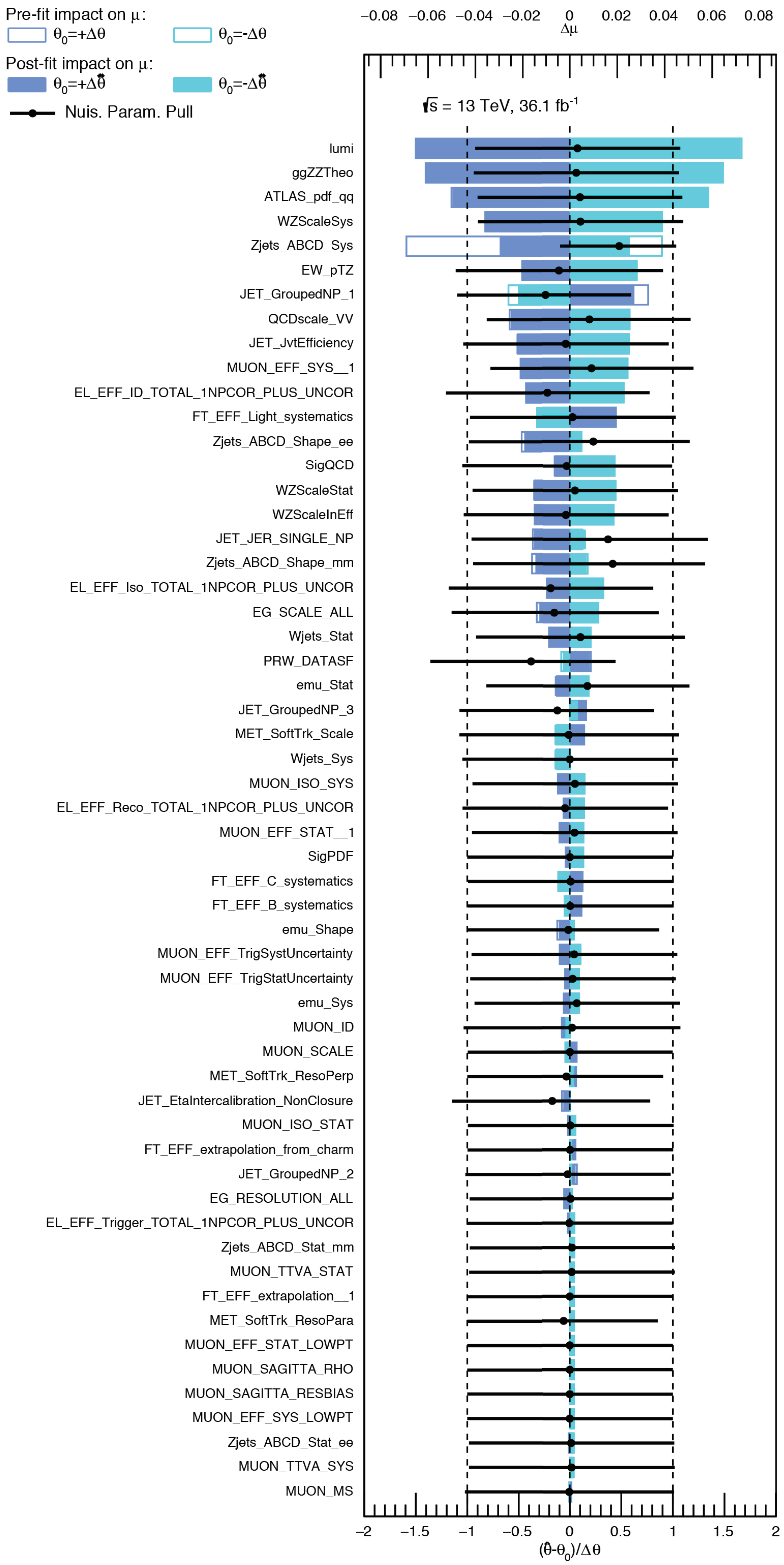

Fig. 4.20 · The nuisance parameter pulls and ranking when fitting signal+background model to data for the $ee + \mu\mu$ channel. Here, μ corresponds to the parameter of interest, $\mathrm{BR}(H \to \mathrm{inv.})$.

4.8.2 Limits

The presence of an excess in the observed data for the $\mu\mu$ channel results in a p-value equal to 0.014, which corresponds to a significance of 2.2σ. Combining this result with the electron channel, the final p-value is equal to 0.06, corresponding to 1.5σ. The result of the discovery test does not reject a background-only hypothesis, an exclusion limit test is therefore performed. Table 4.23 and Figure 4.21 show the 95% CL upper limits on $BR(H \to inv.)$, using for the ZH process the SM cross-section prediction. Given the presence of a small excess in the data in the muon channel the observed limits are less tight than the expected ones. The observed and expected limits on the $BR(H \to inv.)$ for the combined leptonic channels are 67% and 39%. The observed (expected) limit on the cross section for the ZH[1] process is 40 (23) fb at the 95% CL. A signal-plus-background model is fit to the data and the best value for the $BR(H \to inv.)$ is $(30 \pm 20)\%$. The major sources of the systematic uncertainty for this analysis are the theoretical uncertainties on the $qq \to ZZ$ and $gg \to ZZ$ predictions, the luminosity uncertainty, the uncertainties in the data-driven estimation of the WZ and Z+jets backgrounds, and the jet energy scale and resolution uncertainties.

	Obs. $BR(H \to inv.)$ Limit	Exp. $BR(H \to inv.)$ Limit $\pm 1\sigma \pm 2\sigma$
ee	59%	$(51\ ^{+21}_{-15}\ ^{+49}_{-24})$ %
$\mu\mu$	97%	$(48\ ^{+20}_{-14}\ ^{+46}_{-22})$ %
$ee + \mu\mu$	67%	$(39\ ^{+17}_{-11}\ ^{+38}_{-18})$ %

Table 4.23 · The 95% CL upper limits on $BR(H \to inv.)$ for $m_H = 125$ GeV from the ee, $\mu\mu$, and combined $ee + \mu\mu$ channels. Both the observed and expected limits are given, and the 1σ and 2σ uncertainties on the expected limits are also presented.

4.9 Conclusion

This chapter describes in details the search for an invisible decay of the Higgs boson in associated production with a Z boson decaying into a pair of muon or electrons. The results of this analysis show a small excess in the muonic channel. The magnitude of such excess is not sufficient to reject a background only hypothesis, but at the same time worsens the observed limits on the $BR(H \to inv.)$. The final exclusion limits are reported in Table 4.23. The next chapter will describe a multi variate approach to the analysis.

---

[1] Only the electronic and muonic decay of the Z boson are taken into account

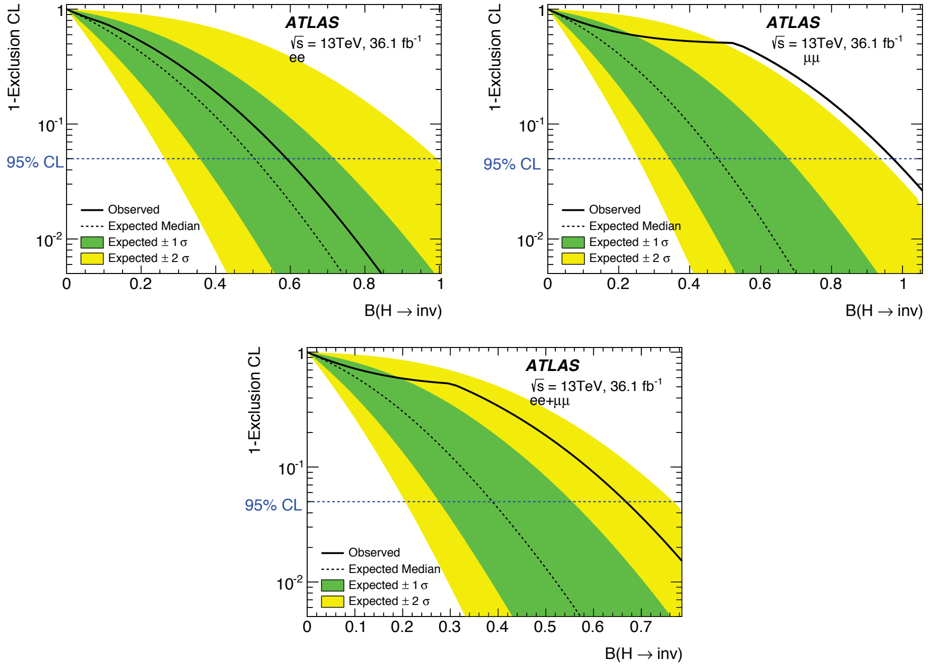

Fig. 4.21 · Scan of "1− Exclusion CL" as a function of $\mathrm{BR}(H \to inv.)$ with $m_H = 125$ GeV using the ee (top left), $\mu\mu$ (top right), and combined $ee{+}\mu\mu$ (bottom) channels. The observed and expected curves are shown in solid and dashed black lines, respectively. The $\pm1\sigma$ ($\pm2\sigma$) error band on the expectation is shown in green (yellow). The crossing point between the dashed blue line and the scan curve gives the observed (expected) upper limit on $\mathrm{BR}(H \to inv.)$ at the 95% CL. The "turning points" in the observed scan curves correspond to the best-fit $\mathrm{BR}(H \to inv.)$ values. The plots have been published in the article [164].

chapter five

Multi variate analysis

This chapter will describe a new approach to the ZH analysis based on the usage of a multivariate technique, specifically a Boosted Decision Tree (BDT) [178]. The aim of this study is to probe the performance of a multivariate analysis for the ZH final signature and to possibly obtain more stringent limits.

5.1 Why a multi-variate analysis

In the last decade, the role of multivariate algorithms has become more and more important in many spheres of human life. Many companies like Google, Facebook or Booking.com introduced multi-variate techniques to analyze the big amount of data in their possession. Also in particle physics, in the latest years, the usage of multi-variate techniques has increased drastically especially in experiments that collect a huge amount of data, as the ones at CERN. This is due to the strong discrimination power a multivariate approach can provide by exploiting non obvious correlation among variables optimizing the signal-background separation. The chosen method for this analysis, the BDT, will be explained in detail in the next section.

5.2 Boosted Decision Tree: a discriminating story

A BDT is a binary sequential splitting algorithm that can be used for the classification of events. Applying a sequence of *pass or fail* cuts will discriminate the events and classify them in two categories, which can be labeled as *Signal* or *Background*. Each time a selection is applied the sample is divided into two parts. In the following step, two different selections will be applied to the sub-samples. This operation can be iterated several times as long as the statistics allow it. This will lead to the formation of a decision tree: the number of iterations, which defines the number of layers of the Tree, is called *Depth*. Each component of the Tree where a selection is applied is called *Node* and the final sub-samples are called *Leaves*. The final result will be a tree with several leaves, each containing a number of events which will be classified as *Signal* or *Background*. A decision tree is therefore a method which uses in each node the most discriminating variable to separate a sample by minimizing the overlap among background and signal events. The scheme of a decision tree is shown in Figure 5.1. Using a decision tree is not very different from applying a series of cuts (cut-based approach): the major difference stands in the boost which is part of the *training* process. Those key elements will be discussed in the next section.

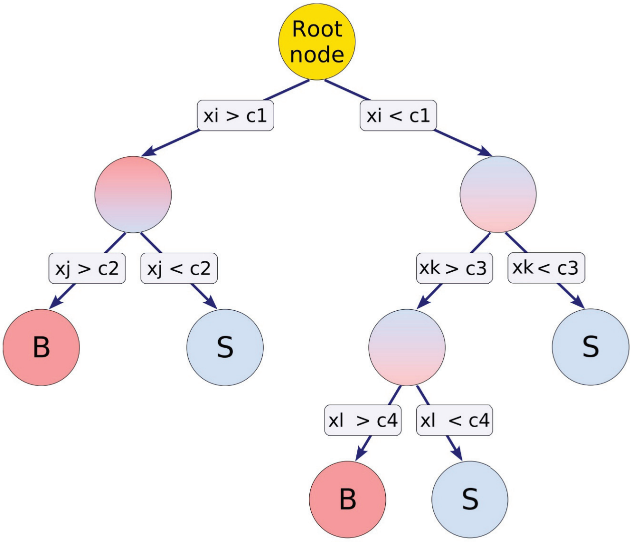

Fig. 5.1 · A scheme of a Decision Tree. Different cuts $c_{1,..,n}$, on different variables $x_{i,..,n}$, can be applied on each node independently. **S** and **B** represent the signal and background leaves. The picture is adapted from [179].

5.2.1 BDT algorithm: training and boost

The BDT training is a process where the algorithm optimizes itself by using the information from a simulated sample of known characteristics, after a number of *trial and error* iterations. At the end of the first classification process for a specified sample, be it signal or background, there will be leaves which will be labeled as signal and other as background. In a perfect scenario with a perfect discriminator, if using as input a background sample, all the events should fill the background leaves, leaving signal ones empty. The real scenario is indeed different and several background events will be labeled as signal. In order to minimize such misclassified events, a boost is applied. There are several boosting techniques: the one used in this analysis is called *Gradient Boost*. The description of the technical aspect of the boosting procedure falls outside the scope of this manuscript: more details can be found in [180]. Once the boost is applied, the algorithm generates another tree. Once the classification is over, the new misclassified events are boosted again and a new tree is generated. This procedure goes on, producing hundreds of trees (a forest) until the algorithm stabilizes itself and the training is over. A crucial parameter for the training is, therefore, the number of trees. A poor choice of parameters could lead to *over-training* where the algorithm learning curve is biased by statistical fluctuations. In other words, in presence of over-training, the BDT focuses on events in corners of the phase-space, discriminating them, not due to real topological differences but mostly driven by statistical fluctuations. To link the BDT to known methods, one can see the BDT algorithm as an n-dimensional cut-based analysis, corrected at each step by using the boost. Each tree applies a multi-rectangular cut to a specific phase-space. The BDT, by averaging hundreds of rectangular shape phase-space selection, has, as a result, a curved cut on the phase-space which better discriminates the signal from the background. This is especially true when the input parameters of the BDT have a non linear correlation. A sketch describing this scenario is shown in Figure 5.2. The figure shows two variables which have a circular correlation. By applying a cut-based approach the discrimination is not optimal because a simple series of cuts cannot exploit the circular correlation. By using a BDT, the algorithm can apply a better performing cut.

Once the training is completed, the performance is tested. In order to do so, the initial sample is divided into two parts: one is used for the training, the other for testing. The output of the training is a variable which is obtained by averaging the different classification results in each tree. Such variable, distributed among -1 and +1, is called *BDT score*. Each event of the sample has a corresponding BDT score value. By construction, the algorithm assigns positive values, on average, to signal-like events, and negative ones for the background-like events. If the BDT output produced by the test sample is statistically compatible with the one provided by the training the method is consistent. A statistical test, the χ^2, is applied to the two BDT score distributions to check their compatibility, as it will be described in section 5.3.1. Another method applied in this analysis to check the consistency of the algorithm is the cross-validation technique described below.

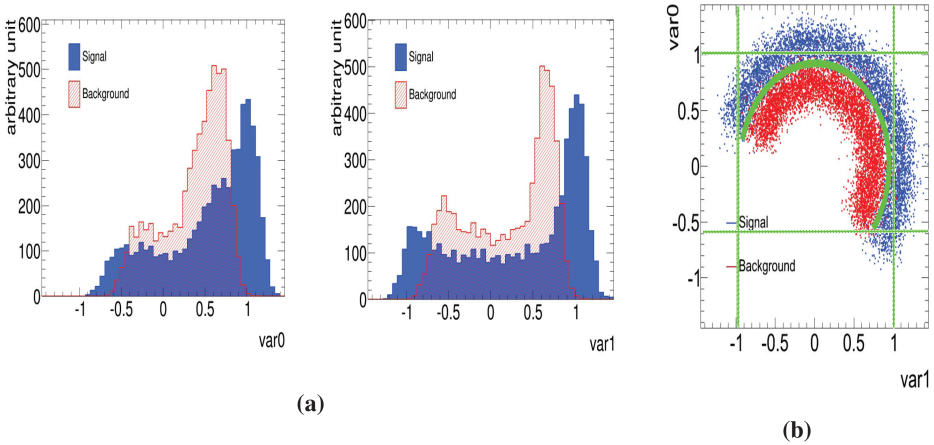

(a)

(b)

Fig. 5.2 · Distribution (a) and scatter plot (b) of two variables with circular correlation for signal (blue) and background (red). A cut-based selection is shown by the orthogonal green lines in the right plot. The selected area is sub-optimal due to the nature of the correlation between the two variables. It is visible that the discriminating power of the BDT (circular green line) is out-performing the cut-based approach (straight lines). The picture is adapted from [179].

Cross validation

The cross-validation [181–183] is a method to estimate the performance of a predictive algorithm by dividing the sample into different sub-samples and training and testing it multiple times. The procedure consists of splitting a sample in K sub-samples and perform the training on K-1 sub-samples and to test it over the one remaining, repeating the procedure K-1 times. The final BDT output will then be the average of all the different BDT outputs in each sub-sample. The cross-validation was performed by choosing K = 2 due to limited statistics. The sample was split into two equal parts and each part has been used for training and testing. The two halves were defined by applying a common pre-selection, and by using a random distribution to populate them equally. The BDT score is evaluated in the following way: the first sample is called sample A and the second sample B. In the first iteration, the training sample is A and the test sample is B. The BDT score trained on sample A, BDT_score_A, will be tested with the events from the sample B. The same procedure will be applied by choosing the sample B as the training one. The final BDT_output will be then the linear combination of the two BDT scores. This method adds a degree of complexity to the execution of the analysis but it is a good way to check for the stability of the method and it increases the statistic available for the training (it actually doubles it, compared to using just half of the initial sample).

5.3 BDT analysis strategy

This section will describe the BDT analysis strategy and its implementation. The chosen strategy consists of the following steps:

1. BDT optimization: the aim is to obtain optimal performances and reliability by tuning properly the BDT.
2. Backgrounds treatment: the scale-factors and corrections obtained with the data-driven methods in the cut-based analysis are applied to the backgrounds used in the BDT analysis. In order to do so, a signal region topologically similar to the one used in the cut-based analysis is chosen.
3. Limit: the BDT score has been chosen to be the discriminant variable for the limit fit.

In the following sections, each of these points will be described in detail.

5.3.1 BDT optimization

This section will present the studies performed on the optimization and validation of the BDT. The key elements used for the optimization are:

1. Pre-selection cuts
2. BDT input variables
3. BDT setup tuning
4. Performance and stability checks

Pre-selection cuts

The BDT algorithm learns and exploits the correlations among the variables during the training. For this reason, the more information a BDT has, the better the final discrimination will be. So the first approach would be to loosen the cuts applied by the cut-based analysis and let the BDT gather information over a bigger phase-space. This method is indeed reasonable but only if it respects two key elements:

- The number of background events should not increase drastically compared to the signal ones.
- The background relative composition after loosening the cuts should be similar to the cut-based one [1].

Increasing the phase-space by removing or loosening a cut, i.e. the b-jet veto, that eliminates a huge amount of background events and slightly removes signal events is sub-optimal. The BDT algorithm will focus mostly on events which are topologically very different from the signal and it will have a great discrimination power (on those) but the final result will be the same if not worse than the cut-based one. This is true especially for this analysis where irreducible backgrounds are the major ones [2]. The best option is to find a compromise between increasing the phase-space and keeping tight cuts on variables which remove topologically different background events. This approach helps also keeping the final composition of the background closer to the one obtained in the cut-based analysis, leading to two major advantages: the BDT can focus its discriminating power on signal-like background events, the most complex to remove in a cut-based analysis; at the same time by having a similar final phase-space composition, the results obtained in the cut-based analysis from the data-driven estimation of the backgrounds can be applied to the BDT analysis. In order to define an optimal phase-space to fulfill both requirements, different cut configurations have been studied checking the relative background composition and the significance σ for the newly defined phase-space. The significance has been defined as the ratio between the number of signal events divided by the square root of the sum of signal and background events as shown in equation 5.1.

$$\sigma = \frac{S_{evts}}{\sqrt{S_{evts} + B_{evts}}} \tag{5.1}$$

Table 5.1 shows the chosen BDT event selection, while Table 5.2 shows the background relative composition for the new phase-space and the new significance. Table 5.2 shows how the significance in the new phase-space is similar to the cut-based one and how the composition of each background is compatible to the one in the cut-based analysis, providing a larger phase space to the BDT to investigate the difference between signal and background without losing performance. Once the phase-space has been defined, the input variables are the second element to look at for the BDT setup.

Input variables

The selection of input variables is an important step for a BDT optimization because the variables are the input parameter set based on which the algorithm discriminates and classifies the samples. The first choice for a set of variables is the one used in the cut-based analysis. Others variables were added to check if they provided an increment in the discriminating power. Figure 5.3 shows the selected input variables for signal and background. In

---

[1] This allows to apply on the BDT estimates the data driven results obtained by the cut-based analysis

[2] ZZ accounts for more than the 50% of the total background

BDT Event Selection
Two same flavour opposite-sign leptons (e^+e^- OR $\mu^+\mu^-$)
Veto of any additional lepton with Loose ID and $p_T > 7$ GeV
$76 < M_{\ell\ell} < 106$ GeV
$E_T^{miss} > 90$ GeV
$\Delta R_{\ell\ell} < (1.8) \rightarrow 2.0$
$\Delta\phi(Z, E_T^{miss}) > (2.7) \rightarrow 2.0$
Fractional p_T difference $< (0.2) \rightarrow 0.3$
$E_T^{miss}/H_T > 0.6$
b-jet Veto

Table 5.1 · List of cuts applied at the event selection level for the $\ell^+\ell^-$+E_T^{miss}BDT analysis. In parenthesis the cut-based selections which have been modified in the multi-variate analysis.

	Background relative composition (%)			
Sample	BDT		Cut Based	
	ee	$\mu\mu$	ee	$\mu\mu$
ZZ	50	51	57	58
WZ	26	25	27	27
$e\mu$	14	13	8	8
Z+jets	10	11	9	7

	Number of events			
Sample	BDT		Cut Based	
Total	557 ± 22	571 ± 19	399 ± 9	426 ± 9
Signal	132 ± 3	124 ± 2	108 ± 2	114 ± 2
Significance	5.0 ± 0.1	4.8 ± 0.1	4.8 ± 0.1	4.9 ± 0.1

Table 5.2 · Background relative composition and significance after the BDT and the Cut Based selection. In the table the $e\mu$ background refers to the sample which are evaluated using the flavor symmetry method control region such as: $t\bar{t}$, WW, $Z \to \tau\tau$.

the figure, the distribution of signal and background are normalized to the same number to show the shape difference between signal and background. It might be tempting to use as many variables as possible, so the BDT can have all the possible information to discriminate the samples. This is actually a sub-optimal scenario[1]: the algorithm selects automatically a sub-sample of variables which are the most discriminant ones. So the strategy is to keep the number of variables to a minimum and keeping at the same time the one with the highest discrimination power. In order to do so, several BDTs were trained with different variables, starting from a configuration with all the variables included and then removing them one by one starting from the least discriminant following the ranking[2] provided by the algorithm output. In order to check the performances, the receiver operating characteristic (ROC) [184] curve[3] was evaluated for each variable setup. The ROC curve provides a good estimate of the discriminating power for a specific selection and it is defined as the signal efficiency versus the background rejection rate. The ROC curve is a tool to estimate the discrimination power of a specific analysis and provides an easy way to compare to a different analysis. The bigger the area underneath the ROC curve, the higher the discrimination power of a specific analysis. Figure 5.4 shows the ROC curve for all the different variable configurations. The cut-based analysis is also shown on the plot as a reference and gives a

---

[1] By implementing all the variables the algorithm is not stable and it does not converge making the output not reliable.

[2] The ranking is a list of variables ordered from the most discriminating to the least discriminating. The algorithm evaluates it by checking how much time a variable is used in a node and at which depth of the tree. The variables that are used in the biggest node and in the majority of the trees are the most discriminating and higher in rank.

[3] The ROC curve shows the discriminating power of an algorithm over a binary system (signal and background) by varying the threshold settings.

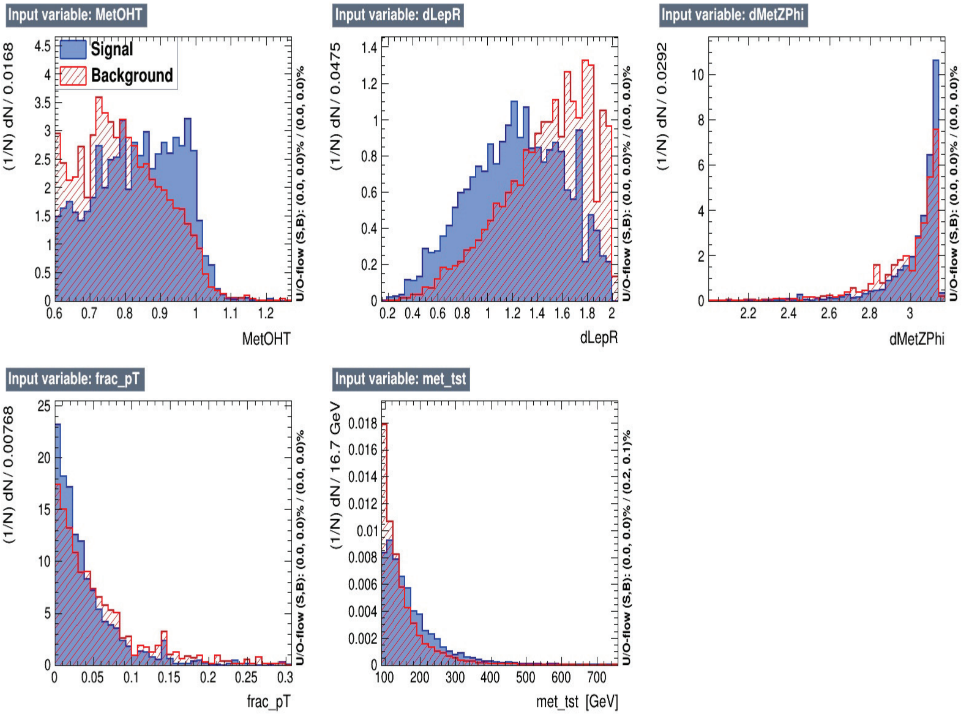

Fig. 5.3 · Shape comparison for the BDT algorithm input variables for signal (blue) and background (red). From top left to bottom right: E_T^{miss}/H_T, $\Delta R_{\ell\ell}$, $\Delta\phi(Z, E_T^{miss})$, Fractional p_T difference, E_T^{miss}. The signal and background distributions are normalized to the same number.

first hint on how much the BDT can outperform the cut-based analysis. Figure 5.4 shows that removing low ranking variables does not reduce the performance of the BDT, therefore the configuration with the minimum amount of input variables has been chosen. The final list of chosen variables[1] and their ranking is reported in Table 5.3. The final step to optimize a BDT analysis is tuning its internal parameters.

Rank	Variable
1	$\Delta R_{\ell\ell}$
2	E_T^{miss}
3	$\Delta\phi(Z, E_T^{miss})$
4	E_T^{miss}/H_T
5	Fractional p_T difference

Table 5.3 · Variable ranking.

BDT setup tuning, performance and stability checks

The BDT algorithm has different options which can be customized to address different scenarios. This section will provide a brief description of the different options of a BDT, their role, their impact and how they were optimized.
BDT options can be divided into three categories:

1. Forest definition: number of trees, depth, minimum node size
2. Boost: type of boost chosen, boost impact (shrinkage)
3. Shape and weight treatment

The number of trees and the depth have been described previously in this chapter. If different configurations provide similar performances, it is preferable to keep the number of trees and depth as low as possible in order to minimize computing time and to minimize over-training[2] risk. The minimum node size is related to the minimum amount of events that each node has to contain. It can be customized to have enough statistic in each node, providing a statistical consistent discrimination.
The type of boost chosen is the Gradient Boost and it was chosen over the Adaptive Boost for two reasons: better discriminating power and robustness against classifying background containing events with negative weights [180]. Figure 5.5 shows the ROC curve for the Gradient Boost and the Adaptive Boost. The figure suggests that the Gradient Boost is more discriminating compared to the Adaptive Boost method. The Gradient Boost allows to use the shrinkage option: this option modifies the boosting by reducing its impact by a fixed factor at each step of the training. This option increases the stability of the method because a smaller shrinkage will provide a milder boost at each step avoiding abrupt changes in

---

[1] The initial set of variables used is shown in Table A.12 in the appendix.

[2] Over-training is defined as a specific training process where the output and the boosting is dominated by statistical fluctuation in a corner of the phase-space rather than the actual features of the signal and background distributions

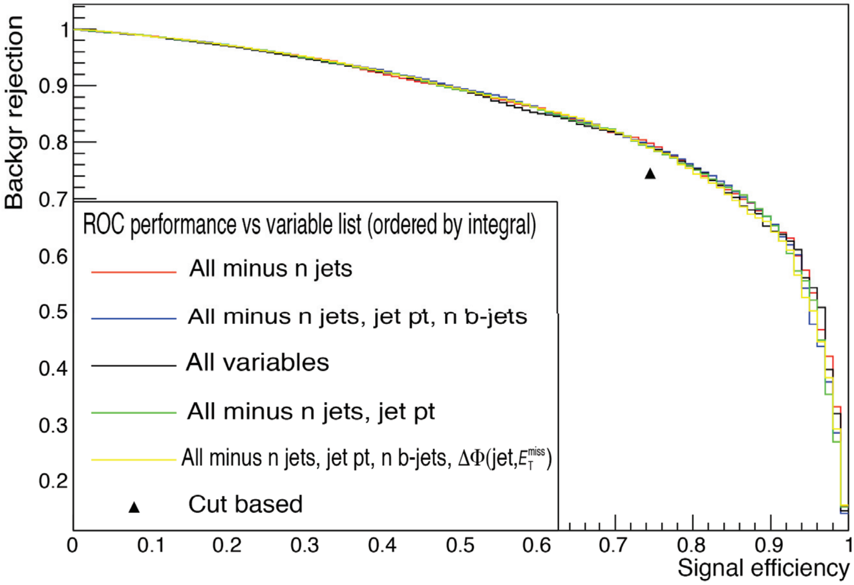

Fig. 5.4 · ROC curves for different input variable setup. Removing variables from the BDT does not modify its performances as clearly visible in the figure. The legend shows the different results ordered by the value of the ROC integral, including the cut-based (black triangle). In order to evaluate the cut-based ROC point, the background rejection vs the signal efficiency was calculated after the BDT pre-selection.

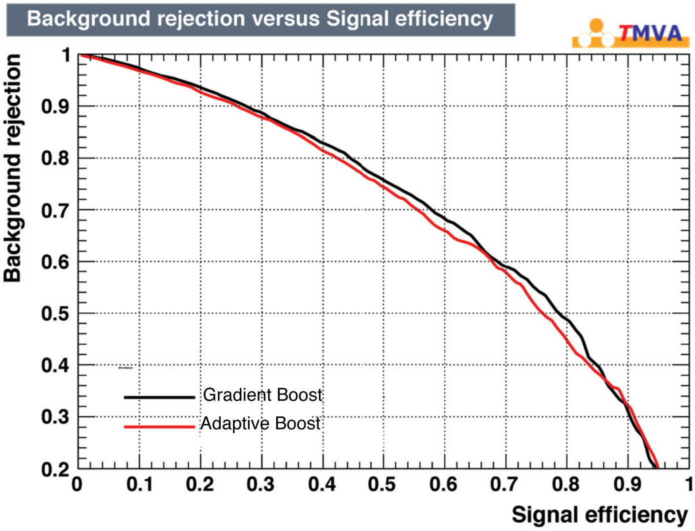

Fig. 5.5 · ROC curve for the Adaptive Boost (red) and the Gradient Boost (black). The BDT Gradient Boost shows a better discrimination power.

the training process that could be caused by a small fraction of events with anomalous phase-space and very high weights. One of the final goals when selecting a BDT setup is to obtain a BDT_score shape without strange features but homogeneous instead. In order to obtain a stable shape, the Bagging option was used. This option allows the BDT to train over a different fraction of the sample each time, providing as final BDT_score the average of all the iterations. The treatment of the weights of the events is crucial especially due to the characteristic of the background samples used. The samples used in the analysis have a considerable amount of events with negative weights and at the same time, some samples contain events with very high weight (order of tens). The issue arises from how the MC generation itself is performed: the Z+jets Sherpa MC generator for example makes use of negative weights in the event simulation. Those weights are therefore not negligible and they are not linked with the BDT training procedure. These two features are both a disadvantage for a BDT analysis where the weight treatment inside the algorithm is capital for the design of each tree and for the shape of the final BDT_score. The algorithm offers the choice to ignore negative weights in the training or to use them. Given the fact that the events with negative weights come from the generator itself and were introduced to better describe the topology of the sample, the selected option was to keep all the events (including the ones with negative weights) in the training and removing only the ones with extremely high event weight (over 100). A summary of the selected setup for the BDT algorithm is shown in Table 5.4.

Stability checks

The final step in the optimization of a BDT analysis relies on finding the configuration which provides the best performance and stability. Once the major parameters of the BDT

Parameter	Selection
Boost	Gradient
Number of trees	300
Depth	3
Minimum Node Size	5%
Shrinkage	0.2

Table 5.4 · Summary of the chosen BDT setup.

are optimized (boost type, forest definition, weight treatment) varying one parameter does not affect the performance significantly, therefore the stability of the BDT becomes the final criteria. There are two major checks to fulfill:

1. Over-training check
2. Cross validation check

The over-training check assures that the algorithm is not training itself over statistical fluctuations. To probe the goodness of each BDT_score a χ^2 test has been implemented between the BDT_score test distribution and the BDT_score training distribution for both signal and background, as shown in Figure 5.6. As already mentioned, the shape of the BDT_score

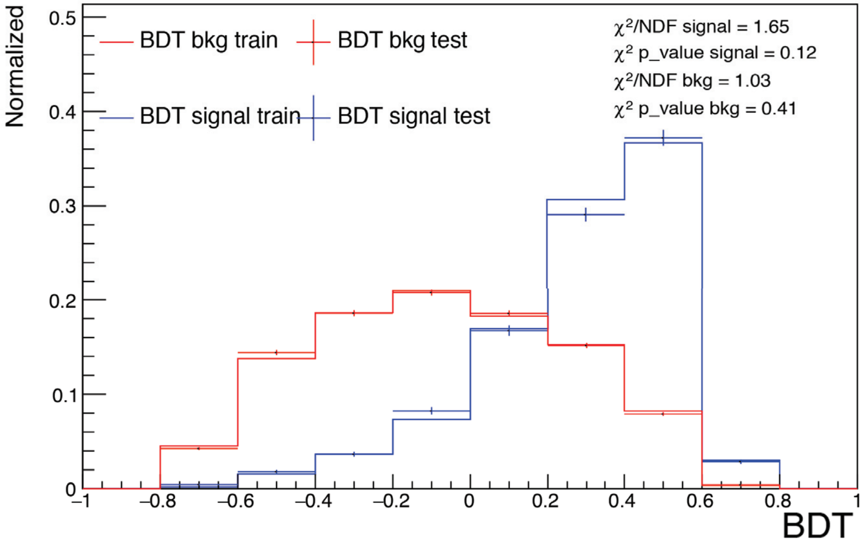

Fig. 5.6 · BDT score for signal (blue) and background (red) for train (solid line) and test (dots). The distributions show a good agreement, with no sign of over-training.

has to be smooth and without strange features. Configurations with accumulation of events in one specific bin or with several bumps were excluded.
The last check is the cross-validation one: the BDT_score_A (output of the training over the sub-sample A) has to be statistically compatible with the BDT_score_B (output of the training over the sub-sample B). Figure 5.7 shows the BDT_score stack distribution for both electron and muon channel with all contributions from the major backgrounds for sample A and sample B. It is noticeable how the two distributions, BDT_score_A and BDT_score_B show different features. The source of the difference has been investigated and is related to differences in the event weight distribution between the two sub-samples due to limited statistic after splitting the MC for specific backgrounds as $\mathrm{Z+jets}$ and $\mathrm{e\mu}$. This conclusion has been made by analyzing the following aspects:

- The distribution of the ratio of sample A vs sample B for each variable (input, BDT_score, and weight) for each background.
- The comparison between sample A and B of the total amount of (weighted) events.

Figure 5.8 and Figure 5.9 show the comparison for each input variable of the BDT between sample A and B for the dominant background ZZ for the electron and muon channel. The figures show a good agreement for all the variables. The source of the difference comes from the $\mathrm{Z+jets}$, specifically from the event weight distribution as shown in Figures 5.10. The event weight distributions, suffering from lack of statistics, are not compatible. This scenario suggests that the problem lies in a different distribution of the weights in the two sub-samples which has an effect on the BDT_score shape. To confirm this hypothesis the number of events and the number of weighted events for both sub-samples for both electron and muon channel were studied. The results are shown in Table 5.5 for the muon channel and Table 5.6 for the electron channel. Even if the majority of the backgrounds have a compatible number of events among the two sub-samples (5% difference) it is visible how fluctuations due to low statistics lead to difference of 20% or higher (80%) for some samples such as the $\mathrm{Z+jets}$, as already shown in the event weight ratio distribution. Even if the number of events would be the same, there is no way to control that the sum of the weighted events is the same, and as it is visible from the table, it is not. This issue affects mostly sub-dominant background such as $\mathrm{Z+jets}$ and $\mathrm{e\mu}$ with low statistics, but still produces differences between the two total BDT_score distributions as shown in Figure 5.11. These differences have been taken into account as a source of systematic uncertainty.

5.3.2 Background estimation

The background estimation for the BDT analysis is based on the cut based results. The estimation of the yields is evaluated in the following way:

- WZ background: the scale factor obtained from the cut based analysis is applied to the MC simulation in the BDT analysis.
- $\mathrm{e\mu}$ and $\mathrm{Z+jets}$ backgrounds: an *ad hoc* scale factor, obtained from the ratio among the data-driven and MC yields in the cut based analysis, is applied to the MC simulation in the BDT analysis.

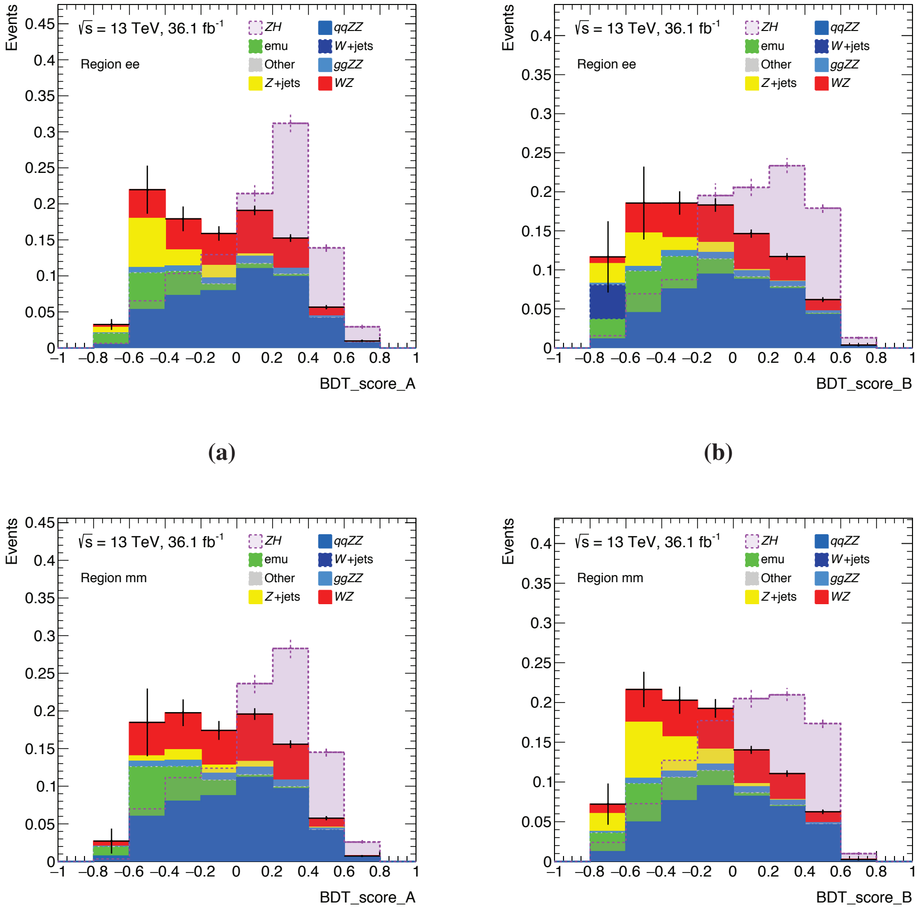

(a)

(b)

(c)

(d)

Fig. 5.7 · BDT score for the sample A (left) and the sample B (right) for the electron (top) and the muon (bottom) channel. Each distribution show the BDT score for each background and the signal. The distributions show different features, which have been studied in detail.

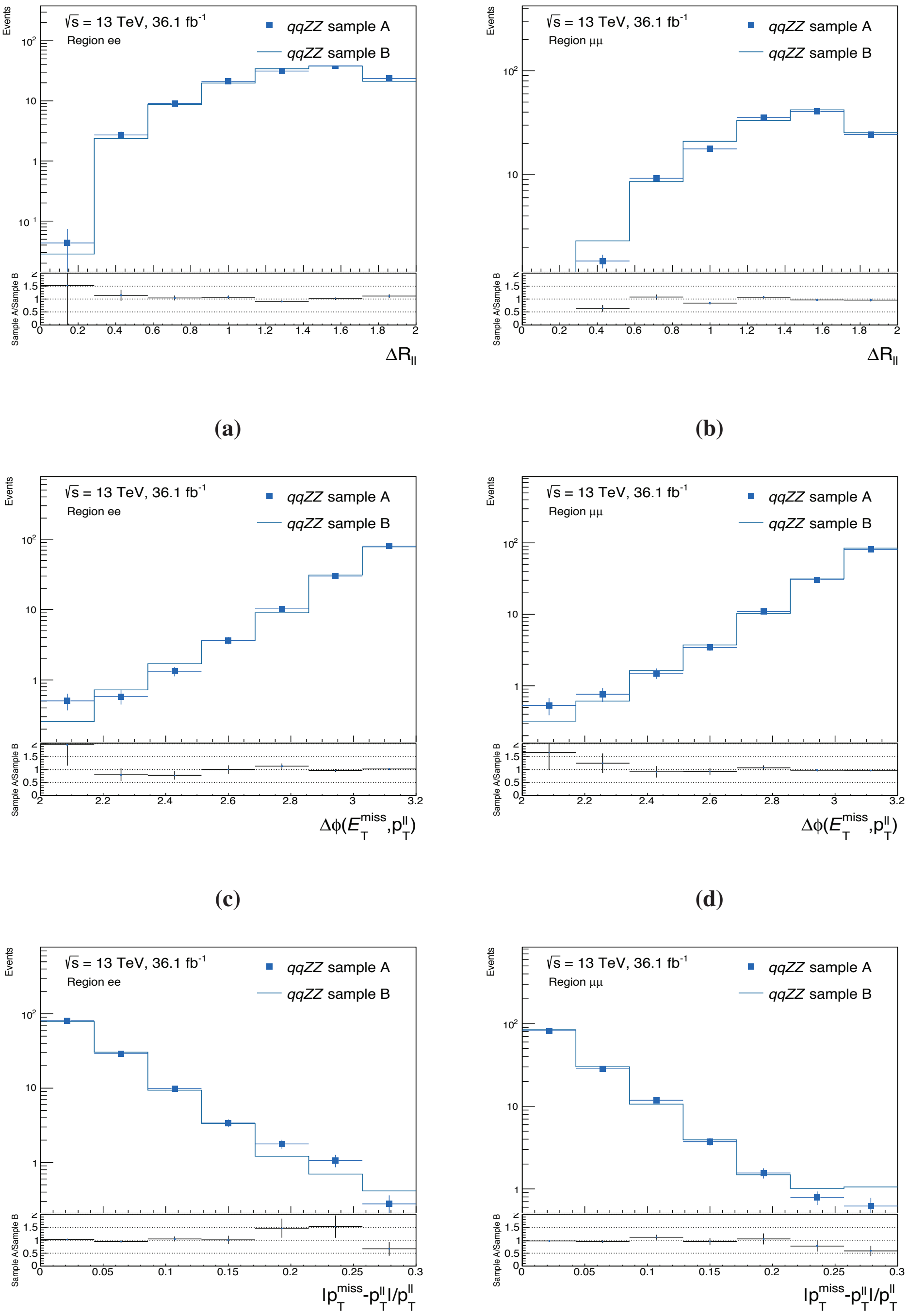

(a)

(b)

(c)

(d)

(e)

(f)

Fig. 5.8 · Kinematic distributions comparison of the BDT input variables for sample A (dots) and sample B (line) for ZZ background. The $\Delta R_{\ell\ell}$ distribution for the (a) ee channel and (b) $\mu\mu$ channel. The $\Delta\phi(Z, E_T^{miss})$ distribution for the (c) ee channel and (d) $\mu\mu$ channel. The fractional p_T difference distribution for the (e) ee channel and (f) $\mu\mu$ channel.

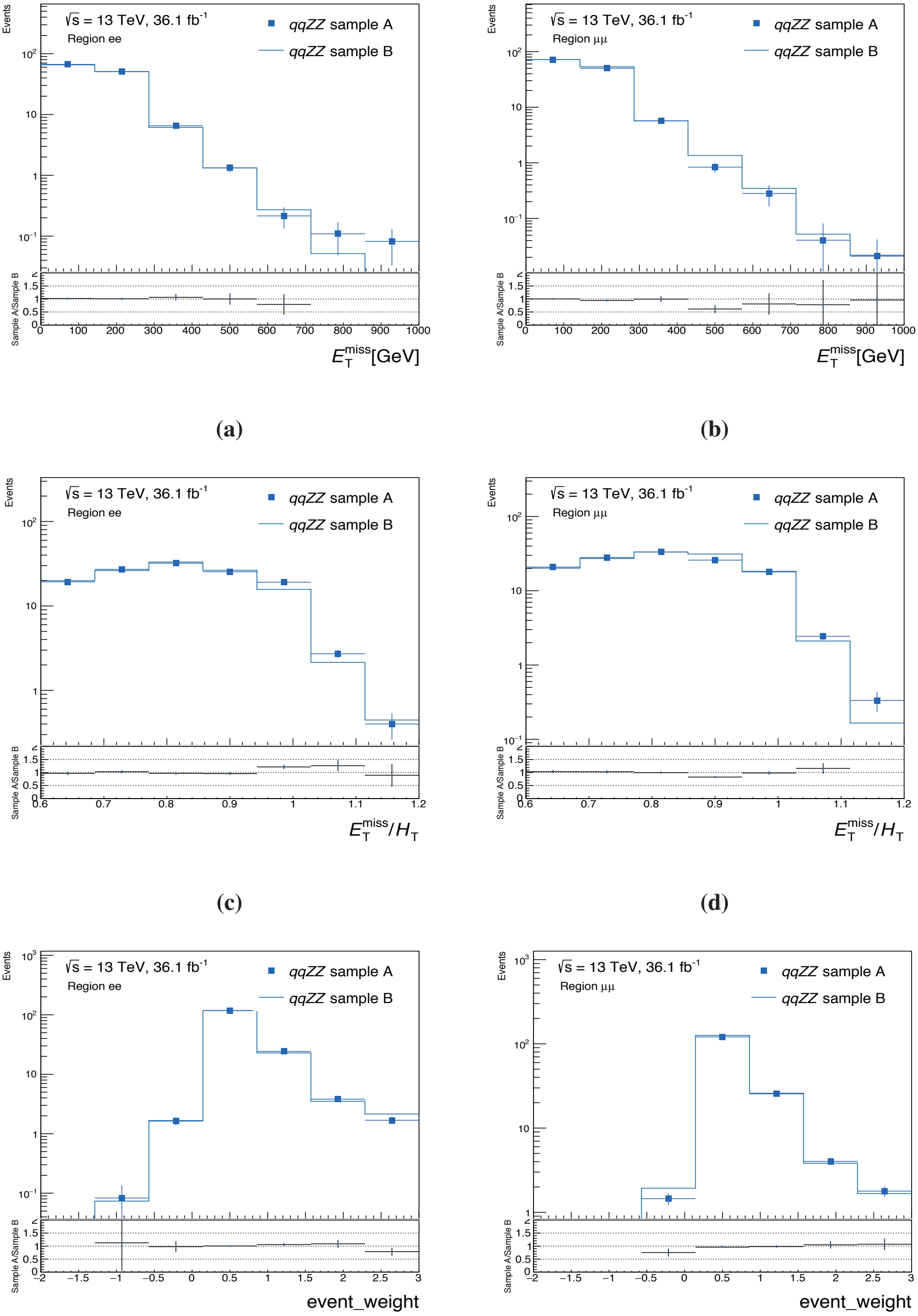

(a)

(b)

(c)

(d)

(e)

(f)

Fig. 5.9 · Kinematic distributions comparison of the BDT input variables for sample A (dots) and sample B (line) for the ZZ background. The E_T^{miss} distribution for the (a) *ee* channel and (b) μμ channel . The E_T^{miss}/H_T distribution for the (c) *ee* channel and (d) μμ channel. The event weight distribution for the (e) *ee* channel and (f) μμ channel.

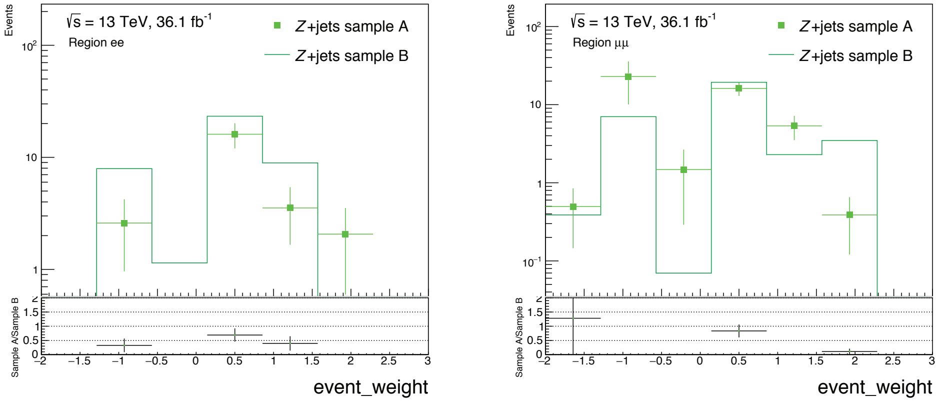

(a) **(b)**

Fig. 5.10 · Event weight distribution comparison of sample A (dots) and sample B (line) for the Z + jets background for the (a) ee channel and (b) $\mu\mu$ channel. For both ee and $\mu\mu$ channel, the two distributions are not statistically compatible.

Background	Events			Weighted events		
	Sample A	Sample B	Difference (%)	Sample A	Sample B	Difference (%)
$e\mu$ $\mu\mu$	180	182	1.1	39.2	38.1	-2.9
WZ $\mu\mu$	1813	1872	3.2	71.6	73.9	3.1
$gg \to ZZ$ $\mu\mu$	3201	3192	-0.3	12.5	12.4	-0.8
$qq \to ZZ$ $\mu\mu$	4390	4552	3.6	129	133	3.0
ZH $\mu\mu$	4727	4806	1.6	64.4	67.6	4.7
Z+jets $\mu\mu$	153	140	-9.3	10.5	49.0	78.6
Total	14464	14744	1.9	327.2	374	12.5

Table 5.5 · Comparison among sample A and sample B of total events and total weighted events for the muon channel.

Background	Events			Weighted events		
	Sample A	Sample B	Difference (%)	Sample A	Sample B	Difference (%)
$e\mu ee$	170	206	17.5	31.8	41.5	23.4
$WZ\ ee$	1691	1658	-2.0	67.7	66.9	-1.2
$gg \rightarrow ZZ\ ee$	3052	3076	0.8	12.2	11.8	-3.4
$qq \rightarrow ZZ\ ee$	4266	4201	-1.5	126	124	-1.6
$ZH\ ee$	4598	4552	-1.0	62.3	61.2	-1.8
Z+jets ee	124	125	0.8	31.8	28.2	-12.8
Total	13901	13818	-0.6	331.8	333.6	0.5

Table 5.6 · Comparison among sample A and sample B of total events and total weighted events for the electron channel.

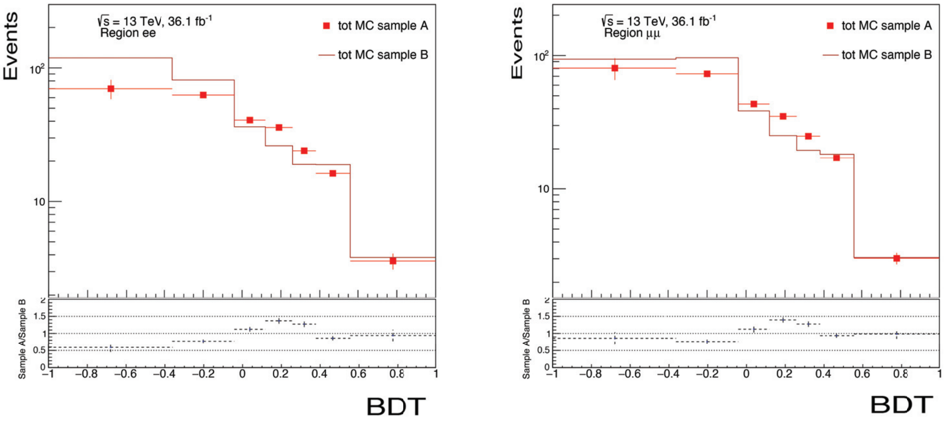

(a) **(b)**

Fig. 5.11 · BDT score distribution comparison of sample A (dots) and sample B (line) for the (a) ee and (b) $\mu\mu$ channel for the total background. The two distributions show different features, especially in the first, fourth and fifth bin for the ee channel and in the fourth and fifth bin for the $\mu\mu$ channel. The shape differences have been taken into account as systematic uncertainty.

The background shapes are evaluated by using the MC simulation. The estimation of the backgrounds used in the BDT analysis, compared to the cut based ones, is summarized in the Table 5.7:

Sample	BDT		Cut Based	
	Shape	Yield	Shape	Yield
ZZ	MC	MC	MC	MC
WZ	MC	Data	MC	Data
$e\mu$	MC	Data	Data	Data
Z+jets	MC	Data	Data	Data

Table 5.7 · Background evaluation method comparison for BDT and Cut Based analyses. The only difference among the two analyses is in the evaluation of the Z+jets and $e\mu$ shape, which is done via MC in the BDT analysis. In the table the $e\mu$ background refers to the sample which are evaluated using the flavor symmetry method control region such as: $t\bar{t}$, WW, $Z \to \tau\tau$.

5.4 Results

In this section, the results obtained with the BDT analysis will be described. At first, a comparison among the cut based and the BDT exclusion limit has been done, with the statistical uncertainties only. As a second step, the limit has been evaluated on both simulation and Data including the systematic uncertainties.

5.4.1 Limits: stats only

In order to obtain a proper comparison among the two methods, the expected limit without systematics has been evaluated for both the cut-based analysis and the BDT one. Table 5.8 show the 95% CL upper limits on $BR(H \to inv.)$ for the electron, muon and combined channel for the two different analyses. The expected limits on the $BR(H \to inv.)$ for the combined leptonic channels are 22% for the BDT and 24% for the cut-based showing an 8% relative improvement with the new method.

5.4.2 Systematics

The treatment of systematic uncertainties in the BDT analysis is the same as the one used in the cut based analysis. The only difference is related to the estimation of the $Z + jets$ background and the BDT score shape systematic.

$Z + jets$ shape systematic

The $Z+jets$ shape systematic is evaluated by reweighting the BDT output shape by a factor obtained by comparing the $Z + jets$ E_T^{miss} data-driven distribution to the MC in the cut based analysis. After verifying the presence of a correlation (30%) among the E_T^{miss} and the BDT output, the procedure applied is the following:

	Exp. $\mathrm{BR}(H \to inv.)$ Limit $\pm 1\sigma \pm 2\sigma$	
	BDT	Cut-based
ee	$(31\,^{+13}_{-9}\,^{+29}_{-15})\%$	$(35\,^{+14}_{-10}\,^{+32}_{-16})\%$
$\mu\mu$	$(31\,^{+12}_{-8}\,^{+28}_{-14})\%$	$(33\,^{+14}_{-10}\,^{+31}_{-16})\%$
$ee + \mu\mu$	$(22\,^{+9}_{-6}\,^{+20}_{-10})\%$	$(24\,^{+10}_{-7}\,^{+22}_{-11})\%$

Table 5.8 · The 95% CL upper limits on $\mathrm{BR}(H \to inv.)$ for $m_H = 125$ GeV from the ee, $\mu\mu$, and combined $ee + \mu\mu$ channels. The expected limits are given including the statistical uncertainty only, and the 1σ and 2σ uncertainties are also presented.

1. A ratio distribution among the data-driven shape and the MC shape is evaluated in bins of E_T^{miss} using the cut-based analysis results.
2. A fit is performed on the ratio distribution and the final weight is the fit function evaluated in the middle of each E_T^{miss} bin.
3. The BDT score is evaluated by reweighting each event by the final weight factor.

BDT shape systematic

The BDT shape systematic is introduced to take into account the uncertainty due to the analysis method itself. This systematic is evaluated as the difference between the nominal BDT distribution and the BDT output distribution for sample A and sample B. The two distributions have been normalized to the nominal one.

5.4.3 Results

Table 5.9 shows the observed data yields, the estimated background contributions and the expectations for the signal process after the final selection. Figure 5.12 shows the simulated and observed BDT distributions for the ee, $\mu\mu$ and combined channel. The data shows a small excess in the muon channel, which is compatible within one sigma uncertainty.

5.4.4 Systematic ranking plot

The systematic ranking plots for the BDT analysis is showed in Figure 5.13a for the electron channel, in Figure 5.13b for the muon channel and in Figure 5.13c for the combined channel. The striking difference compared to the cut based analysis, in Figure 4.20, is the role of the jet systematics and the BDT shape. The jet systematics increase drastically in the ranking and in the magnitude. The reason behind it is the loosening of the cuts ΔR_{ll} and $\Delta\phi(Z, E_T^{miss})$ in the BDT analysis which leads to an increased amount of events with higher number of jets. The uncertainty on the BDT shape due to the implementation of the method itself also effects heavily the fit. So even if the exclusion limit performed with statistics errors only is more stringent, the systematic effect dominates limiting the power of the BDT analysis.

Final State	ee	$\mu\mu$
Observed Data	601	678
Signal		
ZH ($BR(H \to inv.) = 15\%$)	18 ± 20	20 ± 21
Backgrounds		
$qq \to ZZ$	256 ± 12	269 ± 12
$gg \to ZZ$	29 ± 16	30 ± 16
WZ	139 ± 9	152 ± 9
$Z + jets$	90 ± 29	101 ± 26
$t\bar{t}, WW, Wt, Z(\tau\tau)$	80 ± 12	85 ± 19
Others	1.1 ± 0.1	1.1 ± 0.1
Total	614 ± 42	659 ± 35

Table 5.9 · Observed data yields and expectations for the signal and background contributions in the signal region. The error contains both statistical and systematic uncertainty. The signal contribution is shown with $BR(H \to inv.) = 0.15$, which is the value most compatible with data. The $e\mu$ background arises from $t\bar{t}$, Wt, WW and $Z \to \tau\tau$ production. The background contributions from the W+jets, VVV and $t\bar{t}V(V)$ processes are summed and presented with the label "Others". The uncertainty on the total background prediction is quadratically summed from those on the individual background contributions.

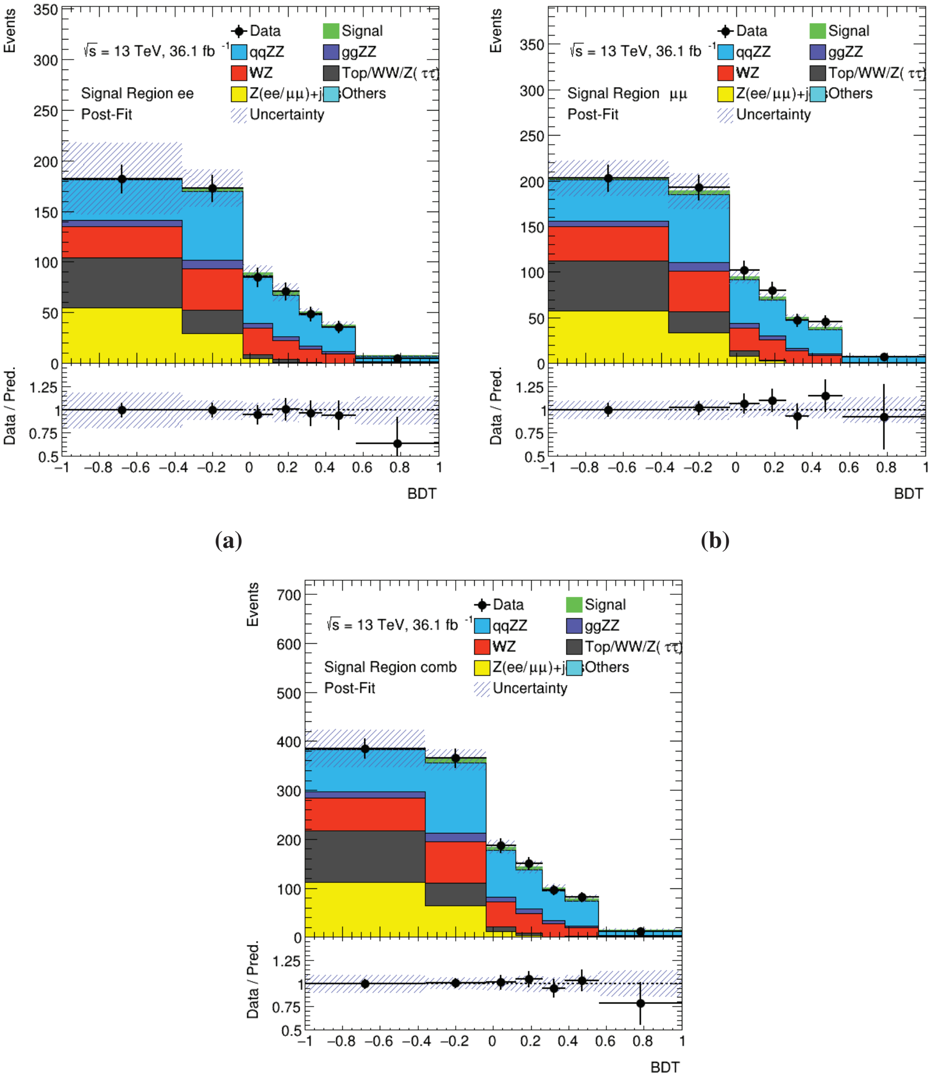

(a) **(b)**

(c)

Fig. 5.12 · Observed BDT distribution in the ee (a),$\mu\mu$ (b) and combined (c) channel compared to the signal and background predictions. The error band shows the total statistical and systematic uncertainty on the background prediction. The ratio plot gives the observed data yield over the background prediction (black points). The ZH signal distribution is shown with $\mathrm{BR}(\mathrm{H} \to \mathrm{inv.}) = 0.15$, which is the value most compatible with data.

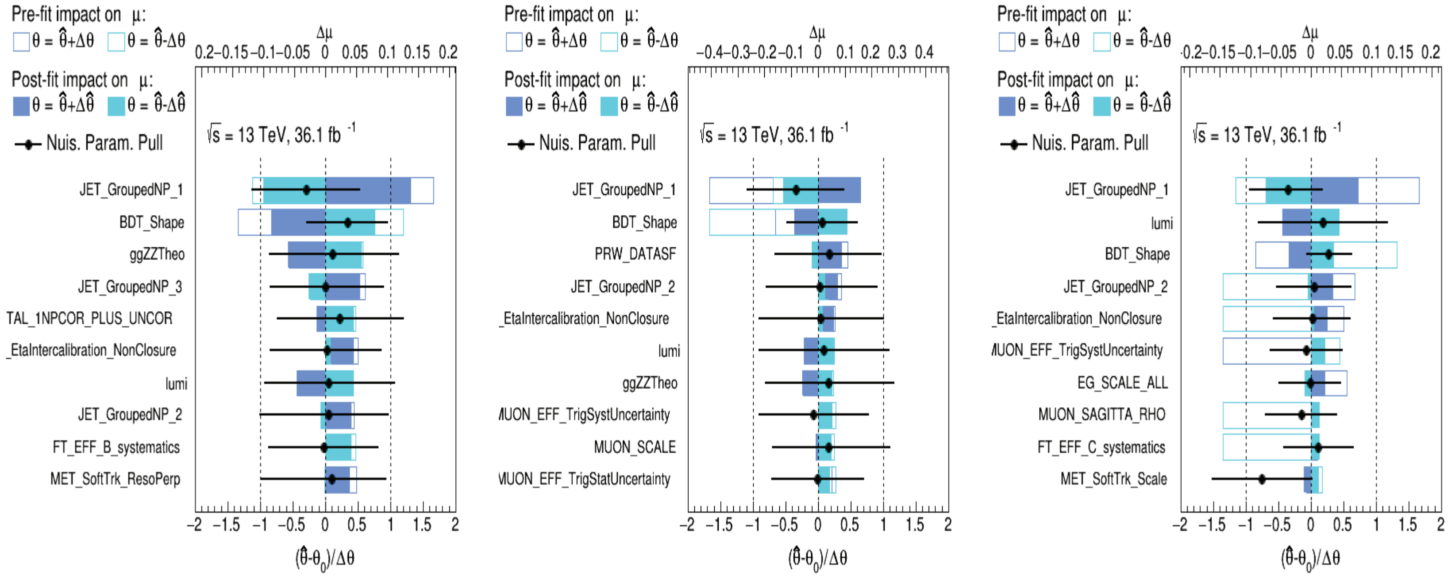

(a) (b) (c)

Fig. 5.13 · The nuisance parameter pulls and ranking when fitting signal+background model to data for (a) *ee*, (b) $\mu\mu$, and (c) $ee + \mu\mu$ channels. The plots show only the ten most important contribution to the systematic uncertainty. One can notice how the jet systematic (named JET_GroupedNP in the figure) has a stronger impact in this analysis compared to the cut-based, shown in Figure 4.20. The BDT shape systematic as well is one of the leading systematic for this analysis. Here, μ corresponds to the parameter of interest, $\mathrm{BR}(H \to inv.)$.

5.4.5 Limits

Table 5.10 and Figure 5.14 show the 95% CL upper limits on $\mathrm{BR}(H \to inv.)$, using for the ZH process the SM cross-section prediction for the BDT analysis. The expected limit after introducing the systematics shows a worst performance of the BDT compared to the cut based one. The 8% improvement exhibited by the statistical only analysis has vanished, covered by the increased jet systematic and BDT shape systematic as described in the previous subsection. As in the cut based analysis, the presence of a small excess in the data in the muon channel worsens the observed limits compared to the expected ones. Nevertheless the looser cuts in the BDT analysis dilute the muon excess: the observed limit of the BDT analysis performs better. The observed and expected limits on the $\mathrm{BR}(H \to inv.)$ for the combined leptonic channels are 60% and 46%. A signal-plus-background model is fit to the data and the best value for the $\mathrm{BR}(H \to inv.)$ is $(15 \pm 16)\%$. The BDT analysis shows no improvements compared to the cut based one for the expected limits (46% vs 39%) while it shows a 10% improvement in the observed limits (60% vs 67%).

	Obs. $\mathrm{BR}(H \to inv.)$ Limit		Exp. $\mathrm{BR}(H \to inv.)$ Limit $\pm 1\sigma \pm 2\sigma$	
	BDT	Cut-Based	BDT	Cut-Based
ee	58%	59%	$(56\ {}^{+22}_{-18}\ {}^{+52}_{-28})\%$	$(51\ {}^{+21}_{-15}\ {}^{+49}_{-24})\ \%$
$\mu\mu$	95%	97%	$(56\ {}^{+26}_{-17}\ {}^{+53}_{-27})\%$	$(48\ {}^{+20}_{-14}\ {}^{+46}_{-22})\ \%$
$ee + \mu\mu$	60%	67%	$(46\ {}^{+20}_{-13}\ {}^{+47}_{-22})\%$	$(39\ {}^{+17}_{-11}\ {}^{+38}_{-18})\ \%$

Table 5.10 · The 95% CL upper limits on $\mathrm{BR}(H \to inv.)$ for $m_H = 125$ GeV from the ee, $\mu\mu$, and combined $ee+\mu\mu$ channels for the BDT and Cut-based analysis. From the values showed in the table the BDT does not show an improvement in the expected limit compared to the cut based, while there is a 10% improvement in the observed one, due to a reduced excess of muon compared to the cut based analysis. Both the observed and expected limits are given, and the 1σ and 2σ uncertainties on the expected limits are also presented.

5.5 Conclusion

This chapter describes in detail the implementation of a new method to investigate the invisible decay of the Higgs boson in associated production with a Z boson decaying into a pair of muon or electrons. The major goal of this study was to assess the competitiveness of a multivariate approach, a BDT specifically, compared to the baseline analysis. The results show that this technique does not outperform the cut-based one. This is due mostly to the nature of the dominant background, the ZZ. This background which has the same final signature as the signal, does not leave much room to the BDT algorithm to improve the discrimination of the background from the signal. By loosening the cuts on the cut-based selection and increasing the statistics, the BDT increases its sensitivity but the systematics, introduced by loosening the cut in the first place, eliminate such advantage. This study

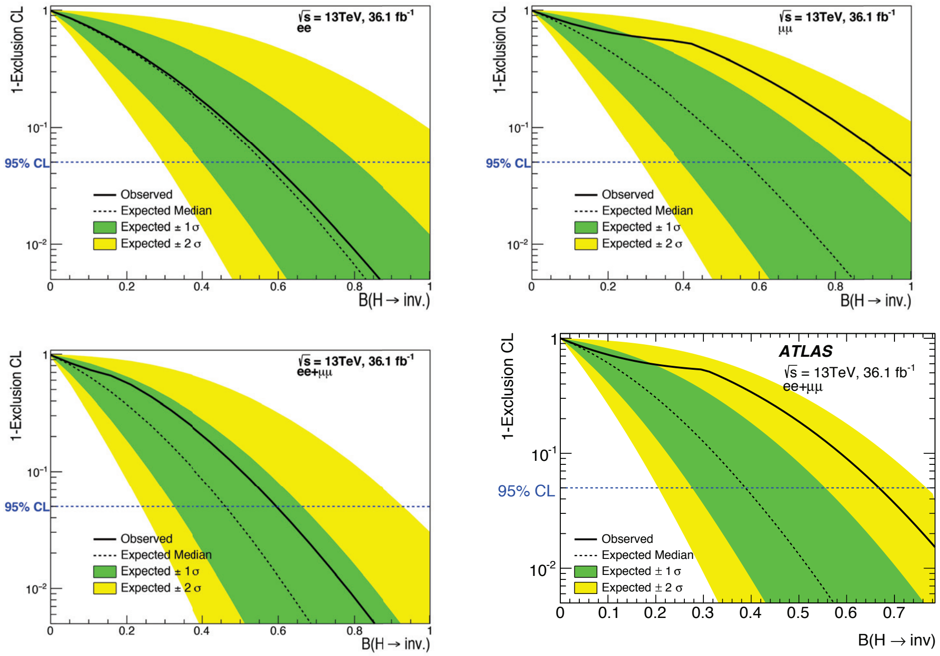

Fig. 5.14 · Scan of "1− Exclusion CL" as a function of $\mathrm{BR}(H \to inv.)$ with $m_H = 125$ GeV using the ee (top left), $\mu\mu$ (top right), and combined $ee + \mu\mu$ (bottom left) channels for the BDT. The bottom right plot shows the combined $ee + \mu\mu$ channel as a comparison with the BDT one. One can see from the plot how the expected limit in the BDT analysis is less stringent compared to the cut-based analysis while the observed one is more. The observed and expected curves are shown in solid and dashed black lines, respectively. The $\pm 1\sigma$ ($\pm 2\sigma$) error band on the expectation is shown in green (yellow). The crossing point between the dashed blue line and the scan curve gives the observed (expected) upper limit on $\mathrm{BR}(H \to inv.)$ at the 95% CL.

suggests that even by applying more complex techniques as a multi class BDT or dedicated control regions and data-driven estimates using the BDT information, this would not necessarily lead to a major gain over the cut based approach, which is still the best suit for this kind of analysis.

chapter six

TADA

This chapter will describe the ATLAS fast physics TAG data monitoring system (TADA) which I worked on as code developer and expert. The chapter will describe the framework structure and the idea behind it, the strategy used for the code migration for the Run-II, the validation and the physics results provided by it. The main goal of this chapter is to provide a clear picture of how a fast physics analysis is performed in ATLAS and the usage of such a tool for physics validation and searches of new phenomena.

6.1 TADA framework and idea

The ATLAS fast physics TADA monitoring is a system to monitor a wide spectrum of new physics channels and aspects of offline data quality and physics performance. Since 2011 this system has operated as part of the ATLAS Tier-0 [185, 186] prompt data processing at CERN to allow for an early detection of anomalies in the different channels. TADA takes benefit from the full offline detector performance provided by the prompt reconstruction of the data after the calibration loop. Its task is to look for early signs of new physics in the data and it allows to monitor the quality of the data. The guiding principle of TADA search is to cover a broad spectrum of final states, while being inspired by the offline selections for the corresponding channels.

6.1.1 TADA work flow

The TADA framework, represented in Figure 6.1, is based on an hybrid C++ and python software approach. The information contained in the input TAG[1] files are processed in C++ while the python code is used for job steering, handling metadata information, bookkeeping and to produce the webpage. TADA uses the full analysis level calibrations: this allows to obtain high quality results in a quasi online framework. The analysis step (in C++) is divided into two parts: a first step select *analysis ready* physics objects which are labeled as *Good*, secondarily different selections are applied for the different analyses. All the information are stored into hybrid pyroot files filled with histograms and metadata. The steering process, handled by python, merges different information using different software:

- Cross sections and data luminosity are used to normalize the MC samples (on which scale factors and corrections are applied). Different MC versions of the same sample are available to optimize the data-MC comparison.

---

[1] The TAG file production will be largely described in the next section

- Only good quality data contained in the Good Run List (GRL) are used. Data-MC comparison is performed after pile up reweighting is applied.
- The luminosity is evaluated by using the official ATLAS Luminosity Calculation tool (LumiCalc) [187]
- The trigger prescales are obtained using COOL [188]
- The Atlas Metadata Interface (AMI) [189] is used to retrieve metadata information on the input files.

After the steering process is executed, the final pass processing creates plots, cut flows and event dumps. All the results are written in a webpage format accessible by the whole ATLAS collaboration. TADA can update the results daily by querying newly processed runs at Tier-0.

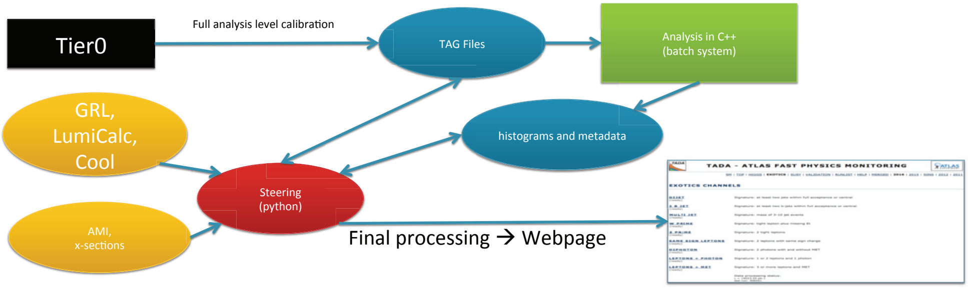

Fig. 6.1 · TADA workflow

6.2 TAG Writing

6.2.1 ATLAS Computing Model

The ATLAS collaboration has developed a software infrastructure to perform data analysis. The whole software structure is based on two basic constituents:

1. The Athena framework
2. The GRID

The Athena framework will be briefly described.

Athena: ATLAS Control Framework

Athena [190] is an object oriented software in which data processing and analysis is performed. Athena is based on Gaudi [191], a C++ framework originally developed by LHCb, later updated by ATLAS. While the main part of the software is written in C++ the scripting and the configuration is handled by Python. The main design principles, which I will just enumerate here, are:

- Abstract interfaces

- Usage of dynamic libraries
- Separation between transient and persistent data.
- Modular structure

The design is aimed to provide a flexible and easy to update framework accessible by the whole collaboration. Athena can conduct a huge amount of operations: Simulation, Reconstruction, High Level Trigger (HLT), xAOD making, analysis. In order to do so the software is provided with several component abstractions:

- Application Manager
- Algorithm and Sequencers
- Tools
- Transient Data Store
- Services
- Selectors, Converters, Properties, Utilities

An object diagram of the GAUDI/Athena Architecture is showed in figure 6.2. This diagram describes the relationships of ownership and usage among the objects. The structure is based on the Application Manager, an algorithm which manages all the other components and instantiates the physics algorithms. Each algorithm executes a specific operation and it can be linked to different algorithms creating a sequence of them. One of the key aspects of GAUDI and Athena is the usage of Transient Data Store (TDS), the so-called "blackboard".

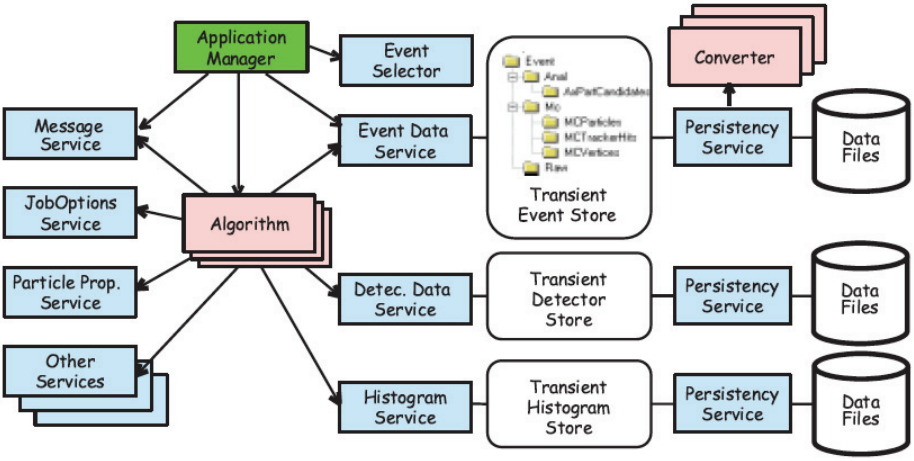

Fig. 6.2 · Object diagram of the GAUDI Architecture. The picture is taken from [191].

Information coming from different data objects are stored temporarily and can be accessed later from different algorithms. This structure allows to uncouple the algorithms from the data objects. The module can use the information in the store without knowing the origin of the data stored. This setup provides enormous benefits and avoids "interface explosion", but the price to the pay is the need of a data model to handle objects. In ATLAS the StoreGate (SG) [192] is the data model used to post or retrieve objects from the GAUDI blackboard. The SG is a dictionary of data objects which manages their memory and it provides an interface to handle references, object lifetimes, memory management for the data objects in the Store. As shown in figure 6.2 Athena also provides a large number of effective services usable by the end-user:

- Job option
- MessageSvc
- HistorySvc
- Histogramming

Among those, the Job option is one of the most interesting feature for the end user. This feature allows to specify the option for each job to be submitted.

6.2.2 How to run a TAG production in ATHENA

As described in the previous sections ATHENA jobs are configured by Python scripts. In those scripts the end user can define option and properties and implement the main reconstruction algorithms. In order to obtain TAG files the reconstruction chain is the following:

$$\text{RDO} \rightarrow \text{ESD} \rightarrow \text{(x)AOD} \rightarrow \text{TAG}.$$

RDO (Raw Data Object) files contain the full information of the detector response, ESD (Event Summary Data) files contain output of detector reconstruction, xAOD (Analysis Object Data) files contain a summary of all reconstructed objects. Once the xAOD files are produced it is then possible to run the TAG reconstruction step.

From AOD to xAOD

During the long shutdown of LHC (LS1) the ATLAS detector as well as the machine were upgraded. Many changes were also applied to the software reconstruction chain. The biggest change was related to the introduction of a new Event Data Model (EDM) file format called the xAOD. This new format replaced and combined the old AOD (Analysis Object Data) together with D3PD file format used during RunI. A brief overview of the xAOD structure will follow. More details can be found in the literature [193]

xAOD EDM

At the end of Run-1 the need for an update in the analysis model arose from the Analysis Model Study Group (AMSG). The goal was to implement a new data format, xAOD, which is ROOT and ATHENA writable and readable. This file format replaced and combined the feature of the old AOD and D3PD used during Run-1. The new EDM is designed to fulfill the following criteria:

- Common file format:
  The main limitation in Run-1 AOD was that they were usable only in Athena.
  The new xAOD can be used in both Athena and ROOT
- Simplicity, performance, flexibility:
  Simple designs were chosen to provide an easy to access interface.
  To increase performance the design is as close as possible to ROOT ntuples.
  The user can manipulate the content of the objects (containers) at runtime
- Designed for current physics analysis:
  Simple to use inside ROOT.
  Inspectable with ROOT::TBrowser
- Migration:
  Easy to adapt to the old AOD Athena code

The new xAOD EDM is based on two separated components:

1. Interface class
    - The interface class, (for example xAOD::IParticle) provides a C++ easy to access object for the end user. The EDM objects information related to each particle are then stored into containers. A custom vector type, DataVector<T> (similar to std::vector<T*>) is used to allow polymorphism and inheritance relationships (a specific data vector type is related to a generic Particle data vector: DataVector<xAOD::Muon> $\rightleftharpoons$ DataVector<xAOD::IParticle>). This custom type is defined in a way to keep the interface code separated from the auxiliary store.
2. Auxiliary Data Store
    - The auxiliary data store are objects that allocate memory for the data and allow the interface class to access this data. This separation allows to read information during analysis, to add, remove and modify variables to an object. Finally the division of the code allows the user to interact with the xAOD without touching the more complex structural code which lies in the background.

From AOD → TAG to xAOD → TAG

In this section the actual migration work will be shown. The philosophy adapted was the following:

- Fix the code in place with minimum amount of changes
- Usage of Reconstruction chain (RecExCommon) to produce TAG files from xAOD directly from Tier0 cache.
- Working with development (dev) nightly

The TAG code was modified in order to adapt to the xAOD format. The usual procedure is as follows:

- The container is retrieved from the Store Gate and iterated over to obtain the information
- Skimming operations are applied using new functions and structures using the xAOD format
- The TAG variables are filled after the selection and stored in the TAG final output file

6.2.3 Releases and software updates

As already mentioned in the previous section, TAG file are produced via a reconstruction chain, using specific software releases. Software releases are organized and divided into different projects: simulation, trigger, analysis. The release are also divided into *stable base* releases and *nightly* releases. The latter ones are temporary development releases which are re-compiled every night (from which the name) for each project. Each nightly is part of a project (Offline, Production et cetera) and it is overwritten every week for a total of six available nightly (rel0 ... rel6). Once all the planned packages present in the nightly are updated, a validation check is run over the nightly in order to check if the output of the reconstruction is the desired one. Once the validation is finalized the nightly is *frozen* and all the packages form a new stable base release. Once the validation is concluded, the release is frozen and the production is initiated. The TAG file composition and updates for each physics element and the validation procedure will be described in the following sections.

6.2.4 TAG file content

The TAG file content has the following structure.

1. Global Event Info
    - Global Event Attributes
    - E_T^{miss} information
    - Detector flags and cleaning variables for jet and E_T^{miss}
    - Trigger Information
2. Physics objects
    - Electrons
    - Photons
    - Muons
    - Tau-Jets
    - Jets

There are two groups of information stored in the TAG files, the Global Event Info which contains information for each event and the Physics Objects which contains info for a specific amount of physics objects is stored. The Global Event Info category contains different information as the E_T^{miss} , detector flags, and trigger information. The other category of information is related to each physical object. The numbers of physics objects stored in the TAG file is shown in Table 6.1. Each object has the following set of information: kinematic (p_T, η, ϕ), number of objects for each event and bit-mask information for Isolation, Quality *et cetera*. In the following section the structure of TAG content and the major changes in the code will be described in detail.

Physics Object	Number
Electrons	4
Muons	4
Photons	2
Taus	2
Jets	6

Table 6.1 · Number of physics objects stored in the TAG files

Missing Energy implementation, an iconic case

The E_T^{miss} object has been completely renewed in the new TAG files version. The major difference is that the E_T^{miss} was previously computed at a previous stage of the reconstruction chain and the information was just retrieved in TAG files, while now it is calculated by using the METMaker algorithm. The latter is implemented with pre-selected objects, using the Combined Performance (CP) group recommendations, with the following selection:

- Calibrated LCTopo jets with : $p_T > 20$ GeV
- Pile up suppression: No jets with $p_T < 50$ GeV, $\eta < 2.4$ and Jet Vertex Tagger (JVT) < 0.64
- All objects are selected following the CP recommendations: electrons, muons, taus, photons, jets.

The introduction of pre-selected objects in the evaluation of the MET was a critical improvement.

Missing transverse energy evaluation and muon pre-selection

The E_T^{miss} is composed of different terms depending on the reconstructed objects used. The term E_T^{miss} usually refers to the absolute value of the bi-dimensional vector built up by taking into account all the input objects(electrons, muons, taus, photons, jets and soft term). All the available E_T^{miss} terms are stored in the TAG file. Another important improvement was the procedure itself of evaluating the E_T^{miss}: the introduction of skimmed Muons container solved several issues in the E_T^{miss} tail shape. The definition of the input objects is crucial for the correct evaluation of the E_T^{miss}. As an example a data TAG file had events with very high energy signature, even above the machine energy. Figure 6.3a shows the E_T^{miss} distribution for 100000 data event. Looking at performance studies the issues was related to bad reconstructed Muons. Parsing to the METMaker pre-selected "Medium"[1] Muons solved the issue, as shown in Figure 6.3b.

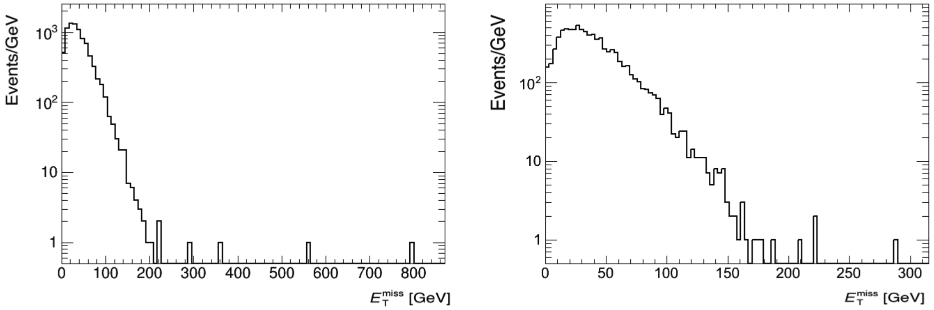

(a) **(b)**

Fig. 6.3 · E_T^{miss} before (a) and after (b) the requirements of only "Medium" Muons used in the METMaker algorithm.

Bit encoded information in TAG files: physics objects, trigger, detector, jet cleaning variable

TAG files store kinematic information (p_T, η, ϕ) for each of the physics objects as well as identification, isolation, quality information.The latter are stored into a bit-mask scheme. Each bit is linked to a specific property of the object that can be fulfilled (bit equals to 1) or not (bit equals to 0). Different information are encoded in different bit-mask: tightness, isolation, particle identification (PID). For each mask different sub-group of information are stored as: Type, Quality et cetera. Trigger information, detector status and commissioning attributes use the same bit-mask scheme. This bit-mask structure allows to store huge amount of information by using little amount of space reducing drastically the CPU time to read and utilize the information on a later stage. Commissioning attributes are stored by propagating a *RawInfoSummary* object through the *ESD* and *AOD* reconstruction chain. In order to prevent to compute bad quality jets a cleaning variable is defined as *JetMissingETWord*. The jets are pre-selected with $p_T > 20\text{GeV}$ and they have to fail the bad criteria.

Pre selection cut on physics object: electrons, muons, photon, taus, jets.

On each physics object a pre-selection is performed before being stored in the TAG file. Table 6.2 shows the list of pre-selections for each object.

6.3 TADA studies in Run2

6.3.1 Selection and object definition at TADA level

After a first pre-selection is applied at Reconstruction level, a new level of selection is applied to obtain close to analysis requirements for all the objects stored in the TAG files. If

---

[1] A "Medium" Muon is a Muon which has passed a specific "quality" selection. This selection is based the fulfillment of specific detector requirement as the number of precision layers triggered by the Muon.

Object	Cut
Electron	$p_T > 7.0$ GeV, $\|\eta\| < 2.47$, *Likelihood Loose* selection
Photon	$p_T > 10.0$ GeV, $\|\eta\| < 2.37$, *Loose* selection
Muon	$p_T > 6.0$ GeV, $\|\eta\| < 2.5$, Medium Quality if Stand Alone , $\|d0\| < 5$ mm
Taus	$p_T > 20.0$ GeV, $\|\eta\| < 2.5$, one track or three, charge equal to ± 1, *Loose* PID
AntiKt4Topo Jets	$p_T > 40.0$ GeV, $\|\eta\| < 2.8$, *Loose* quality/cleaning cut

Table 6.2 · Pre-selection on physics objects.

an object passes the selection it will be tag as *Good* allowing the selections among different final state extremely flexible. In Table 6.3 a resume of all the cuts applied to each object is shown.

Object	Cut
Good Electron	*Tight Likelihood* ID , *Gradient Loose* Isolation
Good Photon	*Tight Likelihood* ID, *Tight* Isolation, *Medium* Quality
Good Muon	*Medium* quality, number of precision layers more then 1, *Gradient Loose* Isolation
Good Taus	*Tight* PID
AntiKt4Topo Jets	JVT > 0.2, $\|\eta\| < 2.4$, *TightBad* veto
AntiKt4Topo B-Jets	MV2c20 >-0.046 (70% working point)

Table 6.3 · Pre-selection on physics objects

6.3.2 Webpage

The information produced by TADA are published on a webpage accessible by the whole ATLAS Collaboration. Each data taking has its own webpage: 2015, 2016 as well as their combination. RunI results (2011, 2012) are available as well. The webpage, updated twice a day, is divided into different categories of physics channels and validation: SM, Top, Higgs, Exotics, SUSY, Validation. More then 300 different selections are applied to fill approximately two thousand histograms. Each physics category has different channels, for example the SM one, shown in Figure 6.4, contains: W(Z) inclusive, W(Z) and 2 jets, W(Z) and b jets, diboson, same sign WW. Each channel provides:

- Main selections: inspired by full analysis selection, divided for lepton flavour.
- Plots grouped by mode: for a given selection the most important variables are plotted.
- Event dumps : all the significant information (run number, event number, luminosity block) of interesting events is displayed.
- 3D views for interesting events, as shown in Figure 6.5

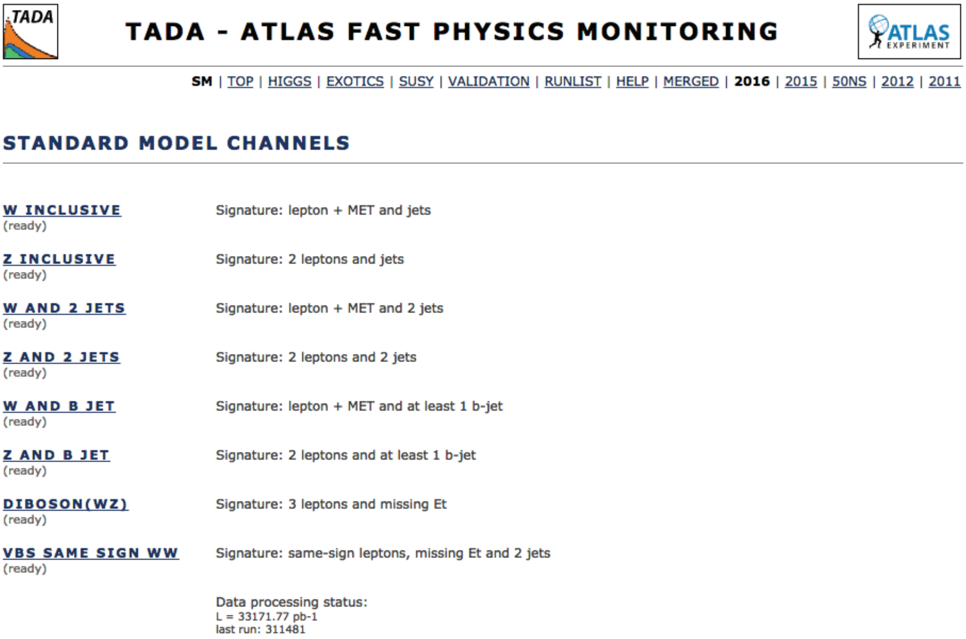

TADA - ATLAS FAST PHYSICS MONITORING

SM | TOP | HIGGS | EXOTICS | SUSY | VALIDATION | RUNLIST | HELP | MERGED | **2016** | 2015 | 50NS | 2012 | 2011

STANDARD MODEL CHANNELS

W INCLUSIVE (ready)	Signature: lepton + MET and jets
Z INCLUSIVE (ready)	Signature: 2 leptons and jets
W AND 2 JETS (ready)	Signature: lepton + MET and 2 jets
Z AND 2 JETS (ready)	Signature: 2 leptons and 2 jets
W AND B JET (ready)	Signature: lepton + MET and at least 1 b-jet
Z AND B JET (ready)	Signature: 2 leptons and at least 1 b-jet
DIBOSON(WZ) (ready)	Signature: 3 leptons and missing Et
VBS SAME SIGN WW (ready)	Signature: same-sign leptons, missing Et and 2 jets

Data processing status:
L = 33171.77 pb-1
last run: 311481

Fig. 6.4 · TADA SM webpage example.

- Cut flows : Event yields after each step of the selection are provided.

6.3.3 Validation and physics performance stability

TADA monitors a lot of physics, trigger, detector performance aspects in different channels involving jets, photons, W, Z, top, missing energy et cetera. As a fast physics monitoring system, TADA can check the stability of the physics performance across the data taking period. It is common practice in collider physics to use well known SM processes (Z boson, $\mathrm{t\bar{t}}$) for calibration and validation procedures. TADA follows the same approach and provides different validation plots for different SM processes. The mean of the invariant mass of the Z boson decaying to a pair of muons versus different run number, as shown in Figure 6.6a, is a good control plot due to its sensitivity to mis-alignment effects. The plot doesn't show any recognizable trend and the mean is stable across different runs. Another validation technique consists of measuring the stability of signal yields: Figure 6.6b shows the yields of the semileptonic decay of $\mathrm{t\bar{t}}$ in one electron, one muon, (b)jets and $\mathrm{E}_{\mathrm{T}}^{\mathrm{miss}}$. The plot shows that the signal yield is stable across different run numbers. Another validation method, known as the γ-jet balance method, will be described in detail in the next section.

The γ-jet balance method

In an hadronic collider the jet energy calibration is crucial to obtain accurate measurements. To cross check the performance and the stability of the jet energy calibration the γ-jet balance method was used in TADA. The topology of back-to-back γ-jet events are a standard

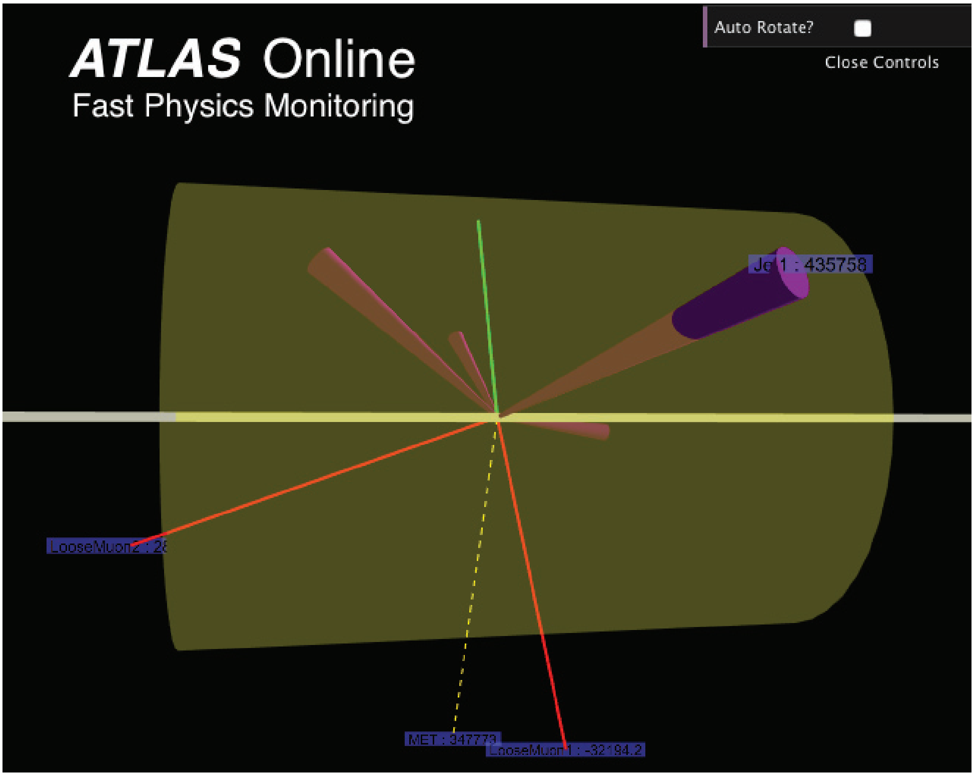

Fig. 6.5 · 3D view of an event selected in TADA. The yellow thick horizontal line represents the beam pipe, the purple cones represent the reconstructed jets, the continuous thin lines (red and green) represent reconstructed leptons (muons and electrons) and the dotted yellow line the missing energy. The opaque yellow cylinder is a representation of the ATLAS detector. The picture has been published in [2].

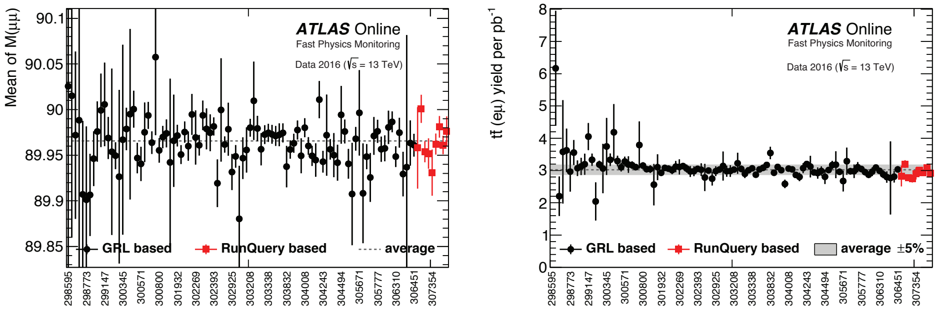

(a) (b)

Fig. 6.6 · Average of the invariant mass of a Z boson decaying into a pair of muons over a certain run number period (a) and stability plot of a semileptonic (eμ) $t\bar{t}$ yield over a certain run number period (b). The pictures have been published in [2].

handle to assess the jet energy calibration. This is due to the fact that to conserve energy in the transverse plane, the ratio of the p_T of the two objects has to be equal to 1.

$$\frac{p_T^{jet}}{p_T^{\gamma} \cdot \cos(\Delta\phi)} = 1 \tag{6.1}$$

The selection of γ-jet events, shown in Table 6.4, is implemented in TADA to monitor the p_T balance, defined in Equation 6.1 , where p_T^{jet} is the transverse momentum of the jet, p_T^{γ} is the transverse momentum of the photon and $\Delta\phi$ the angular difference between the two objects, where ϕ is the azimuthal angle in the transverse plane.The mean of the p_T balance distribution vs p_T^{γ} is shown in Figure 6.7a. The plot shows a good p_T balance between the two objects: the slope at low p_T is due to misidentified objects coming from γ + jet + additional radiative processes. The stability plot in Figure 6.7b shows the mean of the p_T balance over different data periods.

Event Selection
HLT loose trigger cuts
No error in detector flags, loose veto on bad jets
Exactly 1 loose photon
Good photon
Cut on $\Delta R(e, \gamma)$
Cut on the leading γ p_T
Good jet
Cut on leading jet p_T
Exactly 1 jet or 2 jets with more then 90% of the p_T carried by the leading one
Cut on leading jet $\lvert\eta\rvert$
Cut on $\Delta\phi$ among γ and jet

Table 6.4 · γ-jet TADA event selection

6.3.4 Searches in TADA

TADA monitors various physics channels, which are grouped into five categories: Standard Model, top, Higgs, exotics and SUSY searches. Each group contains different searches divided into different final states as shown in Figure 6.4 for the SM. Each final state can have different selections implemented for different lepton flavors (electrons and muons). The most important distributions, like invariant mass and E_T^{miss} are displayed on the webpage as shown in Figure 6.8a and 6.8b.

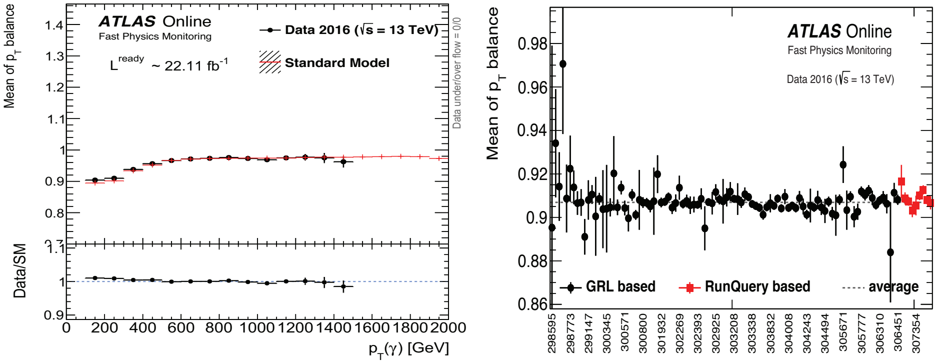

(a) (b)

Fig. 6.7 · Validation plots for the γ-jet balance method: mean of p_T balance vs p_T^{γ} (a) and mean of p_T balance over a certain run number period (b). The pictures have been published in [2].

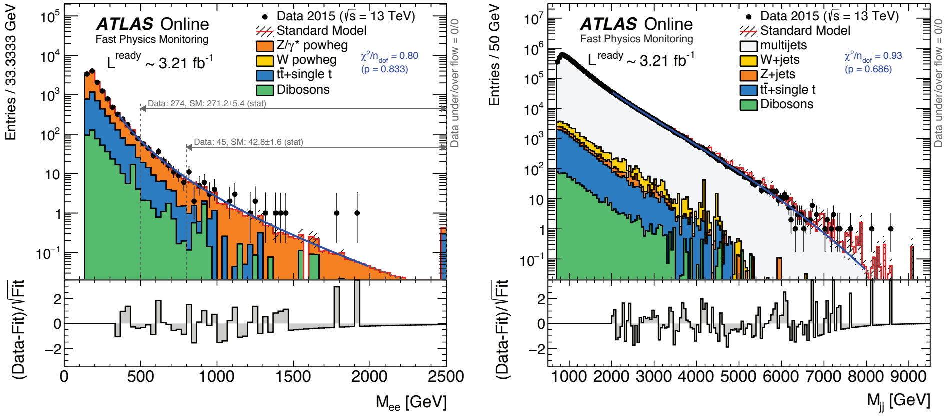

(a) (b)

Fig. 6.8 · Di-electron (a) and Dijets (b) invariant mass distributions for exotics searches. The pictures have been published in [2].

6.3.5 Hunting for new physics: $\gamma\gamma$ example

TADA can also be used as a tool to spot new physics: in case an excess is detected the physics group related to the channel will be immediately alerted. TADA can also monitor the evolution of the significance of such excess and provide results very quickly. An example of this is the diphoton excess that was seen by ATLAS [194] in 2015.

Hint for an excess

Figure 6.9a shows the invariant mass of the diphoton system in the 2015 data: the plot shows a 3σ excess at 750 GeV, the same was seen by the dedicated analyses performed by the ATLAS and CMS [195] Collaboration. The event selection applied in TADA (similar to the offline one) is reported in Table 6.5. TADA also provides the evolution of the significance vs integrated luminosity as shown in Figure 6.9b. The distribution shows a clear excess at the end of the 2015 data taking period. The same plot, shown in Figure 6.10a, was produced

Event selection
HLT loose or *HLT medium* trigger cuts
No errors in detector flag, loose veto on bad jets
At least two loose γ
Good (sub)leading γ
p_T cuts on leading and sub leading γ
Cut on the relative contribution among leading and sub leading γ for the invariant mass
Cut on $M_{\gamma\gamma}$

Table 6.5 · $\gamma\gamma$ TADA event selection

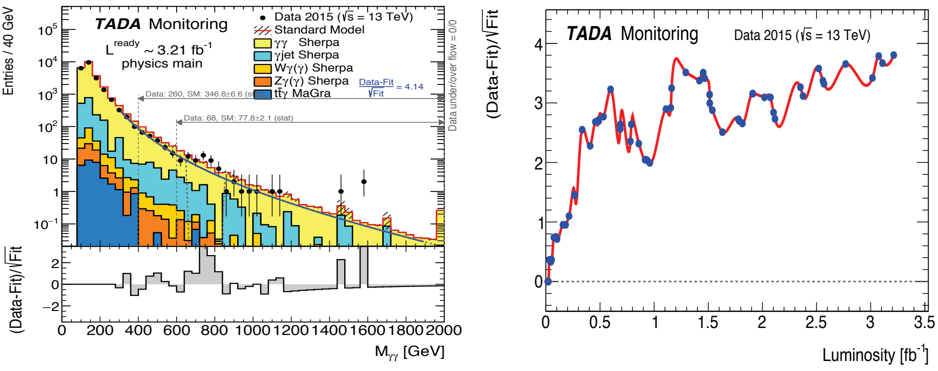

(a) **(b)**

Fig. 6.9 · Invariant Mass of the $\gamma\gamma$ final state showing a 3 σ excess at 750 GeV (a) and significance evolution versus integrated luminosity for 2015 data collection (b).

with the data collected in 2016. In line with the results obtained by the offline analysis, no excess was detected with an integrated luminosity of 33.17 fb^{-1} . The plot showing the evolution of the significance of the $M_{\gamma\gamma}$ excess over the integrated luminosity for the 2016 data taking is reported in Figure 6.10b.The results for the $\gamma\gamma$ final state for the combined

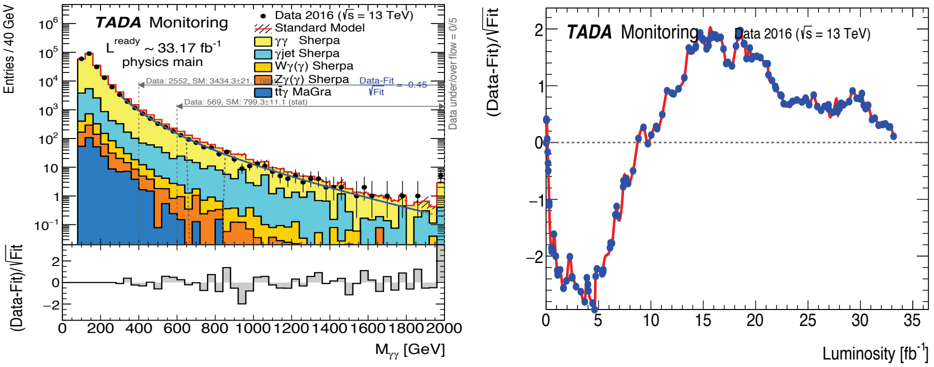

(a) **(b)**

Fig. 6.10 · Invariant Mass of the $\gamma\gamma$ final state showing no deviations from the standard model for the data taking 2016 (a) and significance evolution versus integrated luminosity for 2016 data collection (b).

dataset 2015 and 2016 are shown in Figure 6.11a and 6.11b. The plots don't show any significant excess between data and MC predictions.

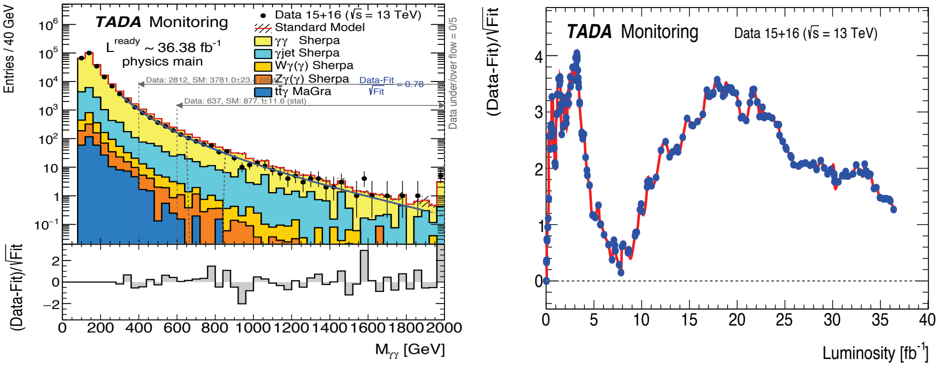

(a) **(b)**

Fig. 6.11 · Invariant Mass of $\gamma\gamma$ final state showing no significant fluctuations from the standard model for the combined data taking 2015 and 2016 (a) and significance evolution versus luminosity (b).

Comparison with Offline results

TADA framework can produce fast results with a precision close to the offline analysis. The differences among the two approaches are due to the structure of the framework itself. The first is the absence of systematic uncertainties:all TADA results are statistical only. Another source of difference is how the objects are pre-selected and the event selection applied. Each offline analysis, can optimize the selection over a specific final signature while TADA goal is to have a broad range of searches, therefore the object definition and cuts will be optimized to cover a wider spectrum of physics phenomena. While the first difference (systematic studies) cannot be changed, the second one can be minimized by using a selection as close as possible to the offline analysis in a specific channel. Keeping those differences in mind, the results of the $\gamma\gamma$ Offline analysis with 3.2 fb^{-1} and 15.4 fb^{-1} [196] shows a similar significance found by the TADA framework. [1] In Figure 6.12a is reported the data versus background-only fit for the $M_{\gamma\gamma}$. As reported in the note the local significance of the excess around 750 GeV for 3.2 fb^{-1} is equal to 3.8 σ which is compatible with the significance seen by TADA as shown in Figure 6.9b. Similarly for 15.4 fb^{-1} (Figure 6.12b) the local significance reported in the note from the Offline analysis for the mass around 750 GeV is equal to 2.3 σ which is compatible with the TADA results shown in Figure 6.11b.

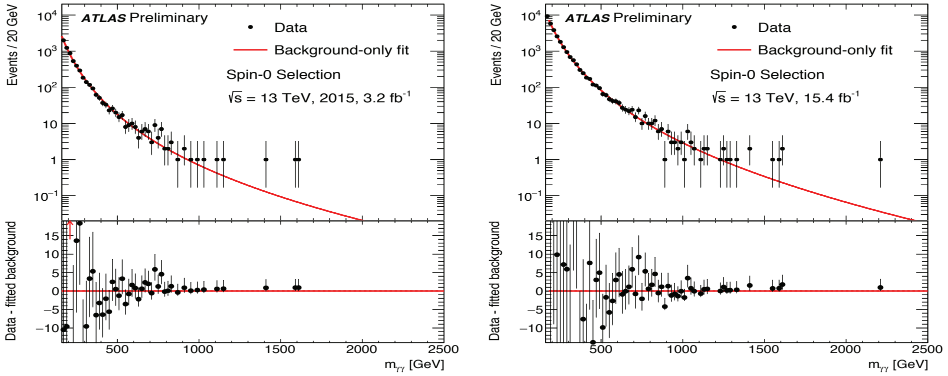

(a) (b)

Fig. 6.12 · Data vs background-only fit for the invariant Mass of $\gamma\gamma$ final state for data taking 2015 with 3.2 fb^{-1} (a) and for the combined 2015 and 2016 data taking with 15.4 fb^{-1} (b). The pictures are taken from [196].

6.4 Conclusion

In this chapter the ATLAS fast physics TAG data monitoring TADA was presented. To better describe the framework and the production of the input TAG files, a description of the ATLAS software infrastructure (ATHENA) was provided. The TAG file content

---

[1] As specified in the $\gamma\gamma$ note the systematic uncertainties effect the significance at the order of few percent, therefore the difference introduced in term of significance is negligible.

was described in details as well as different validation procedures to cross-check the MC simulations versus the data. The last part of the chapter was focused on the physics results provided by TADA with the $\gamma\gamma$ final state signature as an example in comparison to the offline analysis. The results of TADA are remarkably similar to the one obtain by the offline analysis. It is preeminent to notice the huge impact TADA had in the first months of Run2 in the ATLAS Collaboration and how it was widely used for several studies. The system performed data quality monitoring and searches for new physics for Run1, and it is now analyzing the Run2 data[1].

---

[1] TADA analyzed up to 35.60 fb^{-1} for the 2015 and 2016 combined data taking and it is now analyzing the new data taking started in June 2017

appendix one

Appendix

In this chapter it is presented auxiliary material to better describe the work of this thesis.

A.1 MC samples tables

Process	Generator	σ (pb)	k-factor	Filter efficiency
$qq \to ZZ \to \ell^+\ell^-\ell'^+\ell'^-$	POWHEG+Pythia8	1.2673	-	1.0
$qq \to ZZ \to \nu\bar{\nu}\nu\bar{\nu}$	POWHEG+Pythia8	0.54901	-	1.0
$qq \to ZZ \to \ell^+\ell^-\nu\bar{\nu}$	POWHEG+Pythia8	0.91795	-	1.0
$gg \to ZZ \to \ell^+\ell^-\nu\bar{\nu}$	POWHEGgg2vv+Pythia8	0.05187	-	0.66248

Table A.1 · Cross sections at NLO in perturbation theory, k-factors and filter efficiency for ZZ POWHEG+Pythia8 samples at $\sqrt{s} = 13$ TeV. Processes listed refer to both quark-quark and gluon-gluon production modes.

Process	Generator	σ (pb)	k-factor	Filter efficiency
$WZ \to \ell\nu\ell^+\ell^-$	POWHEG+Pythia8	4.4625	-	1.0
$WZ \to \ell\nu\nu\nu$	POWHEG+Pythia8	2.7778	-	1.0
$WW \to \ell\nu\ell\nu$	POWHEG+Pythia8	10.631	-	1.0

Table A.2 · Cross sections at NLO in perturbation theory, k-factors and filter efficiency for WZ and WW POWHEG+Pythia8 samples at $\sqrt{s} = 13$ TeV.

Process	Generator	σ (pb)	k-factor	Filter efficiency
$WWW \rightarrow 3\ell 3\nu$	SHERPA	0.008343	-	1.0
$WWZ \rightarrow 4\ell 2\nu$	SHERPA	0.001734	-	1.0
$WWZ \rightarrow 2\ell 4\nu$	SHERPA	0.0034299	-	1.0
$WZZ \rightarrow 5\ell 1\nu$	SHERPA	0.00021783	-	1.0
$WZZ \rightarrow 3\ell 3\nu$	SHERPA	0.0019248	-	0.44444
$ZZZ \rightarrow 6\ell 0\nu$	SHERPA	1.7059×10^{-5}	-	1.0
$ZZZ \rightarrow 4\ell 2\nu$	SHERPA	0.00044125	-	0.22542

Table A.3 · Cross sections at NLO in perturbation theory, k-factors and filter efficiency for triboson samples at $\sqrt{s}$ = 13 TeV.

A.2 Flavor symmetry CR tables

A.3 BDT auxiliary material

Process	Filter	Generator	σ (pb)	k-factor	Filter efficiency
$Z \rightarrow ee$	$0 < \max(H_T, p_T(V)) < 70$ CVeto B Veto	SHERPA	1981.8	0.9751	0.82106
$Z \rightarrow ee$	$0 < \max(H_T, p_T(V)) < 70$ C Filter B Veto	SHERPA	1980.8	0.9751	0.11295
$Z \rightarrow ee$	$0 < \max(H_T, p_T(V)) < 70$ B Filter	SHERPA	1981.7	0.9751	0.063809
$Z \rightarrow ee$	$70 < \max(H_T, p_T(V)) < 140$ CVeto B Veto	SHERPA	110.5	0.9751	0.69043
$Z \rightarrow ee$	$70 < \max(H_T, p_T(V)) < 140$ C Filter B Veto	SHERPA	110.63	0.9751	0.18382
$Z \rightarrow ee$	$70 < \max(H_T, p_T(V)) < 140$ B Filter	SHERPA	110.31	0.9751	0.11443
$Z \rightarrow ee$	$140 < \max(H_T, p_T(V)) < 280$ CVeto B Veto	SHERPA	40.731	0.9751	0.61452
$Z \rightarrow ee$	$140 < \max(H_T, p_T(V)) < 280$ C Filter B Veto	SHERPA	40.67	0.9751	0.23044
$Z \rightarrow ee$	$140 < \max(H_T, p_T(V)) < 280$ B Filter	SHERPA	40.643	0.9751	0.14966
$Z \rightarrow ee$	$280 < \max(H_T, p_T(V)) < 500$ CVeto B Veto	SHERPA	8.6743	0.9751	0.56134
$Z \rightarrow ee$	$280 < \max(H_T, p_T(V)) < 500$ C Filter B Veto	SHERPA	8.6711	0.9751	0.26294
$Z \rightarrow ee$	$280 < \max(H_T, p_T(V)) < 500$ B Filter	SHERPA	8.6766	0.9751	0.17223
$Z \rightarrow ee$	$500 < \max(H_T, p_T(V)) < 1000$	SHERPA	1.8081	0.9751	1
$Z \rightarrow ee$	$1000 < \max(H_T, p_T(V))$	SHERPA	0.14857	0.9751	1

Table A.4 · Cross section at NNLO in perturbation theory, k-factors and filter efficiency for Z+jets SHERPA $Z \rightarrow ee$ samples at $\sqrt{s} = 13$ TeV.

Process	Filter	Generator	σ (pb)	k-factor	Filter efficiency
$Z \to \mu\mu$	$0 < \max(H_T, p_T(V)) < 70$ CVeto B Veto	SHERPA	1983	0.9751	0.8221
$Z \to \mu\mu$	$0 < \max(H_T, p_T(V)) < 70$ C Filter B Veto	SHERPA	1978.4	0.9751	0.11308
$Z \to \mu\mu$	$0 < \max(H_T, p_T(V)) < 70$ B Filter	SHERPA	1982.2	0.9751	0.064161
$Z \to \mu\mu$	$70 < \max(H_T, p_T(V)) < 140$ CVeto B Veto	SHERPA	108.92	0.9751	0.68873
$Z \to \mu\mu$	$70 < \max(H_T, p_T(V)) < 140$ C Filter B Veto	SHERPA	109.42	0.9751	0.18596
$Z \to \mu\mu$	$70 < \max(H_T, p_T(V)) < 140$ B Filter	SHERPA	108.91	0.9751	0.11375
$Z \to \mu\mu$	$140 < \max(H_T, p_T(V)) < 280$ CVeto B Veto	SHERPA	39.878	0.9751	0.60899
$Z \to \mu\mu$	$140 < \max(H_T, p_T(V)) < 280$ C Filter B Veto	SHERPA	39.795	0.9751	0.23308
$Z \to \mu\mu$	$140 < \max(H_T, p_T(V)) < 280$ B Filter	SHERPA	43.675	0.9751	0.13769
$Z \to \mu\mu$	$280 < \max(H_T, p_T(V)) < 500$ CVeto B Veto	SHERPA	8.5375	0.9751	0.55906
$Z \to \mu\mu$	$280 < \max(H_T, p_T(V)) < 500$ C Filter B Veto	SHERPA	8.5403	0.9751	0.26528
$Z \to \mu\mu$	$280 < \max(H_T, p_T(V)) < 500$ B Filter	SHERPA	8.4932	0.9751	0.17559
$Z \to \mu\mu$	$500 < \max(H_T, p_T(V)) < 1000$	SHERPA	1.7881	0.9751	1
$Z \to \mu\mu$	$1000 < \max(H_T, p_T(V))$	SHERPA	0.14769	0.9751	1

Table A.5 · Cross section at NNLO in perturbation theory, k-factors and filter efficiency for Z+jets SHERPA $Z \to \mu\mu$ samples at $\sqrt{s} = 13$ TeV.

Process	Filter	Generator	σ (pb)	k-factor	Filter efficiency
$Z \to \tau\tau$	$0 < \max(H_T, p_T(V)) < 70$ CVeto B Veto	SHERPA	1981.6	0.9751	0.82142
$Z \to \tau\tau$	$0 < \max(H_T, p_T(V)) < 70$ C Filter B Veto	SHERPA	1978.8	0.9751	0.11314
$Z \to \tau\tau$	$0 < \max(H_T, p_T(V)) < 70$ B Filter	SHERPA	1981.8	0.9751	0.064453
$Z \to \tau\tau$	$70 < \max(H_T, p_T(V)) < 140$ CVeto B Veto	SHERPA	110.37	0.9751	0.68883
$Z \to \tau\tau$	$70 < \max(H_T, p_T(V)) < 140$ C Filter B Veto	SHERPA	110.51	0.9751	0.1829
$Z \to \tau\tau$	$70 < \max(H_T, p_T(V)) < 140$ B Filter	SHERPA	110.87	0.9751	0.110886
$Z \to \tau\tau$	$140 < \max(H_T, p_T(V)) < 280$ CVeto B Veto	SHERPA	40.781	0.9751	0.60821
$Z \to \tau\tau$	$140 < \max(H_T, p_T(V)) < 280$ C Filter B Veto	SHERPA	40.74	0.9751	0.22897
$Z \to \tau\tau$	$140 < \max(H_T, p_T(V)) < 280$ B Filter	SHERPA	40.761	0.9751	0.13442
$Z \to \tau\tau$	$280 < \max(H_T, p_T(V)) < 500$ CVeto B Veto	SHERPA	8.5502	0.9751	0.56036
$Z \to \tau\tau$	$280 < \max(H_T, p_T(V)) < 500$ C Filter B Veto	SHERPA	8.6707	0.9751	0.26245
$Z \to \tau\tau$	$280 < \max(H_T, p_T(V)) < 500$ B Filter	SHERPA	8.6804	0.9751	0.17313
$Z \to \tau\tau$	$500 < \max(H_T, p_T(V)) < 1000$	SHERPA	1.8096	0.9751	1
$Z \to \tau\tau$	$1000 < \max(H_T, p_T(V))$	SHERPA	0.14834	0.9751	1

Table A.6 · Cross section at NNLO in perturbation theory, k-factors and filter efficiency for Z+jets SHERPA $Z \to \tau\tau$ samples at $\sqrt{s} = 13$ TeV.

Process	Generator	σ (pb)	k-factor	Filter efficiency
$W \to e\nu_e, \mu\nu_\mu, \tau\nu_\tau$	POWHEG+Pythia8	11306.0	1.0172	1.0

Table A.7 · Cross sections at NLO in perturbation theory, k-factors and filter efficiency for $W + \mathtt{jets}$ $\mathtt{POWHEG} + \mathtt{Pythia8}$ samples at $\sqrt{s} = 13$ TeV

Process	Generator	σ (pb)	k-factor	Filter efficiency
$t\bar{t}$	POWHEG+Pythia6	696.12	1.1949	0.543
single t (s-channel, $W \to l\nu$, $l = e, \mu, \tau$)	POWHEG+Pythia6	-	-	-
single anti-top (s-channel, $W \to l\nu$, $l = e, \mu, \tau$)	POWHEG+Pythia6	-	-	-
single t (t-channel, $W \to l\nu$, $l = e, \mu, \tau$)	POWHEG+Pythia6	43.739	1.0094	1.0
single anti-top (t-channel, $W \to l\nu$, $l = e, \mu, \tau$)	POWHEG+Pythia6	25.778	1.0193	1.0
Wt (di-lepton, $W \to l\nu$, $l = e, \mu, \tau$)	POWHEG+Pythia6	3.584	1.054	1.0
$W\bar{t}$ (di-lepton, $W \to l\nu$, $l = e, \mu, \tau$)	POWHEG+Pythia6	3.581	1.054	1.0

Table A.8 · Cross sections at NLO in perturbation theory, k-factors and filter efficiency for top-pair, single top and Wt POWHEG+Pythia6 samples at $\sqrt{s} = 13$ TeV.

Process	Generator	σ (pb)	k-factor	Filter efficiency
$ttZ\_Np0, Z \to ll$	MADGRAPH+Pythia8	0.018103	1.2	1.0
$ttZ\_Np1, Z \to ll$	MADGRAPH+Pythia8	0.030629	1.2	1.0
ttW_Np0	MADGRAPH+Pythia8	0.009624	1.35	1.0
ttW_Np1	MADGRAPH+Pythia8	0.017344	1.35	1.0
ttW_Np2	MADGRAPH+Pythia8	0.009625	1.35	1.0
$ttWW$	MADGRAPH+Pythia8	0.008098	1.22	1.0

Table A.9 · Cross sections at NLO in perturbation theory, k-factors and filter efficiency for ttV/ttVV MADGRAPH+Pythia8 samples at $\sqrt{s} = 13$ TeV.

Lepton p_T (lead, sub-lead)	BB	BE	EB	EE
(30-44,20-44)	0.9518 ± 0.0015	0.8785 ± 0.0018	0.8509 ± 0.0018	0.8386 ± 0.0044
(44-52,20-44)	0.9757 ± 0.0016	0.8522 ± 0.0031	0.8334 ± 0.0030	0.8120 ± 0.0024
(44-52,44-52)	0.9402 ± 0.0029	0.7791 ± 0.0074	0.7820 ± 0.0076	0.7347 ± 0.0034
(52-2000,20-44)	1.0029 ± 0.0021	0.8685 ± 0.0040	0.8662 ± 0.0038	0.8009 ± 0.0032
(52-2000,44-52)	0.9730 ± 0.0139	0.8815 ± 0.0108	0.8717 ± 0.0106	0.7810 ± 0.0077
(52-2000,52-2000)	1.0434 ± 0.0037	0.9208 ± 0.0064	0.9165 ± 0.0067	0.8576 ± 0.0064

Table A.10 · Efficiency factor values in bin of p_T and η from MC. Errors contain statistical uncertainty only.

Lepton p_T(lead, sub-lead)	BB	BE	EB	EE
(30-44,20-44)	0.9469 ± 0.0004	0.8745 ± 0.0005	0.8429 ± 0.0004	0.8291 ± 0.0012
(44-52,20-44)	0.9686 ± 0.0004	0.8435 ± 0.0007	0.8226 ± 0.0006	0.7985 ± 0.0006
(44-52,44-52)	0.9380 ± 0.0007	0.7742 ± 0.0019	0.7748 ± 0.0019	0.7248 ± 0.0009
(52-2000,20-44)	0.9980 ± 0.0005	0.8715 ± 0.0008	0.8537 ± 0.0008	0.7898 ± 0.0007
(52-2000,44-52)	0.9808 ± 0.0014	0.8605 ± 0.0030	0.8648 ± 0.0030	0.7639 ± 0.0018
(52-2000,52-2000)	1.0331 ± 0.0019	0.9024 ± 0.0037	0.9180 ± 0.0038	0.8395 ± 0.0028

Table A.11 · Efficiency factor values in bin of p_T and η from Data. Errors contain statistical uncertainty only.

Variable
$\Delta R_{\ell\ell}$
E_T^{miss}
$\Delta\phi(Z, E_T^{miss})$
E_T^{miss}/H_T
Fractional p_T difference
Number of jets
Number of b-jets
$\Delta\phi(jet, E_T^{miss})$
Leading jet p_T
Zp_T
Leading lepton p_T
Subleading lepton p_T

Table A.12 · Initial list of variables used for the BDT training

Summary

The Standard Model (SM) is a theoretical model which describes the nature of elementary particles and their interaction with the three fundamental forces of nature: electromagnetic, nuclear strong and weak. The SM describes the elementary constituents of nature in terms of two different particle fields: fermions and bosons. The elementary components of the known matter are half-integer spin particles, the *fermions*, divided into three flavour families of *quarks (u, d, c, s, t, b)* and *leptons* (e, ν_e, μ, ν_μ, τ, ν_τ). The carriers of the force fields are integer spin particles, the *bosons*: the photon, γ, is the carrier of the electromagnetic force, the $W^{\pm}$ and Z are the carriers of the nuclear weak force and the gluons, g, are the carriers of the nuclear strong force. Thanks to the electroweak spontaneous symmetry breaking mechanism both fermions and bosons acquire mass via the interaction with the Higgs field; the corresponding Higgs boson was discovered in 2012 by ATLAS and CMS. The SM, widely tested in the last decades, has been proven to be a very precise and predictive model; nevertheless it presents several shortcomings such as the absence of a formulation of how matter interacts with gravity or the absence of any description of the observational astrophysics evidence that indicates the existence of Dark Matter.

The exact universe composition is yet unknown: the most successful model, the Standard Cosmological Model, describes an expanding accelerating universe composed mostly of Dark Energy (74%) and Dark Matter (21%), with only a remaining fraction due to baryonic matter (5%). As this model shows Dark Matter accounts for the majority of matter in the universe (75%). A plethora of cosmological pieces of evidence point to its presence in the universe such as rotation curves in galaxies, gravitational lensing and the Cosmic Microwave Background power spectrum. This evidence shows that Dark Matter interacts with ordinary matter only via gravity without any electroweak or strong interaction and that its most promising candidate, a weakly interactive massive particle (WIMP), is at the GeV-TeV scale . This energy range is reachable by nowadays experiments and WIMP Dark Matter can be detected via direct, indirect and production searches. Indirect searches study the radiation spectrum coming from the sky looking for the decay products of Dark Matter pair annihilation, direct searches look for nuclear scattering of Dark Matter against a heavy target of ordinary matter and finally Dark Matter can be produced and detected at high energy colliders.

The work of this thesis is focused on the search of Dark Matter via decay of Higgs bosons produced in proton-proton collisions at the Large Hadron Collider (LHC).

The LHC is a two ring super conducting proton accelerator located at CERN across the French-Swiss border, with a designed center of mass of $\sqrt{s} = 14$ TeV. “A Toroidal LHC Apparatus” (ATLAS) is one of the four detectors installed at the LHC and it is a multi-purpose experiment and its main physics program is based on the search of the Higgs boson, precise measurement of the SM and searches for Beyond the Standard Model phenomena such as Dark Matter and others. The ATLAS detector has been recording, during 2015 and 2016, 36.1 fb^{-1} of proton-proton interactions delivered at $\sqrt{s} = 13$ TeV which constitutes the dataset analyzed in this thesis.

The work of this thesis is a search for Dark Matter via invisible Higgs decay in associated production with a Z boson with a final signature of two leptons and missing transverse energy:

$$pp \to ZH \to l^+l^- + E_T^{\text{miss}}$$

The theoretical model on which this search is based is called Higgs Portal Model. In this model the SM Lagrangian is modified by adding a Dark Matter field that interacts with the SM sector only via the coupling with the Higgs field. In the SM the branching ratio (BR) of the Higgs boson to long-lived invisible particles (i.e. neutrinos) is extremely small, therefore any non zero decay would indicate the presence of new phenomena such as Dark Matter. In order to detect an *invisible* signal (characterized by E_T^{miss}) it is necessary to have a probe element which in the case of this thesis is a Z boson.

The signal is simulated via Monte Carlo (MC) methods by using both gluon-gluon fusion and quark-quark annihilation production methods as shown in Figure S.1. SM processes with two opposite sign leptons and missing transverse energy (fake or real) in the final state can mimic the signal final signature. Those processes are labeled as background and they are reproduced via MC simulations. In the search, a signal region is defined by a series of cuts on kinematic variables that optimize the background rejection versus the signal efficiency. Dedicated control regions have been defined, when possible, to better estimate the background contribution using data driven methods. The observed data yields, the estimated background contributions and the expectations for the signal process after the final selection for the most discriminant variable, the E_T^{miss}, are shown in Figure S.2a. The results do not show evidence for new phenomena beyond the standard model. An exclusion limit has been performed on the Higgs invisible BR and the results are shown in Figure S.2b.

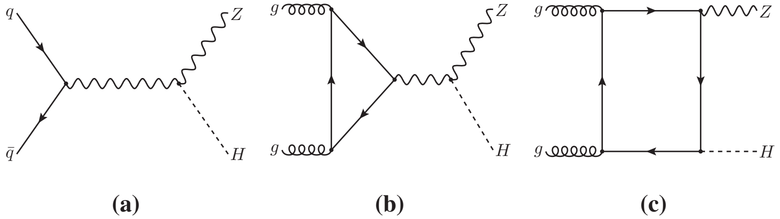

Fig. S.1 · Feynman diagram of ZH production at LHC via quark-antiquark annihilation (a) and gluon-gluon fusion (b),(c)

In recent years the usage of multivariate techniques for data analysis has spread widely in the scientific community. In this thesis a multi-variate approach is applied on the standard analysis, which will be called cut-based analysis for simplicity. The method used is a boosted decision tree (BDT) which is a binary sequential splitting algorithm that can be used for the classification of signal versus background events. Similarly to the cut-based analysis

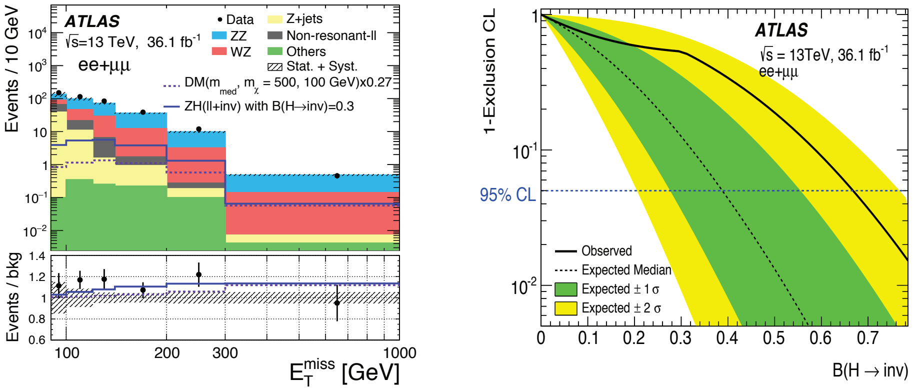

(a) **(b)**

Fig. S.2 · Observed E_T^{miss} distribution for the combined $ee + \mu\mu$ channel for the cut-based analysis (a) and scan of "1− Exclusion CL" as a function of BR($H \to inv.$) with $m_H = 125$ GeV using the combined $ee + \mu\mu$ channel (b)

a series of cuts is applied to define a phase-space region on which the BDT can train and perform the classification procedure. The training procedure provide as output a classifier, the BDT score, which is the chosen discriminant variable of this analysis. The observed data yields, the estimated background contributions and the expectations for the signal process are shown in Figure S.3a. As in the cut-based analysis the results are compatible with the SM predictions. An exclusion limit has been performed on the Higgs invisible BR and the results are shown in Figure S.3b. The comparison between the BDT and cut-based

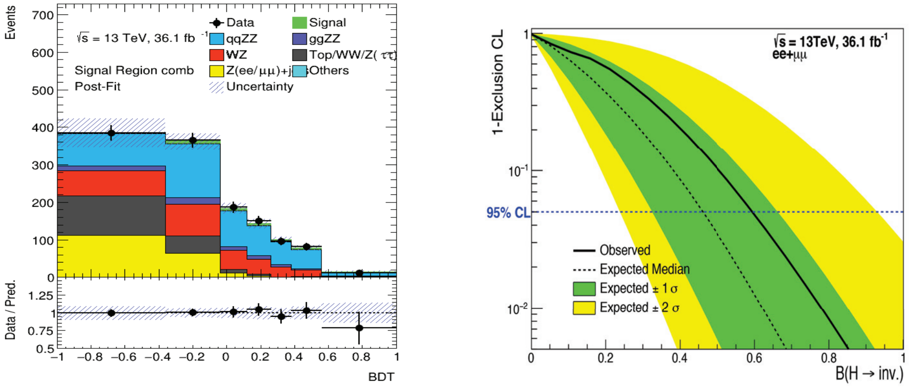

(a) **(b)**

Fig. S.3 · Observed BDT score distribution for the combined $ee + \mu\mu$ channel (a) and scan of "1− Exclusion CL" as a function of BR($H \to inv.$) with $m_H = 125$ GeV using the combined $ee + \mu\mu$ channel (b).

exclusion limits is shown in Table S.1. The BDT analysis shows no improvement compared to the cut-based one. This is due to the effect of systematics uncertainties introduced by the method itself in terms of the BDT output shape and by loosening the kinematic cuts compared to the cut-based selection. Loosening the cuts ensured a gain for the expected limit in statistical terms only, but also introduced an higher contribution of jet systematics which diluted the limit improvement.

For a multi-purpose experiment collecting an enormous amount of data such as ATLAS, a data monitoring system providing fast results is essential. Since 2011 ATLAS implemented a fast physics monitoring system based on a light file format (TAg) for DAta: TADA. The system monitors a wide spectrum of new physics channels, aspects of offline data quality and physics performance. This system is part of the ATLAS Tier-0 data processing at CERN and implements the full analysis level calibrations. The guiding principle of TADA search is to cover a broad spectrum of final states, while being inspired by the offline selections for the corresponding channels. TADA output is available on a website that gets updated daily with data from newly processed runs. Figure S.4a shows an example of the final discriminant variable, the invariant dilepton mass M_{ee}, for an exotic search in the $Z \to ee$ channel. Figure S.4b shows a performance test performed by TADA, specifically the stability plot of a semileptonic $(e\mu)$ $t\bar{t}$ yield over a specified run number period. TADA can also provide hints of potentially interesting physics signals or performance issues that are reported to be followed up by physics or combined performance groups. It is preeminent to notice the huge impact TADA had in the first months of Run-II in the ATLAS Collaboration in terms of its usage for several studies which have been reported in talks, meetings and conferences.

	Obs. $\mathrm{BR}(H \to inv.)$ Limit		Exp. $\mathrm{BR}(H \to inv.)$ Limit $\pm 1\sigma \pm 2\sigma$	
	BDT	Cut-Based	BDT	Cut-Based
ee	58%	59%	$(56\,^{+22}_{-18}\,^{+52}_{-28})\%$	$(51\,^{+21}_{-15}\,^{+49}_{-24})\ \%$
$\mu\mu$	95%	97%	$(56\,^{+26}_{-17}\,^{+53}_{-27})\%$	$(48\,^{+20}_{-14}\,^{+46}_{-22})\ \%$
$ee + \mu\mu$	60%	67%	$(46\,^{+20}_{-13}\,^{+47}_{-22})\%$	$(39\,^{+17}_{-11}\,^{+38}_{-18})\ \%$

Table S.1 · The 95% CL upper limits on $\mathrm{BR}(H \to inv.)$ for $m_H = 125$ GeV from the ee, $\mu\mu$, and combined $ee + \mu\mu$ channel for the BDT and Cut-based analysis.

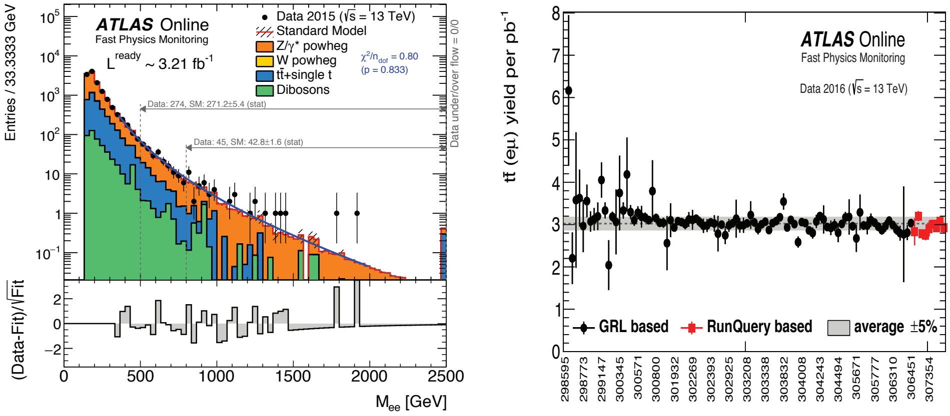

(a) **(b)**

Fig. S.4 · M_{ee} distribution for the $Z \rightarrow ee$ exotic search (a) and stability plot of a semileptonic ($e\mu$) $t\bar{t}$ yield over a specific run number period (b).

Samenvatting

HET STANDAARD MODEL (SM) is een theoretisch model dat elementaire deeltjes beschrijft en hun interactie met de drie fundamentele natuurkrachten: de elektromagnetische kracht, de sterke kernkracht en de zwakke kernkracht. Het SM beschrijft de elementaire bouwstenen van de natuur in termen van twee verschillende deeltjes velden: fermionen en bosonen. De elementaire componenten van materie zijn halftallige spin deeltjes, de *fermionen*, en zijn opgedeeld in drie smaken van *quarks (u, d, c, s, t, b)* en *leptonen* $(e, \nu_e, \mu, \nu_\mu, \tau, \nu_\tau)$. De dragers van de krachtvelden zijn heeltallige spin deeltjes, de *bosonen*: het photon, γ, is de dragen van de electromagnetische kracht, de $W^{\pm}$ en Z zijn de dragers van de zwakke kernkracht en de gluonen, g, zijn de dragers van de sterke kernkracht. Dankzij het spontane symmetriebreking mechanisme verkrijgen zowel fermionen als bosonen hun massa door hun interactie met het Higgs veld: de bijbehorende Higgs boson is in 2012 ontdekt door ATLAS en CMS. Het SM, dat veel getest is in de afgelopen decennia, heeft zich bewezen als een erg precies en voorspellend model; niettemin heeft het een aantal tekortkomingen zoals het ontbreken van een formulering over de interactie tussen materie en zwaartekracht of het ontbreken van enige beschrijving voor het astrofysische bewijs dat aangeeft dat Donkere Materie bestaat.

De exacte compositie van het universum is onbekend: het meest succesvolle model, het Standaard Kosmologische Model, beschrijft een uitdijend versnellend universum wat vooral uit Donkere Energie (74%) en Donkere Materie (21%) bestaat, met alleen een klein gedeelte wat over blijft voor Baryonen (5%). Dit model laat zien dat Donkere Materie zorgt voor het grootste gedeelte van materie in het universum (75%). Een overvloed aan kosmologische bewijsstukken wijzen naar het bestaan van Donkere Materie zoals de rotatie curves van sterrenstelsels, het zwaartekrachtlenseffect en de Komische achtergrondstraling. Deze bewijzen laten zien dat Donkerie Materie alleen een interactie aan gaat met gewone materie via zwaartekracht zonder enige zwakke kernkracht of sterke kernkracht interactie en dat de meest belovende kandidaat een Weakly Interacting Massive Particle (WIMP) is op de GeV-TeV schaal. Deze energie band is in het bereik van hedendaagse experimenten en de WIMP Donkere Materie kan gedetecteerd worden via directe, indirecte en productie onderzoeken. Indirecte onderzoeken kijken naar het straling spectrum vanuit de atmosfeer, zoekende naar verval producten van Donkere Materie paar annihilatie, directe onderzoeken kijken naar nucleaire verstrooiing van Donkere Materie tegen een zwaar doelwit van gewone materie en tenslotte kan Donkere Materie worden geproduceerd en gedetecteerd in hoge energie versnellers.

Het werk van deze thesis gaat over het zoeken naar Donkere Materie via het verval van een Higgs boson geproduceerd in de proton-proton botsingen in de Large Hadron Collider (LHC).

De LHC is een twee ring supergeleidende deeltjes versneller in CERN langs de Frans-

Zwitserse grens, met een onderwerp botsingsenergie van $\sqrt{s} = 14$ TeV. "A Toroidal LHC Apparatus" (ATLAS) is een van de vier detecteren die geïnstalleerd is bij de LHC en het is een multifunctioneel experiment met als hoofdtaken het vinden van het Higgs boson, precisiemetingen aan het SM en onderzoeken naar fysica dat voorbij gaat aan het SM, zoals Donkere Materie. De ATLAS detector heeft, gedurende 2015 en 2016, 36.1 fb^{-1} gemeten aan proton-proton botsingen op een energie van $\sqrt{s} = 13$ TeV, wat de geanalyseerde dataset is in deze thesis.

Het werk van deze thesis is het onderzoek naar Donkere Materie door middel van een onzichtbaar Higgs verval met bijbehorende productie van een Z boson met uiteindelijk twee leptonen en missende energie in de detector:

$$pp \rightarrow ZH \rightarrow l^+l^- + E_T^{\text{miss}}$$

Het theoretische model waarop dit onderzoek is gebaseerd is het Higgs Portal Model. In dit model is de SM lagrangiaan aangepast door het toevoegen van een Donkere Materie veld dat alleen interactie heeft met de SM sector via het Higgs veld. In het SM is de vertakkingsgraad van het Higgs boson naar lang-levende onzichtbare deeltjes (zoals neutrinos) extreem klein, daardoor is het opduiken van de aanwezigheid hiervan een indicatie voor nieuwe fenomenen zoals Donkere Materie. Om een *onzichtbaar* signal (gekarakteriseerd door E_T^{miss}) te meten is het nodig om iets daarbij behorend te meten, wat in deze thesis een Z boson is.

Het signaal is gesimuleerd door Monte Carlo (MC) methodes die zowel gluon-gluon fusie als quark-quark annihilatie productie methoden gebruiken zoals te zien is in Figuur S.1. De geobserveerde data opbrengst, de afgeschatte achtergrond contributies en de verwachtingen voor het signaal process na de uiteindelijke selectie van de meest scheidende variabele, de E_T^{miss}, is te zien in Figuur S.2a. In de recente jaren is het gebruik van multivariabele technieken voor data analyse breed verspreid in de wetenschappelijke gemeenschap. In deze thesis is een multivariabele techniek toegepast op een standaard analyse, wat we de analyse met snedes noemen voor eenvoud. De techniek die gebruikt is heet een boosted decision tree (BDT) wat een binair opeenvolgend splitsings algoritme is dat gebruikt kan worden voor classificatie van signaal versus achtergrond. Vergelijkbaar met de analyse gebaseerd op snedes wordt een een fase ruimte gedefinieerd waarop de BDT getraind kan worden en de classificatie procedure kan uitoefenen. De training procedure verzorgd als output een classificatie, de BDT score, wat de gekozen scheidende variabele is voor deze analyse. De

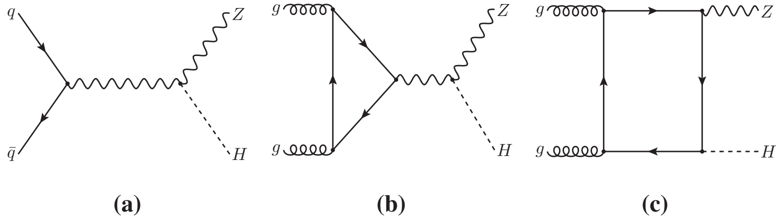

Fig. S.1 · Feynman diagram van ZH productie bij de LHC via quark-antiquark annihilatie (a) en gluon-gluon fusie (b),(c).

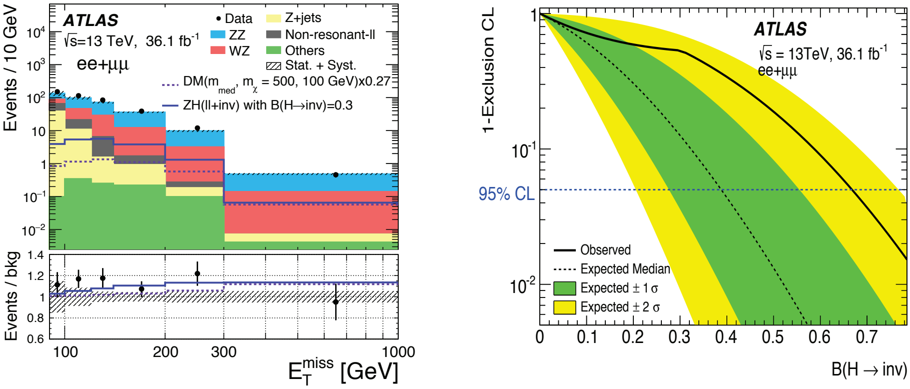

(a) **(b)**

Fig. S.2 · Geobserveerde E_T^{miss} distributie voor het gecombineerde $ee + \mu\mu$ kanalen voor de analyse met snedes (a) en scan van “1− Exclusion CL” als een functie van $BR(H \to inv.)$ met $m_H = 125$ GeV gebruikt makend van de gecombineerde $ee + \mu\mu$ kanalen (b).

geobserveerde data opbrengst, de afgeschatte achtergrond contributies en de verwachtingen van het signaal process zijn te zien in Figuur S.3a. Net zoals in de analyse gebaseerd op snedes is het resultaat compatibel met SM voorspellingen. Een exclusie limiet is gezet op de Higgs naar onzichtbaar verpakkingsgraad en de resultaten zijn te zien in Figuur S.3b. De vergelijking tussen de BDT en op snedes gebaseerde exclusie limieten is te zien in

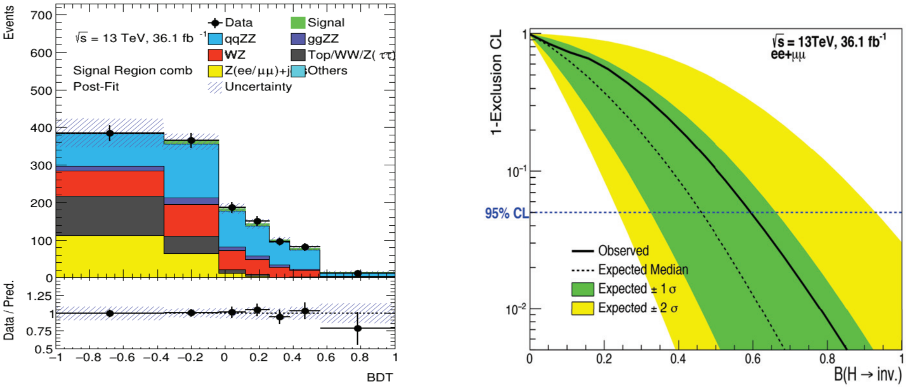

(a) **(b)**

Fig. S.3 · De geobserveerde BDT score distributie voor de gecombineerde $ee + \mu\mu$ kanelen (a) en scan van “1− Exclusion CL” als functie van $BR(H \to inv.)$ met $m_H = 125$ GeV gebruik makende van de $ee + \mu\mu$ kanalen (b).

Tabel S.1. De BDT analyse laat geen verbetering ten opzichte van de analyse gebaseerd op snedes zien. Dit komt door de systematische onzekerheden die geïntroduceerd worden door de methode zelf, de BDT output vorm en het versoepelen van de kinematische snedes, in vergelijking tot de op snedes gebaseerde analyse. Het versoepelen van de cuts zorgt alleen voor een toename van het verwachte limiet in statistische termen, maar introduceert een hogere contributie van jet systematiek wat de verbetering van het limiet vertroebelt.

	Obs. $BR(H \to inv.)$ Limit		Exp. $BR(H \to inv.)$ Limit $\pm 1\sigma \pm 2\sigma$	
	BDT	Snedes	BDT	Snedes
ee	58%	59%	$(56\,{}^{+22}_{-18}\,{}^{+52}_{-28})\%$	$(51\,{}^{+21}_{-15}\,{}^{+49}_{-24})\ \%$
$\mu\mu$	95%	97%	$(56\,{}^{+26}_{-17}\,{}^{+53}_{-27})\%$	$(48\,{}^{+20}_{-14}\,{}^{+46}_{-22})\ \%$
$ee + \mu\mu$	60%	67%	$(46\,{}^{+20}_{-13}\,{}^{+47}_{-22})\%$	$(39\,{}^{+17}_{-11}\,{}^{+38}_{-18})\ \%$

Table S.1 · The 95% CL upper limits op $BR(H \to inv.)$ voor $m_H = 125$ GeV van de ee, $\mu\mu$, en gecombineerde $ee + \mu\mu$ kanalen van de BDT en op snedes gebaseerde analyse.

Voor een multifunctioneel experiment wat een enorme hoeveelheid data verzameld zoals ATLAS, is een data monitor systeem dat snelle resultaten produceert essentieel. Sinds 2011 heeft ATLAS een snel fysica monitor systeem gebaseerd op het lichte bestandsformaat (TAg) for DAta: TADA. Het systeem houdt toezicht op een breed spectrum aan nieuwe fysica kanalen, aspecten van offline data kwaliteit en fysica prestatie. Het systeem maakt onderdeel uit van ATLAS Tier-0 data verwerking op CERN en implementeert de volledige analyse calibratie. Het leidende principe van TADA is om een zo breed spectrum aan mogelijkheden te bekijken, terwijl het geïnspireerd wordt door offline selecties voor de corresponderende kanalen. TADA output is beschikbaar op een website dat elke dag geüpdatet wordt met data van de nieuwe metingen. Figuur S.4a laat een voorbeeld zien van een uiteindelijk scheidende variabele, de invariante dilepton massa M_{ee}, voor een onderzoek naar het $Z \to ee$ kanaal. Figuur S.4b laat een prestatie test zien uitgevoerd door TADA, vooral de stabiliteit plot van het halflleptoninische $(e\mu)$ $t\bar{t}$ opbrengst tijdens een specifieke meningsperiode. TADA kan ook hints geven over potentieel interessante fysica signalen of prestatie problemen die vervolgens weer opgepikt kunnen worden door de desbetreffende groepen. Het is belangrijk op de grote impact van TADA te realiseren in de eerste maanden van Run-II in de ATLAS collaboratie in termen van de verschillende studies die in presentaties naar voren zijn gekomen, of op bijeenkomsten en conferenties.

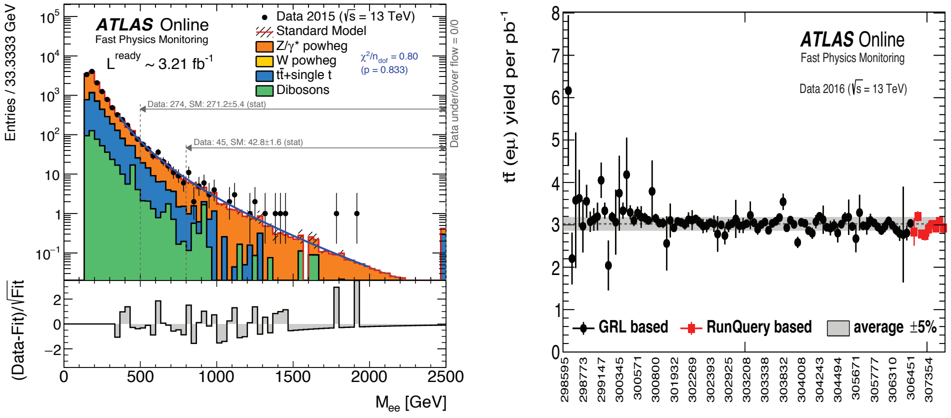

(a) **(b)**

Fig. S.4 · M_{ee} distributie voor het $Z \to ee$ onderzoek (a) en de stabiliteit plot voor het halflleptoninische (eμ) $t\bar{t}$ opbrengst tijdens een specifieke meningsperiode (b).

Bibliography

[1] ATLAS Collaboration, M. Aaboud et al., *Search for an invisibly decaying Higgs boson or dark matter candidates produced in association with a* Z *boson in* pp *collisions at* $\sqrt{s} = 13$ *TeV with the ATLAS detector*, Phys. Lett. **B776** (2018) 318–337, `arXiv:1708.09624 [hep-ex]`. (Cited on pages 2 and 101.)

[2] G. Sabato, M. Elsing, C. Gumpert, S. Kamioka, E. Moyse, A. Nairz, and T. Eifert, *ATLAS fast physics monitoring: TADA*, Journal of Physics: Conference Series **898** (2017) 092015. `https://doi.org/10.1088%2F1742-6596%2F898%2F9%2F092015`. (Cited on pages 2, 143, and 145.)

[3] S. Weinberg, *A Model of Leptons*, Phys. Rev. Lett. **19** (1967) 1264–1266. (Cited on page 3.)

[4] A. Salam, *Weak and Electromagnetic Interactions*, Conf. Proc. **C680519** (1968) 367–377. (Cited on pages 3 and 6.)

[5] S. Glashow, *Partial Symmetries of Weak Interactions*, Nucl. Phys. **22** (1961) 579–588. (Cited on pages 3 and 6.)

[6] S. Weinberg, *A Model of Leptons*, Phys. Rev. Lett. **19** (1967) 1264–1266. (Cited on pages 3 and 6.)

[7] M. E. Peskin and D. V. Schroeder, *An Introduction to Quantum Field Theory*. Westview Press, Boulder, 1995. (Cited on page 3.)

[8] ATLAS Collaboration, *Observation of a new particle in the search for the Standard Model Higgs boson with the ATLAS detector at the LHC*, Phys. Lett. **B 716** (2012) 1–29, `arXiv:1207.7214 [hep-ex]`. (Cited on page 3.)

[9] CMS Collaboration, *Observation of a new boson at a mass of 125 GeV with the CMS experiment at the LHC*, Phys. Lett. **B 716** (2012) 30–61, `arXiv:1207.7235 [hep-ex]`. (Cited on page 3.)

[10] P. W. Higgs, *Broken Symmetries and the Masses of Gauge Bosons*, Phys. Rev. Lett. **13** (1964) 508–509. (Cited on pages 3 and 7.)

[11] C. N. Yang and R. L. Mills, *Conservation of Isotopic Spin and Isotopic Gauge Invariance*, Phys. Rev. **96** (1954) 191–195. `https://link.aps.org/doi/10.1103/PhysRev.96.191`. (Cited on page 4.)

[12] A. Purcell, *Go on a particle quest at the first CERN webfest. Le premier webfest du CERN se lance à la conquête des particules*,. `https://cds.cern.ch/record/1473657`. (Cited on page 5.)

[13] D. J. Gross and F. Wilczek, *Ultraviolet Behavior of Nonabelian Gauge Theories*, Phys. Rev. Lett. **30** (1973) 1343–1346. [,271(1973)]. (Cited on page 4.)

[14] H. D. Politzer, *Reliable Perturbative Results for Strong Interactions?*, Phys. Rev. Lett. **30** (1973) 1346–1349. [,274(1973)]. (Cited on page 4.)

[15] M. Gell-Mann, *A Schematic Model of Baryons and Mesons*, Phys. Lett. **8** (1964) 214–215. (Cited on page 4.)

[16] R. P. Feynman, *Mathematical Formulation of the Quantum Theory of Electromagnetic Interaction*, Phys. Rev. **80** (1950) 440–457. (Cited on page 6.)

[17] T. Nakano and K. Nishijima, *Charge Independence for V-particles*, Prog. Theor. Phys. **10** (1953) 581–582. (Cited on page 7.)

[18] M. Gell-Mann, *The interpretation of the new particles as displaced charge multiplets*, Nuovo Cim. **4** no. S2, (1956) 848–866. (Cited on page 7.)

[19] F. Englert and R. Brout, *Broken Symmetry and the Mass of Gauge Vector Mesons*, Phys. Rev. Lett. **13** (1964) 321–323. [,157(1964)]. (Cited on page 7.)

[20] J. Goldstone, *Field Theories with Superconductor Solutions*, Nuovo Cim. **19** (1961) 154–164. (Cited on page 7.)

[21] J. Ellis, M. K. Gaillard, and D. V. Nanopoulos, *A Historical Profile of the Higgs Boson*, `arXiv:1201.6045 [hep-ph]`. (Cited on page 9.)

[22] P. Langacker, *Grand Unified Theories and Proton Decay*, Phys. Rept. **72** (1981) 185. (Cited on page 11.)

[23] E. Gildener, *Gauge Symmetry Hierarchies*, Phys. Rev. **D14** (1976) 1667. (Cited on page 11.)

[24] B. Pontecorvo, *Neutrino Experiments and the Problem of Conservation of Leptonic Charge*, Sov. Phys. JETP **26** (1968) 984–988. [Zh. Eksp. Teor. Fiz.53,1717(1967)]. (Cited on page 11.)

[25] Super-Kamiokande Collaboration, Y. Fukuda et al., *Evidence for oscillation of atmospheric neutrinos*, Phys. Rev. Lett. **81** (1998) 1562–1567, `arXiv:hep-ex/9807003 [hep-ex]`. (Cited on page 11.)

[26] S. Weinberg, *The U(1) problem*, Phys. Rev. D **11** (1975) 3583–3593. `https://link.aps.org/doi/10.1103/PhysRevD.11.3583`. (Cited on page 11.)

[27] G. ’t Hooft, *Computation of the quantum effects due to a four-dimensional pseudoparticle*, Phys. Rev. D **14** (1976) 3432–3450. `https://link.aps.org/doi/10.1103/PhysRevD.14.3432`. (Cited on page 11.)

[28] A. A. Starobinsky, *A New Type of Isotropic Cosmological Models Without Singularity*, Phys. Lett. **B91** (1980) 99–102. [,771(1980)]. (Cited on page 12.)

[29] E. W. Kolb and M. S. Turner, *The Early Universe*, Front. Phys. **69** (1990) 1–547. (Cited on pages 12, 19, and 20.)

[30] McDonald Observatory, 2019. `https://mcdonaldobservatory.org/file/pie-chartjpg`. (Cited on page 12.)

[31] NOAO/AURA/NSF.
`https://www.noao.edu/image_gallery/images/d6/m33_opta.jpg`. (Cited on page 13.)

[32] F. Zwicky, *Die Rotverschiebung von extragalaktischen Nebeln*, Helv. Phys. Acta **6** (1933) 110–127. [Gen. Rel. Grav.41,207(2009)]. (Cited on page 13.)

[33] G. Bertone and D. Hooper, *A History of Dark Matter*, Submitted to: Rev. Mod. Phys. (2016), `arXiv:1605.04909 [astro-ph.CO]`. (Cited on page 14.)

[34] B. F. R. Carroll, R. Gendler, 2018.
`https://apod.nasa.gov/apod/image/1803/ComaCluster_Carroll_1024.jpg`. (Cited on page 14.)

[35] A. Einstein, *Lens-Like Action of a Star by the Deviation of Light in the Gravitational Field*, Science **84** (1936) 506–507. (Cited on page 15.)

[36] NASA Collaboration, 2013.
`https://cdn.spacetelescope.org/archives/images/screen/heic1317a.jpg`. (Cited on page 15.)

[37] NASA Collaboration, D.Clowe et al., 2006.
`https://apod.nasa.gov/apod/image/0608/bulletcluster_comp_f2048.jpg`. (Cited on page 16.)

[38] D. Clowe, M. Bradac, A. H. Gonzalez, M. Markevitch, S. W. Randall, C. Jones, and D. Zaritsky, *A direct empirical proof of the existence of dark matter*, Astrophys. J. **648** (2006) L109–L113, `arXiv:astro-ph/0608407 [astro-ph]`. (Cited on page 16.)

[39] Planck Collaboration, Y. Akrami et al., *Planck 2018 results. I. Overview and the cosmological legacy of Planck*, `arXiv:1807.06205 [astro-ph.CO]`. (Cited on page 17.)

[40] W. Hu and M. J. White, *Acoustic signatures in the cosmic microwave background*, Astrophys. J. **471** (1996) 30–51, `arXiv:astro-ph/9602019 [astro-ph]`. (Cited on page 18.)

[41] Planck Collaboration Collaboration, Ade et al., *Planck 2015. XX. Constraints on inflation*, Astron. Astrophys. **594** no. arXiv:1502.02114, (2015) A20. 65 p.
`http://cds.cern.ch/record/1987798`. 68 pages, 59 figures, 18 tables; updates to match the published version. (Cited on page 18.)

[42] M. Dine, W. Fischler, and M. Srednicki, *A Simple Solution to the Strong CP Problem with a Harmless Axion*, Phys. Lett. **104B** (1981) 199–202. (Cited on pages 17 and 22.)

[43] Planck Collaboration, N. Aghanim et al., *Planck 2018 results. VI. Cosmological parameters*, `arXiv:1807.06209 [astro-ph.CO]`. (Cited on page 21.)

[44] H. P. Nilles, *Supersymmetry, Supergravity and Particle Physics*, Phys. Rept. **110** (1984) 1–162. (Cited on page 21.)

[45] H. V. Klapdor-Kleingrothaus et al., *Latest results from the Heidelberg-Moscow double beta decay experiment*, Eur. Phys. J. **A12** (2001) 147–154, `arXiv:hep-ph/0103062 [hep-ph]`. (Cited on page 21.)

[46] S. Dodelson and L. M. Widrow, *Sterile-neutrinos as dark matter*, Phys. Rev. Lett. **72** (1994) 17–20, `arXiv:hep-ph/9303287 [hep-ph]`. (Cited on page 21.)

[47] S. P. Martin, *A Supersymmetry primer*, Adv. Ser. Direct. High Energy Phys. **21** (2010) 1–153, `arXiv:hep-ph/9709356 [hep-ph]`. (Cited on page 21.)

[48] H. K. Dreiner, S. Heinemeyer, O. Kittel, U. Langenfeld, A. M. Weber, et al., *Mass Bounds on a Very Light Neutralino*, Eur. Phys. J. **C 62** (2009) 547–572, `arXiv:0901.3485 [hep-ph]`. (Cited on page 21.)

[49] T. Kaluza, *Zum Unitatsproblem der Physik*, Sitzungsber. Preuss. Akad. Wiss. Berlin (Math. Phys.) **1921** (1921) 966–972, `arXiv:1803.08616 [physics.hist-ph]`. (Cited on page 22.)

[50] O. Klein, *Quantum Theory and Five-Dimensional Theory of Relativity. (In German and English)*, Z. Phys. **37** (1926) 895–906. [,76(1926)]. (Cited on page 22.)

[51] L. Randall and R. Sundrum, *A Large mass hierarchy from a small extra dimension*, Phys. Rev. Lett. **83** (1999) 3370–3373, `arXiv:hep-ph/9905221 [hep-ph]`. (Cited on page 22.)

[52] D. Hooper and S. Profumo, *Dark matter and collider phenomenology of universal extra dimensions*, Phys. Rept. **453** (2007) 29–115, `arXiv:hep-ph/0701197 [hep-ph]`. (Cited on page 22.)

[53] H.-C. Cheng, J. L. Feng, and K. T. Matchev, *Kaluza-Klein dark matter*, Phys. Rev. Lett. **89** (2002) 211301, `arXiv:hep-ph/0207125 [hep-ph]`. (Cited on page 22.)

[54] A. Djouadi, G. Moreau, and R. K. Singh, *Kaluza-Klein excitations of gauge bosons at the LHC*, Nucl. Phys. **B797** (2008) 1–26, `arXiv:0706.4191 [hep-ph]`. (Cited on page 22.)

[55] M. Kamionkowski and J. March-Russell, *Planck scale physics and the Peccei-Quinn mechanism*, Phys. Lett. **B282** (1992) 137–141, `arXiv:hep-th/9202003 [hep-th]`. (Cited on page 22.)

[56] E. W. Kolb, D. J. H. Chung, and A. Riotto, *WIMPzillas!*, AIP Conf. Proc. **484** no. 1, (1999) 91–105, `arXiv:hep-ph/9810361 [hep-ph]`. [,592(1999)]. (Cited on page 22.)

[57] N. Arkani-Hamed, A. G. Cohen, E. Katz, and A. E. Nelson, *The Littlest Higgs*, JHEP **07** (2002) 034, `arXiv:hep-ph/0206021 [hep-ph]`. (Cited on page 22.)

[58] D. N. Spergel and P. J. Steinhardt, *Observational evidence for selfinteracting cold dark matter*, Phys. Rev. Lett. **84** (2000) 3760–3763, `arXiv:astro-ph/9909386 [astro-ph]`. (Cited on page 22.)

[59] H. M. Hodges, *Mirror baryons as the dark matter*, Phys. Rev. D **47** (1993) 456–459. `https://link.aps.org/doi/10.1103/PhysRevD.47.456`. (Cited on page 22.)

[60] A. de Rújula, S. L. Glashow, and U. Sarid, *Charged dark matter*, Nuclear Physics B **333** (1990) 173–194. (Cited on page 22.)

[61] J. I. Read, *The Local Dark Matter Density*, J. Phys. **G41** (2014) 063101, `arXiv:1404.1938 [astro-ph.GA]`. (Cited on page 22.)

[62] A. M. Green, *Astrophysical uncertainties on direct detection experiments*, Mod. Phys. Lett. **A27** (2012) 1230004, `arXiv:1112.0524 [astro-ph.CO]`. (Cited on page 22.)

[63] M. C. Smith et al., *The RAVE Survey: Constraining the Local Galactic Escape Speed*, Mon. Not. Roy. Astron. Soc. **379** (2007) 755–772, `arXiv:astro-ph/0611671 [astro-ph]`. (Cited on page 22.)

[64] XENON100 Collaboration, *Dark Matter Results from 225 Live Days of XENON100 Data*, Phys. Rev. Lett. **109** (2012) 181301, `arXiv:1207.5988 [astro-ph.CO]`. (Cited on pages 23, 24, and 33.)

[65] J. Billard, L. Strigari, and E. Figueroa-Feliciano, *Implication of neutrino backgrounds on the reach of next generation dark matter direct detection experiments*, Phys. Rev. **D89** no. 2, (2014) 023524, `arXiv:1307.5458 [hep-ph]`. (Cited on pages 23 and 24.)

[66] XENON Collaboration, E. Aprile et al., *Dark Matter Search Results from a One Ton-Year Exposure of XENON1T*, Phys. Rev. Lett. **121** no. 11, (2018) 111302, `arXiv:1805.12562 [astro-ph.CO]`. (Cited on pages 23 and 24.)

[67] DAMA Collaboration, *First results from DAMA/LIBRA and the combined results with DAMA/NaI*, Eur. Phys. J. **C 56** (2008) 333–355, `arXiv:0804.2741 [astro-ph]`. (Cited on pages 23 and 24.)

[68] XENON Collaboration, E. Aprile et al., *Physics reach of the XENON1T dark matter experiment*, JCAP **1604** no. 04, (2016) 027, `arXiv:1512.07501 [physics.ins-det]`. (Cited on page 24.)

[69] C. Savage, K. Freese, P. Gondolo, and D. Spolyar, *Compatibility of DAMA/LIBRA dark matter detection with other searches in light of new galactic rotation velocity measurements*, Journal of Cosmology and Astroparticle Physics **2009** no. 09, (2009) 036–036. (Cited on page 24.)

[70] CDMS Collaboration, R. Agnese et al., *Silicon Detector Dark Matter Results from the Final Exposure of CDMS II*, Phys. Rev. Lett. **111** no. 25, (2013) 251301, `arXiv:1304.4279 [hep-ex]`. (Cited on page 24.)

[71] XENON10 Collaboration Collaboration, J. Angle, E. Aprile, F. Arneodo, L. Baudis, A. Bernstein, A. I. Bolozdynya, L. C. C. Coelho, C. E. Dahl, L. DeViveiros, A. D. Ferella, L. M. P. Fernandes, S. Fiorucci, R. J. Gaitskell, K. L. Giboni, R. Gomez, R. Hasty, L. Kastens, J. Kwong, J. A. M. Lopes, N. Madden, A. Manalaysay, A. Manzur, D. N. McKinsey, M. E. Monzani, K. Ni, U. Oberlack, J. Orboeck, G. Plante, R. Santorelli, J. M. F. dos Santos, S. Schulte, P. Shagin, T. Shutt, P. Sorensen, C. Winant, and M. Yamashita, *Search for Light Dark Matter in XENON10 Data*, Phys. Rev. Lett. **107** (2011) 051301. `https://link.aps.org/doi/10.1103/PhysRevLett.107.051301`. (Cited on page 24.)

[72] SuperCDMS Collaboration, R. Agnese et al., *Search for Low-Mass Weakly Interacting Massive Particles with SuperCDMS*, Phys. Rev. Lett. **112** no. 24, (2014) 241302, `arXiv:1402.7137 [hep-ex]`. (Cited on page 24.)

[73] PandaX Collaboration, M. Xiao et al., *First dark matter search results from the PandaX-I experiment*, Sci. China Phys. Mech. Astron. **57** (2014) 2024–2030, `arXiv:1408.5114`

`[hep-ex]`. (Cited on page 24.)

[74] DarkSide Collaboration, P. Agnes et al., *Results From the First Use of Low Radioactivity Argon in a Dark Matter Search*, Phys. Rev. **D93** no. 8, (2016) 081101, `arXiv:1510.00702 [astro-ph.CO]`. [Addendum: Phys. Rev.D95,no.6,069901(2017)]. (Cited on page 24.)

[75] LUX Collaboration, *First results from the LUX dark matter experiment at the Sanford Underground Research Facility*, Phys. Rev. Lett. **112** (2014) 091303, `arXiv:1310.8214 [astro-ph.CO]`. (Cited on page 24.)

[76] E. Bulbul, M. Markevitch, A. Foster, R. K. Smith, M. Loewenstein, and S. W. Randall, *Detection of An Unidentified Emission Line in the Stacked X-ray spectrum of Galaxy Clusters*, Astrophys. J. **789** (2014) 13, `arXiv:1402.2301 [astro-ph.CO]`. (Cited on page 23.)

[77] D. Hooper and L. Goodenough, *Dark Matter Annihilation in The Galactic Center As Seen by the Fermi Gamma Ray Space Telescope*, Phys. Lett. **B697** (2011) 412–428, `arXiv:1010.2752 [hep-ph]`. (Cited on page 23.)

[78] PAMELA Collaboration, O. Adriani et al., *An anomalous positron abundance in cosmic rays with energies 1.5-100 GeV*, Nature **458** (2009) 607–609, `arXiv:0810.4995 [astro-ph]`. (Cited on page 23.)

[79] AMS Collaboration, *High Statistics Measurement of the Positron Fraction in Primary Cosmic Rays of 0.5–500 GeV with the Alpha Magnetic Spectrometer on the International Space Station*, Phys. Rev. Lett. **113** (2014) 121101. (Cited on page 23.)

[80] B. Acharya et al., *Introducing the CTA concept*, Astroparticle Physics **43** (2013) 3–18. (Cited on page 25.)

[81] H.E.S.S. Collaboration, F. Aharonian et al., *Observations of the Crab Nebula with H.E.S.S*, Astron. Astrophys. **457** (2006) 899–915, `arXiv:astro-ph/0607333 [astro-ph]`. (Cited on page 25.)

[82] J. Aleksia et al., *Optimized dark matter searches in deep observations of Segue 1 with MAGIC*, Journal of Cosmology and Astroparticle Physics **2014** no. 02, (2014) 008. `http://stacks.iop.org/1475-7516/2014/i=02/a=008`. (Cited on page 25.)

[83] Fermi-LAT Collaboration, M. Ackermann et al., *Searching for Dark Matter Annihilation from Milky Way Dwarf Spheroidal Galaxies with Six Years of Fermi Large Area Telescope Data*, Phys. Rev. Lett. **115** no. 23, (2015) 231301, `arXiv:1503.02641 [astro-ph.HE]`. (Cited on page 25.)

[84] K. N. Abazajian, N. Canac, S. Horiuchi, and M. Kaplinghat, *Astrophysical and Dark Matter Interpretations of Extended Gamma-Ray Emission from the Galactic Center*, Phys. Rev. **D90** no. 2, (2014) 023526, `arXiv:1402.4090 [astro-ph.HE]`. (Cited on page 25.)

[85] C. Gordon and O. Macias, *Dark Matter and Pulsar Model Constraints from Galactic Center Fermi-LAT Gamma Ray Observations*, Phys. Rev. **D88** no. 8, (2013) 083521, `arXiv:1306.5725 [astro-ph.HE]`. [Erratum: Phys. Rev.D89,no.4,049901(2014)]. (Cited on page 25.)

[86] T. Daylan, D. P. Finkbeiner, D. Hooper, T. Linden, S. K. N. Portillo, N. L. Rodd, and T. R. Slatyer, *The characterization of the gamma-ray signal from the central Milky Way: A case for annihilating dark matter*, Phys. Dark Univ. **12** (2016) 1–23, `arXiv:1402.6703 [astro-ph.HE]`. (Cited on page 25.)

[87] F. Calore, I. Cholis, and C. Weniger, *Background model systematics for the Fermi GeV excess*, Journal of Cosmology and Astroparticle Physics **2015** no. 03, (2015) 038–038. (Cited on page 25.)

[88] IceCube Collaboration Collaboration, M. G. Aartsen et al., *Search for Dark Matter Annihilations in the Sun with the 79-String IceCube Detector*, Phys. Rev. Lett. **110** (2013) 131302. `https://link.aps.org/doi/10.1103/PhysRevLett.110.131302`. (Cited on page 25.)

[89] Super-Kamiokande Collaboration Collaboration, Choi et al., *Search for Neutrinos from Annihilation of Captured Low-Mass Dark Matter Particles in the Sun by Super-Kamiokande*, Phys. Rev. Lett. **114** (2015) 141301. `https://link.aps.org/doi/10.1103/PhysRevLett.114.141301`. (Cited on page 25.)

[90] ANTARES Collaboration, S. Adrian-Martinez et al., *Limits on Dark Matter Annihilation in the Sun using the ANTARES Neutrino Telescope*, Phys. Lett. **B759** (2016) 69–74, `arXiv:1603.02228 [astro-ph.HE]`. (Cited on page 25.)

[91] KM3NeT Collaboration, S. Adrian-Martinez et al., *Letter of intent for KM3NeT 2.0*, J. Phys. **G43** no. 8, (2016) 084001, `arXiv:1601.07459 [astro-ph.IM]`. (Cited on page 25.)

[92] XENON100 Collaboration Collaboration, E. Aprile, M. Alfonsi, K. Arisaka, F. Arneodo, C. Balan, L. Baudis, B. Bauermeister, A. Behrens, P. Beltrame, K. Bokeloh, A. Brown, E. Brown, G. Bruno, R. Budnik, J. M. R. Cardoso, W.-T. Chen, B. Choi, A. P. Colijn, H. Contreras, J. P. Cussonneau, M. P. Decowski, E. Duchovni, S. Fattori, A. D. Ferella, W. Fulgione, F. Gao, M. Garbini, C. Ghag, K.-L. Giboni, L. W. Goetzke, C. Grignon, E. Gross, W. Hampel, F. Kaether, A. Kish, J. Lamblin, H. Landsman, R. F. Lang, M. Le Calloch, D. Lellouch, C. Levy, K. E. Lim, Q. Lin, S. Lindemann, M. Lindner, J. A. M. Lopes, K. Lung, T. Marrodán Undagoitia, F. V. Massoli, A. J. Melgarejo Fernandez, Y. Meng, M. Messina, A. Molinario, K. Ni, U. Oberlack, S. E. A. Orrigo, E. Pantic, R. Persiani, G. Plante, N. Priel, A. Rizzo, S. Rosendahl, J. M. F. dos Santos, G. Sartorelli, J. Schreiner, M. Schumann, L. Scotto Lavina, P. R. Scovell, M. Selvi, P. Shagin, H. Simgen, A. Teymourian, D. Thers, O. Vitells, H. Wang, M. Weber, and C. Weinheimer, *Limits on Spin-Dependent WIMP-Nucleon Cross Sections from 225 Live Days of XENON100 Data*, Phys. Rev. Lett. **111** (2013) 021301. `https://link.aps.org/doi/10.1103/PhysRevLett.111.021301`. (Cited on page 26.)

[93] D. B. Kaplan, *Effective field theories*, in *Beyond the standard model 5. Proceedings, 5th Conference, Balholm, Norway, April 29-May 4, 1997.* 1995. `arXiv:nucl-th/9506035 [nucl-th]`. (Cited on page 27.)

[94] G. Busoni, A. De Simone, E. Morgante, and A. Riotto, *On the Validity of the Effective Field Theory for Dark Matter Searches at the LHC*, Phys. Lett. **B728** (2014) 412–421, `arXiv:1307.2253 [hep-ph]`. (Cited on page 27.)

[95] J. Abdallah et al., *Simplified Models for Dark Matter and Missing Energy Searches at the LHC*, `arXiv:1409.2893 [hep-ph]`. (Cited on page 27.)

[96] A. Leike, *The Phenomenology of extra neutral gauge bosons*, Phys. Rept. **317** (1999) 143–250, `arXiv:hep-ph/9805494 [hep-ph]`. (Cited on page 27.)

[97] D. Abercrombie et al., *Dark Matter Benchmark Models for Early LHC Run-2 Searches: Report of the ATLAS/CMS Dark Matter Forum*, `arXiv:1507.00966 [hep-ex]`. (Cited on page 29.)

[98] ATLAS Collaboration, *Dark Matter Summary*, 2017. `https://atlas.web.cern.ch/Atlas/GROUPS/PHYSICS/CombinedSummaryPlots/EXOTICS/ATLAS_DarkMatter_Summary/ATLAS_DarkMatter_Summary_201703.png`. (Cited on page 29.)

[99] ATLAS Collaboration, G. Aad et al., *Constraints on new phenomena via Higgs boson couplings and invisible decays with the ATLAS detector*, JHEP **11** (2015) 206, `arXiv:1509.00672 [hep-ex]`. (Cited on pages 29 and 34.)

[100] A. Djouadi, O. Lebedev, Y. Mambrini, and J. Quevillon, *Implications of LHC searches for Higgs–portal dark matter*, Phys. Lett. **B709** (2012) 65–69, `arXiv:1112.3299 [hep-ph]`. (Cited on page 30.)

[101] G. Breit and E. Wigner, *Capture of Slow Neutrons*, Phys. Rev. **49** (1936) 519–531. (Cited on page 30.)

[102] L. Evans and P. Bryant, *LHC Machine*, JINST **3** (2008) S08001. (Cited on page 35.)

[103] *LEP design report*. CERN, Geneva, 1984. (Cited on page 35.)

[104] ATLAS Collaboration, *The ATLAS Experiment at the CERN Large Hadron Collider*, JINST **3** (2008) S08003. (Cited on page 35.)

[105] CMS Collaboration, *The CMS experiment at the CERN LHC*, JINST **3** (2008) S08004. (Cited on page 35.)

[106] ALICE Collaboration, *The ALICE experiment at the CERN LHC*, JINST **3** (2008) S08002. (Cited on page 35.)

[107] LHCb Collaboration, *The LHCb Detector at the LHC*, JINST **3** (2008) S08005. (Cited on page 35.)

[108] C. Lefèvre, *The CERN accelerator complex. Complexe des accélérateurs du CERN*, `https://cds.cern.ch/record/1260465`, Dec, 2008. (Cited on page 36.)

[109] ATLAS Collaboration, *Luminosity Results Run 2*, `https://twiki.cern.ch/twiki/bin/view/AtlasPublic/LuminosityPublicResultsRun2`. (Cited on pages 37 and 38.)

[110] ATLAS Collaboration, *Measurement of the Inelastic Proton-Proton Cross Section at* $\sqrt{s} = 13$ *TeV with the ATLAS Detector at the LHC*,. (Cited on page 38.)

[111] ATLAS Collaboration, *ATLAS data summary*, `https://atlas.web.cern.ch/Atlas/GROUPS/DATAPREPARATION/DataSummary`. (Cited on page 38.)

[112] O. S. Bruning, P. Collier, P. Lebrun, S. Myers, R. Ostojic, J. Poole, and P. Proudlock, *LHC Design Report Vol.1: The LHC Main Ring*,. (Cited on page 38.)

[113] ATLAS Collaboration, *ATLAS detector and physics performance: Technical Design Report, 1*. No. ATLAS-TDR-14 in Technical Design Report ATLAS. CERN, Geneva, 1999. (Cited on page 39.)

[114] ATLAS Collaboration, *ATLAS detector and physics performance: Technical Design Report, 2*. No. ATLAS-TDR-15 in Technical Design Report ATLAS. CERN, Geneva, 1999. (Cited on page 39.)

[115] ATLAS Collaboration, G. Aad et al., *The ATLAS Experiment at the CERN Large Hadron Collider*, JINST **3** (2008) S08003. (Cited on pages 39, 41, 42, and 44.)

[116] ATLAS Collaboration, *ATLAS inner detector: Technical design report. Vol. 1*,. (Cited on page 40.)

[117] ATLAS Collaboration, *ATLAS inner detector: Technical design report. Vol. 2*,. (Cited on page 40.)

[118] ATLAS Collaboration, Y. Takubo, *The Pixel Detector of the ATLAS experiment for the Run2 at the Large Hadron Collider*, JINST **10** no. 02, (2015) C02001, `arXiv:1411.5338 [physics.ins-det]`. (Cited on page 40.)

[119] ATLAS Collaboration, *ATLAS liquid-argon calorimeter: Technical Design Report*. No. ATLAS-TDR-2 in Technical Design Report ATLAS. CERN, Geneva, 1996. (Cited on page 42.)

[120] ATLAS Collaboration, *ATLAS tile calorimeter: Technical Design Report*. No. ATLAS-TDR-3 in Technical Design Report ATLAS. CERN, Geneva, 1996. (Cited on page 43.)

[121] ATLAS Collaboration, *ATLAS muon spectrometer: Technical design report*,. (Cited on page 43.)

[122] ATLAS Collaboration, A. Ruiz-Martinez et al., *The Run-2 ATLAS Trigger System*, Tech. Rep. ATL-DAQ-PROC-2016-003, CERN, Geneva, Feb, 2016. `https://cds.cern.ch/record/2133909`. (Cited on page 44.)

[123] T. Cornelissen, M. Elsing, S. Fleischmann, W. Liebig, E. Moyse, and A. Salzburger, *Concepts, Design and Implementation of the ATLAS New Tracking (NEWT)*, Tech. Rep. ATL-SOFT-PUB-2007-007, CERN, Geneva, Mar, 2007. (Cited on page 47.)

[124] R. E. Kalman, *A New Approach to Linear Filtering and Prediction Problems*, Trans. ASME J. Basic Eng. **D 82** (1960) 35–45. (Cited on pages 47 and 51.)

[125] D. Wicke, *A New Algorithm For Solving Tracking Ambiguities*,. (Cited on page 47.)

[126] ATLAS Collaboration, *Early Inner Detector Tracking Performance in the 2015 data at* $\sqrt{s}$ = *13 TeV*, Tech. Rep. ATL-PHYS-PUB-2015-051, CERN, Geneva, Dec, 2015.

`https://cds.cern.ch/record/2110140`. (Cited on page 48.)

[127] A. Sidoti, *Minimum Bias Trigger Scintillators in ATLAS Run II*, Journal of Instrumentation **9** no. 10, (2014) C10020–C10020. (Cited on page 48.)

[128] T. Sjöstrand, S. Mrenna, and P. Z. Skands, *A Brief Introduction to PYTHIA 8.1*, Comput. Phys. Commun. **178** (2008) 852–867, `arXiv:0710.3820 [hep-ph]`. (Cited on page 48.)

[129] W. Waltenberger, R. Frühwirth, and P. Vanlaer, *Adaptive vertex fitting*, J. Phys. **G 34** (2007) N343. (Cited on page 48.)

[130] ATLAS Collaboration, M. Aaboud et al., *Performance of the ATLAS Track Reconstruction Algorithms in Dense Environments in LHC Run 2*, Eur. Phys. J. **C77** no. 10, (2017) 673, `arXiv:1704.07983 [hep-ex]`. (Cited on page 48.)

[131] ATLAS Collaboration, *Vertex Reconstruction Performance of the ATLAS Detector at* $\sqrt{s} = 13\ \mathrm{TeV}''$, Tech. Rep. ATL-PHYS-PUB-2015-026, CERN, Geneva, Jul, 2015. `http://cds.cern.ch/record/2037717`. (Cited on page 49.)

[132] S. Pagan Griso, K. Prokofiev, A. Andreazza, K. Grimm, E. Guido, F. Meloni, M. Rudolph, A. Salzburger, and A. Wildauer, *Vertex reconstruction plots: Collision performance plots for approval*, Tech. Rep. ATL-COM-PHYS-2012-474, CERN, Geneva, Apr, 2012. `https://cds.cern.ch/record/1445579`. (Cited on page 49.)

[133] W. Lampl, S. Laplace, D. Lelas, P. Loch, H. Ma, et al., *Calorimeter Clustering Algorithms: Description and Performance*, Tech. Rep. ATL-LARG-PUB-2008-002, CERN, Geneva, Apr, 2008. (Cited on page 49.)

[134] T. G. Cornelissen, M. Elsing, I. Gavrilenko, J. F. Laporte, W. Liebig, M. Limper, K. Nikolopoulos, A. Poppleton, and A. Salzburger, *The global chi**2 track fitter in ATLAS*, J. Phys. Conf. Ser. **119** (2008) 032013. (Cited on page 50.)

[135] ATLAS Collaboration, *Improved electron reconstruction in ATLAS using the Gaussian Sum Filter-based model for bremsstrahlung*, Tech. Rep. ATLAS-CONF-2012-047, CERN, Geneva, May, 2012. (Cited on page 50.)

[136] ATLAS Collaboration Collaboration, *Electron efficiency measurements with the ATLAS detector using the 2015 LHC proton-proton collision data*, Tech. Rep. ATLAS-CONF-2016-024, CERN, Geneva, Jun, 2016. `https://cds.cern.ch/record/2157687`. (Cited on page 50.)

[137] ATLAS Collaboration, G. Aad et al., *Muon reconstruction performance of the ATLAS detector in proton–proton collision data at* $\sqrt{s}$ *=13 TeV*, Eur. Phys. J. **C76** no. 5, (2016) 292, `arXiv:1603.05598 [hep-ex]`. (Cited on pages 51 and 52.)

[138] ATLAS Collaboration, *Measurement of the muon reconstruction performance of the ATLAS detector using 2011 and 2012 LHC proton–proton collision data*, The European Physical Journal C **74** no. 11, (2014) 3130. `https://doi.org/10.1140/epjc/s10052-014-3130-x`. (Cited on page 51.)

[139] R. O. Duda and P. E. Hart, *Use of the Hough Transformation to Detect Lines and Curves in Pictures*, Commun. ACM **15** no. 1, (1972) 11–15.

`http://doi.acm.org/10.1145/361237.361242`. (Cited on page 51.)

[140] K. G. Wilson, *Confinement of quarks*, Phys. Rev. D **10** (1974) 2445–2459. `https://link.aps.org/doi/10.1103/PhysRevD.10.2445`. (Cited on page 52.)

[141] M. Cacciari, G. P. Salam, and G. Soyez, *The anti- k t jet clustering algorithm*, Journal of High Energy Physics **2008** no. 04, (2008) 063. `http://stacks.iop.org/1126-6708/2008/i=04/a=063`. (Cited on pages 52 and 61.)

[142] The ATLAS Collaboration, *Properties of Jets and Inputs to Jet Reconstruction and Calibration with the ATLAS Detector Using Proton-Proton Collisions at* $\sqrt{s}$ *= 13 TeV*. ATL-PHYS-PUB-2015-036, 2015. `http://cds.cern.ch/record/2044564`. (Cited on page 53.)

[143] ATLAS Collaboration, *Jet energy measurement and its systematic uncertainty in proton-proton collisions at* $\sqrt{s}$ *= 7 TeV with the ATLAS detector*, `arXiv:1406.0076 [hep-ex]`. (Cited on page 53.)

[144] ATLAS Collaboration, M. Aaboud et al., *Jet energy scale measurements and their systematic uncertainties in proton-proton collisions at* $\sqrt{s} = 13$ TeV *with the ATLAS detector*, Phys. Rev. D **96** (2017) 072002. `https://link.aps.org/doi/10.1103/PhysRevD.96.072002`. (Cited on pages 53 and 55.)

[145] ATLAS Collaboration, G. Aad et al., *Performance of pile-up mitigation techniques for jets in* pp *collisions at* $\sqrt{s} = 8$ *TeV using the ATLAS detector*, Eur. Phys. J. **C76** no. 11, (2016) 581, `arXiv:1510.03823 [hep-ex]`. (Cited on page 53.)

[146] ATLAS Collaboration, G. Aad et al., *Performance of* b*-Jet Identification in the ATLAS Experiment*, JINST **11** no. 04, (2016) P04008, `arXiv:1512.01094 [hep-ex]`. (Cited on page 53.)

[147] ATLAS Collaboration, M. Aaboud et al., *Measurements of b-jet tagging efficiency with the ATLAS detector using* $t\bar{t}$ *events at* $\sqrt{s} = 13$ *TeV*, JHEP **08** (2018) 089, `arXiv:1805.01845 [hep-ex]`. (Cited on pages 53 and 54.)

[148] ATLAS Collaboration, M. Aaboud et al., *Performance of missing transverse momentum reconstruction with the ATLAS detector using proton-proton collisions at* $\sqrt{s}$ *= 13 TeV*, Eur. Phys. J. **C78** no. 11, (2018) 903, `arXiv:1802.08168 [hep-ex]`. (Cited on pages 55 and 56.)

[149] S. Agostinelli et al., *GEANT4: A simulation toolkit*, Nucl. Instrum. Meth. **A506** (2003) 250–303. (Cited on page 57.)

[150] *HZZ Derivation Framework*. `https://twiki.cern.ch/twiki/bin/view/AtlasProtected/HiggsZZstarRun2OldDerivation2016`. (Cited on page 58.)

[151] P. Nason, *A new method for combining NLO QCD with shower Monte Carlo algorithms*, JHEP **0411** (2004) 040, `arXiv:hep-ph/0409146 [hep-ph]`. (Cited on page 58.)

[152] T. Sjöstrand, S. Mrenna and P. Z. Skands, *A Brief Introduction to PYTHIA 8.1*, Comput.Phys.Commun. **178** (2008) 852–867, `arXiv:0710.3820 [hep-ph]`. (Cited on page 58.)

[153] LHC Higgs Cross Section Working Group, *Handbook of LHC Higgs Cross Sections: 3. Higgs Properties: Report of the LHC Higgs Cross Section Working Group*, Tech. Rep. arXiv:1307.1347. CERN-2013-004, Geneva, 2013. `https://cds.cern.ch/record/1559921`. Comments: 404 pages, 139 figures, to be submitted to CERN Report. Working Group web page: https://twiki.cern.ch/twiki/bin/view/LHCPhysics/CrossSections. (Cited on page 58.)

[154] T. Gleisberg et al., *Event generation with SHERPA 1.1*, JHEP **02** (2009) 007, `arXiv:0811.4622 [hep-ph]`. (Cited on page 60.)

[155] J. Alwall et al., *The automated computation of tree-level and next-to-leading order differential cross sections, and their matching to parton shower simulations*, JHEP **1407** (2014) 079, `arXiv:1405.0301 [hep-ph]`. (Cited on page 60.)

[156] ATLAS Egamma Combined Performance Group, *Electron Identification*. `https://twiki.cern.ch/twiki/bin/view/AtlasProtected/EGammaIdentificationRun2#Electron_identification`. (Cited on page 60.)

[157] ATLAS Collaboration, *Electron reconstruction and identification efficiency measurements with the ATLAS detector using the 2011 LHC proton–proton collision data*, Eur. Phys. J. C **74** (2014) 2941, `arXiv:1404.2240 [hep-ex]`. (Cited on page 60.)

[158] ATLAS Muon Combined Performance Group, *MCPAnalysisGuidelinesMC15*. `https://twiki.cern.ch/twiki/bin/view/AtlasProtected/MCPAnalysisGuidelinesMC15`. (Cited on page 61.)

[159] ATLAS Collaboration, *Muon reconstruction performance of the ATLAS detector in proton–proton collision data at* $\sqrt{s} = 13$ *TeV*, Eur. Phys. J. C **76** (2016) 292, `arXiv:1603.05598 [hep-ex]`. (Cited on page 61.)

[160] ATLAS Collaboration, *Jet Calibration and Systematic Uncertainties for Jets Reconstructed in the ATLAS Detector at* $\sqrt{s}$*=13 TeV*. ATL-PHYS-PUB-2015-015, 2015. `https://cds.cern.ch/record/2037613`. (Cited on pages 61 and 95.)

[161] The ATLAS Collaboration, *Commissioning of the ATLAS b-tagging algorithms using* $t\bar{t}$ *events in early Run-2 data*. ATL-PHYS-PUB-2015-039, 2015. `http://cds.cern.ch/record/2047871`. (Cited on page 62.)

[162] The ATLAS Collaboration, *Expected performance of missing transverse momentum reconstruction for the ATLAS detector at* $\sqrt{s}$ *= 13 TeV*. ATL-PHYS-PUB-2015-023, 2015. `http://cds.cern.ch/record/2037700`. (Cited on pages 62 and 95.)

[163] The ATLAS Collaboration, *Study of* $\ell^+\ell^-+E_T^{miss}$*final state in HZZ group with proton–proton collisions at* $\sqrt{s}$ *= 13 TeV: objects definition and background estimation*. ATL-COM-PHYS-2015-1275, 2016. `https://cds.cern.ch/record/2058246/`. (Cited on page 64.)

[164] ATLAS Collaboration, *Search for an invisibly decaying Higgs boson or dark matter candidates produced in association with a* Z *boson in* pp *collisions at* $\sqrt{s} = 13$ *TeV with the ATLAS detector*, Tech. Rep. ATL-COM-PHYS-2017-283, CERN, Geneva, Mar, 2017.

`https://cds.cern.ch/record/2256304`. Paper Draft for H->ZZ->llnn Low Mass Analysis targeting for Summer 2017. (Cited on pages 67, 68, 69, 70, 76, 80, 101, and 106.)

[165] M. Grazzini, S. Kallweit, S. Pozzorini, D. Rathlev, and M. Wiesemann, *W+W- production at the LHC: fiducial cross sections and distributions in NNLO QCD*, Journal of High Energy Physics **2016** no. 8, (2016) 140. `http://dx.doi.org/10.1007/JHEP08(2016)140`. (Cited on page 73.)

[166] M. Grazzini, S. Kallweit, and D. Rathlev, *Status of diboson production in NNLO QCD*, in *Proceedings, 12th International Symposium on Radiative Corrections (Radcor 2015) and LoopFest XIV (Radiative Corrections for the LHC and Future Colliders): Los Angeles, CA, USA, June 15-19, 2015*. 2016. `arXiv:1601.06036 [hep-ph]`. `https://inspirehep.net/record/1416662/files/arXiv:1601.06036.pdf`. (Cited on page 73.)

[167] J. Meyer, S. Heim, and R. Di Nardo, *Theoretical uncertainties and inputs occurring in H→ZZ analyses*, Tech. Rep. ATL-COM-PHYS-2015-1278, CERN, Geneva, Oct, 2015. `https://cds.cern.ch/record/2058253`. Authors: The HZZ group. (Cited on pages 73 and 97.)

[168] F. Caola et al., *QCD Corrections to W^+W^- production through gluon fusion*, `arXiv:1511.08617 [hep-ph]`. (Cited on page 73.)

[169] F. Caola et al., *QCD Corrections to ZZ Production in Gluon Fusion at the LHC*, Phys. Rev. D92.9 **D92.9** (2015) 094028, `arXiv:1509.06734 [hep-ph]`. (Cited on page 73.)

[170] Kirill Melnikov, Matthew Dowling, *Production of two Z-bosons in gluon fusion in the heavy top quark approximation*, Phys. Lett. B **744** (2015) 43–47, `arXiv:1503.01274 [hep-ph]`. (Cited on page 73.)

[171] Marco Bonvini, Fabrizio Caola, Kirill Melnikov, Giovanni Ridolfi, *Signal-background intereference effects for $gg \to H \to W^+W^-$ beyond leading order*, Phys. Lett. D **88** (2013), `arXiv:1304.3053 [hep-ph]`. (Cited on page 73.)

[172] Sheng Li et al., *Soft gluon resummation in the signal-background interference process of* $gg \to h* \to ZZ$, JHEP (2015), `arXiv:1504.02388v2 [hep-ph]`. (Cited on page 73.)

[173] HZZ Group, *Theoretical Uncertainties Occurring In $H \to ZZ$ analyses*. `https://cds.cern.ch/record/2232040`. (Cited on pages 74 and 97.)

[174] ATLAS Collaboration, *Luminosity Determination Using the ATLAS Detector*. ATLAS-CONF-2010-060, 2010. `https://cds.cern.ch/record/1281333`. (Cited on page 94.)

[175] ATLAS Collaboration, *Energy calibration prerecommendation for Run 2*. `https://cds.cern.ch/record/2060328`. (Cited on page 94.)

[176] G. Watts, F. Filthaut, G, Piacquadio, *Extrapolating Errors for b-tagging*. ATL-COM-PHYS-2015-711. `https://cds.cern.ch/record/2034234`. (Cited on page 95.)

[177] G. Cowan, K. Cranmer, E. Gross, and O. Vitells, *Asymptotic formulae for likelihood-based tests of new physics*, Eur. Phys. J. **C71** (2011) 1554, `arXiv:1007.1727 [physics.data-an]`. [Erratum: Eur. Phys. J.C73,2501(2013)]. (Cited on page 98.)

[178] L. Breiman, J. H. Friedman, R. A. Olshen, and C. J. Stone, *Classification and regression trees*. The Wadsworth statistics/probability series. Wadsworth & Brooks/Cole Advanced Books & Software, Monterey, CA, 1984. `https://cds.cern.ch/record/2253780`. (Cited on page 107.)

[179] S. R. Christian Boser, Simon Fink. `https://indico.scc.kit.edu/event/48/contributions/3410/attachments/1690/2312/BDT_KSETA_Freudenstadt.pdf`. (Cited on pages 108 and 109.)

[180] A. Hocker et al., *TMVA - Toolkit for Multivariate Data Analysis*, `arXiv:physics/0703039 [physics.data-an]`. (Cited on pages 108 and 115.)

[181] M. Stone, *Cross-Validatory Choice and Assessment of Statistical Predictions*, Journal of the Royal Statistical Society. Series B (Methodological) **36** no. 2, (1974) 111–147. `http://www.jstor.org/stable/2984809`. (Cited on page 109.)

[182] S. Geisser, *The Predictive Sample Reuse Method with Applications*, Journal of the American Statistical Association **70** no. 350, (1975) 320–328. `http://www.jstor.org/stable/2285815`. (Cited on page 109.)

[183] D. M. Allen, *The Relationship between Variable Selection and Data Agumentation and a Method for Prediction*, Technometrics **16** no. 1, (1974) 125–127. `http://www.jstor.org/stable/1267500`. (Cited on page 109.)

[184] J. P. Egan, *Signal detection theory and ROC-analysis*. New York : Academic Press, 1975. Includes bibliographies and index. (Cited on page 113.)

[185] L. Mascetti et al., *Disk storage at CERN*, J. Phys. Conf. Ser. **664** no. 4, (2015) 042035. (Cited on page 133.)

[186] ATLAS Collaboration, D. Adams et al., *The ATLAS Computing Model*,. (Cited on page 133.)

[187] S. Mattig, *The online luminosity calculator of ATLAS*, J. Phys. Conf. Ser. **331** (2011) 022035. (Cited on page 134.)

[188] A. Valassi et al., *LCG persistency framework (CORAL, COOL, POOL): Status and outlook*, J. Phys. Conf. Ser. **331** (2011) 042043. (Cited on page 134.)

[189] S. Albrand, J. Fulachier, and F. Lambert, *The ATLAS metadata interface*, J. Phys. Conf. Ser. **219** (2010) 042030. (Cited on page 134.)

[190] P. Calafiura, W. Lavrijsen, C. Leggett, M. Marino and D. Quarrie, *The athena control framework in production, new developments and lessons learned,*. (Cited on page 134.)

[191] M. Cattaneo et al., *Status of the GAUDI event-processing framework*, CHEP 2001 **Proceedings.** (2001) 757. (Cited on pages 134 and 135.)

[192] P. Calafiura, C. G. Leggett, D. R. Quarrie, H. Ma, and S. Rajagopalan, *The StoreGate: A Data model for the Atlas software architecture*, eConf **C0303241** (2003) MOJT008,

`arXiv:cs/0306089 [cs-se]`. (Cited on page 136.)

[193] A. Buckley, T. Eifert, M. Elsing, D. Gillberg, K. Koeneke, A. Krasznahorkay, and E. Moyse, *Report of the xAOD design group*, Tech. Rep. ATL-COM-SOFT-2013-022, CERN, Geneva, Sep, 2013. `https://cds.cern.ch/record/1598793`. (Cited on page 136.)

[194] ATLAS Collaboration, M. Aaboud et al., *Search for resonances in diphoton events at* $\sqrt{s}$*=13 TeV with the ATLAS detector*, JHEP **09** (2016) 001, `arXiv:1606.03833 [hep-ex]`. (Cited on page 146.)

[195] CMS Collaboration, *Search for new physics in high mass diphoton events in* $3.3\ \mathrm{fb}^{-1}$ *of proton-proton collisions at* $\sqrt{s} = 13$ TeV *and combined interpretation of searches at* 8 TeV *and* 13 TeV,. (Cited on page 146.)

[196] ATLAS Collaboration, *Search for scalar diphoton resonances with 15.4 fb*$^{-1}$ *of data collected at* $\sqrt{s}$*=13 TeV in 2015 and 2016 with the ATLAS detector*, Tech. Rep. ATLAS-CONF-2016-059, CERN, Geneva, Aug, 2016. `https://cds.cern.ch/record/2206154`. (Cited on page 148.)

Acknowledgments

Fashionably late, I reached the final chapter of this scientific and personal journey. So many things have changed since the day I first landed in the Netherlands, little I did know about what was waiting for me. I would have not be able to reach this moment without the contribution of all the people I met along my way. I would like to thank first of all my promoter Paul de Jong and my supervisor David Berge. Paul, especially in the last year, you were always available and ready to help, guiding me in one of the most difficult period of this journey. I really would like to thank you for your patience and wise guidance. David, since the very beginning we went along very well and when the time was tough you never gave up on me. I really appreciate that you invited me in Berlin in the last months to work close to you to finish the thesis. I also want to thanks the members of the committee for the time and efforts they spent in reading my thesis and preparing for my defense.

Along all these years I worked on different projects with different people, it is impossible to thank everyone but I will try my best. From the TADA team I would like to thank Markus Elsing, Till Eifert and Elmar. Markus you always have been a role model, inspiring and enthusiastic, always ready to push the line one step further. Working with you has been a pleasure and an honor. Another big thank goes to Elmar, my TADA sparring partner. We had so much work and so much fun in order to migrate that code! Thanks for sharing so many nice moments, chats and lunches at R1. Another thank goes to Attila, you did not know me, I was not your responsibility, but you answered all my questions and emails all the time. The time has come to thank my analysis group...I would like to start from the Victoria people: Alison, Kayla, Monica. Alison, thanks for welcoming me and sharing with me all these hours of work, discussion and confrontation. Kayla, it was nice and crazy to work together as editors of the note with nine time zone difference between us. Monica, thanks for all the advises and suggestions about the analysis. I would like to thank the Oxford people especially my step-supervisor Giacomo and the sparring partner I always wanted but I never had Mariyan. Giacomo, I really appreciated all the help you gave me and the discussion we had especially on the development of my solo project on the BDT. Mariyan thanks for the chats, the help and the nice time we had in Geneva together. A special mention goes to my friend Francesco Lo Sterzo aka “The Grasshopper” (Cicala). We never worked together but you were there for me at 09:00 AM to have breakfast at R1. Thanks for your friendship and advice in the moment I needed it the most.

It is also time to thank the big NIKHEF family. A big thanks goes to my paranymph Broos. In my last year at NIKHEF we shared the office and so many talks, fun, lunch break at the gym. I hope I was able to teach you one of the most important skills needed to be a successful PhD at NIKHEF: how to play table soccer! A special thanks goes to David Salek and Marcus Morgenstern. David, we had so much fun especially in the first years: beers on a skyscraper in Chicago, dinners, concerts together! We had a great time. Marcus, thanks for all the chats and help you gave me for my BDT project, but do not think I forgot you still owe me a pizza for your lost bet on Trump election! One day we will go to Luigia and we will fix that. Thanks also to Wouter, we shared the isolation office room at CERN and we made the best out of it. Thanks for all the nice chats and funny jokes. A special mention goes to Bram, I met you few months before leaving Amsterdam but we shared really great moments. Thanks for welcoming me in your life and for all the great parties we went together. I would like to thank the members of the PhD council of which I was proudly part of for 3 years: Alice, Stergios(e) and especially Joris(e). Joris, thanks for your friendship, laughs, and evening outs. Another thanks goes to the Numerieke Natuurkunde group, in particular to Ronald with whom I worked two years in a row as a teacher assistant. I would like now to thank all the personal department members that made my life easier especially Ed and Natalie. You both helped me a lot for the housing, bureaucracy and any possible problem I had, thanks! A final thanks goes to all the PhD comrades who fought at my side over the years in good and bad times, among them: Tim, Peo, Ivan, Mark, Zappon, Priscilla, Tiseni, Castelli, il giovane Melini, Hartger.

Now it is time to thank the people that helped me outside of my work environment. The first thanks goes to my friend and paranymph, Andre. We shared so much along the years: chats, trips, dinners, long political discussions. These chats were rare gems and the ultimate antidote against what we were exposed to on an everyday base. I will always remember the day I was leaving Amsterdam, even if we were at odds, you came to wish me luck and it was a new beginning for us. Thanks for all the whiskey and the hutspot we had together and for your loyal friendship. Another thank goes to my “hippie step family” in Amsterdam: Inge and Mau. Even if sometimes we had divergences in the way we see the world, we had so much fun and we went to so many parties and shared so many great moments together. You let me feel always welcomed and you exposed me to a different reality and for this I will be always grateful, Dank u wel! A special mention goes to Mira, Agnes and Julian. Mira, you were close to me in one of my darkest moment, thanks. Agnes, I really appreciated our chats at the university about the PhD and your support. Julian, my patient zero, it has been a pleasure to teach you, to know you and to share moments of my life with you. You hosted me when I had no place to go. Nicolas, thanks for helping me with the moving and for the nice chats about classical music, mathematics and physics. Valeria, where I would be without your support? Honestly, you help me change so much in these years. I really appreciate all the work we did together and we still do. If I manage to reach this point is also thanks to you. I would like to thank my friends in Geneva: especially Alessandro, Oxana and Alexandra. Ale and Ksu, you are the sweetest and most beautiful couple I ever met in my life. You helped me in any possible ways and you were there when I needed it, thanks. Alex, mea fur cupri, you were and you still are one of the few persons I could open completely and be myself. Another great thanks goes to La Barra Argentina: Alejandro “maestro”, “el colo” Estaban y Alejandro Jaime. Gracias por estar a mi lado. I would like also to thank those great artists that were with me in the most difficult moments, among others: Luciano Pavarotti, Maria Callas, Paolo Conte, Anibal Troilo. When the code was crashing and the sky was grey “Casta Diva” or “Pour mon ame” arias always gave me hope, strength and the energy to keep going. The last but not the least thank goes to my family.

Mi siete sempre stati vicino sopportandomi e supportandomi. Mi avete accolto dopo anni a casa vostra e mi avete sempre aiutato, questo e’ anche un vostro successo.